Fluorescent Proteins: Spectroscopic Studies, Microfluidic Analysis, and Generation of Improved Variants.

by

Kevin M. Dean

B.A., Willamette University, 2006

A thesis submitted to the

Faculty of the Graduate School of the

University of Colorado in partial fulfillment

of the requirements for the degree of

Doctor of Philosophy

College of Arts & Sciences Department of Chemistry & Biochemistry

2013

This thesis entitled:
Fluorescent Proteins: Spectroscopic Studies, Microfluidic Analysis, and Generation of Improved Variants.
written by Kevin M. Dean
has been approved for the College of Arts & Sciences Department of Chemistry & Biochemistry

Amy E. Palmer

Ralph Jimenez

Date

The final copy of this thesis has been examined by the signatories, and we find that both the content and the form meet acceptable presentation standards of scholarly work in the above mentioned discipline.

Dean, Kevin M. (Ph.D., Biochemistry)

Fluorescent Proteins: Spectroscopic Studies, Microfluidic Analysis, and Generation of Improved Variants.

Thesis directed by Prof. Amy E. Palmer

Fluorescent proteins (FPs) are powerful tools that permit real-time visualization of cellular processes. The utility of a given FP for a specific experiment depends strongly on its effective brightness, and propensity to undergo photodegradation and dark-state conversion. However, photobleaching of fluorescence is a complex phenomenon that depends on a variety of experimental and environmental factors. Under single-molecule conditions, FPs are particularly subject to photobleaching, emitting 10-100× less photons than their small-molecule counterparts. Here, we present methodology that can be used to measure irreversible photobleaching, its adaptation for high-throughput microfluidics-based directed evolution, and its use in the development of improved Red FPs (RFPs). Progress towards incorporation of frequency-domain fluorescence lifetime assays is also discussed. Given the quantitative and high-throughput nature of the microfluidic photobleaching platform, this technology complements existing methods for fluorescent protein selection, thereby facilitating the development of next-generation RFPs for single-molecule research.

Dedication

To my friends and family, both past and present, for whom none of this would have been possible without.

Acknowledgements

"It takes a village to raise a child" - Few proverbs ring more true, and as such, I owe a great deal of gratitude to the many people who have helped guide me along my way. First, I would like to acknowledge my parents, Bruce and Margaret Dean, who from a very early age taught me the value of hard-work. Their guidance and support has never been taken for granted. To my grandparents, Jack and Pat Dean, and Frank and Gene Rizzo, for providing me with a sense of history, companionship, and endless support. To my siblings, Eric Slabaugh, Tracy Grafton and Joanna Dean, for being both friends, and family. I'd also like to thank Gary and Carol Wheeler, who treated me as a son, and were involved in my life from nearly the very start. To the city of Weed, CA, for being home, and for also being home to so many truly caring people.

I also would like to express my appreciation for my friends, all of whom constantly made me smile. First and foremost, I would like to thank Allison Dellwo, with whom I have shared many incredible experiences. From here, the list becomes long, but I would like to thank Skylar Swinford, Alex MacKenzie, Jeff Gazaille, Robert Hall, Geoff Bee, Ryan Wheeler, Gabe Bell, and Lea Witkowsky. To those who away always made me feel at home when I visited, including Ben Weyerhaeuser, Jimmy Williams, Jimmy Whiteley, Mike Plank, Megdy Khoury, Win Head, Dane Meier, Phil Dirt, Matt Perez, C.J. Washington, Josh Barker, Adam Beebe, Cameron Walton, Jose Rios, Fitz Paccione, Drew Lazzeri, Wes Randall, Calvin-Keyser Allen, Eki Yandall, Drew Lazzeri, Mitch MacCready, Elliot Bates, Travis Stiles, Dan Mackinnon, Phil Calibrese, Heather Hudson, Sarah Potts, Carly Santoro, Molly Engle, Erin Kerrigan, and more... Last but not least, Luna, for reminding me to take a walk every once in a while.

I would also like to acknowledge those who have helped educate me, especially those who made particularly important contributions. Specifically, I would like to thank Mr. John Soletti, who made it clear

from the onset that he expected my very best both on and off of Weed High School's campus. To the endless number of coaches who taught me to stay low, and to keep my feet moving - a metaphor that is just as true in life, as in football. My appreciation also goes out to Dr. David E. Goodney, who triggered my passion for Chemistry the moment I stepped into the classroom at Willamette University. I am also particularly grateful for Dr. J. Charles Williamson for hiring me as a sophomore to work in his lab, for teaching me not only thermodynamics and quantum mechanics, but also how to use a lathe, how to design an experiment critically, and for helping me with my first peer-reviewed manuscripts. Willamette University was truly an amazing place to receive an education, and many more faculty and staff deserve recognition, including Chuck Myers, Nancy Norton, Gordy James, Glenn Fowles, Dr. Ortwin Knorr, Dr. Alexandra Opie, Dr. Sarah Kirk, Dr. Karen McFarlane Holman, and Dr. Colin Starr. You are all living examples of the university motto, *non nobis solum anti sumus*.

I am also infinitely thankful for the wonderful environment that the University of Colorado at Boulder has provided me with. I am lucky to have had the support of a fantastic department, with such great faculty, staff, post-docs, graduate-students, and undergraduates. Much of what I did was with the help of a talented lab-partner, Dr. Jennifer Lubbeck. Our work together, and late nights running microfluidics with music shaking the walls of JILA, will not be forgotten. I also greatly appreciate Dr. Ralph Jimenez, for treating me as if I were his own graduate student, providing me with excellent advice, great feedback, and all the while, watching our experiments with genuine excitement.

Lastly, I would like to thank Dr. Amy E. Palmer, who managed to inspire, guide, and enable me. Any attempt to accurately articulate my appreciation for her would likely fall short. As such, I can only say thank you.

Contents

Chapter

Tables

Table

Figures

Figure

Chapter 1

Introduction

1.1 Publication Status and Author Contributions

Dean, K.M., Qin, Y., Palmer, A.E. Visualizing Metal Ions in Cells: An Overview of Analytical Techniques, Approaches, and Probes. *Biochim. Biophys. Acta.* 2012. Sep;1823(9)1406-15.

K.M.D., Y.Q, and A.E.P wrote the paper. The section "Methods for Labeling Cellular Structures" was adapted for this dissertation.

1.2 History of Fluorescent Proteins

In the early 1960's, while attempting to isolate luciferin and luciferase from *Aequorea victoria* off the coast of Seattle, WA, Osamu Shimomura discovered a pH-inhibitable and Ca^{2+}-responsive bioluminescent protein in cell-free extracts [1]. Later named Aequorin, this protein copurified with trace amounts of another protein, that when excited with blue light, fluoresced green. After many years, and 10's of thousands of jellyfish, Shimomura unexpectedly discovered that the fluorescent moiety in "green protein" was generated following oxidation and dehydration of the protein chain (structure shown in Figure 1.3D) [2]. Following this discovery, reported in 1979, it would take an additional 13 years for Douglas Prasher, while working at Wood's Hole, to publish the nucleotide sequence for green-fluorescent protein (GFP) [3]. Even in 1992, Prasher envisioned that GFP, by genetically fusing it to other proteins, would enable fluorescent imaging of gene-expression in living organisms.

Prasher would go on to collaborate with Martin Chalfie, who was interested in mechanotransduction in

C. elegans. For years, Chalfie had relied upon immunofluorescence, *in situ* hybridization, and β-galactosidase to image nematodes, all methods that required extensive sample preparation and fixation. However, upon receiving the DNA for GFP, and with a stroke of luck, Chalfie managed to express GFP in bacteria, and shortly thereafter, in touch receptor neurons within living nematodes [4]. In doing so, Chalfie dispelled the hypothesis that other enzymes were necessary for GFP's fluorescence. Nevertheless, inspired principally by nematode mechanotransduction, Chalfie quickly refocused his efforts back towards biology and the use, rather than development, of GFP.

Around the same time that Chalfie began collaborating with Prasher, Roger Tsien, at the University of California San Diego, also became interested in GFP. Inspired by the need to measure cyclic adenosine 3',5'-monophosphate (cAMP), Tsien envisioned fusing different color fluorescent proteins to separate domains in Protein Kinase A (PKA), and relying upon Förster resonance energy transfer (FRET) to report on conformational changes in the presence and absence of cAMP. To these means Tsien enlisted a post-doc by the name of Roger Heim, who subjected GFP to random mutagenesis, and immediately discovered mutations that altered the hue and brightness of GFP [5–7]. In this brief moment, Tsien and coworkers had begun setting the stage for a renaissance in cellular imaging, where GFP not only used to image molecules in cells, but "sensed" them too [8–10]. Two atomic resolution structures of GFP soon followed [11, 12], and uninterrupted development of GFP and GFP-homologues has continued ever since.

At the onset of 1999, researchers had a variety of fluorescent proteins that could be used to mark gene expression, follow cell lineage, sense cellular processes, and much more. However, the unexpected discovery of homologous fluorescent proteins in sea coral, with ≈ 70 nm red-shifted absorption relative to GFP, triggered yet another revolution [13]. The protein, known as DsRed, followed a similar developmental trajectory as GFP. First, it's biochemical properties were evaluated, revealing that DsRed existed as an obligate tetramer [14], and that its chromophore underwent a second oxidation reaction, generating an acylimine moiety, to provide additional electron conjugation [15]. DsRed's atomic structure was solved, paving the way for structure-guided mutagenesis [16, 17]. Then, through methodical work, mutagenesis overcame many of DsRed's limitations, including slow and incomplete chromophore maturation and oligomerization, resulting in the creation of the first monomeric red fluorescent protein [18, 19]. Mutagenesis has continued at a fever

pace since 2002, both on descendants of DsRed, as well as RFPs from other homologous organisms, resulting in a "palette" of fluorescent proteins that now spans from ultraviolet to the red [20–27].

1.3 Structure and Function of Fluorescent Proteins

Fluorescent proteins are composed of an 11-stranded β-barrel with a chromophore-containing central α-helix (Figure 1.1). The β-barrel is ≈ 2.5 nm in diameter, and ≈ 4 nm in height. Each β-strand is connected either through loops at the top or bottom of the protein, or through the central α-helix. The overall protein follows a canonical anti-parallel β-sheet structure, with excellent hydrogen-bonding distances ($\approx$ 2.9 Å) between adjacent β-strands, with the exception of the interface between β-strands 7 and 10 (Apparent in Figure 1.1, left). The chromophore is perpendicular to the long-axis of the fluorescent protein, and largely protected from solvent [11]. In RFPs, the original proteins existed as tightly bound and symmetric tetramers, with A/B and A/C interfaces.

Chromophore formation is a multistep oxygen-dependent process that appears to be initiated by protein-folding-induced distortions of the central α-helix [28]. In GFP, this maturation process is thought to proceed through a cyclized intermediate that is subsequently oxidized and then dehydrated (Figure 1.2) [29]. In RFPs, however, there is continuing debate about the details of chromophore formation. For example, the second oxidation step adds additional complexity to the reaction, and the presence of immature "GFP-like" chromophores has confounded results. Initially the GFP-like chromophore was hypothesized to be an intermediate en route to a red chromophore [30]. However, recent evidence suggests that the GFP-like chromophore is a competitive reaction that occurs shortly after cyclization [31–34], and may be influenced by *cis-trans* isomerization of the Phe64/Gln66 peptide bond immediately adjacent to the chromophore tripeptide [35].

The chemical composition of the chromophore plays an important role in the photophysical attributes of the FP. The chromophore tripeptide, e.g., Ser65-Tyr66-Gly67 in wild-type GFP, can tolerate substitution within the first two positions, but not the third, due to its role in backbone cyclization. The second position, plays a major role in in altering the spectral properties (See Figure 1.3). For example, within the GFP context, position 66 has been mutated to a phenylalanine in UV-excitable FPs [36], histidine in blue FPs [5,37,

Figure 1.1: Crystal structure of GFP (Green, PDB 1EMA) and DsRed (Red, PDB 1G7K). Originally a monomer, GFP is $\approx$ 2.5 nm in diameter and $\approx$ 4 nm in height. The structure follows a canonical anti-parallel β-barrel with the exception of the β-sheet 7/10 interface, where a β-bulge interrupts the structure. All of the β-sheets are connected through loops at the top or bottom of the structure, or via the central α-helix. DsRed, originally a tetramer, is shown and one set of the A/B and A/C interfaces are highlighted.

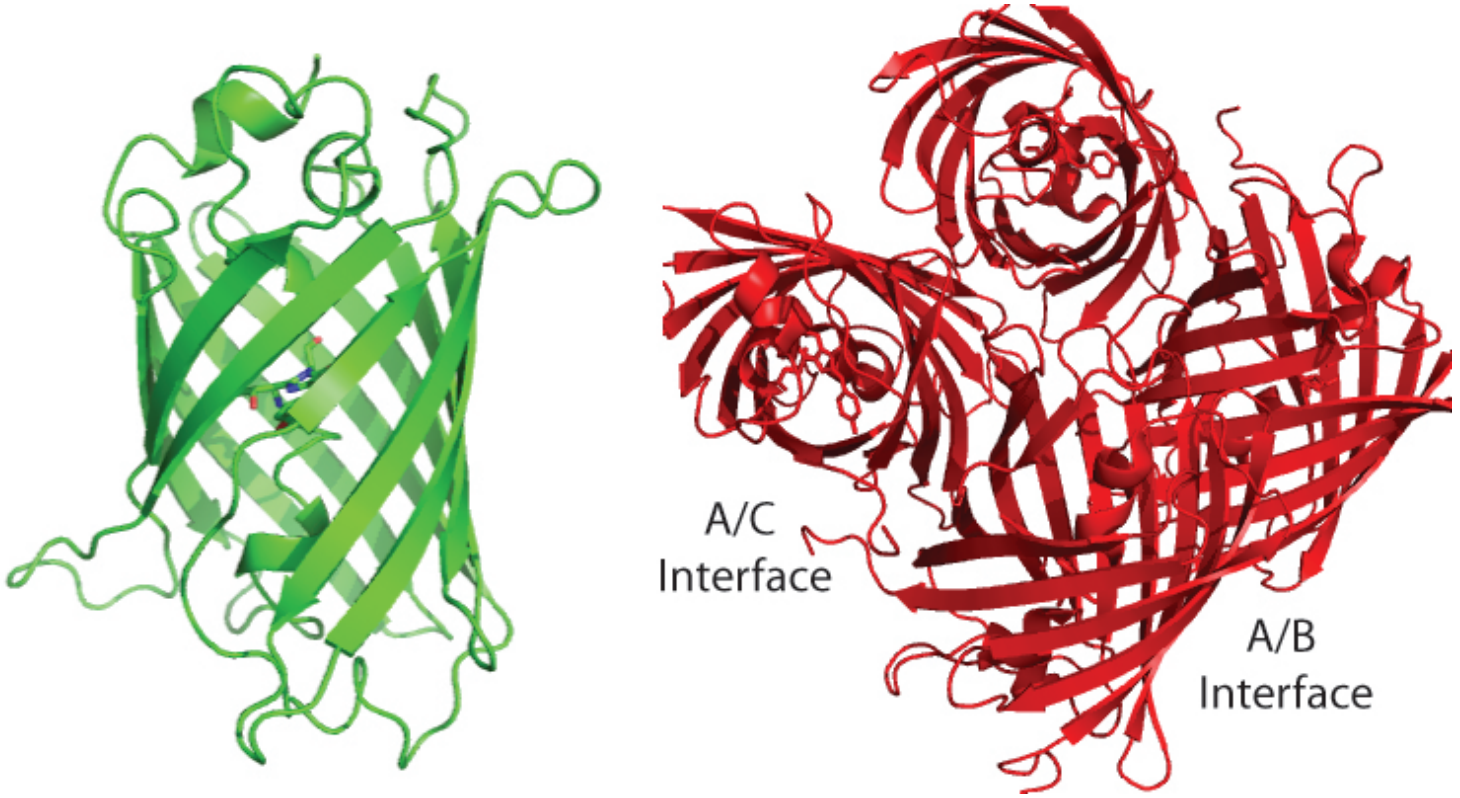

Figure 1.2: Chromophore formation in green and red emitting FPs. In GFP, chromophore formation is initiated by (A) cyclization of the peptide backbone, (B) formation of a high-energy enolate, (C) dehydration, (D) oxidation of the tyrosine β-carbon and (E) deprotonation of the tyrosine hydroxyl group. In RFPs, chromophore formation is thought to follow a similar pathway as GFP. RFP chromophore formation is (F) triggered through cyclization of the peptide chain, (G), formation of a high-energy enolate, (H) dehydration, (K) oxidation of the glutamine peptide backbone to create the acylimine moiety, (L) oxidation of the tyrosine β-carbon and (L) deprotonation of the tyrosine hydroxyl group. An additional pathway competes with acylimine formation, shown with the horizontal arrow between D and I, and accounts for the formation of a "GFP-like" population of chromophores. In both cases, formation of the enolate is stabilized through an electrostatic interaction with Arg96. Oxidation is carried out by molecular oxygen and produces stoichiometric amounts of H_2O_2. Figure adapted from [33].

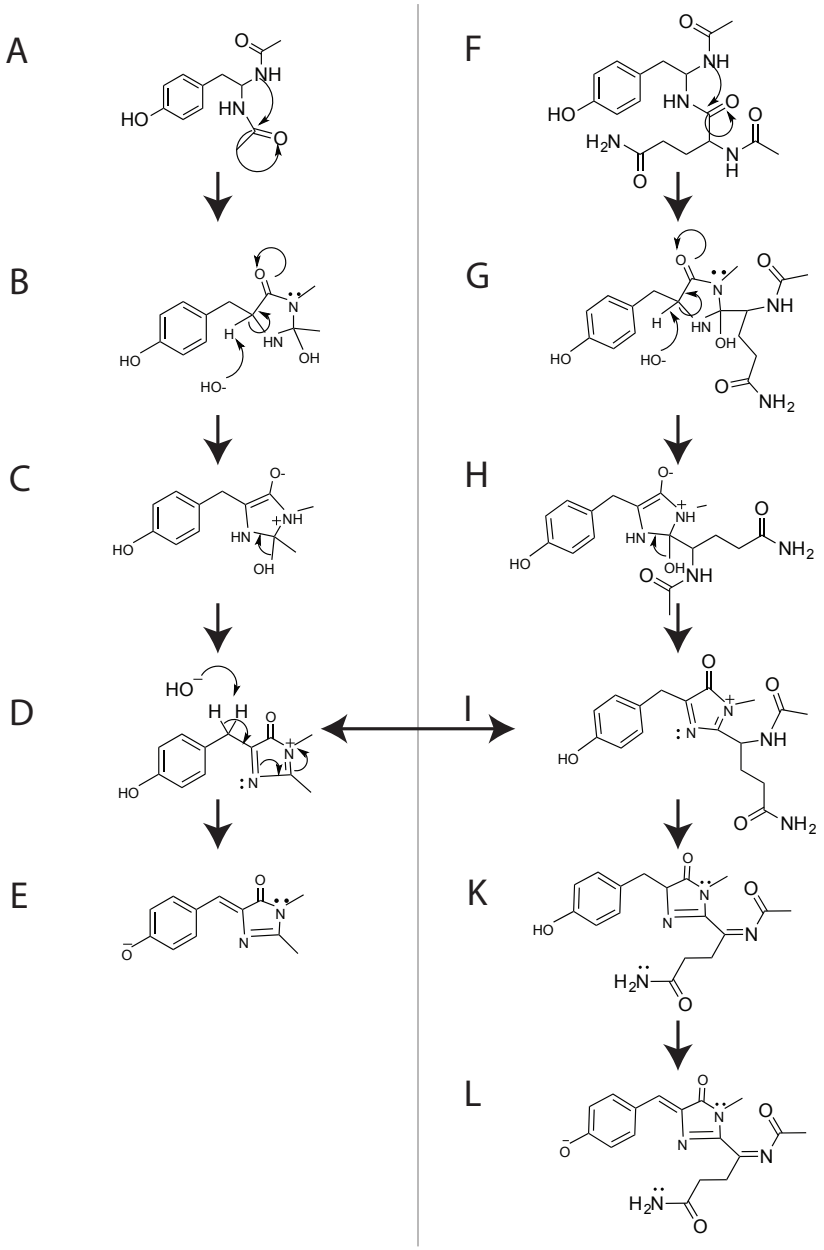

38], tryptophan in cyan FPs [5,39–41], and tyrosine in green and yellow FPs [6]. Within RFPs, this position is most commonly a tyrosine, but has also been mutated to leucine and phenylalanine in blue-fluorescent mutants [25], and tryptophan in yellow variants [20]. Interestingly, even with a tyrosine, combinations of mutations can be found that prevent oxidation of the tyrosine β-carbon, resulting in a UV-excitable blue-fluorescent mutant [25, 31]. The first residue also plays a role by altering the pKa of the chromophore [6], facilitating folding, subtly altering the excitation wavelength, or in the case of mOrange (Ser65) [20, 42], mOrange2 (Ser65) [23], and mKO (Cys64) [43,44], providing a nucleophile that undergoes an intramolecular cyclization reaction with the acylimine. The presence of a histidine at position 66 can also trigger light-activated β-elimination of the protein backbone, and has been used in a variety of photoactivatable FPs [45–48].

The immediate vicinity surrounding the chromophore also alters FP photophysics. For example, in the absence of protein matrix, the chromophore methylene bridge undergoes rapid *cis-trans* isomerization, and is thus non-fluorescent [49]. Mutations proximal to the chromophore can alter the planarity of the chromophore, influencing the extinction coefficient and quantum yield of fluorescence [42]. Mutations can uniquely influence the ground and excited-states, altering absorption, excitation, and emission wavelengths [50]. Residues can also engage in π-π or cation-π interactions, as is found in yellow and far-red fluorescing FPs [26, 51–53]. The chromophore environment can promote excited-state proton relays, which occurs in wild-type GFP [54, 55], UV-excitable yet green-fluorescent variants (e.g., T-Sapphire FP) [56], and RFPs engineered for long Stokes shifts [57, 58]. Local electrostatic interactions with the chromophore can alter the absorption wavelength through a quadratic Stark effect [59], also potentially altering chromophore bond-lengths [60]. Different local environments for *cis* and *trans* chromophores can alter the protonation state of the p-hydroxybenzylidene moiety, permitting light-driven *cis-trans* isomerization and reversible photoswitching [61,62]. Lastly, substitutions in the vicinity of the chromophore can enable functional light-driven chemistry, including chromophore assisted light inactivation [63–65], decarboxylation in photoactivatable-GFP [66, 67], and photoconversion in PAmOrange2 [27, 68].

Although there is substantial evidence of its importance, the role of the more distal parts of FPs role in photophysics is more challenging to interpret [69]. Presumably through improvements in the folding efficiency

Figure 1.3: Chemical structures of common chromophores. (A) Phenylalanine-based chromophore found in UV-excitable blue FPs. λ_{ex}=355 nm, λ_{em}=424 nm. [36](B)Histidine-based chromophores found in blue FPs. λ_{ex}=380 nm, λ_{em}=446 nm. [5, 37, 38](C) Tryptophan-based chromophore found in cyan FPs. λ_{ex}=433 nm, λ_{em}=475 nm. [5, 39–41](D) Standard tyrosine-based chromophore. In cases where the phenolic chromophore is deprotonated, λ_{ex}=488 nm, λ_{em}=507 nm. If the phenolic chromophore is protonated, λ_{ex}=405 nm, λ_{em}=507 nm. If π-π stacking with another tyrosine, as found in yellow FPs, λ_{ex}=514, λ_{em}=528. (E) Non-conjugated tyrosine chromophores found in near-UV excitable blue FPs. λ_{ex}=399 nm, λ_{em}=456 nm. [25, 31](F) Tricyclic chromophore found in mOrange1, mOrange2, and mKO. λ_{ex}=548 nm, λ_{em}=559 nm. [20, 23, 42–44] (G) Tyrosine-based chromophore with histidine in the first amino-acid position. Following absorption of high energy light ($\lambda_{ex} \approx$ 405 nm), peptide oxidation and fragmentation places histidine in conjugation with the remainder of the protein, red-shifting the excitation and emission. Found in photoactivatable FPs, including Eos, and Kaede [45–48]. λ_{ex}=508 nm, λ_{em}=518 nm. prior to photoactivation, and λ_{ex}=572 nm, λ_{em}=582 nm. following photoactivation. (H) Standard tyrosine-based RFP chromophore. λ_{ex}=580 nm, λ_{em}=610 nm [42]

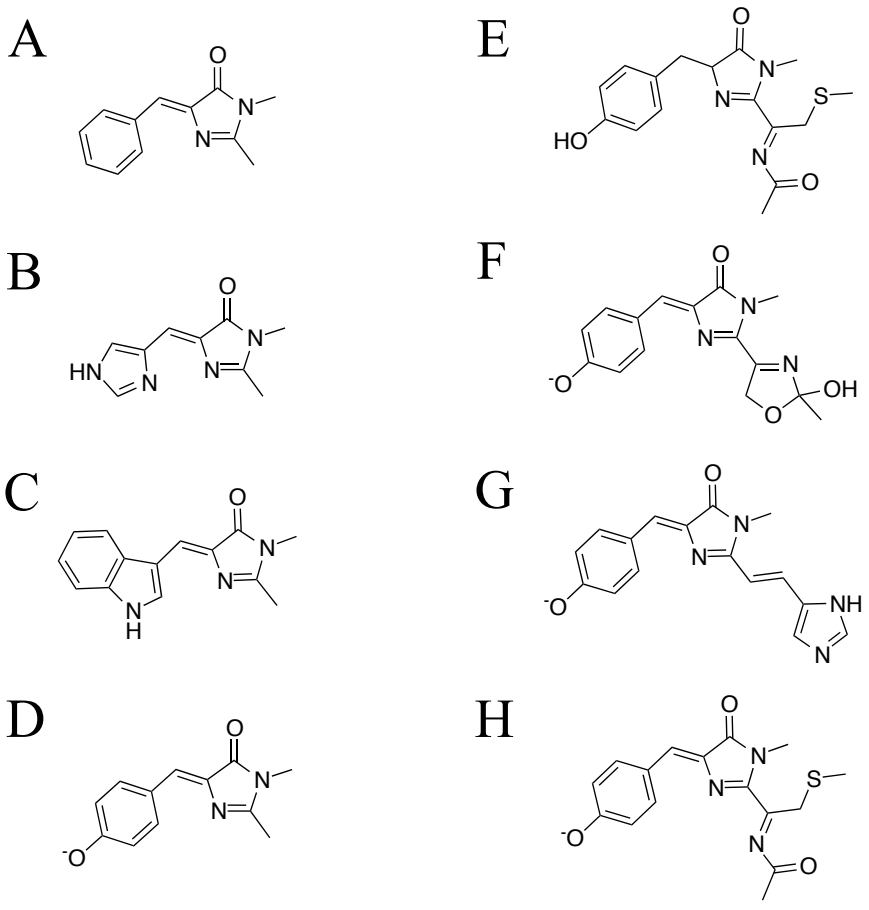

.

and chromophore maturation, mutations can result in improved fluorescence yield, while not altering the measured extinction coefficient or quantum yield [70,71]. Furthermore, improved stability appears to permit fusion to a greater repertoire of proteins, with greater tolerance for chemically challenging environments (e.g., the secretory pathway). FPs with heightened stability are also more resilient to mutations, and can be subject to circular permutation [72], splitting for bimolecular fluorescence complementation [73], and even global alteration of its surface charge [74]. Breathing motions in β-sheets 7 and 10 is thought to facilitate oxygen entry in both chromophore maturation [75], and photobleaching [76]. Furthermore, the protein structure, by providing a thoroughly rigid scaffold, can increase the quantum yield of fluorescence [77]. Ultimately, all of these contributions, both local and distal, contribute to the fluorescent properties of FPs in ways that will continue to be elucidated for years to come.

1.4 Use of Fluorescent Proteins and Fluorophores for Labeling Cellular Structures

Fluorescent proteins revolutionized biomolecular imaging by allowing real-time visualization of cellular processes and structures with molecular specificity. Beyond traditional imaging, FPs have been tailored to "sense" cellular phenomena, including protein phosphorylation state, pH alterations, Ca^{2+} signaling, mitosis, and much more. These advances in imaging tools, as well as imaging methodology, has allowed our understanding of biology, biochemistry, and biophysics to reach the single-molecule level. These advances, given their widespread importance, have also triggered a revolution in alternative methods for labeling cellular structures.

When labeling biomolecular structures for live-cell imaging, there are three major fluorescence-based platforms from which one can choose: small-molecule fluorophores, fluorescent proteins, and hybrid probes that integrate small-molecule fluorophores with genetically encoded elements (e.g., SNAP-tag [78]). Each system offers its own advantages and disadvantages, including ease of use, brightness, specificity, and ability to be targeted to specific sub-cellular organelles and/or proteins. In general, no single probe (or class of probes) is likely to be the magic bullet, ideal for addressing the wide array of scientific questions related to quantitative and dynamic imaging of cells and tissues.

Small-molecule fluorophores (e.g., Cy3, AlexaFluor488, etc.) have large extinction coefficients, excellent quantum yields, high photon outputs prior to irreversible photobleaching, and can often be chemically and spectroscopically optimized for specific applications (e.g., super-resolution microscopy) [79–81]. Despite these advantages, small-molecule fluorophores must be introduced into the intracellular environment in a minimally invasive manner, and the most common method, immunofluorescence, typically requires chemical fixation of the sample under study. If the fluorophore is membrane permeable, introduction of the fluorophore can be accomplished by simply adding fluorophore into the extracellular media prior to imaging. However, given the charged nature of many fluorophores, electrostatic charge typically renders the fluorophore membrane impermeable. If the probe permits, partial neutralization of the charge by acetoxymethyl (AM) esters can facilitate translocation across the membrane and restoration of the native fluorophore after cleavage by intracellular esterases (Figure 1.4B) [82]. This approach has found widespread usage in several commercially available fluorophores, particularly Ca^{2+} indicators.

Other strategies include microinjection [84], covalent or electrostatic attachment of the fluorophore to cell-penetrating peptides [85], or analogous to DNA transfection, encapsulation of the fluorophore in a biologically inert matrix. Some fluorophores, however, are capable of targeting sub-cellular compartments through incorporation of signal sequences or reliance on membrane potential (e.g., MitoTracker, ER-Tracker, and LysoTracker) [79, 86, 87]. Probes with long alkyl chains are routinely used for imaging the plasma membrane, and intercalating agents are excellent for labeling nuclear DNA (e.g., DAPI, Propidium iodide). Nevertheless, specificity remains a challenge when labeling particular proteins. Quantum dots, despite their incredible photon output and brightness, suffer from many of the same troubles as small-molecule fluorophores, with the added disadvantage of their large size (>10 nm). Consequently, quantum dots are most commonly used in immunofluorescence, or in studies involving the extracellular leaflet of plasma-membranes (e.g., single-particle tracking) [88, 89].

Fluorescent proteins (FPs), given their genetically encodable nature, provide a number of advantages. Perhaps most importantly, the generation of a fluorescent moiety requires only transcription and translation of the DNA sequence by a host organism in the presence of molecular oxygen. FPs are relatively small ($\approx$ 2.5 nm in diameter, 4 nm in height) in comparison to many proteins, and in most cases, fusion to

Figure 1.4: Alternative mechanisms of labeling cellular structures. (A) Small-molecule biarsenical fluorophore, FlAsH shown, selectively binds tetracysteine motif engineered on the intracellular loop of a G-protein coupled receptor (PDB 2RH1). (B) Translocation across the plasma membrane is facilitated by masking charges on the small-molecule fluorophore, FluoZin-3 shown, with acetoxymethyl (AM) esters. Upon exposure to intracellular esterases, the AM-esters are cleaved, exposing charges on the carboxylic acids, and thereby trapping the fluorophore within the cell [82]. (C) Sub-cellular spatial control over small-molecule fluorophores is accomplished by genetically targeting O^6-Alkylguanine-DNA Alkyltransferase (AGT, aka SNAP-Tag, PDB 3KZY and 3LOO), an enzyme that catalyzes covalent bond formation with a benzylguanine (BG) small-molecule fluorophore [83].

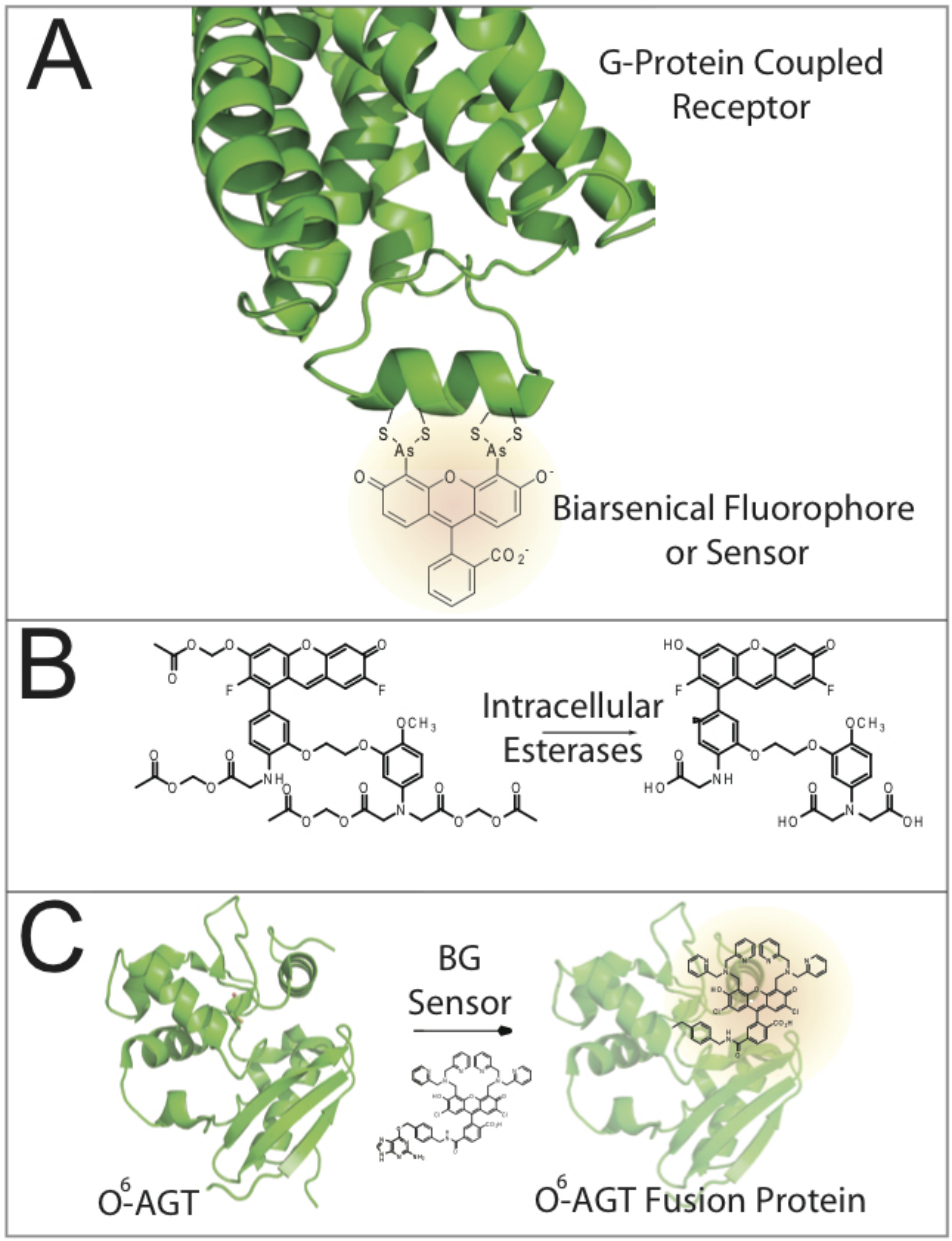

endogenous proteins works well. Placing an FP under control of a cell-specific promoter, or fusing the FP to a particular localization signal sequence, can target the FP to distinct cell-types within tissues, as well as specific sub-cellular locations within the cell. For example, FPs can be targeted with high fidelity to places where their small-molecule counterparts often face challenges, including the pre-synaptic cleft of a hippocampal neuron [90]. Additionally, the use of viral gene-transfer techniques allows FPs to be expanded to living organisms, a technique that has enabled long-term imaging of neuronal processes, and tracking of neuronal projections throughout a brain [91–93]. Nevertheless, FPs are accompanied with some disadvantages. FPs are typically dimmer than most small-molecule fluorophores, have limited wavelengths, decreased photostabilities [94], release H_2O_2 upon chromophore maturation [95], and can perturb particularly sensitive cellular processes. Their size, although typically not a problem, makes FPs ill-suited for direct measurements of small biomolecules (e.g., fatty acids, and cholesterol) [96, 97].

Hybrid-probes seek to enable the genetic specificity afforded by fluorescent proteins with the spectral diversity, decreased size, and excellent photophysical properties afforded by small-molecule fluorophores. For example, the SNAP-tag system has been used to provide small-molecule fluorophores with intracellular specificity [83, 98, 99]. Here, genetically fusing O^6-alkylguanine transferase (AGT) provides protein-specific localization, which undergoes site-specific cysteine alkylation and covalent labeling by benzylguanine-tethered fluorophores (Figure 1.4C) [78]. This approach has been used in living cells to target small molecule zinc-responsive fluorophores to the mitochondria and Golgi apparatus [83], label histone H2B [100], cytoskeletal proteins [101], and much more.

Other enzymatic methods have appeared as well. Biotin ligase from *E. coli* has been adapted for heterologous expression and site-specific attachment of biotin, and biotin analogues, to a lysine present within a genetically encodable 15-amino-acid acceptor peptide [88, 89]. Lipoic acid ligase, another enzyme from *E. coli*, has been engineered to enzymatically couple coumarin derivatives to an acceptor peptide intracellularly [102], as well as azides for site-specific azide-alkyne chemistry [103]. An alternative strategy includes tethering a fluorophore to a biarsenical FlAsH motif, which recognizes a specific tetracysteine peptide *in vivo* with pM affinity (Figure 1.4A) [104–106]. Additionally, phage-display has been used to develop peptides that selectively and with high-affinity bind fluorophores *in vivo* [107]. Nevertheless, these

systems still suffer to varying extents from non-specific and fluorescent background due to incomplete removal of the fluorophore, or in the case of FlAsH, palmitoylation or partial oxidation of the biarsenical motif. To date, these methods have yet to achieve the level of specificity, and contrast, that GFP-based methods have.

Regardless of the fluorophore one chooses, verifying that the label is not perturbing the system under study is paramount. Given the size of fluorescent proteins (30 kDa), or the SNAP-tag system (20 kDa), it is important to confirm that fusion to endogenous proteins does not alter their function *in vivo*, or perturb vital cellular functions (e.g., cell division). Additionally, the brightness of the fluorophore, defined as the product of the extinction coefficient and the quantum yield, as well as its excitation wavelength, are important to minimize cellular phototoxicity. For example, longer wavelengths probes are preferable to those excited at UV wavelengths, and brighter probes enable more sensitive detection and shorter image acquisition durations.

1.5 Spectroscopic Features of Fluorescent Proteins

Given their unique fluorescent attributes, FPs have been the subject of intense theoretical and experimental analysis. FP absorption, excitation, and emission wavelengths depend upon the chemical composition of the chromophore and it's surrounding amino-acids, and can vary from 355-605 nm for absorption and excitation, and 430-670 nm for emission [36,53]. In unique cases, additional red-shifts in absorption, excitation, and emission wavelengths can be achieved through light-driven reactions that increase electron conjugation, irreversibly alter the local environment, or improve chromophore linearity [27,68,108]. Extinction coefficients also vary depending upon the chemical nature of the chromophore, but tend to be between $\approx$ 30,000-100,000 M^{-1} cm^{-1}. However, it should be noted that the extinction coefficient only reflects the functional population of FPs, and that a large population of non-functional FPs may also exist.

The difference between the excitation and emission wavelengths, also known as the Stokes shift, varies substantially for different FPs. In a classical sense, the Stokes shifts reflects the amount of solvent reorganization taking place in the excited-state, and often depends upon solvent polarity and the magnitude of the fluorophore's excited-state dipole moment [109]. Since the chromophore acts as a photoacid, FPs with a protonated ground-state undergo excited-state proton transfer (ESPT) in the excited-state, substantially decreasing the excited-state energy and thereby increasing the Stokes shift ($\Delta\lambda \approx$ 110-160 nm.) [54, 57,

58, 110]. In deprotonated ground-state chromophores, Stokes shifts are significantly smaller ($\Delta\lambda \approx$ 10-65 nm), and reflect excited-state chromophore stabilization and/or excited-state chromophore flexibility [50, 53]. Given that the chromophore is inherently flexible, increases in the Stokes shift are frequently accompanied with decreases in the fluorescence quantum yield, and quantum yields can vary from 0.00-0.93 [41, 53, 111, 112]. FPs with higher quantum yields tend to have narrower excitation and emission bandwidths, increased vibronic character, smaller Stokes shifts, and longer fluorescence lifetimes [40].

Photobleaching refers to the gradual decrease in fluorescence intensity following excitation of the fluorophore. In FPs, total photon-yield prior to photobleaching is 10-100$\times$ worse than many small-molecule fluorophores and limits imaging duration, contrast, and for super-resolution microscopy, resolution [23, 80, 94]. The mechanism(s) for photobleaching remain unclear, but likely involve oxygen-dependent and oxygen-independent pathways through triplet and radical states, ultimately oxidizing the chromophore and/or chromophore environment [113, 114]. Evidence for the triplet state in photoreactions has been observed in FPs. For example, with 100-picosecond one-photon, or 100-femtosecond two-photon pulsed excitation of GFP, an increase of the inter-pulse interval from 10 ns to 2 μs, to allow triplet-state relaxation between pulses, leads to decreased irreversible photobleaching and an increase in the total photon yield by a factor of 5-25 [115]

Formation of long-lived dark-states also likely contributes to irreversible photobleaching. Dark-states here refer to light-driven transitions of the chromophore or chromophore environment into a non-absorbing, non-fluorescent, or less fluorescent state(s) [116]. At the single-molecule level, dark-state conversion and recovery appears as fluorescence "blinking" [117]. At the ensemble level, this process is manifested by a rapid yet reversible decay in the fluorescence intensity [60]. More recent evidence suggests that solvent viscosity and oligomerization state can alter dark-state conversion [118, 119], highlighting the role of global protein motions in chromophore *cis-trans* isomerization and dark-state conversion.

1.6 Selection Methods for Generating Improved Fluorescent Proteins

A common workflow in FP development involves structure-guided design of amino-acid residues at key positions in the protein to influence a spectral phenotype followed by directed evolution to find combinations of residues at supporting positions to tune the photophysical properties [120]. Usually this process is achieved

by *in vitro* random mutagenesis coupled with bacterial expression and screening to isolate high-performing mutants. Several successive rounds of mutagenesis and selection are generally required. Moreover, the major high-throughput screening approach traditionally used for directed evolution is sorting of bacterial libraries using a fluorescence activated cell sorter (FACS) or screening of bacterial colonies. Throughout 1990's and early 2000's, most screens adopted one or both of these approaches, typically using fluorescence brightness as the sole-selection criteria. The following section aims to describe interesting methodologies that have been harnessed for generating improved FPs.

In addition to error-prone PCR, a variety of mechanisms have been developed and/or adopted for randomly mutating FPs. For example, *in vitro* recombination with DNA shuffling [121] or staggered extension PCR (StEP) [122] has been used to introduce errors and genetic crossover in homologous FPs (Figure 1.5) [72, 123–126]. Alternatively, consensus amongst homologous proteins can also be used to successfully generate hybrid proteins [127]. With the exception of consensus engineering, these methods tend to be inefficient mechanisms for generating functional protein diversity. In part, this is due to the steric and electrostatic incompatibilities of most mutations with the protein fold. Nevertheless, improved library design strategies could circumvent this issue, providing a greater yield of functional diversity. One approach is to prescreen mutations *in silico*, and eliminate predicted non-functional combinations prior to laboratory screening. Indeed, the Mayo lab has used this method to generate libraries of GFP with increased functional diversity [128], as well as red-shift RFPs [129].

Recently, more advanced bacteria screens have been developed. For example, the Campbell lab used a high-power LED array to screen bacteria colonies for photostability, generating the more photostable teal variant mTFP1 [131]. Shortly thereafter the Tsien lab adopted a similar approach using a solar simulator on mOrange and TagRFP, resulting in mOrange2, and TagRFP-T, respectively [23]. To develop photoswitchable and photoactivatable FPs, Verkhusha and colleagues adapted the technique for *E. coli* cultures, permitting higher-throughput FACS enrichment of clones with the desired properties [27, 132–134]. Alternatively, the Gadella lab has developed colony-based fluorescence lifetime screens, improving the quantum yield of cyan-emitting FPs to 0.93 % [40, 41]. Through careful analysis of cell-viability, less-cytotoxic variants of FPs can be developed [135]. FPs can also be engineered to report on fusion protein solubility [136], protein

Figure 1.5: DNA shuffling and staggered extension PCR. (A) A schematic of DNA shuffling. DNA encoding the genes to be shuffled are mixed, and subjected to DNaseI treatment. The temperature and duration of the DNaseI treatment allows control of the digestion. The DNaseI treated DNA fragments are purified, and reassembled using PCR with primers specific to the 5' and 3' ends of the DNA. The resulting PCR product has homology-dependent genetic crossover throughout the gene. (B) A schematic of staggered extension PCR (StEP). PCR fragments specific to the 5' and 3' ends of the DNA are used to amplify small fragments of the gene using PCR. The fragment size is controlled by adjusting the temperature and time of the elongation step in the PCR reaction. After multiple cycles, the PCR fragments begin to serve as primers for subsequent PCR cycles. After $\approx$ 100 cycles, the full-length PCR product is constructed, with homology-dependent DNA crossover between the genes. Figures adapted from [130].

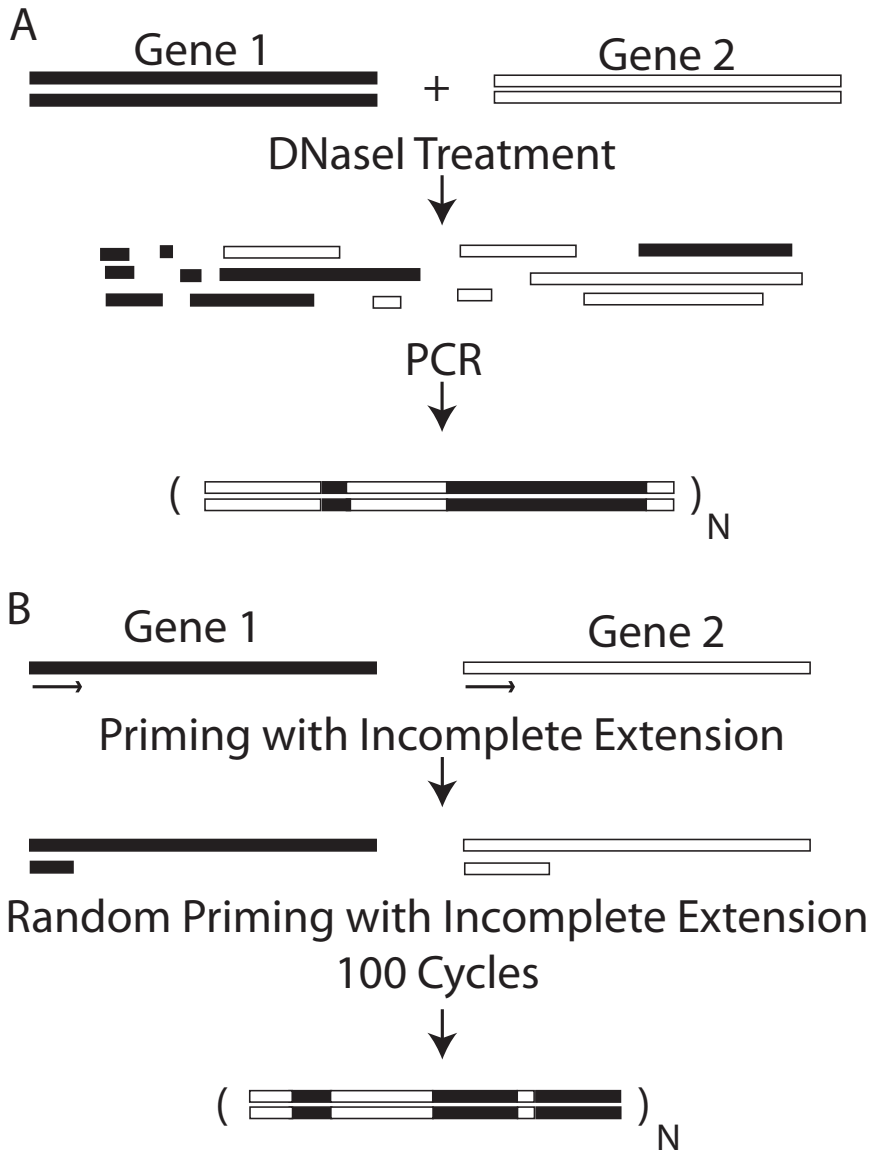

thermostability [126], and improved tolerance to fusions [72].

Sequential mutagenesis, whereby multiple mutation-selection iterations occur, can be a slow and arduous procedure. However, there are methods that allow continual evolution of a protein, thereby providing a major boost in throughput and efficient exploration of sequence-space. For example, somatic hypermutation is the process where B-lymphocytes undergo continual evolution of immunoglobulin genes via affinity maturation [137]. Wang et al. were able to capitalize upon this process of continual mutagenesis in B-lymphocytes in the development of mPlum, an RFP with a large Stokes shift and far-red emission ($\lambda_{em} = 549$ nm) [111]. However, their methodology cannot truly be defined as continual evolution, since selection of the RFP was provided through external means, in this case, repetitive FACS sorting of the population. More recently, a method involving continual culture and selection of bacteriophage following infection of *E. coli* was used to reengineer the promoter specificity of T7 RNA polymerase [138]. If such a system could be adapted for light-activated processes, FP development strategies could be pursued.

1.7 Advantages of Microfluidics in Next-Generation Directed-Evolution

Microfluidics offer a number of advantages over traditional laboratory methods, including precise spatiotemporal control of particles, solutions, and solution mixing [139], minimal sample consumption (<100 μL), decreased cost, as well as the capacity to be integrated with optical, electrical, mechanical, and temperature-based perturbations. Consequently, microfluidics have been used for a wide-variety of research, including DNA sequencing [140], single-molecule enzymology [141], recapitulation of lung-function [142], isolation of low-abundance circulating tumor cells [143], and even chromosome capture and haplotyping [144].

In comparison with FACS instrumentation, which typically only measures fluorescence intensity and light scatter at a single time-point, microfluidics offer incredible potential for high-throughput directed evolution. When combined with particle sorting mechanisms (e.g., optical-force [145], dielectrophoresis [146], surface acoustic waves [147,148], etc.), nearly any microscopy technique can be adapted for multipoint time-dependent microfluidic flow cytometry. Examples include fluorescence spectrum detection [149], 2-photon excitation fluorescence [150], dynamic FRET measurements [151], and coherent-antistokes Raman scattering (CARS) [152]. These methods are not mutually exclusive, and may be combined, enabling multiparametric

screens and greater control over selection pressures in directed evolution. Furthermore, microfluidics can encapsulate single cells within microdroplet emulsions [153], confining enzymatic reactions to femtoliter volumes, thereby permitting the directed evolution of challenging low-turnover enzymatic processes [154–157]. State-of-the-art microfluidic cytometers can now screen and sort cells at a rate of >2,000 Hz, enabling libraries of $\approx 10^7$ to be screened in a an hour [156]. Furthermore, microfluidic cytometers can be parallelized, providing additional boosts in throughput [158].

1.8 Alternative Avenues for the Development and Use of FPs

Despite nearly three decades of uninterrupted FP development, there is still substantial room for improvement in both FP selection methodology, as well as FP use. Microfluidics, as discussed above, provides one legitimate avenue for FP development. However, others exist, and they will be discussed briefly here. For example, many time-correlated single-photon counting (TCSPC) techniques have not yet been used in the development of an FP. Here, measurements could be performed in living cells, or on purified proteins through the use of liquid-handling robotics, and their TCSPC analysis automated on a motorized microscope stage. In particular, fluorescence correlation spectroscopy (FCS) could simultaneously measure the diffusion coefficient, as well as the population and lifetime of both the triplet-state and dark-state populations [159]. Following FCS, the fluorescence lifetime could be measured, providing an insight into the fluorescence quantum yield [40], and photon-counting histograms could provide an accurate measure of the absolute molecular brightness [160]. If coupled with a 2-photon excitation source, this strategy could develop mutants with improved 2-photon absorption cross-sections, enabling multiphoton *in vivo* microscopy with improved sensitivity [161, 162].

Another interesting possibility is the use of a recently reported frequency-domain method capable of measuring dark-state populations and relaxation rates [163]. Importantly, this method is amenable to high-throughput and colony-based methods. Less feasible, but intriguing, is the possibility of radiative-rate engineering through fluorophore-metal interactions [109]. This effect has been shown for GFP on silver nano-particles, and resulted in 6- and 10-fold improvements in the fluorescence intensity and photon-output prior to photobleaching, respectively [164]. Indeed, metal-binding sites have been engineered into existing

protein structures [165]. The true feasibility of this concept depends upon the nature of the metal-fluorophore interaction, and if it could be accomplished at the single-metal-ion level.

Increasingly advanced imaging modalities emerge every year. Present day imaging systems are imaging deeper, faster, and with greater resolution and specificity than ever imagined. Fluorescent proteins, perhaps the original catalyst for this imaging revolution, will continue to contribute in unique and unforeseen ways. For example, non-fluorescent proteins have been imaged using non-linear stimulated emission microscopy [166]. Similarly, fluorescent proteins, due to their highly polarizable chromophore and unique Raman spectrum, could be used to improve the sensitivity in emerging stimulated Raman imaging techniques [96, 97]. By developing an FP with a large acoustic response following absorption of a photon, optoacoustic imaging at the mesoscale and macroscale would be facilitated [167]. Nevertheless, the future remains bright for fluorescent proteins and related technologies.

Chapter 2

Spectroscopic Analysis of Dark-State Conversion and Photobleaching in Red-Fluorescent Proteins

2.1 Abstract

Fluorescent proteins (FPs) are powerful tools that permit real-time visualization of cellular processes. The utility of a given FP for a specific experiment depends strongly on its effective brightness and overall photostability. However, the brightness of FPs is limited by dark-state conversion (DSC) and irreversible photobleaching, which occur on different timescales. Here, we present *in vivo* ensemble assays for measuring DSC and irreversible photobleaching under continuous and pulsed illumination. An analysis of closely related red FPs reveals that DSC and irreversible photobleaching are not always connected by the same mechanistic pathway. DSC occurs out of the first-excited singlet state, and its magnitude depends predominantly on the kinetics for recovery out of the dark state. The experimental results can be replicated through kinetic simulations of a four-state model of the electronic states. The methodology presented here allows light-driven dynamics to be studied at the ensemble level over six orders of magnitude in time (microsecond to second timescales).

2.2 Publication Status and Author Contributions

Dean, K.M., Lubbeck, J.L., Binder, J.K., Schwall, L.R., Jimenez R, and Palmer, A.E. Analysis of Red-Fluorescent Proteins Provides Insight into Dark-State Conversion and Photodegradation. *Biophys. J.* 2011. Aug 17; 101(4)961-9.

K.M.D., J.L.L., R.J, and A.E.P. designed the research. K.M.D. and J.L.L. performed research. K.M.D. performed data analysis and numerical simulations. J.K.B. and L.R.S. provided reagents and assisted in research. K.M.D., R.J., and A.E.P wrote the paper.

2.3 Introduction

Despite a wealth of information regarding the photophysics of FPs (See Chapter 1), it remains poorly understood why FPs routinely emit 10-100 fewer photons than do small-molecule fluorescent dyes [23, 94]. One mechanism that may contribute to this diminished photon output is dark-state conversion (DSC, also known as reversible photobleaching or blinking). In green fluorescent protein (GFP) and its yellow-emitting variants, investigators have identified two DSC processes that occur on the 0.01-1 ms timescale [168–170]. One, which is pH-dependent, is attributed to protonation of the p-hydroxybenzylidene moiety, and the other, which is pH-independent, is attributed to a conformational change of the chromophore and/or its environment into a nonradiative configuration (Figure 2.1A and B). Additionally, a separate submicrosecond process has been identified in GFP, likely involving intersystem crossing to the triplet state, that when given sufficient time for relaxation, increases total photon output before photobleaching >20-fold [115].

In red-emitting FPs (RFPs), DSC can be both pH-sensitive [171,172] and pH-insensitive [168,173,174], with photophysical processes taking place on the ms (e.g., the triplet state) and 0.1 ms (conformational dynamics) timescales [172, 174]. Although investigators have examined a variety of RFPs, the published models are in disagreement and provide little insight into irreversible photobleaching. As a result, it is not clear whether irreversible photobleaching occurs out of these transient and long-lived dark states. In this study, we analyze multiple closely related proteins to explore how diverse photophysical properties coevolve with one another. Our goal is to provide a model that combines DSC and irreversible photobleaching in the context of additional photophysical properties (e.g., quantum yield and extinction coefficient), and to shed light on how these properties change upon mutation of the protein structure.

TagRFP and a closely related variant, mKate, are ideal candidates for evaluating how photophysical properties vary within a series of FPs [22]. mKate was first derived from TagRFP by directed evolution with selection pressure for red-shifted emission, and characterized by the incorporation of four mutations

(R67K, N143S, F174L, and H197R) [21, 22]. Subsequent studies identified a single mutation in TagRFP, S158T, that improved its photostability ninefold and is referred to here as TagRFP-T [23]. In mKate, an S158A mutation (hereafter referred to as mKate2) improved the brightness (defined as the product of the extinction coefficient and quantum yield) 2.8-fold [23, 175]. In light of the limited number of mutations that are needed to evaluate this pathway, as well as its diverse phenotypes and sensitivity to modest structural perturbations (e.g., S158T), we chose to characterize the photophysics of this system and introduce a pulsed photo-excitation method that separately resolves the magnitudes and kinetics for irreversible photobleaching and DSC.

2.4 Experimental Methods

2.4.1 In Vitro Fluorescent Protein Characterization

TagRFP-T was cloned into pBAD and mutations were introduced using overlap extension mutagenesis. Upon commercial DNA sequencing, mutants were transformed into Top10 E. coli, induced with 0.02 % arabinose for 24 hours at room temperature, purified using His-tag/Ni-NTA chromatography, and buffer exchanged into 15 mM MOPS, 100 mM KCl, pH=7.0. UV-Visible spectroscopy was performed in a dual-beam reference mode spectrometer with baseline correction. Excitation and emission spectra were collected for dilute fluorescent protein solutions ($\approx 1\ \mu$M) on a fluorimeter and corrected for temporal and spectral lamp intensity fluctuations with a beam splitter and photodiode prior to the sample cuvette. The observed emission intensity was corrected for the wavelength dependent PMT quantum efficiency. Extinction coefficients were determined using the dynamic alkaline denaturation method which permits one to distinguish between red and "immature" (i.e., blue, teal, and green) chromophores [24]. In all cases, an isosbestic point was observed between the red chromophore and the alkaline denatured green chromophore (λ_{abs}=447 nm, ϵ = 44,000 M^{-1} cm^{-1}), and the average change in absorption was used to determine the extinction coefficient of the red chromophore [176]. Quantum yields were measured in two steps. First, the optical density was determined within a 40 mm cuvette to improve instrument accuracy for weakly absorbing solutions. The resulting solution, which had an optical density well below 0.1 per 10 mm of cuvette pathlength to minimize secondary absorption artifacts, was transferred into a clean 10 mm fluorescence cuvette and the integrated fluorescence intensity was immediately measured. All calculations included corrections for the refractive indices of solvents and were cross-calibrated using rhodamine 101 in absolute ethanol [177], and cresyl violet in absolute methanol [178], as reference standards. Experimental uncertainty was assessed from the cross-calibration of rhodamine 101 and cresyl violet, and the error was kept below 10 percent.

2.4.2 Mammalian Cell Culture

HeLa cells were cultured in minimum essential medium supplemented with Earles salts, 10 % fetal bovine serum, and 1 % penicillin-streptomycin. FPs were localized to the nucleus by fusing a nuclear

localization signal peptide (KPKKKRKVEDA) to the C-terminus of the FP. Nuclear localized FPs in a pcDNA3 mammalian expression vector were transiently transfected using commercially available reagents 48 hours prior to imaging, and the cells were placed in Hepes-Buffered Hanks Balanced Salt Solution (HHBSS, pH 7.4) prior to all imaging experiments.

2.4.3 In Vivo Photobleaching Measurements

To eliminate diffusion artifacts, all photobleaching measurements were performed on freely diffusing FPs within the nucleus of living adherent HeLa cells. Laser based photobleaching measurements on the microsecond timescale were performed by directing a 532 nm continuous wave (CW) laser through an acousto-optic modulator (AOM). Undesired light scattering originating from AOM optical heterogeneities were eliminated with a spatial filter, and the resulting first-order diffracted light was directed into an inverted microscope, reflected off of a dichroic mirror, and focused onto the adherent cell by a 10x, 0.40 NA air-objective. At the focus, the laser beam had a Gaussian profile with a full-width half-max (FWHM) of 9.1 μm, thereby completely illuminating the nucleus of the cell (diameter $\approx 5\mu$m). Due to the Gaussian beam waist profile, the excitation intensity at the periphery of the nucleus was 19 % less than the intensity at the center of the nucleus. The resulting fluorescence emission was collected in epi-mode through the same objective, separated from the excitation light with a dichroic mirror and a long-pass filter, and detected by a red-optimized photomultiplier tube (PMT). The resulting photocurrent was converted into a voltage without any additional signal processing, and recorded using custom software. To avoid PMT saturation effects, i.e., PMT blinding [179], the applied PMT voltage was decreased, enabling operation in a low-gain mode. Furthermore, the observed photophysical responses of cells did not change with cellular brightness, and no fluorescence recovery was observed for analogous photobleaching assays performed on commercially available fluorescent beads of comparable brightness (data not shown). Wide-field photobleaching measurements were performed on a commercial epi-fluorescence microscope equipped with a Xenon arc lamp, a 540/25 excitation filter, 590 nm dichroic, and 630/60 emission filter, CCD camera, and 40x 1.3 N.A. oil-immersion objective. Wide-field measurements were performed without neutral density filters, resulting in an excitation intensity of $\approx$100 W/cm^2.

2.4.4 Photobleaching Data Analysis

To compare FPs with different excitation profiles and molar absorptivities, all photobleaching spectra were normalized for the rate of excitation. For laser-based measurements, the rate of excitation was calculated by multiplying the absorption cross-section at 532 nm with the laser intensity, defined throughout as the average laser intensity at FWHM. For wide-field photobleaching measurements, the rate of excitation was determined by integrating the product of the lamp spectral output, excitation filter transmission, dichroic reflectivity, FP excitation profile, and light intensity at the objective focus.

Laser-based photobleaching measurements at intensities of 25.0 kW/cm^2 and 2.5 kW/cm^2 were collected with 1 and 10 μs temporal resolutions, respectively, and each data set spanned 6 orders of magnitude in time. To weight the data equally and avoid a bias in subsequent exponential fits, a smoothing spline was applied to the data and values were interpolated at equally spaced log-time intervals. For each data set, a minimum number of exponentials were used to fit the data, and an optimal global fit was found after iteratively optimizing the exponential decays for the fast monoexponential (<3 ms) and slow biexponential (>10 ms) phases independently. For each fit the confidence intervals, coefficient of determination (R^2), and residuals were evaluated, and many fits showed minor oscillations (<3 %) in the residuals. In addition to the coefficient of determination, confidence intervals were also used to interpret the quality of the fit parameters. Here, confidence intervals suggested accurate time-constants in both the fast and slow phases. However, the confidence intervals for the pre-exponential terms for the fast and slow phases appeared too large for accurate comparison. Consequently, the amplitude of the initial decrease in fluorescence intensity was determined by fitting the initial phase to a single-exponential decay with a constant offset. Subtraction of the offset from the normalized fluorescence intensity provided the amplitude of the fast process. mApple and mKate2 were excluded from analysis given their complicated photobleaching kinetics, i.e., rapid dark-state conversion followed by photoactivation and subsequent photobleaching. All fits were performed in MatLab (Mathworks).

2.4.5 In vitro Fluorescence Lifetime Measurements

The experimental setup used here has been described elsewhere [180]. Briefly, dilute solutions ($\approx$ 100 nM) of purified protein were excited with 1 kW/cm^2 of light originating from a diode-pumped solid-state 532 nm laser. Fluorescence was collected in the epi-direction and separated from the excitation light using a dichroic mirror, focused through a 50 μm pinhole, detected with avalanche photodiodes, and binned into 1064 channels using a commercial time-correlated photon counter. All signals were background corrected, and the resulting fluorescence decay was subjected to a single or biexponential fit, and the initial 1 ns of the decay was omitted to avoid artifacts originating from deconvolution.

2.4.6 Calculation of the Absorption Rate

To evaluate the possibility of transient absorption during the laser-based photobleaching measurements, we calculated the average excitation rate (k_{Ex}) using the Beer-Lambert law (Equation 2.1). Here, light intensity I decreases in magnitude with respect to distance x as it passes through a solution containing n molecules per cm^3, with an absorption cross-section σ in cm^2 (8).

$$\frac{dI}{dx} = -I\sigma n \tag{2.1}$$

Using the conditions $I = I_0$, and x=0 cm, integration results in equation 2.2, the Beer-Lambert law, where D is the path length for light absorption in centimeters:

$$ln(\frac{I_o}{I}) = \sigma n D \tag{2.2}$$

Equation 2.3 is another form of the Beer-Lambert law where ϵ is the decadic molar extinction coefficient (M^{-1} cm^{-1}), C is the molar (mol/L) concentration, and D is the path length for light absorption.

$$log(\frac{I_o}{I}) = \epsilon C D \tag{2.3}$$

Combining equation 2.2 with equation 2.3 allows one to relate the experimentally measured decadic molar extinction coefficient to the absorption cross-section for a single-molecule in terms of cm^2, where the

factor of 2.303 results from the log/natural log conversion, and the factor of 1000 accounts for the conversion between milliliters (cm^3) and liters.

$$\sigma = 2.303 \times 1000 \frac{\epsilon}{N} \tag{2.4}$$

Multiplication of the absorption cross-section in cm^2 with the laser intensity in W/cm^2 gives the total joules per second absorbed, which is converted into photons absorbed per second (kEx) using the relationship between Plancks constant ($h = 6.626068 \times 10^{-34}$ J s) and the speed (c) and wavelength λ of light (Equation 2.5). Consequently, fluorescent proteins with extinction coefficients of $\approx$ 100,000 M^{-1} cm^{-1} will absorb 2.5×10^7 photons s^{-1}, or alternatively, one photon every 40 nanoseconds.

$$k_{Ex} = \frac{\sigma I \lambda}{hc} = 2.303 \times 1000 \times \frac{\epsilon I \lambda}{NhC} \tag{2.5}$$

2.4.7 Kinetic Simulations

All simulations were performed with a commercially available kinetic analysis software package. Simulations involving continuous laser illumination were modeled using Runge-Kutta analysis [181]. Rates for emission (k_{em}), conversion from S1 to D1 (k_{S1D1}, conversion from D1 to S1 (k_{D1S1}), D1 internal conversion (k_{ic}), and ground-state recovery (k_{dsr}) were, 2.5×10^8 - 1×10^{10} s^{-1}, 5×10^5 s^{-1}, 0 - 5×10^5 s^{-1}, 1×10^9 - 1×10^{12} s^{-1}, and 1×10^1 - 1×10^6 s^{-1}, respectively. Figure 2.7A presents the molecular states and transitions in graphical format.

Pulsed illumination was analyzed using a suite of nonlinear and differential and algebraic solvers (SUNDIALS) [182]. Here, the rate of excitation was provided with a Fourier series according to Equation 2.6, where t is time, L is the duration of the pulse in seconds and n is number of odd integer harmonics. To compare the effects of pulsed versus continuous illumination, numeric modeling was performed in the presence (two-way) or absence (one-way) of dark-state excitation. For two-way simulations, k_{D0ex} was arbitrarily set to equal k_{S0ex}, as was k_{S1D1} and k_{D1S1}. For one-way simulations, k_{D0ex} and k_{D1S1} were set equal to zero.

$$3 \times 10^7 + 2.5 \times 10^7 \times \frac{4}{\pi} \times \sum \left(\frac{1}{n} \times \sin\left(\frac{n\pi t}{L}\right)\right) \tag{2.6}$$

2.5 Spectral Changes Associated with Mutations

To characterize the photophysical properties of a series of closely related FPs, we generated variants of TagRFP with combinations of the four mutations that convert TagRFP into mKate (R67K, N143S, F174L, and H197R). These mutations are illustrated in Figure 2.1, which depicts the chromophore environment of TagRFP and mKate. We also incorporated additional mutations (S158A/C/T and H197I/Y) to explore the influence of these amino acid substitutions on photostability and red shift, respectively [26]. A total of 27 proteins were generated, purified, and compared with six mFruits (mApple [23], mCherry [20], mOrange [20], mOrange2 [23], mStrawberry [20], and mPlum [145]). Table 2.1 lists the excitation and emission wavelength, extinction coefficient, quantum yield, and fluorescence lifetime measured for each protein. Not surprisingly, these parameters varied widely across the proteins, and the influence of each individual mutation on the photophysical properties was strongly dependent on context (i.e., on the other mutations present). For example, incorporation of F174L into TagRFP R67K S158T caused a dramatic reduction in the quantum yield from 0.36 to 0.04, but the same mutation introduced into TagRFP N143S S158T caused a slight increase in the quantum yield from 0.25 to 0.40.

It was previously shown that TagRFP and mKate crystal structures reveal *trans* and *cis* chromophore configurations, respectively (Figure 2.1) [31, 175], consistent with spectroscopic and electronic structure calculations that suggested *trans*-to-*cis* isomerization of the p-hydroxybenzylidene moiety into a negatively charged electrostatic environment would cause a red shift in the excitation [183, 184]. For the mutant proteins examined here, the maximum excitation wavelength generally clustered in two groups, perhaps corresponding to proteins with chromophores in either the *trans* or *cis* configuration (Figure 2.1c). However, the excitation spectra of some proteins exhibited a bimodal distribution (i.e., TagRFP N143S S158T; Figure 2.1d), suggesting that a mixture of two chromophore configurations exists throughout the transformation of TagRFP-T to mKate2. These results suggest that the change in free energy between the *cis* and *trans* ground-state configurations may be relatively small and acutely sensitive to the mutational context in TagRFP-T variants.

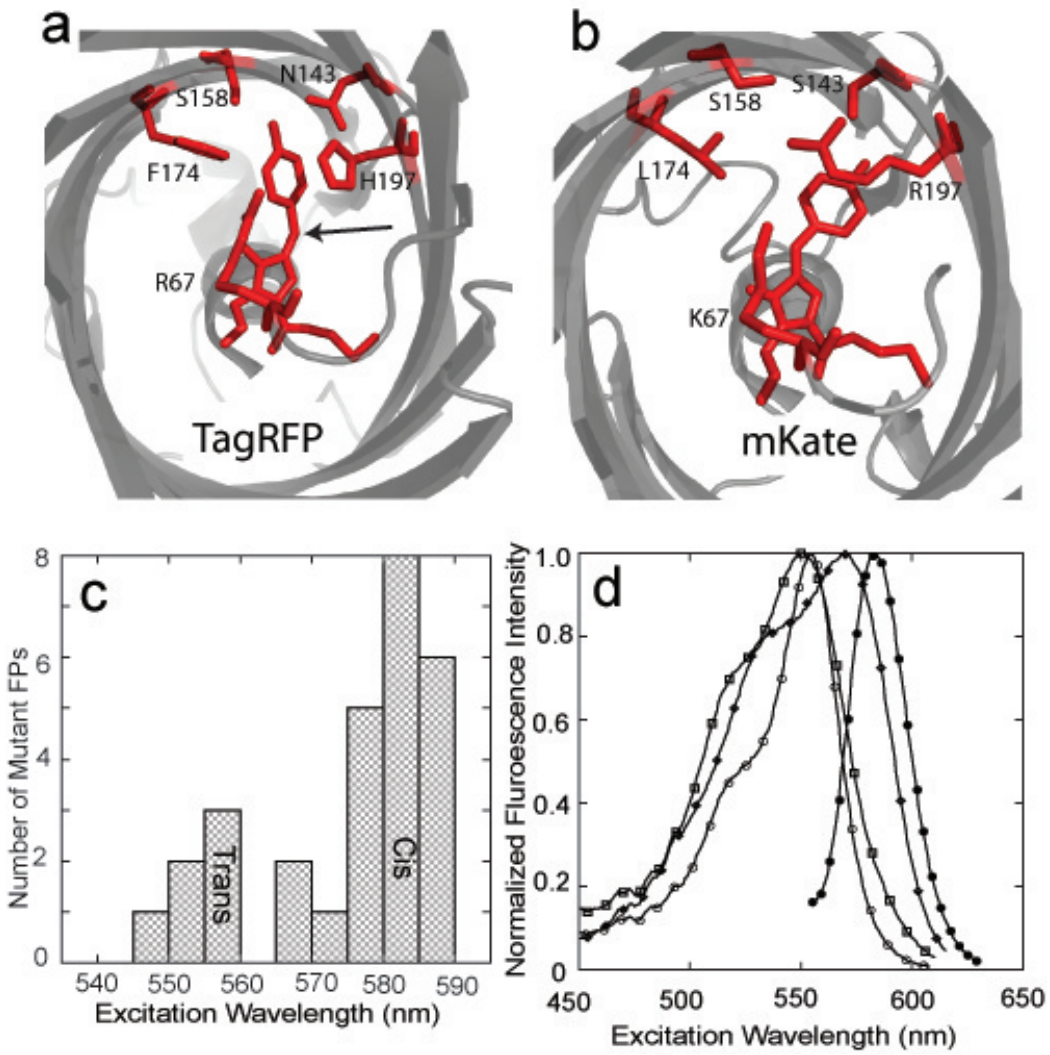

Figure 2.1: Structural and spectral changes associated with FPs. Crystal structures of the chromophore pocket for TagRFP (a) and mKate (b). The crystal structures show TagRFP (PDB 3M22) and mKate (PDB 3BXB) in the *trans* and *cis* configurations, respectively, due to rotation around the bond marked by the arrow. Mutations explored in this study include R67K, N143S, S158A/C/T, F174L, and H197I/R/Y. (c) A bimodal distribution of excitation wavelengths, likely indicative of a mixture of the *trans* and *cis* configurations of the chromophore throughout the transformation of TagRFP to mKate. Table 2.1 summarizes the measured extinction coefficients, quantum yields, fluorescence lifetimes, and excitation and emission wavelengths for these mutant FPs. (d) Excitation spectra of single mutants in the TagRFP-T background: TagRFP-T (open circle), TagRFP-T R67K (open square), TagRFP-T N143S (black diamond), and TagRFP-T F174L (black circle). Note the broadened excitation spectra for TagRFP-T N143S, likely indicative of two ground-state configurations, both of which absorb.

Table 2.1: *In vitro* spectral properties of fluorescent proteins N.D. = Not determined, accurate extinction coefficient and quantum yield could not be obtained due to protein misfolding and/or lack of red chromophore formation.

Fluorescent Protein	Ex/Em (nm)	Extinction Coefficient (M^{-1} cm^{-1})	Quantum Yield	Fluorescence Lifetime (ns)
TagRFP	555/579	95,000	0.48±.04	2.42
TagRFP S158T (TagRFP-T)	555/580	104,000	0.47±.08	2.71
TagRFP S158C	570/589	77,000	0.24±.01	
TagRFP S158A	556/589	70,000	0.1 ± 01	
TagRFP R67K S158T	550/579	105,000	0.36±.09	
TagRFP N143S S158T	569/590	110,000	0.25±.06	
TagRFP S158T F174L	584/590	89,000	0.05±.01	
TagRFP S158T H197R	548/559	N.D.	0.45±.10	
TagRFP R67K N143S S158T	580/602	100,000	0.41±.12	
TagRFP R67K N143S S158A	578/607	120,000	0.30±.12	
TagRFP R67K N143S S158C	580/608	100,000	0.39±.16	
TagRFP R67K N143S	576/596	115,000	0.30±.10	2.36
TagRFP R67K S158T F174L	577/593	93,000	0.04±.01	
TagRFP R67K S158T H197R	556/580	N.D.	N.D.	
TagRFP N143S S158T F174L	582/594	100,000	0.40±.12	
TagRFP N143S S158T H197R	578/609	N.D.	0.17±.04	
TagRFP S158T F174L H197R	N.D.	N.D.	N.D.	
TagRFP R67K N143S S158T H197Y	589/623	72,000	0.11±.04	
TagRFP R67K N143S S158T F174L	578/601	93,000	0.34±.12	
TagRFP R67K S158T F174L H197R	576/616	N.D.	N.D.	
TagRFP R67K N143S S158T H197R	578/617	N.D.	0.20±.05	
TagRFP N143S S158T F174L H197R	580/610	N.D.	N.D.	
TagRFP R67K N143S S158T F174L H197R	566/621	77,000	0.25±.06	
TagRFP R67K N143S F174L H197R (mKate)	586/619	105,000	0.25±.02	
TagRFP R67K N143S S158C F174L H197R	583/615	115,000	0.22±.03	
TagRFP R67K N143S S158A F174L H197R (mKate2)	585/618	89,000	0.38±.16	2.79
TagRFP R67K N143S S158T F174L H197Y	588/618	100,000	0.08±.01	
mApple	569/590	88,000	0.49±N.D.	3.11
mCherry	586/606	97,000	0.16±.02	1.87
mOrange	547/562	100,000	0.67±N.D.	3.62
mOrange2	550/564	110,000	0.55±.04	3.28
mPlum	583/633	75,000	0.08±.02	
mStrawberry	575/594	98,000	0.35±.04	2.04

2.6 Ensemble Photobleaching: Differentiating DSC and Irreversible Photobleaching

Photobleaching (i.e., the gradual decay of fluorescence upon exposure to light) significantly limits the photon output of FPs; however, the mechanisms of fluorescence decay remain poorly characterized. To examine photobleaching for a panel of FPs *in vivo*, we expressed freely diffusing, nuclear localized FPs in HeLa cells and continuously illuminated them using a Xenon arc lamp or continuous-wave (CW) laser. Figure 2.2 provides a representative image of FP localization and the extent of photobleaching observed. We selected TagRFP-T mutants from the previous experiments to include well-maturing variants (i.e., predominantly red-absorbing) with diverse spectral properties, which allowed us to assess how photobleaching correlates with different photophysical attributes (e.g., quantum yield and fluorescence lifetime).

Figure 2.3 shows that the FPs exhibit a wide range of photo-bleaching behaviors and kinetics upon exposure to either wide-field or laser (2.5 kW/cm^2 and 25 kW/cm^2) illumination. The observed responses include mono- and multiexponential decay, photoactivation, and rapid decreases in fluorescence intensity followed by a transient increase and subsequent decay. As expected, increasing the illumination intensity led to faster photobleaching. However, there were also unexpected responses, suggesting that FPs may exhibit different mechanisms of photobleaching upon wide-field versus laser illumination or at different intensities of laser illumination. For example, TagRFP-T undergoes photoactivation with wide-field illumination (Figure 2.3a). However, when it is illuminated at 25 kW/cm^2, the same protein undergoes a rapid decrease in fluorescence intensity followed by multiexponential decay with negligible photoactivation (Figure 2.3c). The inset in Figure 2.3c highlights the fact that at 25 kW/cm^2, photobleaching is characterized by a rapid decrease in fluorescence intensity during the first 5 ms of illumination, followed by a slower decay.

The most commonly observed behavior involved rapid decay followed by a slower decrease. Because fluorescence decay occurred over a wide range of timescales, decay curves were interpolated and converted to time points equally spaced over six orders of magnitude in log-time. Figure 2.4a shows a typical FP fluorescence decay curve in log time. Decay is characterized by three separate kinetic phases: 1, an initial monoexponential decay (<800 ms); 2, a steady-state phase (800 ms to 5 ms) during which fluorescence

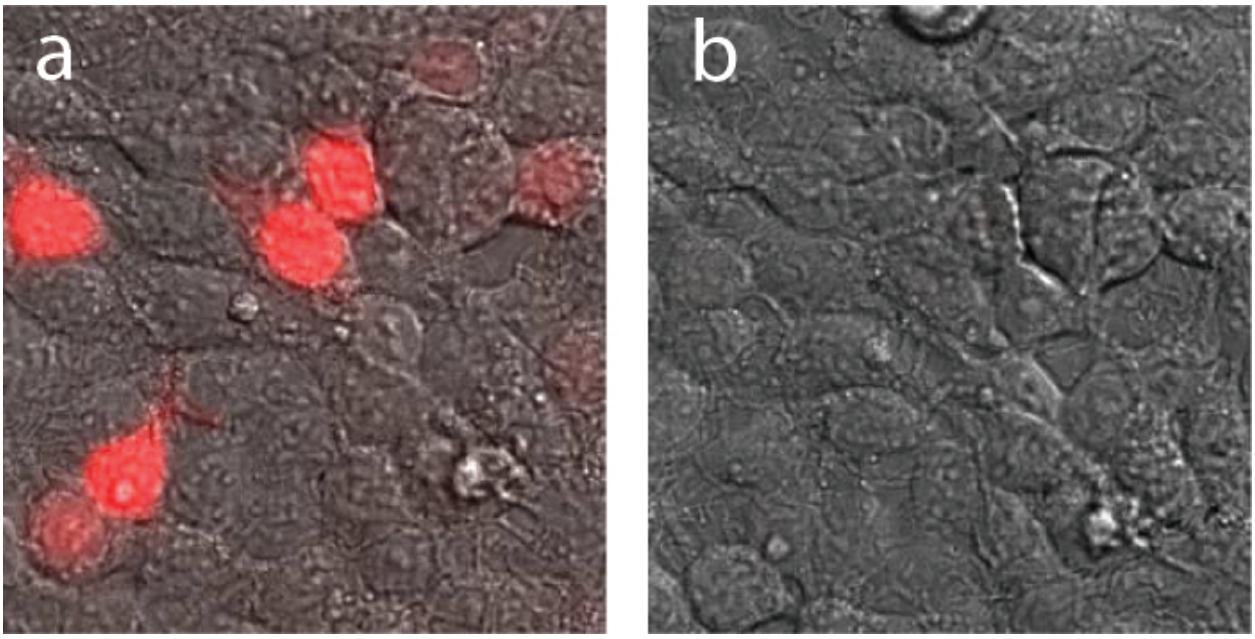

Figure 2.2: FP nuclear localization and extent of photobleaching observed in HeLa cells. Overlay of mOrange fluorescence (red) and DIC (Differential Interference Contrast) images before (a) and after (b) photobleaching. Cells were continuously illuminated with arc-lamp illumination and the final fluorescence intensity was 12 % of the initial fluorescence intensity. Circular shape of fluorescence image characteristic of nuclear localization, and was observed for all FPs studied here.

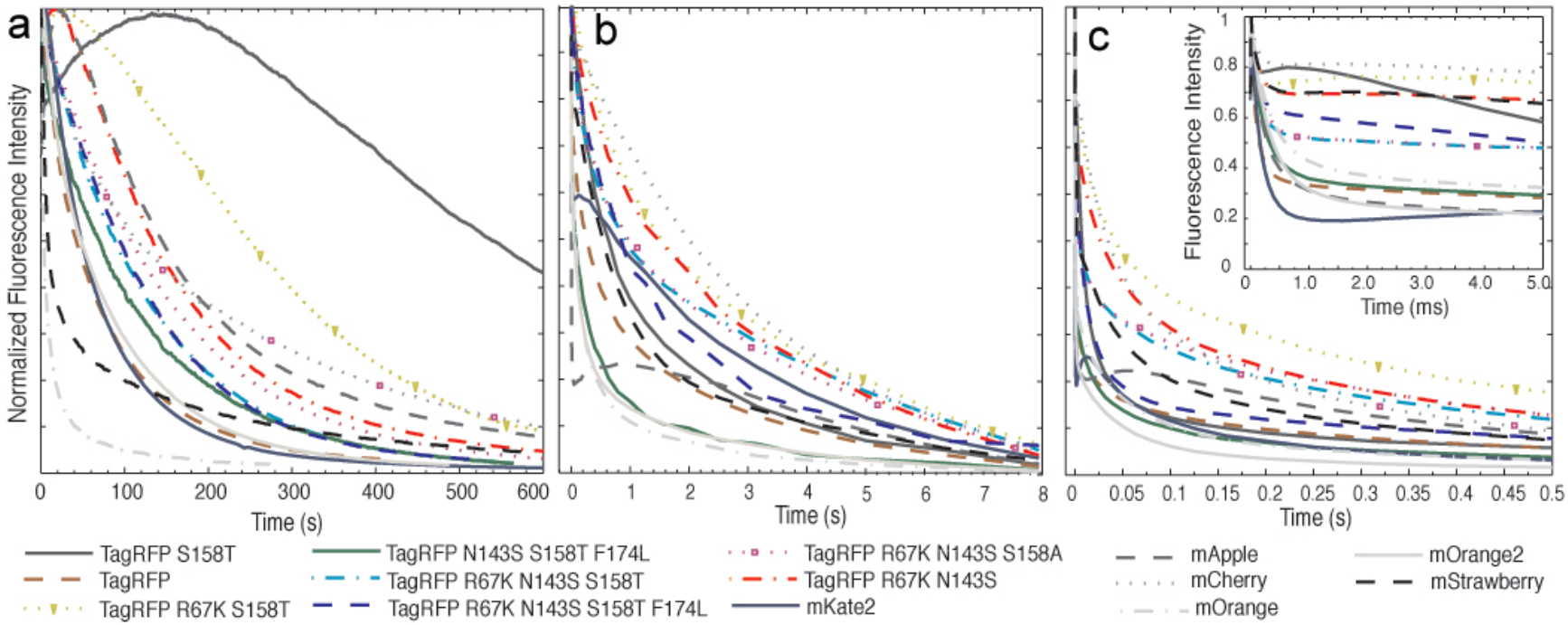

Figure 2.3: TagRFP-T mutant and mFruit photobleaching spectra. Continuous photobleaching curves were collected under (a) wide-field illumination conditions (I=100 W/cm^2) and (b) 2.5 kW/cm^2 and (c) 25 kW/cm^2 532 nm laser illumination. The inset in c provides closer inspection of the first 5 ms for the photobleaching decay. Each line is representative of the photobleaching observed for a single cell.

intensity remains constant; and 3, a gradual biexponential phase (>5 ms).

To gain insight into this complex behavior, we compared photobleaching upon continuous illumination with photobleaching using a train of 2 ms 25 kW/cm^2 pulses separated by 8 ms dark periods. Hereafter, we refer to this excitation scheme as pulsed excitation. Figure 2.4b shows a characteristic photobleaching curve using pulsed excitation. The inset of Figure 2.4b demonstrates that the initial monoexponential decay phase (i.e., <800 ms) observed during continuous illumination was replicated in each excitation pulse, and was largely reversible. Accordingly, we hypothesized that this rapid decay corresponds to conversion to a transient dark state. In this context, the term "dark state" refers to a state that is nonfluorescent, less fluorescent, less absorbing, or nonabsorbing at the wavelength used (e.g., the protonated chromophore, or the triplet state).

To quantify the extent of fluorescence recovery, we defined the percent recovery as Equation 2.7, where F_L and F_R are the initial fluorescence intensities of the first and second excitation pulses, respectively; and F_B is the final fluorescence intensity of the first excitation pulse (Figure 2.4b, inset) [23]. The percent recovery values for each protein are listed in Table 2.2 and vary from 55 % to 100 %. Fluorescence recovery appeared to be complete within 8 ms, as prolonged durations in the dark (up to 10 s) did not lead to statistically significant increases in percent fluorescence recovery (TagRFP, mOrange2, and mCherry; analysis of variance, P >0.05). However, in some cases (e.g., mKate2), the percent recovery changed depending on the number of pulse exposures, presumably due to residual dark-state accumulation.

$$PercentRecovery = (F_R - F_B)/(F_L - F_B) \tag{2.7}$$

To quantify the photobleaching of different FPs and to differentiate irreversible photobleaching from DSC, we fit the data to a sum of exponentials. The fitted rate constants enabled us to evaluate the time constants (defined as the reciprocal of the rate constant) for the different phases of fluorescence decay. At 25 kW/cm^2, continuous photobleaching data were fit to a sum of three exponential decays, allowing the kinetics of the fast and the weighted average of the slow biexponential phase to be independently determined. A representative fit is shown in Figure 2.4. Because our pulsed excitation suggested that the initial fast decay was largely reversible, this phase is referred to as DSC. Conversely, the second slower phase appeared to be

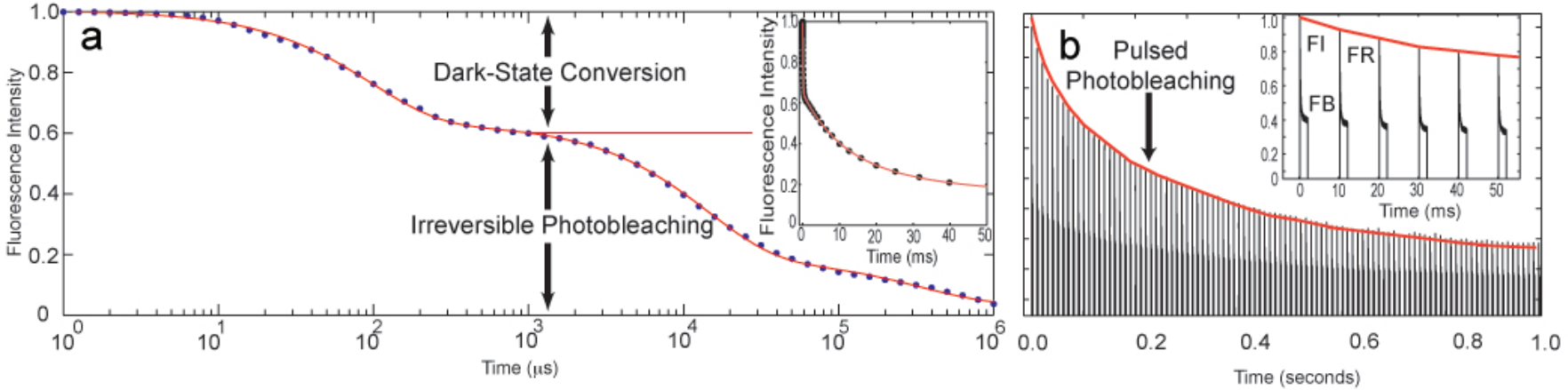

Figure 2.4: Photobleaching decay for TagRFP Arg67Lys Asn143Ser Ser158Thr Phe174Leu. (a) Photobleaching kinetics and the respective triexponential fit (red) in log time. Initial decay representative of DSC (i.e., <1 ms), steady-state plateau (i.e., $\approx$ 1 ms), and irreversible photobleaching phase (i.e., >5 ms). The inset in panel a shows photobleaching kinetics plotted in linear time. (b) Pulsed photobleaching kinetics (red line) is defined as the exponential decay of the peak fluorescence intensity of each pulse under pulsed excitation. The inset in b shows the percent recovery after 2 ms excitation and 8 ms in the dark. Percent fluorescence recovery is defined as $(F_R\text{-}F_B)/(F_L\text{-}F_B)$, where F_L and F_R are defined as the fluorescence intensities of the initial and second pulses, respectively, and F_B is the final fluorescence intensity after 2 ms of excitation.

Table 2.2: Percent Dark-State Conversion, Percent Recovery, and Irreversible Photobleaching Time-Constants Obtained Under Pulsed and Continuous Illumination. Reported error is the standard deviation, and n represents the number of measurements performed for each FP. DSC was measured at 25 kW/cm2 and was determined by fitting the initial fluorescence decay to an exponential decay with a y-offset. Irreversible photobleaching was determined after fitting the entire decay to a triexponential fit, and is reported as the weighted average of the two slow components. Pulsed photobleaching was found by locating the peak fluorescence intensity of each excitation pulse and fitting these to an exponential decay. N.D. = Not Determined, in cases where rapid decrease and subsequent transient increase in fluorescence intensity prohibited accurate fitting by a sum of three exponentials.

Fluorescent Protein	**Percent Recovery**	**Percent DSC**	**Irreversible Photobleaching Time-Constant (ms)**	**DSC Time-Constant (µs)**	**Pulsed Photobleaching Time-Constant** (ms)	**Irreversible Photobleaching Time-Constant (ms)**
Laser Intensity	**25 kW/cm^2**					**2.5 kW/cm^2**
TagRFP S158T	59±11 (n=3)	25±5 (n=3)	12.0± 0.5 (n=3)	29 ± 4 (n=3)	74±7 (n=3)	550±100 (n=3)
TagRFP	83±5 (n=3)	69±7 (n=3)	10.8±0.4 (n=3)	73 ± 17 (n=3)	113±12 (n=2)	385±80 (n=3)
TagRFP R67K S158T	72±11 (n=3)	29±2 (n=3)	80.9±0.9 (n=3)	48 ± 4 (n=3)	470±150 (n=2)	1700±110 (n=3)
TagRFP R67K N143S S158T	82±11 (n=3)	45±3 (n=3)	40.0±1.0 (n=3)	118 ± 22 (n=3)	82±17 (n=2)	936±160 (n=2)
TagRFP N143S S158T F174L	83±4 (n=3)	68±3 (n=3)	14.8±0.9 (n=3)	173 ± 3 (n=3)	98±9 (n=2)	225±4 (n=2)
TagRFP R67K N143S S158T F174L	77±4 (n=3)	46±3 (n=3)	16.0±2.0 (n=3)	99 ± 3 (n=3)	81±9 (n=2)	801±27 (n=3)
TagRFP R67K N143S S158A	85±1 (n=3)	50±2 (n=3)	34.0±3.8 (n=3)	132 ± 11 (n=3)	98±31 (n=2)	654±192 (n=X)
TagRFP R67K N143S	85±3 (n=2)	34±4 (n=2)	50±13 (n=3)	101 ± 8 (n=3)	253±45 (n=2)	1167±150 (n=2)
TagRFP R67K N143S S158A F174L H197R (mKate2)	102±2 (n=3)	79±1 (n=3)	N.D.	187 ± 29 (n=3)	236±72 (n=3)	N.D.
mApple	55±5 (n=3)	77±3 (n=3)	N.D.	N.D.	N.D.	N.D.
mCherry	88±5 (n=3)	18±3 (n=3)	57.0±4.6 (n=3)	73 ± 29 (n=3)	744±35 (n=2)	3457±670 (n=3)
mOrange	90±1 (n=3)	70±10 (n=3)	1.27±2.0 (n=3)	147 ± 89 (n=3)	183±9 (n=2)	229±170 (n=2)
mOrange2	80±5 (n=3)	74±2 (n=3)	0.96±0.2 (n=3)	180 ± 14 (n=3)	212± 13 (n=2)	262±74 (n=2)
mStrawb-erry	88±4 (n=3)	30±1 (n=3)	9.68±0.4 (n=3)	79 ± 34 (n=3)	296± 25 (n=3)	719±400 (n=3)

irreversible and hence is referred to as irreversible photobleaching. Table 2.2 summarizes the parameters obtained from the fits of 14 different proteins, including the amplitude of DSC (defined as the percentage of the total decay attributable to DSC), as well as the time constants for DSC and irreversible photobleaching for FPs exposed to 25 kW/cm^2. Besides a small decrease in fluorescence intensity ($\approx$ 1-4 %) at 10 ms, no convincing evidence of triplet state dynamics was observed. At 2.5 kW/cm^2, the steady-state plateau was less pronounced, and thus the more gradual part of the photobleaching was fit to a biexponential decay (weighted time constant presented in Table 2.2). Under wide-field conditions, the three phases were not broadly identifiable, and consequently this approach was not used to fit these data.

To quantitatively assess whether photobleaching occurs out of transient dark states, we also performed photobleaching assays under pulsed excitation conditions. For each FP, the time constant of irreversible photobleaching for pulsed excitation conditions was determined by locating the maximum fluorescence intensity (i.e., F_R) for each excitation pulse and fitting the decrease in peak fluorescence intensity to a monoexponential decay (inset and red curve in Figure 2.4b). Hereafter, the results from this kinetic analysis are referred to as the pulsed irreversible photobleaching time constant (values are presented in Table 2.2). For all of the FPs studied, photobleaching under pulsed excitation is slower than photobleaching under continuous illumination. The extreme cases are mCherry, which exhibits a 13-fold gain in the photobleaching time constant under pulsed illumination, and TagRFP R67K N143S S158T, which shows only a twofold gain. This result suggests that for some FPs, irreversible photobleaching from dark states is minimized by pulsed excitation when the pulse separation is sufficient for these states to depopulate between excitation pulses.

2.7 Comparison of Irreversible Photobleaching in FP Variants

By measuring photobleaching in a panel of FPs under different illumination conditions, we were able to identify general trends and hence common themes in fluorescence decay. Figure 2.5a compares the irreversible photobleaching time constant under continuous illumination at 2.5 and 25 kW/cm^2. Overall, time constants at 2.5 kW/cm^2 were significantly greater than at 25 kW/cm^2, indicating a slower rate of fluorescence decay at lower-intensity illumination. In general, the time constants were correlated so that FPs that were more susceptible to photobleaching at 2.5 kW/cm^2 were also more susceptible at 25 kW/cm^2 (see mOrange and

mOrange2). However, some FPs showed heightened sensitivity to increases in excitation intensity. For example, mCherry was 30 % less photostable than TagRFP R67K S158T at 25 kW/cm^2, but twofold more photostable at 2.5 kW/cm^2. This observation points to the need to understand photostability in terms of photoexcitation rates relative to timescales of excited-state population transfer. Figure 2.5b compares the photobleaching time constant for pulsed versus continuous illumination at 25 kW/cm^2. Here, the two parameters are poorly correlated among the proteins tested, suggesting that some proteins experience gains in photostability when subjected to pulsed excitation and others do not. For example, although mCherry is less photostable than TagRFP R67K S158T under continuous illumination at 25 kW/cm^2, it becomes more photostable when subjected to pulsed excitation at the same intensity.

2.8 Comparison of DSC in FP Variants

Figure 2.6a presents a comparison of the percent DSC (i.e., the fast reversible phase of photobleaching under continuous illumination) and the irreversible photobleaching time constant (i.e., the slow and irreversible phase under continuous illumination) at 25 kW/cm^2. For these FPs, as the percent DSC increases, the photobleaching time constant decreases (correlation indicated by the dashed line), suggesting that as DSC increases, the propensity to photobleach also tends to increase (as observed for mOrange, mOrange2, TagRFP, etc.). However, there are significant exceptions. For example, a single mutation in TagRFP S158T solely affects DSC (Figure 2.6a, arrow 1), whereas incorporation of R67K into TagRFP S158T exclusively modulates irreversible photobleaching (Figure 2.6a, arrow 2). Conversely, some mutations simultaneously modulate both DSC and irreversible photobleaching rates (Figure 2.6a, arrow 3).

To examine the effect of excited-state lifetime on DSC, we compared the fluorescence lifetimes of purified proteins with the observed DSC kinetics for FPs in cells. Figure 2.6b reveals a correlation between increasing fluorescence lifetime and increased percent DSC. Theoretically, the radiative rate of fluorescence is dictated by the Strickler-Berg equation. However, the non-radiative rate, which accounts for all non-radiative processes that may take place out of the excited state, is variable in nature and depends on the local environment. In the case of FPs, the non-radiative rate appears to be principally determined by the rate of thermal internal conversion back to the ground state, but consists of, to a lesser extent, intersystem crossing

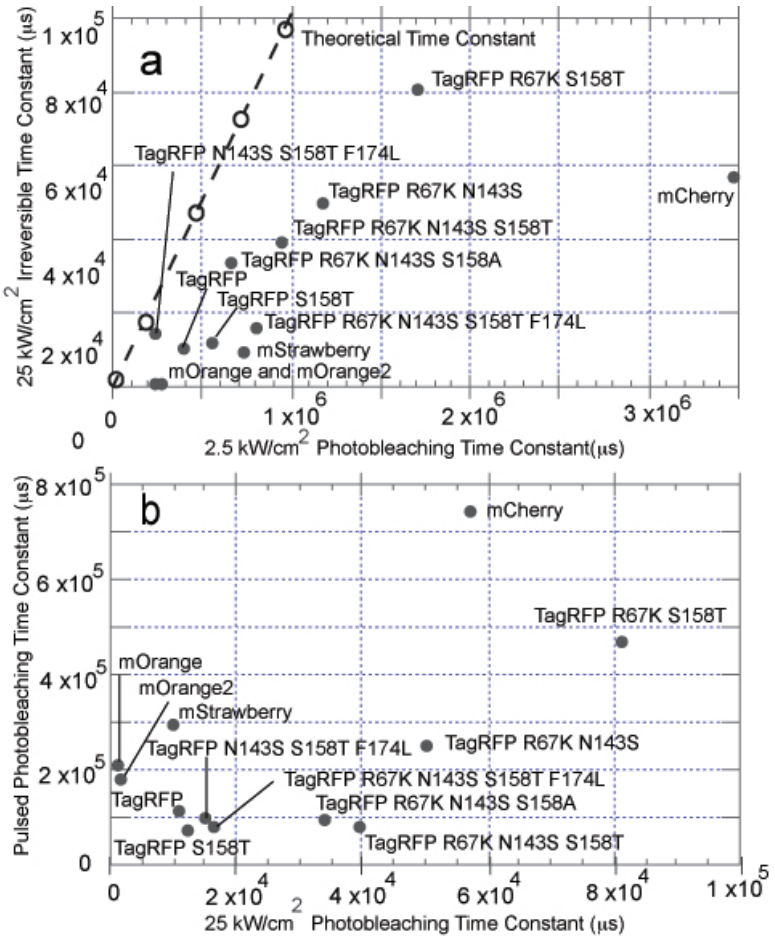

Figure 2.5: Comparison of irreversible photobleaching parameters of the different FPs. (a) Correlation between irreversible photobleaching time constants at 2.5 kW/cm^2 and 25 kW/cm^2 laser illumination shows that different proteins have different sensitivities to heightened excitation rates, and the rank order of photostability changes with intensity. The dashed line shows the anticipated correlation for a simple three-state system (e.g., ground, excited, and bleached) in which 10-fold increases in excitation intensity result in 10-fold decreases in the photobleaching time constant. (b) Comparison of the irreversible photobleaching time constant obtained for continuous versus pulsed illumination. Under pulsed illumination, FPs with photoreactive dark states become more photostable, whereas FPs with photoprotective dark states do not.

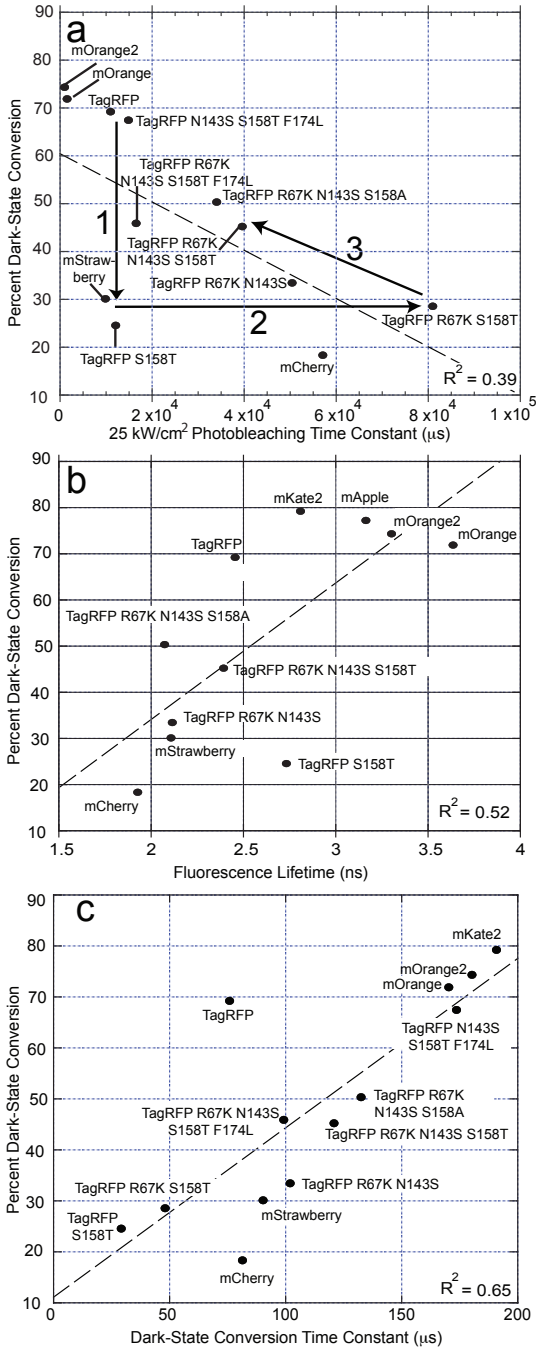

Figure 2.6:
Dark-state conversion correlation plots. (a) Single mutations perturb the percent DSC (arrow 1), irreversible photobleaching time constant (arrow 2), or both parameters simultaneously (arrow 3). A weak correlation (dashed line) suggests that increases in the percent DSC are accompanied by decreased photostability. (b) Comparison of the percent DSC and fluorescence lifetime suggests that DSC is competitive with emission from the first excited singlet state. (c) Percent DSC versus the time constant of DSC. Linear correlation reveals that the percent DSC increases in proteins with slower rates, or larger time constants, of DSC.

and dark-state conversion. If the rate of internal conversion slows, but the rate of intersystem crossing and dark-state conversion does not, overall the fluorescence lifetime and quantum yield of fluorescence will increase (See Equations 2.8 and 2.9, respectively). However, since dark-state conversion is a low quantum efficiency process, it overall does not affect the observed fluorescence lifetime. Instead, increased durations in the excited state, as is observed for FPs with higher quantum yields, does provide additional time for dark-state conversion to occur.

$$\tau = \frac{1}{k_{Rad} + k_{NonRad}} \tag{2.8}$$

$$\phi = \frac{k_{Rad}}{k_{Rad} + k_{NonRad}} \tag{2.9}$$

An alternative possibility is that transient absorption to higher-order excited-states leads to DSC, and therefore DSC is more prominent in FPs with longer excited-state lifetimes. To evaluate the possibility of transient absorption, the rate of excitation was calculated using the Beer-Lambert Law (See Experimental Methods). For the fluorescent proteins studied here (ϵ = 100,000 M^{-1} cm^{-1}), this gives a maximum excitation rate of 2.5 $\times$ 10^7 s^{-1}, or on average 1 photon absorbed every 40 nanoseconds. However, due to off-peak excitation, the actual excitation rates are likely to be $\approx$ 4-fold slower. Furthermore, the radiative rate, as estimated from the fluorescence quantum yield and lifetime ($\phi = k_{Rad} \times \tau$), was found to be independent of the mutational context. These results suggest that DSC is competitive with radiative decay from the first excited singlet state. Consequently, FPs that exhibited the longest fluorescence lifetimes, and hence had the greatest percent DSC and propensity to undergo irreversible photobleaching, also tended to have the largest quantum yields.

As mentioned above, both the amplitude and kinetics of DSC varied substantially for different FP variants. Figure 2.6c shows the time constant of DSC versus percent DSC for different FPs. Of interest, this comparison reveals that RFPs that have a slower rate of DSC, and hence reach the steady-state phase of photobleaching more slowly, have a greater percent DSC. This observation will be explained by the kinetic modeling described below.

2.9 Kinetic Modeling

A careful examination of the RFP photobleaching behavior at 25 kW/cm^2 revealed clear trends in the percent DSC, the measured rate of DSC, the fluorescence lifetime, and the measured rate of irreversible photobleaching. Given these observations, we sought to expand upon existing models for DSC to see whether we could quantitatively replicate the trends observed and, if so, gain additional insight into the mechanisms of DSC and irreversible photobleaching. Previously, Dickson et al. [117] proposed a four-state model consisting of two anionic and two neutral chromophore states to describe the blinking of yellow-emitting GFP variants at the single-molecule level. Here, we performed numerical simulations on an analogous four-state system consisting of two bright states (S0 and S1) and two dark (or less-fluorescent) states (D0 and D1). In the context of RFPs, dark states likely represent a mixture of neutral (nonabsorbing at 532 nm) and/or isomerized (absorbing at 532 nm) chromophore states. A schematic of this model is presented in Figure 2.7a. The simulations consisted of the following coupled ordinary differential equations (See Equations 2.10, 2.11, 2.12, and 2.13).

$$\frac{d[S0]}{dt} = -k_{S0ex}[S0] + k_{em}[S1] + k_{dsr}[D0] \tag{2.10}$$

$$\frac{d[S1]}{dt} = k_{S0ex}[S0] - k_{S1B}[S1] - k_{em}[S1] - k_{S1D1}[S1] + k_{D1S1}[D1] \tag{2.11}$$

$$\frac{d[D0]}{dt} = k_{S1D1}[S1] - k_{D1S1}[D1] - k_{D1B}[D1] - k_{IC}[D1] + k_{D0ex}[D0] \tag{2.12}$$

$$\frac{d[D0]}{dt} = -k_{dsr}[D0] + k_{ic}[D1] - k_{D0ex} \tag{2.13}$$

In this four-state model, absorption of a photon (i.e., electronic transition from S0 to S1) is followed by depopulation through emission of a photon (kem), nonradiative internal conversion, or a low-quantum-efficiency (ϕ_{dsc} 10^{-3}, k_{S1D1} 5×10^5 s^{-1}) [173] conversion to the weakly or non-radiative D1 state. D1 can decay to D0 (k_{ic}), which can subsequently be converted back to S0 (k_{dsr}). The rates input into the kinetic simulations are referred to as "microscopic," and the rates measured by fitting the results from the numerical

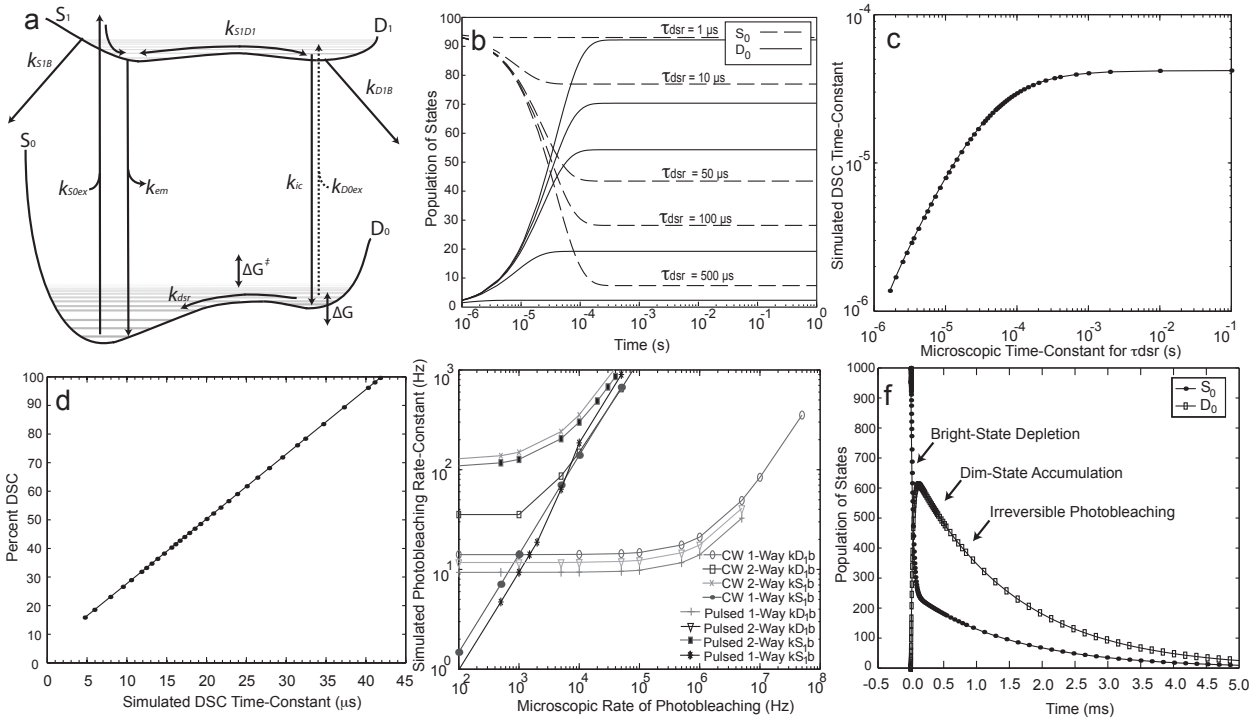

Figure 2.7: (a) The four-state model includes the rate of excitation (k_{S0ex}), fluorescence emission (k_{em}), conversion from S1 to D1 (k_{S1D1}), internal conversion from D1 to D0 (k_{ic}), and dark-state recovery (k_{dsr}). Photobleaching was incorporated out of both S1 (k_{S1B}) and D1 (k_{D1B}). In some FPs, dark-state excitation (k_{D0ex}) is included and D1 may be weakly fluorescent. (b) The influence of dark-state recovery kinetics on S0 depletion at 25 kW/cm^2. As the microscopic time constant for dark-state recovery (τ_{dsr}) increases, the S0 state is depleted and a significant increase in the D0 population is observed. (c) Microscopic time constant of dark-state recovery versus the time constant obtained by fitting the simulated DSC. At fast timescales, the measured time constant of DSC accurately reflects the time constant of ground-state recovery, with increasing deviations observed for FPs with particularly slow DSC kinetics (long time constants). (d) Percent DSC versus time constant of DSC. The kinetics of DSC were determined by fitting the results from the numerical simulation. The model predicts that the percent DSC linearly increases with the time constant of DSC. (e) Numerical modeling of photobleaching out of S1 and D1. Kinetic modeling was performed in the presence (2-Way) and absence (1-Way) of dark-state excitation for both CW and pulsed illumination. The x axis represents the microscopic photobleaching rate for S1 or D1, and the y axis represents the photobleaching kinetics obtained by fitting the numerical simulations. For example, CW 1-Way D1 Bleach represents a continuously illuminated numerical simulation in which the dark state does not absorb (i.e., one-way) and the D1 bleaching rate is iteratively adjusted while the S1 bleaching rate is held constant. Modeling demonstrates that when D0 does not absorb, the observed photobleaching rate is independent of bleaching out of D1 and linearly correlated with bleaching out of S1. Under two-way conditions, D1 bleaching becomes significant for continuous illumination but is minimized upon pulsed illumination. (f) The four-state model explains the complex photophysical behavior observed for mKate2 and mApple under continuous photobleaching at 25 kW/cm^2. In cases where D1 may be weakly fluorescent due to changes in the fluorescence quantum yield or excitation rate, the rapid decrease and subsequent transient increase in fluorescence intensity represent population transfer from a bright state to a dim state before the onset of irreversible photobleaching.

simulations are referred to as the "simulated" time-constant. The kinetic analysis from experimental data is referred to as "measured." In accordance with Dickson et al. [117], recovery from D0 to S0 was assumed to be rate-limiting. As shown in Figure 2.7b, variation of the microscopic time constant for dark-state recovery (τ_{dsr}) from 1 to 500 ms altered the populations of the S0 ground state and D0 dark state (i.e., the percent DSC). This result suggests that the measured variation in the percent DSC (from 18 % to 87 %; Table 2.2) reflects changes in the kinetics of recovery from the dark state (τ_{dsr}). To test whether the DSC time constant obtained by fitting the fast phase of fluorescence decay reflects the rate of ground-state recovery (i.e., the transition from D0 to S0), we varied the microscopic time constant for dark-state recovery (τ_{dsr}) and determined the corresponding time constant for DSC from the numerical simulations. At fast timescales (i.e., <100 ms), the time constant of DSC is correlated with the microscopic dark-state recovery kinetics (Figure 2.7c), whereas at longer timescales (i.e., >100 ms) the parameters are uncorrelated. For some of the FPs (7 out of 13), the measured DSC time constant is within the linear range of the simulated parameters, suggesting that for these FPs the observed fluorescence decay directly reflects the kinetics of ground-state recovery.

The four-state model also explains the correlation between the fastest timescale of fluorescence decay and the magnitude of DSC. Here, FPs with slower rates of ground-state recovery will have an increased population buildup in D0. In agreement with our experimental results, simulations predict that the percent DSC is linearly proportional to the DSC time constant (Figure 2.7d). Additionally, in agreement with our experimental data (Figure 2.7b), modeling confirms that DSC increases linearly with the lifetime of S1 (τ_{fl} = 0.5-4.0 ns), with small changes (≈2-fold) in the simulated kinetics of DSC (results not shown).

Kinetic pathways for photodegradation out of both S1 and D1 (k_{S1B} and k_{D1B}, respectively; Figure 2.7a) were incorporated into the four-state model. Simulations of both CW and pulsed illumination experiments were performed as a function of both microscopic photobleaching rates (Figure 2.7e). In cases where excitation from D0 to D1 did not occur (1-Way in Figure 2.7e), the microscopic rate k_{S1B} was found to correlate linearly with the observed photobleaching rate for both pulsed and CW illumination. In this case, photobleaching from the dark state was negligible, and required k_{D1B} rates 1000-fold greater than k_{S1B} to significantly alter the observed photobleaching kinetics. This result indicates that nonabsorbing or

weakly absorbing dark states are photoprotective. In the case where the excitation from D0 to D1 did occur (2-Way in Figure 2.7e), large differences were observed in the photobleaching rate between CW and pulsed illumination. For CW illumination, the photobleaching rate was no longer linearly correlated with changes in k_{S1B}, and changes in the observed photostability became significant for k_{D1B} at rates comparable to k_{S1B} (i.e., $>10^3$ s^1). However, pulsed illumination minimized the contribution of kD1B to the observed photobleaching kinetics. These simulations suggest that a comparison of photobleaching under pulsed and CW illumination provides insight into whether the dark state is photoprotective (bleaching does not occur from D1) or photoreactive (bleaching does occur from D1). For example, FPs with photoprotective dark states (e.g., TagRFP R67K S158T) likely do not absorb at the given excitation wavelength (i.e., the transition from D0 to D1 is insignificant).

2.10 mCherry, Differences Between in vivo, in vitro, and Published FCS Data

Using the rapid-photobleaching methodology, we measured 18 % DSC for mCherry *in vivo* using 532 nm CW illumination at 25 kW/cm^2. This is in contrast to FCS measurements performed by Hendrix et al., where they found a 46 % DSC for mCherry *in vitro*, using 543 nm CW illumination at 24 kW/cm^2 [172]. Prompted by the apparent discrepancy between our mCherry data and that by Hendrix et al., we performed rapid photobleaching and dark-state conversion assays on purified mCherry *in vitro*. To facilitate comparison, we prepared fresh protein under identical buffer conditions as Hendrix et al. (Phosphate Buffered Saline, pH=7.4, 50:50 v/v glycerol), and localized freely diffusing protein within aqueous microdroplets inside of an insoluble octanol organic phase [68, 185]. To test if glycerol changed the observed DSC, samples were prepared with and without glycerol (50 % v/v). Importantly, no statistically significant difference (two-tailed t-test, P=0.83) was observed between samples that contained glycerol (25.4 % DSC, n=11) and those that did not (25.1 %, n=10). Interestingly, the percent DSC did change from 18 % (n=3) *in vivo* to 25 % (n=21) *in vitro* (two-tailed t-test, P=0.0003), perhaps owing to changes the local environment.

Nevertheless, the 7 % increase in dark-state conversion upon going from an *in vivo* to an *in vitro* environment could not entirely describe the observed percent DSC reported by Hendrix et al. Furthermore,

the change in excitation intensity and excitation wavelength seems unlikely to account for the remainder of the discrepancy. Consequently, we hypothesized that the remainder of the difference was due to artifacts arising from FCS analysis [186–188]. More specifically, FCS does not differentiate between fluorescence fluctuations due to reversible or irreversible processes, unless they occur on largely disparate timescales.

To test this hypothesis quantitatively, we calculated the expected irreversible photobleaching that could occur during the transit time through the excitation beam in FCS. For example, Hendrix et al., report that an apparent diffusion coefficient of 56 μm^2 s^{-1}, which according to the Einstein-Stokes relation (Equation 2.14), predicts a hydrodynamic radius of 3.89 nm for mCherry. Here K_b is the Boltzmann constant, T is the temperature, η is the solvent viscosity (1.002 mPa s for water at 20° Celsius, and 8.4 mPa s for 50:50 v/v water glycerol mixture at 20° Celsius), D is the diffusion coefficient, and r is the hydrodynamic radius.

$$r = \frac{K_b T}{6\pi\eta D} \tag{2.14}$$

Assuming diffraction limited excitation and collection volume for FCS, the lateral (Equation 2.15) and axial dimensions (Equation 2.16) of the excitation volume at full width and half maximum (FWHM) are approximately 200 and 500 nm, respectively [189]. Here, λ is the wavelength of light, η is the refractive index of the immersion liquid (water = 1.33), and α is the angle for which the objective can collect light (66° for a 1.2 numerical aperture objective).

$$d(lateral) = \frac{\lambda}{2\eta sin(\alpha)} \tag{2.15}$$

$$d(axial) = \frac{\lambda}{\eta sin^2(\alpha)} \tag{2.16}$$

Under these conditions, the transit time for a single FP through the excitation volume can be estimated using Brownian diffusion (Equation 2.17).

$$t \approx \frac{x^2}{2D} \tag{2.17}$$

Using the aforementioned hydrodynamic radius of mCherry (3.89 nm), and the viscosity of a 50:50 v/v glycerol water solution (8.4 mPa s), this equation dictates that it takes, on average, 3.7 and 19.2 ms to travel through the excitation volume in the lateral and axial directions, respectively. Using our measured irreversible photobleaching time-constant for mCherry of 57 ms, we predict that 6.3 % of the molecules traversing the beam in the lateral direction will undergo irreversible photobleaching, and 28.6 % for those traversing the axial direction. This observed photobleaching is even more problematic for FPs with accelerated photobleaching, including mStrawberry (9.77 % and 41.34 %), and mOrange (97.5 % and 100 %).

Indeed, this is consistent with our observation that mCherry undergoes irreversible photobleaching within the first 2 ms of pulsed excitation (See Table 2.2, and Figure 2.4b). Combining these values with the observed increase in DSC upon going from *in vivo* to *in vitro* conditions (18 to 25 %), in addition to subtle excitation wavelength effects, we infer that the remaining 20 % of DSC observed by Hendrix et al. results form irreversible photobleaching. Lastly, this is also consistent with the observation that Hendrix et al. observed relaxation longer time-constants (98.6 μs) than ours (73 μs), as this likely represents a weighted average of the time-constants for irreversible photobleaching dark-state relaxation. Consequently, we attribute these discrepancies to difficulties in differentiating reversible and irreversible fluorescence fluctuations in FCS.

2.11 Discussion

Rapid, irreversible photobleaching and DSC remain major obstacles that limit the use of FPs for single-molecule applications, low-copy gene expression, and particle tracking *in vivo*. A better understanding of DSC and new methods for measuring it will permit a detailed characterization of different FPs and may provide insight into which FP is most suited for a particular application. For example, our results (Figure 2.3a) and those of Shaner et al. [23] suggest that TagRFP-T may be the most photostable FP for low-excitation-intensity imaging (e.g., wide-field arc-lamp, total internal reflection fluorescence, and live-cell laser scanning confocal microscopy). However, in single-molecule applications (e.g., single-particle tracking and FCS), where excitation intensities exceed 1 kW/cm^2, mCherry and TagRFP R67K S158T appear to be substantially better than TagRFP-T (Figure 2.3, b and c). These observations, as well as those regarding

excitation wavelength dependence (7), illustrate that extensive data on excitation intensity and wavelength dependence data for each FP are necessary to select the optimum FP for a particular imaging application.

We explored whether a simple four-state model could explain the complex and often highly variable photophysical behavior of a panel of FPs. Numerical simulations demonstrate that a simple four-state model can explain how the magnitude of DSC varies with the kinetics of DSC and fluorescence lifetime, and how DSC contributes to irreversible photobleaching. The modeling also suggests that the measured kinetics of the initial decrease in fluorescence (i.e., kinetics of DSC) reflect the rate of dark-state recovery (τ_{dsr}), that the percent DSC is sensitive to changes in τ_{dsr}, and that a comparison of CW and pulsed excitation measurements provides insight into coupling of the dark state to photodegradation. In addition to replicating general trends, the four-state model can also explain the complex behavior of select FPs, such as mKate2 and mApple. These FPs undergo a rapid decrease in fluorescence intensity followed by a transient rise in fluorescence intensity before irreversible photobleaching occurs (Figure 2.3, b and c). This behavior can be explained by considering population transfer from the initially excited bright state to a less fluorescent state (i.e., decreased quantum yield ϕ_{D1Fl} and/or absorption rate $k_{D0ex)}$ rather than a strictly dark state. Consequently, a transient rise in fluorescence intensity represents a population buildup in the less-fluorescent state before the onset of irreversible photobleaching (Figure 2.7f).

The kinetic analysis of photobleaching at 25 kW/cm^2 revealed a clear trend in mutations that act synergistically or antagonistically to impact irreversible photobleaching. For example, the introduction of R67K into TagRFP S158T resulted in a 6.4-fold increase in the irreversible photobleaching time constant without significantly altering the percent DSC (Table 2.2). Likewise, single mutations in the context of TagRFP R67K S158T, including N143S, T158S, and T158A, all exhibited excellent photostability, although to a lesser extent than TagRFP R67K S158T alone. Of interest, in all tested cases, the presence of F174L decreased the photostability (Table 2.2), rendering the FP similar or worse in performance to the parent TagRFP S158T. These results suggest that mutations act in concert with regard to irreversible photostability, and that significant gains in photostability may be possible within the correct mutational context.

The kinetic simulations suggest that the rate of D0 excitation dictates the extent to which D1 is populated, and hence whether D1 is a significant precursor along a photodegradative pathway. For example,

at 25 kW/cm^2, mCherry is markedly more photostable under pulsed illumination than under CW illumination, suggesting that mCherrys dark state is photoreactive. Alternatively, TagRFP R67K S158T does not experience as large of a gain in photostability under pulsed conditions, suggesting that its dark state is more photoprotective than photoreactive. For TagRFP R67K S158T, our numerical modeling simulations suggest that this behavior could result from a decreased dark-state excitation rate, which could result from transient changes in the conformation or protonation state of the chromophore, whose kinetics are sensitive to the local environment.

The variability of photobleaching out of dark states also provides some explanation for the contrasting behavior of mCherry and TagRFP R67K S158T at 25 kW/cm^2 compared with 2.5 kW/cm^2 . At moderate intensities (tens of kW/cm^2), the DSC rates scale linearly with excitation intensity [168]. Consequently, FPs with more photoreactive dark states will show a heightened sensitivity to increases in excitation intensity relative to those with less reactive dark states. Our experimental results and kinetic simulations also provide some context for published results that demonstrate the excitation wavelength dependence of FP DSC and photostability [23,173,174]. This wavelength dependence may be explained by changes in the excitation rate of D0 relative to S0, which varies in accordance with their corresponding excited-state absorption spectra. In cases where dark-to-bright-state conversion occurs, the final steady-state distribution of dark state will depend on the rate of k_{D0ex}. For irreversible photobleaching, the relative rates of k_{D0ex} and k_{S0ex} dictate whether D1 or S1 will be the dominant pathway for photobleaching.

Our pulsed excitation method is advantageous for FPs primarily because DSC and photobleaching occur on widely varying timescales, which are probed by the microsecond time-resolved fluorescence transients that are repetitively observed during the millisecond excitation/dark intervals. The method therefore resolves kinetics over six orders of magnitude in time, and in particular extends measurements beyond the millisecond timescale. Experiments with a narrower experimental time window, such as FCS, do not directly resolve both timescales and therefore require a rigorous analysis of irreversible photobleaching (which has only been performed in a few cases [190–192]) for the DSC time constants to be accurately determined. Another key advantage of the broad time window in our method is that it can be employed over the three orders of magnitude in excitation intensities encompassed by many commonly used imaging techniques, and thus

potentially can provide one set of measurements for quantitative comparisons of signal intensities.

In conclusion, our examination of several closely related RFPs with pulsed excitation provides evidence for dark states of varying reactivity and highlights the role of these states in irreversible photobleaching. This work introduces a spectroscopic method for independently measuring DSC and irreversible photobleaching at the ensemble level. In comparison with DSC kinetics measured on single molecules [168, 169, 171–173], our methodology provides additional insight into slow events, such as irreversible photobleaching, without requiring surface immobilization, and allows measurements to be obtained inside living mammalian cells.

Chapter 3

Generation of Microfluidic Methods for High-Throughput Single-Cell Photobleaching

3.1 Abstract

Traditional flow cytometers are capable of rapid cellular assays on the basis of fluorescence intensity and light scatter. Microfluidic flow cytometers have largely followed the same path of technological development as their traditional counterparts; however, the significantly smaller transport distance and resulting lower cell speeds in microchannels provides for the opportunity to detect novel spectroscopic signatures based on multiple, nontemporally coincident excitation beams. Here, we characterize the design and operation of a cytometer with a three-beam, probe/bleach/probe geometry, employing HeLa suspension cells expressing fluorescent proteins. The data collection rate exceeds 20 cells/s under a range of beam intensities (5 kW to 179 kW/cm^2). The measured percent photobleaching (ratio of fluorescence intensities excited by the first and third beams: S_{Beam_3}/S_{Beam_1}) partially resolves a mixture of four red fluorescent proteins in mixed samples. Photokinetic simulations are presented and demonstrate that the percent photobleaching reflects a combination of the reversible and irreversible photobleaching kinetics. By introducing a photobleaching optical signature, which complements traditional fluorescence intensity-based detection, this method adds another dimension to multichannel fluorescence cytometry and provides a means for flow-cytometry-based screening of directed libraries of fluorescent protein photobleaching.

3.2 Publication Status and Author Contributions

Lubbeck, J.L., Dean, K.M., Ma, H., Palmer, A.E., Jimenez, R. Microfluidic Flow Cytometer for Quantifying Photobleaching of Fluorescent Proteins in Cells. *Anal. Chem.* 2012. May 7;9(5):1425-34.

J.L.L., K.M.D., A.E.P, and R.J. designed the research. J.L.L. and K.M.D. performed research. H.M. performed optical calculations. J.L.L. performed data analysis and photobleaching numerical simulations. J.L.L., A.E.P., and R.J wrote the paper.

3.3 Introduction

Traditional flow cytometers employ light-scattering and fluorescence-based detection to assess spectral diversity [193–195], cell size [196], fluorescence brightness [197–199], fluorescence lifetime [200, 201], and analyte concentration [202] on individual cells flowing through one or more tightly focused excitation beams at speeds of $\approx$ 1-10 m/s. In this operating regime, the time window for optical excitation and detection is approximately a few microseconds per beam and hundreds of microseconds between beams. In contrast, the short transport dimensions and confining properties of microfluidic channels enable highly stable flows at cell speeds of 10^{-6} to 10^{-3} m/s. We exploited these properties to develop the ability to screen with optical or photophysical properties that are manifested at longer time-scales (tens of milliseconds or slower) by implementing multipoint fluorescence excitation measurements in a microfluidic flow cell. We specifically investigate the probing of photobleaching in flow. Although it is likely to be ubiquitous in flow cytometry, few studies have investigated photobleaching in detail, and there are no reports of fluorophore screening or sorting based on photobleaching. Previous reports by van den Engh et al. and Doornbos et al. focused on understanding photobleaching and photon saturation in DNA stains, fluorescein conjugates, phycoerythrin, and allophycocyanin, via pulse shape and power-dependence measurements, primarily with the goal of optimizing the magnitude of fluorescence signals [203, 204]. The excitation conditions in those studies accessed time windows of 2 μs to 2 ms, at excitation intensities of 5-3200 kW/cm^2. Here, we report the design of a cytometer for assessing photobleaching of genetically encodable fluorescent proteins, at excitation intensities comparable to those used for confocal imaging and single molecule spectroscopy (10-100 kW/cm^2).

Since the advent of green fluorescent protein (GFP), genetically encodable fluorescent proteins (FPs) [205] in a diversity of excitation and emission wavelengths have found widespread use in molecular and cell biology due to the ability to fuse them to a protein of interest and target them to specific subcellular structures [206]. Despite these advantages, FPs exhibit complex excited-state dynamics which limit their photon output. In these fluorophores, irreversible photobleaching, which refers to photodestruction of the chromophore, usually occurs in the presence of reversible photobleaching, which involves transient conversion to a nonfluorescent or dimly fluorescent state. Depending on the FP, reversible photobleaching has been attributed to triplet state conversion [115], excited state proton-transfer [50], or photoinduced isomerization of the chromophore and nearby side chains [62, 116, 207]. Subsequent ground-state recovery occurs in tens of microseconds to minutes [168, 208] and may depend on the chromophore environment of the FP [208]. In ensemble measurements, reversible photobleaching is manifested as an initial fast decay of fluorescence that recovers when the excitation light is turned off [23, 206, 208, 209]. The magnitudes and time-constants of both reversible and irreversible photobleaching depend on the fluorophore, excitation intensity, and excitation wavelength [23, 206, 208, 209]. Although these factors make the composite photobleaching process tricky to quantify, there is a clear potential for using it in flow-cytometric screening for the development of new fluorescent proteins. This approach would be significantly faster than microplate or colony-based screening. Due to the longer time scale photophysics in FPs compared to small molecule fluorophores, a cytometry-based screening system will require that a correspondingly longer time-window be accessible to the measurement.

In the previous chapter, we described the use of millisecond pulse sequences to dissect the photobleaching process of FPs in individual HeLa cells [209]. Here, to measure photobleaching of cells in flow, we implemented a design that quantifies photobleaching on the millisecond time scale, independent of fluorophore concentration, fluorescence quantum yield or extinction coefficient. We employ three spatially separated beams: a low-intensity probe beam (5 kW/cm^2) to measure initial fluorescence, followed by a high-intensity bleach beam (5-179 kW/cm^2) to initiate photodestruction of the fluorophores, followed by a second low-intensity probe beam, of equal intensity to the first, to assess the extent of photobleaching. This approach simplifies data acquisition compared to direct measurement of a time-resolved fluorescence decay because ratios of peak signal intensities are easier to fit and define than the multiexponential decays which

characterize the photobleaching process.

Here, we combine microfluidics and spectroscopy techniques in a flow cytometer for measuring the combined effect of reversible and irreversible photobleaching at a rate of >20 cells/s. To our knowledge, this capability has not previously been reported. We present calculations guiding the optical design of a multibeam cytometer describing how to optimize measurement precision and alignment tolerance in a simple 2D hydrofocusing geometry. The technique is demonstrated on four different red fluorescent proteins (RFPs), under a variety of excitation conditions, which uncovered a diverse range of reversible and irreversible photobleaching on the millisecond time scale. Lastly, we present kinetic simulations to examine the effects of reversible and irreversible photobleaching rates on the capability of our method to discriminate populations.

3.4 Experimental Methods

3.4.1 Microfluidics and Optical Layout

Microfluidic devices were built by anodically bonding a 25 μm thick 2 in. diameter silicon wafer to a 1.7 mm thick glass-slide. Silicon was etched down to the glass in the pattern of the channels using standard photolithography and plasma etching techniques [210]. This method results in optically transparent channels of 25 μm height $\times$ 150 μm width $\times$ 1 mm length for the central interrogation channel. Sample ports of 1 mm diameter were drilled in a second, identical glass slide before bonding to the silicon.

The microfluidic was compression fit with "O" rings against a manifold constructed from polytetrafluoroethylene (PTFE; to minimize nonspecific adsorption of cells) with 200 μL sample reservoirs (Figure 3.1). The microfluidic device and combined manifold assembly were mounted onto the stage of a commercial inverted microscope. Flow was driven using three closed-loop air-pressure controllers connected by PTFE tubing to the sample ports. By independently varying the pressures on all three inlets, the hydrodynamic focal width was kept constant at 15 μm as measured by imaging the fluorescence from a dye flowing in only the center cell channel [211]. The cell speed in the interrogation region was varied from 1 to 15 mm/s to control exposure time to the bleach beam. The speed was calculated from measurements of cell transit times between probe beams 1 and 2 using fluorescence signals, and measurements of spatial separation of

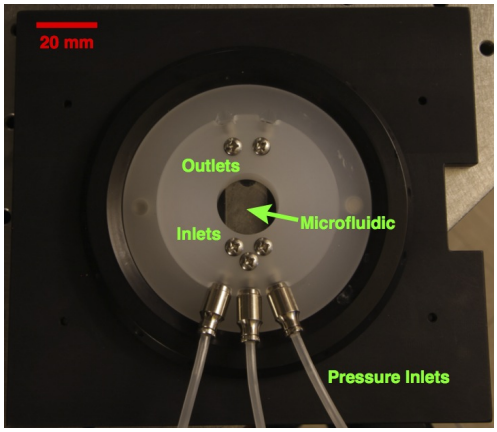

Figure 3.1: Microfluidic device and manifold assembly. Pressure is provided through tubing shown at the bottom. Cells are placed in the middle inlet, and the outer inlets contain sheath solution for hydrodynamic focusing of the cells. The transparent microfluidic is located in the middle of the manifold, allowing delivery of light in both the epi and trans directions. Microfluidic outlets are provided at the top.

the beams (Figure 3.2; typically 240 $\pm$ 3 μm). The cell speed distribution typically had a standard deviation of 1 %. The flow was visualized with a CMOS camera, and wide-field transillumination was provided by a home-built condenser.

The three-beam geometry consisted of two equal intensity probe beams measuring the peak fluorescence from a cell before and after a higher-intensity photobleaching beam. To implement this experimental geometry, a 2 W 532 nm continuous wave laser was split into three beams by a series of beam splitters (30:70 and 50:50) and waveplate-polarizer pairs, thereby allowing independent control of each beams excitation intensity. After splitting, all beams were shaped by a cylindrical lens (150 mm focal length), directed into the microscope, reflected from a 532 nm dichroic mirror, and focused inside of the microfluidic channels by a 20x, 0.45 NA air-objective (Figure 3.2a). Shaping the beams with the cylindrical lens results in elliptical beams (75 μm length $\times$ 3.5 μm width, FWHM, as measured by imaging light scattered from the sample focal plane onto a CMOS camera) that stretch the entire width of the hydrofocus. The beams were distributed over a 240 μm distance with the bleach beam located midway between the two probe beams (Figure 2b). The probe beam intensity was 5 kW/cm^2 and the bleach beam was 170 kW/cm^2 (calculated from the FWHM of the beam dimensions and laser power measured at the sample plane ($\pm$5 %)). The probe beams were matched in intensity before each experiment. Fluorescence was collected through the same objective and separated

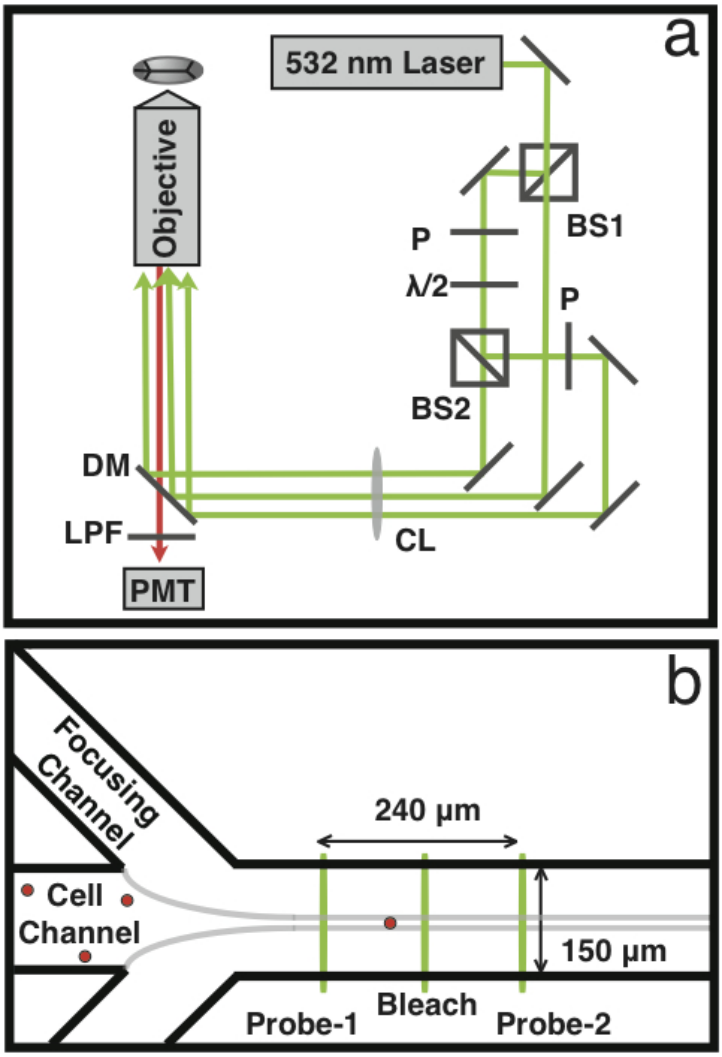

Figure 3.2: Three-beam microfluidic cytometer experimental design. (a) Schematic of the optical setup. Relevant components include the following: 20x 0.45 NA air immersion objective (obj); 532 nm dichroic mirror (DM); 545 nm long-pass filter (LPF); red-enhanced photomultiplier tube (PMT); 150 mm focal length, cylindrical lens (CL, placed 19 cm from back aperture of objective); half-wave plate ($\lambda/2$); Glan-Thompson polarizer (P); 70:30 beam splitter (BS1); 50:50 beam splitter (BS2). (b) Schematic of the microfluidic channel geometry at the interrogation region. Cells were hydrodynamically focused to a width of 15 μm before encountering the elliptical bleach and probe beams (FWHM 3 $\times$ 75 μm).

from excitation light by the 532 nm dichroic mirror and a 545 nm long-pass filter. The emission was detected by a red- sensitive photomultiplier tube (PMT, Hamamatsu, R9880U- 20) on the primary imaging port of the microscope. At this port, the fluorescence signals from the three beams are spatially resolved, which allowed for placement of a mask at the focal plane which blocks the photobleaching beam. A lens is used to refocus fluorescence from the two probe beams onto the PMT.

3.4.2 Data Acquisition and Processing

The PMT photocurrent was processed by a custom-built AC-coupled trans-impedance operational amplifier, which improves the signal-to-noise ratio by removing high and low frequency noise components outside the band-pass of 160 mHz to 106 kHz. The resulting voltage levels were digitized at 250 kHz with a PC-based data acquisition board (16 bit ADC) and custom software (LabView, National Instruments). After fitting each peak to a Gaussian, the peak fluorescence signals for the first and second probe beams (S_{Beam_1} and S_{Beam3}) were recorded. Typical fluorophore transit times through each beam varied from 0.2 to 3.5 ms depending on the cell velocity (1-15 mm/s) and neglecting fluorophore diffusion within the cell.

3.4.3 Sample Preparation

HeLa suspension (HeLa-S, mean diameter = 14.4 μm, CV = 21.8 %, as measured from images taken on a widefield microscope) cells were maintained in spinner flasks at 37° Celsius in a 5 % CO_2 atmosphere using spinner-modified Dulbeccos Modified Eagles Medium, 10 % fetal bovine serum, and 1 % penicillin-streptomycin. HeLa-S cells were virally transduced according to manufacturers protocols with an FP either under a constitutive cytomegalovirus promoter (TagRFP, and TagRFP-T in pCLNCX) or an inducible tet-responsive promoter (mCherry, mOrange2, pCL-TRE). Briefly, virus was generated by transfecting the appropriate combination of DNA (pCLNCX-FP, pCLTRE-FP, pCL-Ampho, pCL-TetOn, pVSV-G) into HEK293FT cells. After two days, the virus-containing supernatant was collected, passed through a 0.45 μm cellulose acetate filter, and added to HeLa suspension cells with 12 μg/mL polybrene and, if appropriate, expression was induced with 1 μg/mL doxycycline.

To establish the cell lines, the fluorescent population was enriched once by fluorescence-activated cell

Table 3.1: Fluorescent protein cell-lines, viral vectors, and observed fluorescence intensity distribution, represented at a coefficient of variation (CV).

Fluorescent Protein	Vector	Fluorescence CV
TagRFP-T	pCLNCX	130 %
TagRFP	pCLNCX	160 %
mCherry	pCL-TetOn	250 %
mOrange2	pCL-TetOn	150 %

sorting (FACS) with a Dako Cytomation Mo-Flo cell sorter. For FACS, cells were placed into Ca^{2+} and Mg^{2+} free HHBSS, pH=7.4, at a concentration of approximately 10^6 cells/mL. Excitation was performed with a 568 nm krypton laser, forward scatter was used to trigger acquisition, and the fluorescence emission was separated from the excitation scatter by use of a 630/30 band-pass filter. The PMT was set at 450 volts, and forward scatter, side-scatter, and fluorescence were all operated in logarithmic modes. The flow-cytometer was maintained at around 2,000 events/second. Sufficient optical alignment was confirmed by a narrow (1.3 %) CV using Beckman Coulter Flow-Check Fluorospheres (part number: 6605359, diameter = 10 μm). Uninfected, and thus non-fluorescent, HeLa suspension cells were used to set the threshold (or gate) and so the sort attempted to select all cells with fluorescence greater than cellular autofluorescence. FACS was only performed initially for each individual cell-line, and G418 (working concentration of 1 mg/mL) was applied to select against potential loss of retroviral gene insertion. The distribution in fluorescence intensities and viral vector used for the four cell-lines studied here are reported in Table 3.1.

For microfluidic studies, aliquots of cells were concentrated via swinging-bucket centrifugation at 1000 rpm for 5 min. To prevent clumping and settling within the microfluidic reservoirs, cell pellets were resuspended in a density-matched medium using a commercially available density-matching solution and HEPES-buffered Hank's balanced salt solution (HHBSS), pH 7.4 solution, supplemented with 1 % bovine serum albumin. Experiments involving beads utilized 6 μm diameter fluorescently labeled beads from an Invitrogen LinearFlow Deep Red Flow Cytometry Intensity Calibration Kit, suspended in a density-matched 20 % (v/v) glycerol in water solution. The microfluidic channels were passivated with a 1 % solution of bovine serum albumin prior to each run. Cell suspensions were loaded into the center reservoir in 150 μL aliquots at a concentration of $\approx 5\times10^5$ cells/mL. The side channels were filled with 150 μL aliquots of HHBSS, pH =

7.4, for the sheath flow.

3.5 Design Considerations

One of the design goals was to ensure that the distribution of measured fluorescence intensities for a population accurately reflects cellular RFP expression heterogeneity rather than instrument resolution. Even for a single-beam fluorescence measurement of each cell in flow, the excitation intensity and therefore the observed emission signal is strongly dependent on the trajectory of each cell as it traverses through the 3D laser focus in the microchannel. Although, in principle, 3D hydrofocusing geometries would more precisely define these cellular trajectories, we show that simpler-to-fabricate 2D hydrofocusing devices can provide sufficient precision for properly designed multibeam excitation/detection geometries. In 2D hydrofocusing, cells flowing past a cross-junction with two channels of sheath flow at higher pressures are laterally confined by the flow to dimensions significantly narrower than the channel width (Figure 3.3a) [211]. Nevertheless, there will always be lateral and axial variation (relative to the optical axis of the microscope objective: see Figure 3.3) in trajectories from cell to cell. We quantify the effects of this variation on the fluorescence signal, along with the effects of slight misalignment of the two probe beams relative to the flow axis of the microfluidic. We minimized the alignment sensitivity by introducing a cylindrical lens (f = 150 mm) positioned $\approx$ 190 mm before the objective lens, to shape the Gaussian beam into an elliptical profile in the microchannel, in which the focused beam size perpendicular to the flow direction (y-axis) is much larger than along the flow direction (x-axis).

To quantify the impact of cell transit variation on the fluorescence signal, we first calculated the astigmatic transformation of a Gaussian beam through a cylindrical lens and objective optical system with a number of experimental constraints. We assumed that each cell was 14 μm in diameter (the mean cell size observed for HeLa-S cells on a wide-field microscope), had a uniform RFP concentration (i.e., an RFP-containing sphere), and traveled between two 4 μm diameter (FWHM) laser beams (Figure 3.3a,b). This beam size matched our measurements of the focused probe beam sizes produced with a 20$\times$, 0.45 NA air-objective (Figure 3.2). The observed fluorescence signal, S, is the convolution of the RFP density, s(x,y,z), and the three-dimensional Gaussian intensity profile at the laser focus, B(x,y,z) (Equation 3.1).

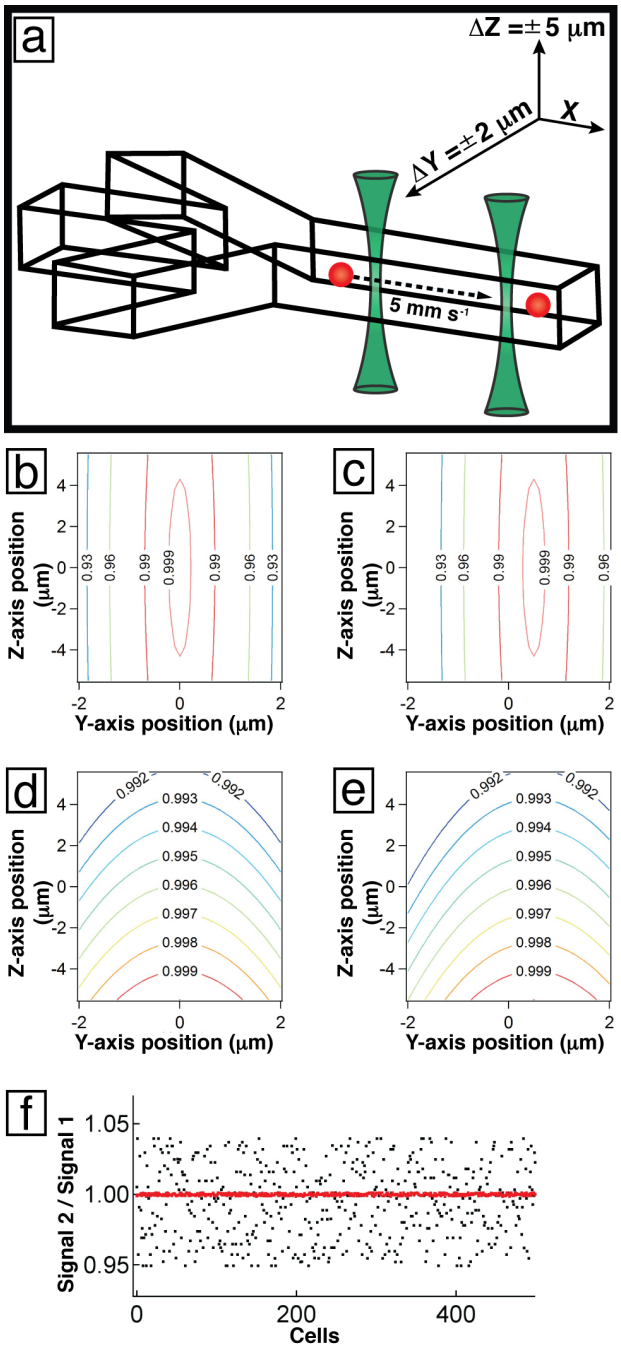

Figure 3.3: (a) Schematic of hydrodynamically focused cells traveling through two circularly shaped Gaussian laser beams where ΔZ and ΔY refer to the cell axial and lateral displacement from the center of the channel. (b-e) Contour plots showing peak fluorescence signal as a function of the cell displacement (ΔZ and ΔY) as it flows through circularly (b, c) and elliptically (d, e) shaped Gaussian beams. Parts b and d represent the fluorescence signal if the two beams are perfectly centered in the channel, whereas parts c and e represent the fluorescence signal if the second beam is displaced 0.5 μm along the y-axis relative to the center of the channel. (f) For the misaligned beams, a scatter plot of the ratio of peak fluorescence signals (I_1/I_2) from 500 cells randomly displaced from the center of the channel (within $\Delta Y = \pm 2$ μm and $\Delta Z = \pm 5.5$ μm) shows that the signal variance from elliptically shaped beams (red) is 35-fold smaller than that from circularly shaped beams (black).

$$S(x_o, y_o, z_o) = \iiint s(x - x_o, y - y_o, z - z_o) \times B(x, y, z) dx dy dz \tag{3.1}$$

The intensity function of a radially symmetrical Gaussian beam may be written as Equation 3.2, where P is the total power of the beam and ω(z)is the beam radius where the intensity drops to $1/e^2$ of its peak value.

$$B(x, y, z) = \frac{2P}{\pi\omega^2(z)} \times \exp(-\frac{2(x^2 + y^2)}{\omega^2(z)}) \tag{3.2}$$

For a Gaussian beam propagating through a cascade of optical elements in space, its wave function is modified by the optical elements (e.g. lenses) it passes through. Due to the unique transform characteristics of the Gaussian beam, its propagation can be treated analogous to geometric optics following a general ABCD matrix method [212] and by defining a complex radius of curvature according to Equation 3.3.

$$\frac{1}{\tilde{q}} = \frac{1}{R_z} - i\frac{\lambda}{\pi\omega^2(z)} \tag{3.3}$$

Here, R_z is the radius of curvature of the wave at position z, where R_z is the radius of curvature of the wave at position z. The evolution of the Gaussian beam along the propagation direction, divined as the z-axis here, is described in Equation 3.4. Here, at the Rayleigh range ($z_r = \frac{\pi\omega_o^2}{\lambda}$), where $z = z_r$, the radius of the beam is $\sqrt{2}$ times larger than its waist value ω_o, or the beam area doubles.

$$\omega_i(z) = \omega_o\sqrt{1 + \frac{z^2}{z_r^2}} \tag{3.4}$$

In the case of astigmatic transformation, for example, the propagation of a Gaussian beam through a cylindrical lens, the evolution of the beam in the x and y directions differ and the evolution in each orthogonal direction can be treated independently. In our experiment, a Gaussian beam from the laser first passes through a cylindrical lens (f_y=150 mm), then is focused by an objective lens (20x, NA=0.45) onto the sample. The sample is placed at the x-axis focal point of the objective lens, where the beam has passed the y-axis focal point and is therefore expanded across the microfluidics channel. We first deduced the analytical propagation equation of the Gaussian beam in this astigmatic optical system, then calculated the emission

signal intensity of the fluorescent cells as they traverse through the beams. Here for simplicity we treated the objective lens as a simple lens with a specified focal length of 9 mm, as it is neither practical nor necessary to trace the beam propagation through each one of the dozens or more individual optical elements in a modern objective lens. In the x direction in which the cylindrical lens does not focus, the beam transfer matrix may be written as Equation 3.5. Here, z_0 is the distance between the objective lens and the sample, which is placed at the x-axis waist position, and F_{obj} is the focal length of the objective lens. The transfer matrix in the y direction can be calculated in a similar way, except that the cylindrical lens needs to be included in the transfer matrix.

$$M_x = \begin{bmatrix} 1 - \frac{Z_o}{Fobj} & z_o \\ -\frac{1}{Fobj} & 1 \end{bmatrix} \tag{3.5}$$

The deduced analytical form of the Gaussian beam after the objective can be written as Equation 3.6, where ω_x(z) and ω_y(z) follow similar definitions as ω_z.

$$B(x, y, z) = \frac{2P}{\pi\omega_x(z)\omega_y(z)} \times \exp(-(\frac{2x^2}{\omega_x^2(z)} + \frac{2y^2}{\omega_y^2(z)})) \tag{3.6}$$

If we define the center of the objective lens as the z-axis origin where z=0, ω_x(z) and ω_y(z) may be written as Equation 3.7, where where i denotes x or y, and ω_0(i) specifies the beam waist in the i direction.

$$\omega_i(z) = \omega_o(i)\sqrt{1 + \frac{(z - z_o(i))^2}{z_r^2(i)}} \tag{3.7}$$

The calculated beam radius at the sample, which is positioned at the x-axis waist position, is $\omega_x(\mathrm{z})\mathrm{I}_{(z=zo)} = 2$ μm and $\omega_y(\mathrm{z})\mathrm{I}_{(z=z0)} = 56$ μm, which is consistent with the measured beam radius of $\omega_x = 3$ μm and $\omega_y = 67$ μm. The distribution of peak signal intensities from a cell traversing a spherically and cylindrically focused beam centered on the hydrodynamic flow are shown in Figure 3.3b and 3.3d, respectively. These contour plots reveal how the observed fluorescence signal varies as a function of the cell axial and lateral position with respect to the center of the channel (ΔZ =ΔY = 0). Figure 3.3c and 3.3e are similar but correspond to the case in which the beam is displaced laterally (ΔY = 0.5 μm) with respect to the center of the channel. This displacement represents the precision of experimental alignment. Because of the

relatively low NA of the optical system, the signal intensity is insensitive to cell axial positioning (± 5.5 μm is the maximum range for a 14 μm diameter cell in a channel of 25 μm height) for both spherical and cylindrical focusing. However, in the lateral direction, a comparison of spherical vs cylindrical beam shaping reveals very different sensitivity to cell position and beam alignment. In particular, if the beams are misaligned or the cell drifts by $\Delta Y = 0.5$ μm, the difference in the peak fluorescence intensity of the second beam relative to the first beam is significantly smaller with the cylindrical focus (Figure 3.3d,e). Consequently, we consider cells transiting only along the X-axis between the two probe beams at randomly chosen axial and lateral positions in the range $\Delta Y = \pm 2$ μm and $\Delta Z = \pm 5.5$ μm. If the two beams are perfectly aligned, then for both cases, the ratio of fluorescence intensities ($Beam_3/Beam_2$) = 1. However, for the misaligned geometry, this signal ratio depends on the cell position in the channel. Figure 3.3f shows that cylindrically focused beams yield a 35-fold lower dispersion in the signal intensities compared to the spherically focused beams. This result indicates that pairs of cylindrically focused beams will lead to substantially smaller variability in fluorescence measurements.

3.6 Instrument Validation and Single-RFP Population Photobleaching

The measured quantity in all experiments described below is the %bleach, which is defined in terms of the measured peak fluorescence signal for the first and third beams (S_{Beam_1} and S_{beam3}, respectively), as Equation 3.8

$$\%Bleach = 100 \times (1 - (\frac{S_{Beam_3}}{S_{Beam_1}})_o \times (\frac{S_{Beam_3}}{S_{Beam_1}})_b) \tag{3.8}$$

To correct for small differences in beam intensity, and lateral misalignments of probe beams, the %bleach is defined as the function of reference measurements taken in the absence of the bleach beam. Note that %bleach may be composed of a combination of reversible and irreversible photobleaching, as dictated by the excited-state dynamics of the fluorophores. To shed light on the molecular origins of the measured %bleach in terms of the rate constants for reversible and irreversible photobleaching, we present and discuss numerical simulations of the signals in terms of a four-state model of RFP photophysics.

3.7 Single-RFP Population Photobleaching

We first performed multibeam fluorescence measurements on fluorescently labeled beads to verify the precision of the measurement matched predictions from the design considerations discussed above. Data from one probe beam yields a fluorescence intensity coefficient of variation (CV) ranging from 6 % to 16 %, depending on the fluorescence intensity of the bead type (higher intensity beads yielded lower CV, Figure 3.4). The CV value averaged over all three populations of beads was within 10 % of the average value obtained on a Dako Cytomation Mo-Flo FACS. This variability is lower than many other 2D-focusing microfluidic cytometers (CV of 25-30 %) [145, 213] and comparable to 3D-focusing microfluidic cytometers (CV of 1-9 %) [214, 215] but remains larger than state-of-the-art flow cytometers (e.g., CV <3 %, BD FACSAria). For a two-probe beam measurement with a mixture of beads, a plot of S_{Beam_3} vs S_{Beam_1} was linear, with a coefficient of determination, $R^2 = 0.99$ with a 7 % CV in the ratio of S_{Beam_3} vs S_{Beam_1} for greater than 3000 events (Figure 3.4).

Two-beam measurements (without a bleach beam) on HeLa-S cells expressing TagRFP-T were fit to a line with a coefficient of determination of 0.99 and an 11 % CV in the ratio of S_{Beam_3} vs S_{Beam_1} (Figure 3.5). In principle, for two probe beams of identical intensity, and in the absence of photobleaching, we expect a slope of 1 for a plot of S_{beam3} vs S_{Beam_1}. In general, we observed slopes of slightly less than 1 for both the beads (0.93, CV = 7 %, Figure 3.4) and TagRFP-T-expressing cells (0.94, CV = 11 %) which were statistically the same by an unpaired t test (T = 1.42). Under these probe beam conditions, we expect photobleaching of the beads, and even the less photostable RFPs, to be negligible. For example, using photobleaching kinetics parameters measured for TagRFP-T at 532 nm in immobilized HeLa cells at similar intensities, [209] we estimate 0.4 % photobleaching occurs. It seems likely that the non-unity slope occurs primarily due to a slight mismatch in the probe beam power transmitted through the objective, which we observe to be highly sensitive to alignment into the microscope. In our definition of %bleach, we account for this mismatch in probe beam intensities, to provide for a corrected measure of the bleaching magnitude. For TagRFP-T cells, with a bleach beam intensity of 170 kW/cm^2 and flow speed of 27.9 mm/s (exposure time of 125 μs), the slope decreases to 0.52 (Figure 3.5), which indicates a significant amount of bleaching

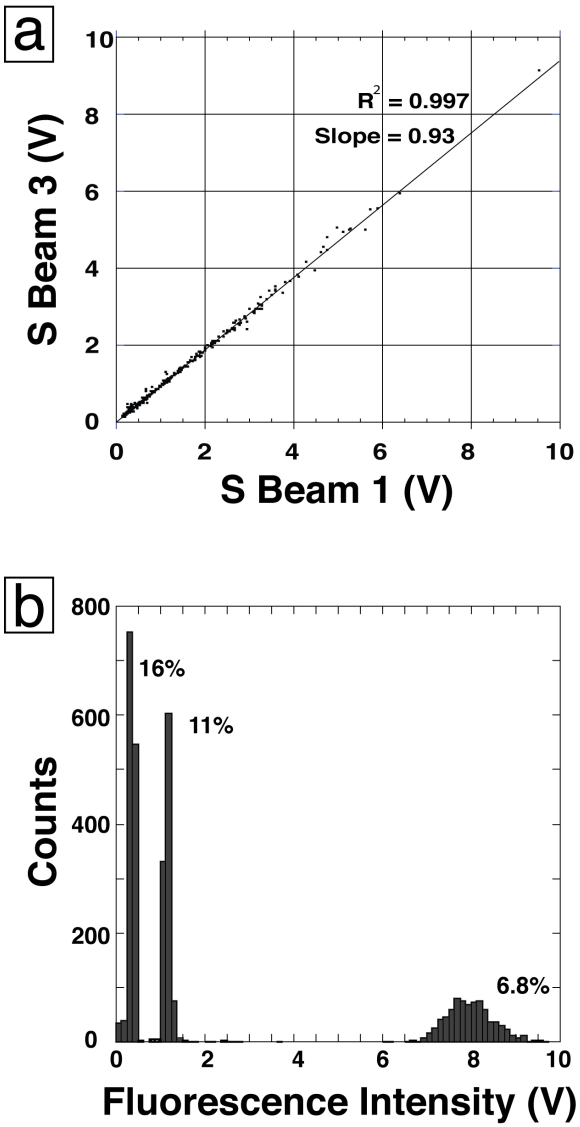

Figure 3.4: Commercially available intensity calibration beads (Invitrogen LinearFlow Deep Red Flow Cytometry Intensity Calibration Kit), suspended in a density matched 20 % (v/v) glycerol in water solution were used to characterize the microfluidic cytometer. (a) Using a mixture of beads with different fluorescence intensities, the correlation between the two probe beams was determined to be linear. The data collected in this run resulted in a slope of 0.93 with a CV of 7 %. (b) With a single excitation beam (10 kW/cm^2), mixtures of polystyrene beads with three different fluorophore densities were resolved and yielded fluorescence intensity coefficients of variation (CV, listed as % in the above figure) similar (less than 10 % different on average) to those measured individually on a FACS in a linear fluorescence mode (from left to right: 12.1 %, 11.3 %, and 7.8 %). Additionally, our microfluidic platform detected all but the most-weakly fluorescent beads, those which have intensities comparable to cellular autofluorescence on a standard flow cytometer. Furthermore, the flexibility of our microfluidic platform permitted accurate measurement of fluorescence intensities spanning three orders of magnitude (0.1-10.0 V). Our signal to noise was limited by the noise-floor of our trans-impedance amplifier and saturation of our PMT or analog-to- digital conversion hardware, enabling the user to tune the cytometer for maximum utility within a specific range of fluorescence intensities.

(%bleach = 51 %, from Equation 4). The same performance for all measurements were reproduced with the beams intersecting the hydrofocused stream anywhere along the ≈1 mm length from immediately after the hydrofocus to the end of the interrogation channel.

3.8 Resolving Fluorescent Protein Populations

To evaluate the ability to resolve subpopulations on the basis of photobleaching, three-beam measurements were performed on a mixture of HeLa-S cells expressing TagRFP [22], TagRFP-T [23], mOrange-2 [23], and mCherry [20]. Photophysical properties of these FPs are summarized in Table 3.2. With a bleach beam intensity of 170 kW/cm^2 and flow speed of 12.9 mm/s (exposure time of 270 μs), the beam spacing resulted in an 8 ms average cell transit time between beams. This time scale permits complete recovery from higher-ordered excited states and dark states [209] (Table 3.2). Under these conditions, four populations of cells were apparent in the plots of S_{Beam_3} vs S_{Beam_1} (Figure 3.6). Each RFP-expressing cell population was identified by measurements on the individual cell types under identical flow and intensity conditions. A histogram of %bleach for the ≈1891 cells in this sample also reveals four subpopulations, corresponding to the four RFPs (Figure 3.6). The rank order of average fluorescence intensities for the cell lines measured in the microfluidic cytometer agreed with those measured by FACS (TagRFP-T = TagRFP >mOrange2 >mCherry). The differences in fluorescence brightness for different RFP-expressing cell lines may result from differences in the relative absorption cross-section at 532 nm (Table 3.2) or from differences in cellular RFP concentrations, which in turn may result from incomplete chromophore maturation and differences in the transcription promoter strength. As stated previously, the cells assayed in the cytometer were not prescreened or enriched for brightness; therefore, a large range (CV >130 %) of intensities were screened. Tuning the PMT gain to optimize detection of weakly fluorescent cells would permit improved resolution of the photobleaching response in these cells [109]. In Figure 3.6c, we plot the measured %bleach vs prebleach fluorescence intensity for the cell mixture. These data show a resolution of the mixture into four populations and demonstrate that the measured %bleach depends on the RFP but is largely independent of the fluorophore concentration (as given by the prebleach emission level). The ability of %bleach to resolve the mixture of four RFPs may be quantified by fitting the histogram (Figure 3.6b) to a sum of four Gaussians.

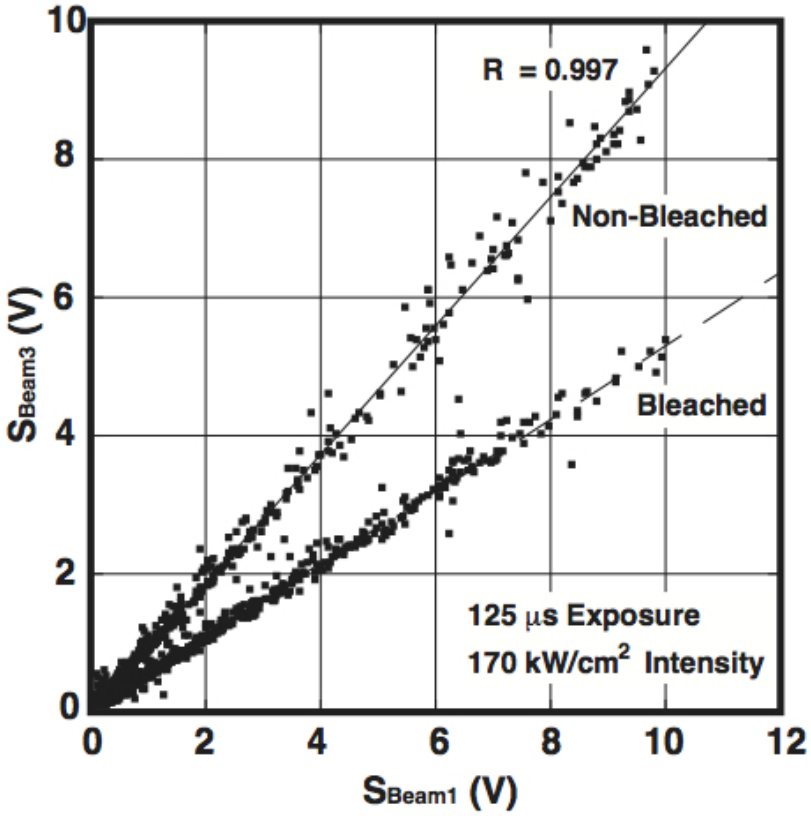

Figure 3.5: Single cell photobleaching of HeLa-S cells transduced with TagRFP-T interrogated with the two probe beams indicate that the cytometers response is linear with respect to fluorescence intensity and the signals from each probe beam are highly correlated (CV = 11 %, R^2 = 0.997, nonbleached slope = 0.94). Upon addition of the bleach beam, the slope decreases (bleached slope = 0.52), indicating that photobleaching occurs. Here, each point represents a measurement performed on a single cell.

Table 3.2: Photophysical properties for the four RFPs studied here. Reported photostabilities are from Shaner et al. [23]

FP	$\lambda_{Ex/Em}$	$\sigma_{abs@532nm}$ (cm^2)	QY	Photostability $t_{1/2}$ (s)
mOrange2	550/563	1.36×10^{-16}	0.55 ± 0.04	2,900
mCherry	586/609	1.45×10^{-16}	0.16 ± 0.04	1,800
TagRFP	554/579	2.55×10^{-16}	0.48 ± 0.04	550
TagRFP-T	555/580	2.93×10^{-16}	0.47 ± 0.04	6,900

The fit parameters (Figure 3.6 caption) reveal that the mean %bleach values for mOrange2, mCherry, and TagRFP were separated by at least 1σ, whereas the TagRFP-T population was separated from the others by at least 2σ. The percentages of cells that could be uniquely assigned to one population with at least 99.9 % confidence were obtained by determining the confidence interval of the Gaussian fit for a given cell population which has less than 0.1 % overlap from the Gaussian fits for the other cell populations. This confidence interval defines the percentage of cells in a population that can be assigned to a given Gaussian fit with 99.9 % confidence. The percentages resolved by this criterion are as follows: 1 % of the mOrange 2 cells were resolved from the mCherry cells, 43 % of the mCherry cells from the mOrange 2 and TagRFP cells, 10 % of the TagRFP cells from the mCherry and TagRFP-T cells, and 100 % of the TagRFP-T cells from the others.

3.9 Photokinetic Simulations

To understand the connection between microfluidic photobleaching measurements and fluorophore photophysics, we performed numerical simulations based on a four-state system consisting of the ground state (S_0), the first excited state or bright state (S_1), and two dark or weakly fluorescent states (D_0 and D_1) (Figure 3.7a). Table 3.3 contains a summary of the reactions and kinetic parameters. Photobleaching was permitted out of S1 and D1. Recently we used this four-state model to describe the excited-state dynamics of RFPs in immobilized single cells exposed to a series of millisecond time scale excitation pulses and demonstrated that this model faithfully captured trends for reversible and irreversible photobleaching for a panel of 13 FPs (See Chapter 2) [209]. A similar model has been used to examine reversible photobleaching (i.e., blinking) of GFP [117]. We modified our previous simulations by approximating the excitation profile

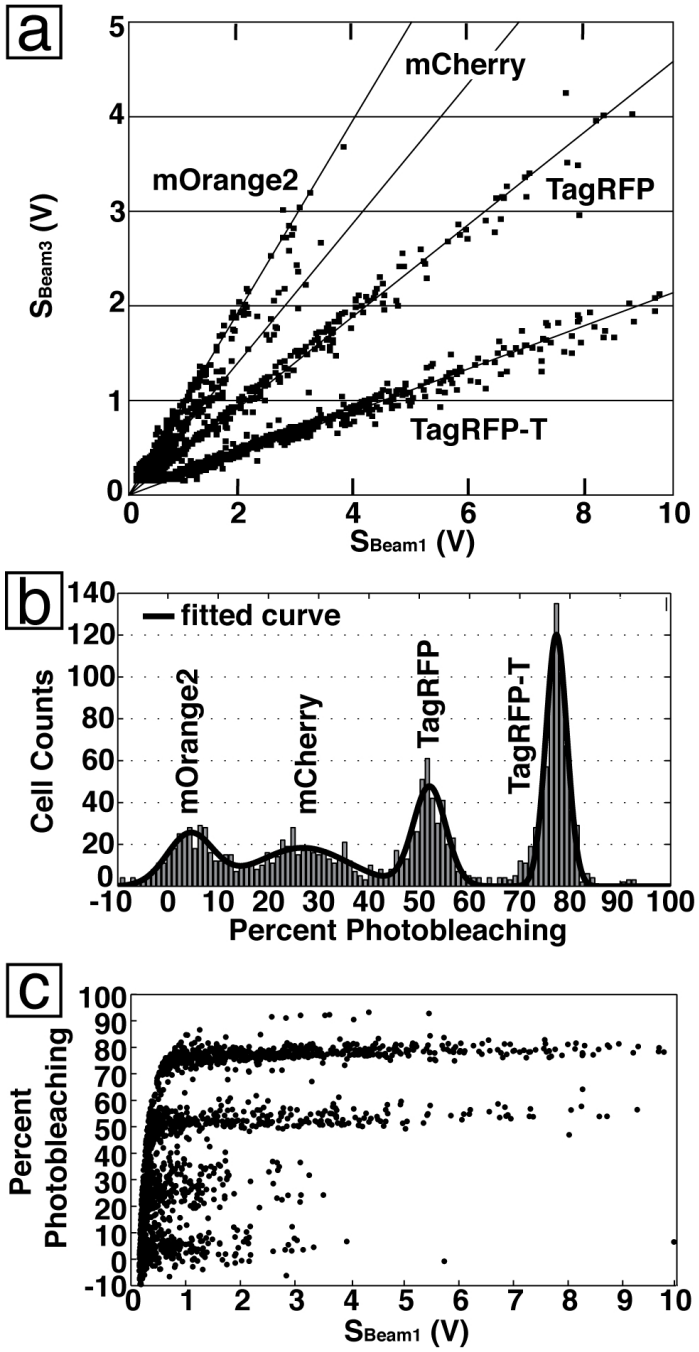

Figure 3.6: Resolving RFPs based on photobleaching in a microfluidic cytometer. (a) A mixture of cells expressing one of four RFPs was resolved on the basis of photobleaching. Each point represents an individually assayed cell and the slope of the S_{Beam_3} versus S_{Beam_1} plot yields the %bleach for each RFP. (b) The mean %bleach for each RFP-expressing cell line (upon measurement of 200-300 cells) was 4.4 (CV = 145 %) %bleach for mOrange2, 26.8 (CV = 49 %) %bleach for mCherry, 52.0 (CV = 9 %) %bleach for TagRFP, and 77.3 (CV = 4 %) %bleach for TagRFP-T as determined using a fitting program which fit a sum of four Gaussian functions to the histogrammed data. (c) Plot of %bleach vs prebleach intensity, showing the resolving power provided by bleaching measurements. The signal level corresponding to cellular autofluorescence is below the baseline of 27.8 mV.

Table 3.3: Summary of reactions and equations used in the photokinetic model.

Process	Reaction	Reaction Rate	Rate Constant Value (s^{-1})
Emission and Non-Radiative Decay	$S_1 \rightarrow S_0$	$[S_1]\, k_{Em}$	$k_{Em} = 1\times10^9$
Reversible Photobleaching	$S_1 \rightarrow D_1$	$[S_1]\, k_{Rev}$	k_{Rev} = Varied = 0 - 1×10^6
Dark-State Decay	$D_1 \rightarrow D_0$	$[D_1]\, k_{DSD}$	$k_{DSD} = 1\times10^9$
Ground-State Recovery	$D_0 \rightarrow S_0$	$[D_0]\, k_{GSR}$	$k_{GSR} = 1\times10^4$
S_1 Bleach	$S_1 \rightarrow$ Null	$[S_1]\, k_{S1Bleach}$	$k_{S1Bleach}$ = Varied = 0 - 5×10^6
D_1Bleach	$D_1 \rightarrow$ Null	$[D_1]\, k_{D1Bleach}$	$k_{D1Bleach}$ = Varied = 0 - 5×10^{10}
Excitation	$S_0 \rightarrow S_1$	$[S_0]\, k_{Ex}$	k_{Ex} = Gaussian

as a sum of Gaussian pulses that replicate the durations and excitation rates experienced by the fluorophores as they flow through the three beams in the cytometer.

Previous investigations of photodynamics in flow cytometry primarily focused on photobleaching and photon saturation [203,204], which are the dominant processes operative at the $\approx 10^3$ kW/cm^2 intensities and microsecond time scales considered in those investigations. Photon saturation occurs when the average time between excitation-photon absorption approaches the time the fluorescent molecule spends in the excited state. We estimate that the average arrival time between excitation photon for our highest intensity beam (170 kW/cm^2) beam was 1.7 photons per μs. Because the excited-state lifetime of the RFPs are in the range of 2-3 ns [209], photon saturation is negligible under the conditions employed here. We therefore focused on photobleaching and dark-state conversion processes.

The excitation rate was calculated using the measured, average-excitation intensity to find the peak-excitation intensity, which was then used to calculate the maximum rate of excitation for a representative RFP (TagRFP-T, which was chosen because its photophysical properties represent the median of the four proteins assayed) using its extinction coefficient at 532 nm (52,000 M^1 cm^1) and the Beer-Lambert law (Equation 3.9). Here, σ is the absorption cross-section, I is the light intensity, is the wavelength, $\bar{h}$ is Plancks constant ($\bar{h}$ = h/2), c is the speed of light, ϵ is the decadic molar extinction coefficient, and N is the number of molecules.

$$k_{ex} = \frac{\sigma I \lambda}{\bar{h}c} = 2.303 \times 1000(\frac{\epsilon I \lambda}{Nhc}) \tag{3.9}$$

The fluorophores first experience an excitation rate corresponding to the first probe beam. The rate

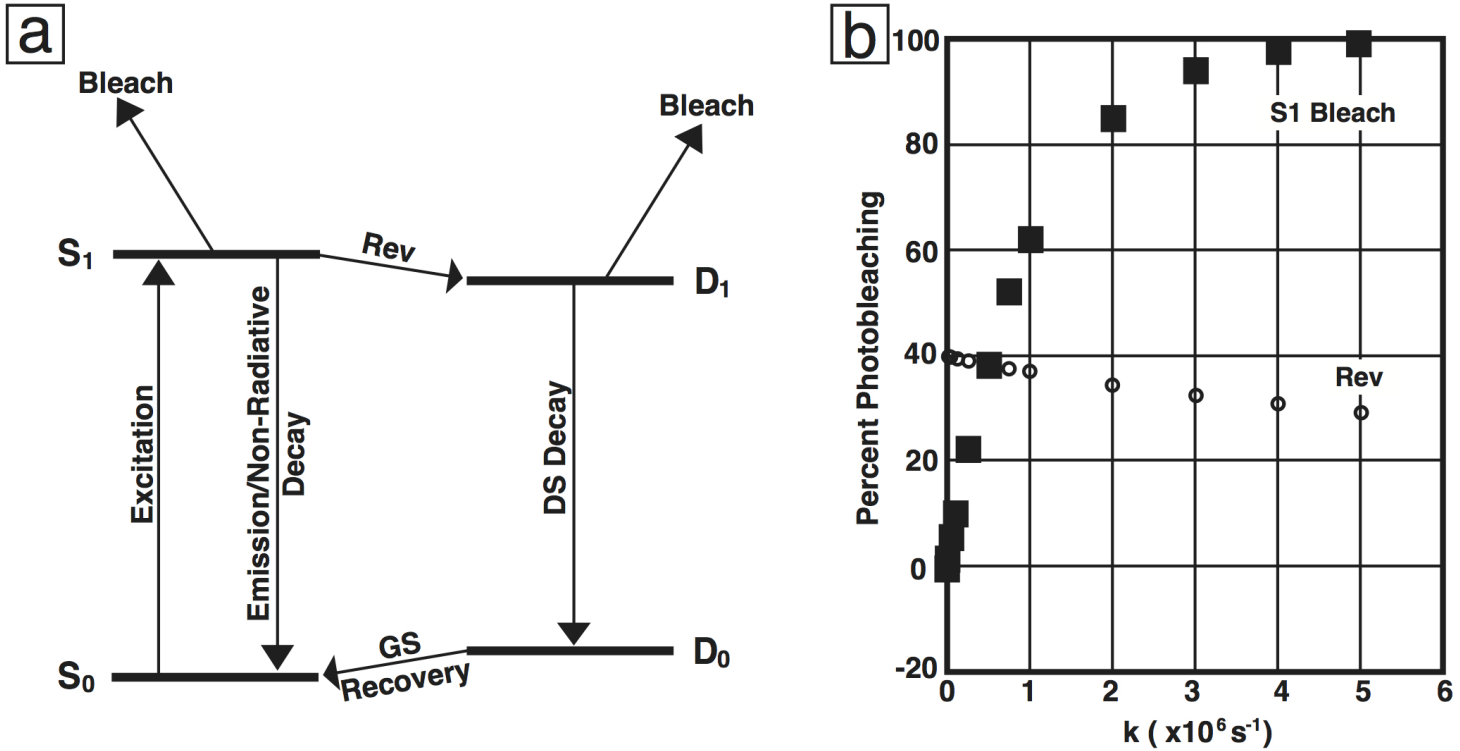

Figure 3.7: Kinetic modeling results. (a) Jablonski diagram depicting four-state model used for photokinetic modeling results. (b) Simulated percent photobleaching as a function of $k_{S1bleach}$ and k_{rev}. Increasing rates of irreversible photobleaching out of the first excited singlet state and reversible photobleaching have opposite effects on observed photobleaching.

of excitation increases and then decreases in a Gaussian profile in time from zero up to the peak rate of excitation (8×10^4 s^{-1}) and then back to zero over the course of 0.54 ms. The excitation rate remains at zero for 20 ms (as mentioned previously, ground state recovery is complete after 8 ms) before experiencing the excitation of the bleach beam (maximum rate of 1.6×10^6 s^{-1}) and, last, the third probe beam. In accord with the calculations and measurements on the cylindrical beam shaping, the excitation profile was assumed to be constant in the direction perpendicular to the cells travel. The FWHM of the laser spatial profile was transformed into time coordinates assuming an average cell velocity of 6 mm/s which is approximately the midpoint of the range of speeds used in these experiments. The peak of the time-dependent fluorescence profiles from the first and third excitation beams was then used to calculate the %bleach.

The values of the rate constants for each step in the four-state model were taken from our previous work (Table 3.3) [209]. In particular, three parameters were varied individually and the magnitude of photobleaching was calculated for each simulation. First, the rate of bleaching out of the higher-energy dark-state ($k_{D1bleach}$) was varied while k_{rev} and $k_{S1bleach}$ were held at 5×10^5 s^{-1}. A negligible increase in %bleach was observed for all but extremely large rate constants (1×10^{10} s^{-1}) indicating that, in this model, the dark state acts photoprotectively, i.e., the fluorophore does not bleach out of the dark state. Next, the rate of bleaching out of the first excited state ($k_{S1bleach}$) was increased from 0 to 5×10^6 s^1 while k_{rev} was held at 5×10^5 s^{-1} and k_{D1} bleach was held at 0. This perturbation resulted in an expected increase in %bleach because the increased rate of bleaching allowed the bleaching process to compete more successfully with the other S1 depopulation pathways. Lastly, the rate of reversible photobleaching (k_{rev}) was increased over the same range while $k_{S1bleach}$ was held at 5×10^5 s^{-1} and $k_{D1bleach}$ was held at 0, leading to a decrease in %bleach. This trend shows that reversible and irreversible photobleaching are competing processes because an increase in the rate of either process leads to opposite impacts on the observed %bleach. Although the results of our model indicate that the $k_{S1bleach}$ has an effect greater than that of k_{rev} on the observed values of %bleach, note that, in general, the rates of both processes are known to change with excitation intensity, pulsed vs continuous wave illumination, and excitation wavelength [208, 209].

For the four RFPs investigated here, the rates of reversible and irreversible photobleaching vary over 1-2 orders of magnitude across the range of excitation intensities characteristic of widefield and confocal

microscopies (10 W/cm^2 to 1 kW/cm^2) [23]. Therefore, for completeness, these calculations were performed using a range of rate values (Table 3.3), covering both experimental and modeling estimates [117, 172, 174, 204, 208, 209]. Our kinetic simulations indicate it is likely that the rates of both reversible and irreversible photobleaching are in the range from 1×10^5 to 1×10^6 s^{-1} because experimental and modeling results for the observed %bleach are in agreement in this range. Furthermore, these simulations predict that, for the current set of measurements, the magnitudes of reversible and irreversible photobleaching are anticorrelated (Figure 3.7b). Consequently, the effects of reversible photobleaching significantly influence the observed extent of irreversible photobleaching.

The four proteins examined in this study represent closely related fluorophores. In particular, TagRFP and TagRFP-T differ by only one point mutation and have similar fluorescence spectra and quantum yields (Table 3.2). However, as emphasized by the resolution of the populations in Figure 3.6, the FPs differ significantly in their photostabilities and propensities for reversible photobleaching. Our photokinetic simulations show that the four cell populations are differentiated with our three-beam geometry by measuring the amount of irreversible photobleaching after a single high-intensity illumination cycle, a process that is influenced by the extent of reversible dark-state conversion. For this reason, additional resolving power will be necessary if the dark-state conversion and irreversible photobleaching processes are to be separated. For example, according to pulsed photobleaching experiments performed on stationary, individual cells (Figure 3.8), mCherry is less prone to both irreversible and reversible photobleaching than mOrange2. However, the significant contribution of reversible photobleaching for mOrange2 causes it to appear very similar to mCherry, if only %bleach is considered. Building on the multibeam geometry described here, other excitation schemes may be devised to separately measure the rates of both processes.

3.10 Discussion

To our knowledge, this is the first cytometer designed to quantify photobleaching in mixed populations. This multibeam flow cytometer capitalizes on the spatiotemporal properties of the cells in microfluidic flow to measure photobleaching with a ratiometric approach, which inherently differs from previous experiments with one or two beams. We demonstrated the capability to characterize the individual cells within a mixed

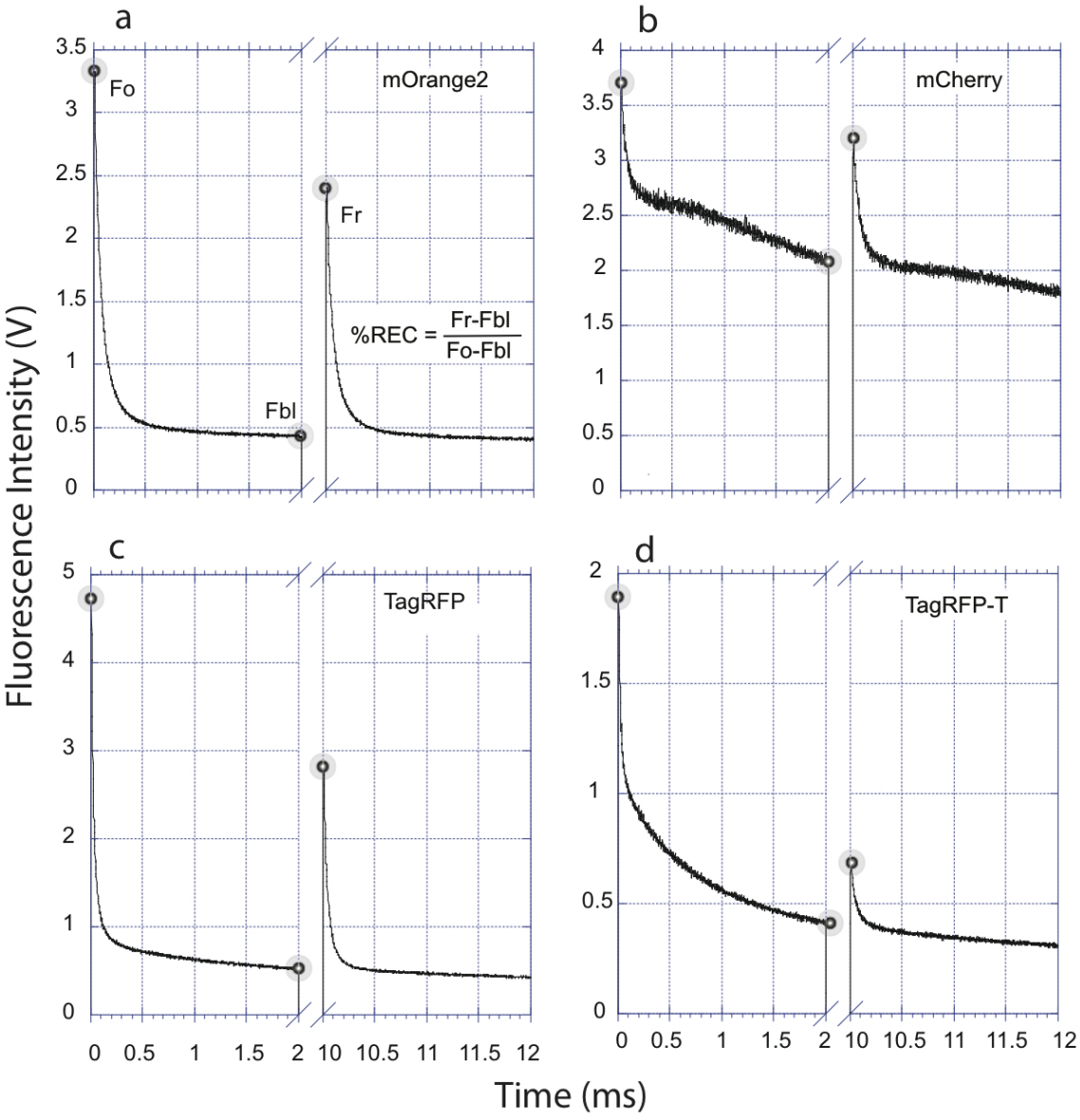

Figure 3.8: Photobleaching measurements were conducted with a 2 ms, 25 kW/cm^2 pulse of illumination from a 532 nm CW laser. The cells were then kept in the dark for 8 ms allowing for fluorescence recovery before the next 2 ms pulse. This duty cycle was designed to resemble cytometry experimental parameters. However, due to experimental limitations, the intensity was reduced to an eighth of the cytometry bleach-beam (a) mOrange2 fluorescence recovery of 80 ± 5 % (n=3). (b) mCherry fluorescence recovery of 92 ± 6 % (n=3). (c) TagRFP fluorescence recovery of 76 ± 7 % (n=3). (d) TagRFP-T fluorescence recovery of 58 ± 18 % (n=3).

population and note that our experiment resolves two RFPs (Tag-RFP [22] and Tag-RFP-T [23]) that cannot be resolved by previously available spectral signatures (e.g., fluorescence lifetime, excitation/emission spectra, absorption).

As revealed in these experiments and simulations, this three-beam pulse sequence probes both irreversible and reversible photobleaching. These two processes are highly interdependent and must be considered in tandem. To discriminate reversible from irreversible photobleaching, the excitation pulse sequence would need to operate on time scales that create a steady-state dark-state population. Generally, by controlling the cell velocity, excitation intensity, and dimensions of the beam and fluidic channel and by employing time-resolved fluorescence detection, it will be possible to implement specific probes of other photophysical dynamics, at high throughput. Furthermore, building on a recent suggestion in the literature [120], the method reported here can be integrated with measurements of fluorescence lifetime [200, 201] and microfluidic cell-sorting techniques [145, 216] to enable the screening of genetic libraries of FPs on the basis of photostability and fluorescence quantum yield. This work, which is currently underway in our laboratory, will enable the development of a next generation of more photostable FPs.

Chapter 4

Application of Optical Gradient Forces for Mammalian Cell-Sorting

4.1 Abstract

This chapter presents a novel microfluidic cytometer for mammalian cells that rapidly measures the irreversible photobleaching of red fluorescent proteins expressed within each cell and achieves high purity (>99 %) selection of individual cells based on these measurements. The selection is achieved by using sub-millisecond timed control of a piezo-tilt mirror to steer a focused 1064-nm laser spot for optical gradient force switching following analysis of the fluorescence signals from passage of the cell through a series of 532-nm laser beams. In transit through each beam, the fluorescent proteins within the cell undergo conversion to dark states, but the microfluidic chip enables the cell to pass sufficiently slowly that recovery from reversible dark states occurs between beams, thereby enabling irreversible photobleaching to be quantified separately from the reversible dark-state conversion. The microfluidic platform achieves sorting of samples down to sub-milliliter volumes with minimal loss, wherein collected cells remain alive and can subsequently proliferate. The instrument provides a unique first tool for rapid selection of individual mammalian cells on the merits of photostability and is likely to form the basis of subsequent lab-on-a-chip platforms that combine photobleaching with other spectroscopic measurements for on-going research to develop advanced red fluorescent proteins by screening of genetic libraries.

4.2 Publication Status and Author Contributions

Davis, L.M., Lubbeck, J.L., Dean, K.M., Palmer, A.E., Jimenez, R. Microfluidic cell sorter for use in developing red fluorescent proteins with improved photostability. Submitted to *Lab Chip*.

J.L.L., K.M.D., A.E.P., and R.J. designed research. L.M.D. designed and built the optical trap, and also performed real-time programming. J.L.L. and K.M.D. performed research. L.M.D., A.E.P., and R.J. wrote the paper.

4.3 Introduction

The microfluidic instrument described in this chapter is unique in that it combines this rapid measurement of irreversible photobleaching with immediate analysis for real-time sorting of live mammalian cells. Several methods can be used for sorting of cells within microfluidic devices. Early devices used switching of electro-osmotically driven flow [217, 218]. Other possible cell sorting techniques include use of acoustic waves [147, 148], and fluidic displacement induced by pulsed laser cavitation bubble formation [219]. Use of optical forces for sorting cells, which is based on early work on optical trapping of cells [220], is particularly suited for use within microfluidic devices. Optical sorting of cells in a microfluidic device has been demonstrated by switching on a tightly focused line from a 980-nm diode bar laser so cells flow along the line [221] and also by pushing a cell by the optical scattering force along the laser direction into a separate fluidic channel in a multilayer device [222]. Computer controlled holographic optical trapping with a high numerical aperture (NA) microscope objective to provide tight focusing has been reported for manipulating and sorting of human embryonic stem cells [223].

In this work, sorting using optical gradient force switching was chosen because it is compatible with a single layer microfluidic device, it does not require high NA optics and it is suitable for live mammalian cells [145]. As depicted in Figure 4.1, a single focused 1064-nm laser spot is turned on and moved at an angle across the microfluidic channel, to deflect a cell by the optical gradient force so that it follows the trajectory of the spot towards a separate exit channel. As the speed of translation of the laser spot is matched to the flow velocity, the optical force does not have to be strong enough to overcome the flow, hence strong axial

trapping is not needed and only a low NA lens is required for focusing the laser beam. The technique has previously been demonstrated to maintain the viability of HeLa cells with a 1064-nm laser power of >10 W and exposure of several milliseconds, which provides sufficient optical forces for efficient cell selection [145]. Other authors have used a similar approach for sorting of mouse macrophage cells infected by a fluorescently labelled pathogen [224].

In each of these earlier works, the fluorescence signal from transit of a cell through a single laser beam was passed to a hardwired circuit with a leading-edge discriminator, which triggered custom electronics18 or a programmed function generator [224] to drive an AOM after a pre-set delay to deflect the beam and translate the laser spot. In contrast, in the present work, analysis of the multi-beam photobleaching signature is performed in software on a separate computer using the Real-Time module of LabView (National Instruments) to achieve deterministic (about ±0.005 ms), low-latency (<3 ms), adjustably timed control of the sweep of the laser spot using a piezo-tilt mirror.

The instrument reported in this paper is an application of miniaturization and automation that presents marked advantages over existing manual techniques used in developing new RFPs. In previous work by Tsien and coworkers, directed evolution of orange and red fluorescent proteins with increased photostability was achieved by manual selection of colonies of bacterial cells that maintained fluorescence following prolonged (10-120 min) wide-field exposure [23]. Similarly, manual sorting of E-coli bacterial colonies in a petri dish following fluorescence lifetime measurements has been used to screen a structure-guided library of the Cerulean fluorescent protein, which has a quantum yield of 49 %, to develop a cyan fluorescent protein with an almost 2-fold gain in fluorescent quantum efficiency [40]. While the decreasing of photobleaching could potentially yield a far larger gain in total photon signal, technology for sorting individual cells based on photobleaching has not been previously available. In contrast to these previously used techniques, the present instrument enables high-speed automated selection of individual mammalian cells. It uses photobleaching irradiance levels similar to those used in many fluorescence imaging experiments ($\approx$ 2-25 kW/cm^2) and it achieves high purity (>99 %) in the selected population, as demonstrated by experiments with known mixtures of cells. It hence provides an important new tool for efforts to develop novel RFPs with enhanced photostability and low toxicity in mammalian cells. It is likely to lead the lab-on-

Figure 4.1: Schematic of a cell flowing through a series of line-focused 532-nm laser beams to yield a measure of irreversible photobleaching, which is used to decide its possible selection, made by turning on and translating a focused 1064-nm laser beam for optical gradient force switching.

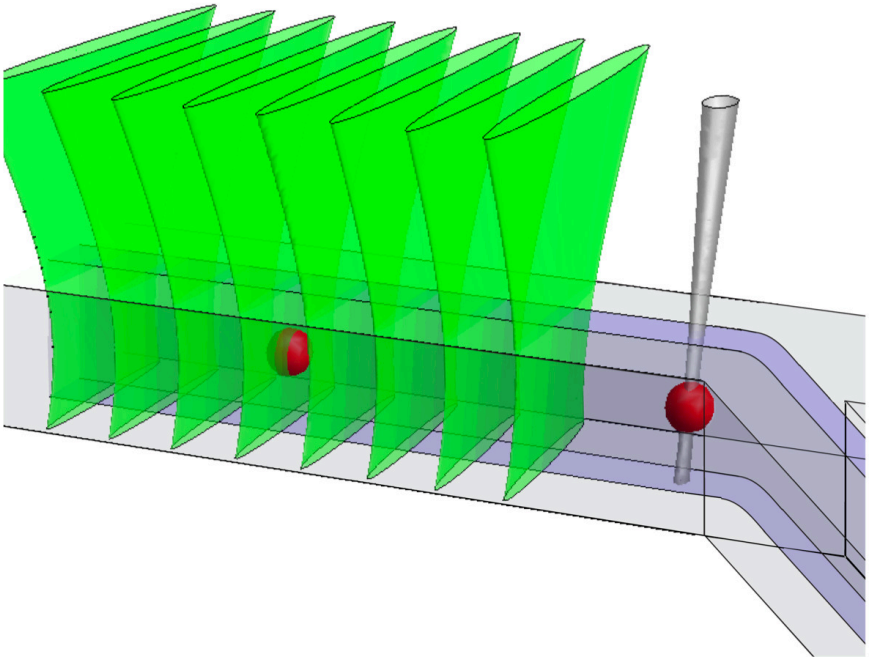

a-chip community to develop subsequent cell sorters that combine photobleaching with other spectroscopic measurements [225].

4.4 Experimental Methods

4.4.1 Microfluidic Chip, Microscope, and Optical Detection

Figure 4.2 shows a schematic of the entire experimental system, with specific details for key components given in the figure or figure caption. An expanded diagram of the microfluidic chip is at the top left in the figure. The cell sorting uses up to 20 W of 1064-nm laser light, so to avoid absorption of this light by the device and possible burning or damage, the microfluidic chip (custom fabricated by Micronit, Netherlands) is made entirely from borosilicate glass. The ports of the chip are sealed to a polytetrafluoroethylene (PTFE) manifold using compression fit o-rings. For each of the 5 inlet/outlet ports, the manifold contains a reservoir connected at the top to an access hole, sealed by a cap screw, which is removed for loading and recovering samples with a micropipette, and also to a side line for delivery of compressed air to enable the headspace of the reservoir to be pressurized. The outlet reservoirs (channels E and F) are left open to atmospheric pressure and three adjustable, electronic pressure controls (Pneutronics, OEM EPS10-5-0-2) with a range of 0-2 psi above atmospheric pressure are used to regulate the inlet flow rates of the sample (in channel A, Figure 4.2) and two buffer streams (in channels B) to achieve hydrodynamic focusing of the sample stream (in channel D), and adjust its path within the microfluidic device so that it exits into the side channel (channel F).

As shown in Figure 4.2, the microfluidic chip (1) and manifold are mounted on an inverted microscope that uses a dry objective (2) for epi-illumination and collection of fluorescence. The beam from a 532-nm laser is split into 9 beams (only 5 are shown) of adjustable powers with a series of beamsplitters and neutral density filters. The beams pass through a cylindrical lens (3), enter the side port of the microscope and reflect from a dichroic mirror (4) to form line-focused beams within the microfluidic device (1) (8 of the beams in channel D, as depicted in Figure 4.1, and the 9th monitor beam in channel E, for counting of selected cells, as discussed below). Any of the beams may be blocked, including the monitor beam; oftentimes only

Figure 4.2: Schematic of the experimental system. (1)=the microfluidic chip, shown within the system and at top left: Channel lengths (mm), widths (μm) are: A 20, 100; B 15, 130; C 5, 130; D 0.5, 15, E 27, 125; F 27, 125. All channels are wet etched to 25 μm depth into a 0.7 mm thick borosilicate glass substrate, which is bonded to a 1.1 mm thick glass cover-plate that has powder-blasted vias of 0.61.7 mm (bottomtop) diameter ($\approx$1.2 μL volume). Key system components are: (2)=Olympus IX71, inverted microscope with Olympus LUC Plan FLN 20$\times$ UIS2 NA0.45/∞/cc0-2 mm objective; (3)=Thorlabs LJ1996L1-A, plano-convex cylindrical lens, focal length f=300 mm; (4)=Chroma z532 rdc, dichroic filter (reflects 532 nm, transmits >550 nm); (5)=Semrock FF01-720/SP-25, short-pass filter (transmits 320-690 nm, blocks >720 nm with optical density OD>7); (6)=Chroma HQ545LP, dichroic filter (transmits >545 nm, blocks <540 nm OD>5); (7)=Physik Instrumente S-315, piezo-tilt mirror, (8)=Newport 10QM20HM.15, dielectric mirror (reflects 1064 nm, transmits ¡900 nm); (9)=Thorlabs A397TM-C, aspheric lens, f=11 mm; (10)=Maglite, Krypton bulb; (11)=Semrock FF01-736/LP-25, long-pass filter (transmits >750 nm, blocks ¡736 nm OD>3); (12)=Semrock FF720-SDi01-25$\times$36 dichroic filter (transmits 400-700 nm, reflects 720-890 nm).

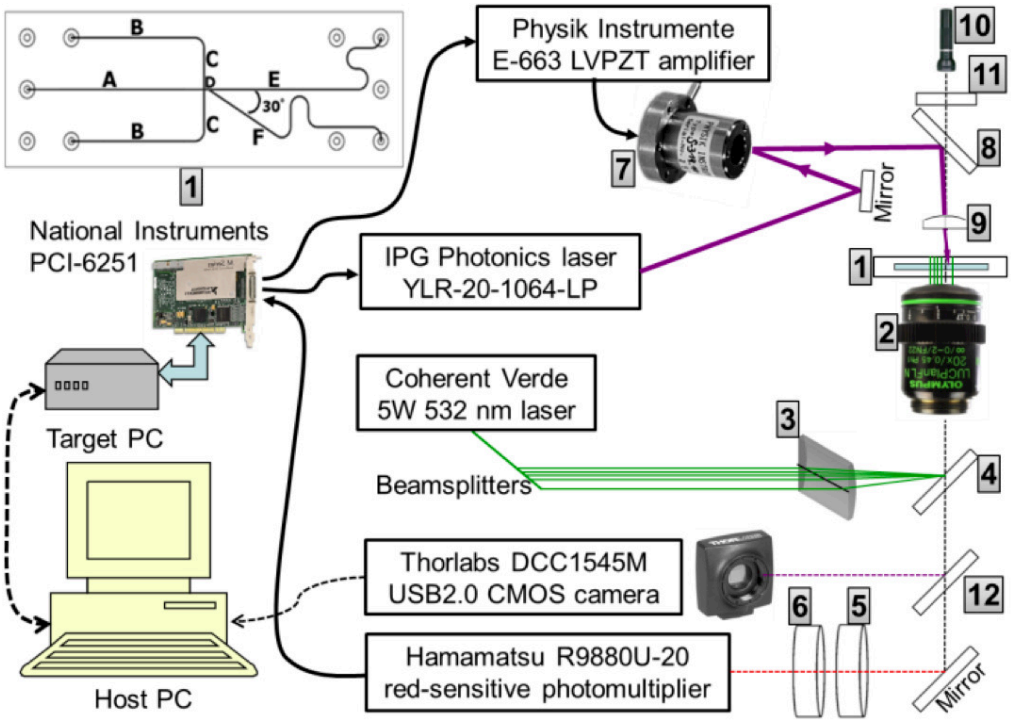

4 or 5 beams are used. Red fluorescence from cells passing through these beams is isolated using filters (5, 6) (pass-band 545-690 nm) and detected with a photomultiplier (operated at ≈650 V). The photomultiplier signal is conditioned by a custom-built trans-impedance amplifier (which gives 10V output for a 100 μA input and 0.16-10.6 kHz band-pass) and digitized at 125 kHz, 16-bit resolution by a multifunction data acquisition (DAQ) card (National Instruments PCI-6251 with NI-SCXI). This card also provides a digital output for switching the 1064-nm laser on/off and two 0-10 V analogue outputs for control of two actuators of the piezo-tilt mirror (7) through a low-voltage piezo amplifier. The DAQ card is operated in a separate computer (Target PC) controlled by the main computer (Host PC). For sorting of cells, the piezo-tilt mirror steers the beam from a 1064-nm laser, which is reflected from a dielectric mirror (8) and focused in through the top of the microfluidic chip by an aspheric lens (9). In order to visualize cells during operation of the sorter, trans-illumination of the chip is provided a Krypton bulb (10) and a long-pass filter (>750 nm) (11) and scattered light from cells is separated by a dichroic filter (12) for viewing with a CMOS camera.

4.4.2 Optical Design of Gradient Force Switching

The 1064-nm optical deflection beam is focused through the top cover-plate of the microfluidic device using an aspheric lens (9) with focal length f=11 mm. The lens is antireflection coated and provides high transmission (>99 %) and low loss compared to a microscope objective. Although the lens is designed for use at a wavelength of 670 nm and for focusing through a laser diode window of 0.275 mm thickness with NA 0.3, Zemax optical design software indicates that when the Gaussian 1064-nm laser beam is focused by the lens through the 1.1 mm thick glass top of the microfluidic device at a NA of 0.25, the focused spot size, as seen in the inset of Figure 4.3, is close to the diffraction limited size of the Airy disk over the entire trajectory. As the depth of the microfluidic channel is only 25 μm compared to 50 μm in earlier work,18 a higher NA was chosen (0.25 rather than 0.2) to produce a sharper axial optical field gradient (the spot area doubles over the Rayleigh range of $\pm$4.1 μm rather than $\pm$6.3 μm).

The piezo-tilt mirror used to translate the focused spot within the microfluidic channel has an equilateral tripod mount that gives up to $\pm$600 μrad of tilt in total when two of the three actuators are oppositely extended over their full range. The full angular tilt in a beam reflected from the mirror is two times that

Figure 4.3: Layout of optical components for optical force switching; M=Mirror, PM=Piezo-tilt mirror (rays are shown for the extreme tilts), L=Lens (Thorlabs), L1=Plano-concave f=-50 mm (LC1715-C), L2=Plano-convex f=175 mm (LA1229-C), L3=Plano-convex f=1000 mm (LA1464-C), L4=Plano-convex f=300 mm (LA1484-C), L5=convex aspheric f=11 mm (A397TM-C). Separations between component vertices are: L1-L2=125.2 mm; PM-L3=998.5 mm; L3-L4=1289.0 mm; L4-L5= 289.4 mm. L1 orientation is reversed to balance spherical aberration. The inset shows the Huygens point spread function of the laser beam at the focus.

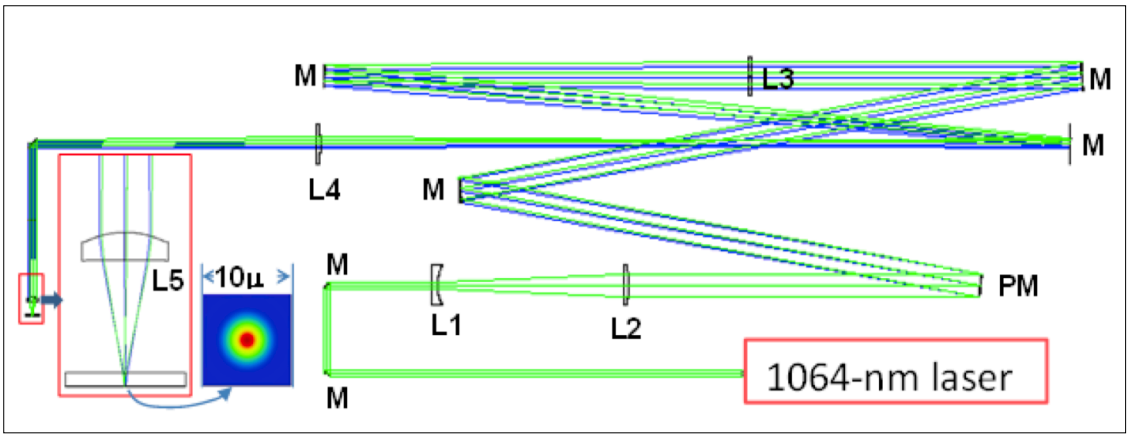

value, or 2400 μrad in total. If this tilt is applied at the entrance pupil of the 11 mm focal length aspheric lens, the scan distance of the spot would be 11 mm $\times$ 2.4 $\times$ 10^{-3} = 26.4 μm. To increase the scan distance, as shown in the optical layout in Figure 4.3, the piezo-tilt mirror [PM] is imaged onto the entrance pupil of the aspheric lens [L5] with a magnification of 3.33, using a pair of lenses [L3 and L4], which are spaced so that the collimated beam from the piezo-tilt mirror is re-collimated at the aspheric focusing lens. With adjustment of two of the three actuators, the laser spot can be scanned in the microfluidic channel over an area with longest diagonal of 88 μm. The tilt mirror is driven by a 3-channel 100 V amplifier controlled by 0-10 V analogue input signals. The minimum time taken to scan the full range is approximately 2 ms. Manipulation of beads has been demonstrated with the same piezo-tilt mirror.23

To achieve the desired numerical aperture in focusing, the 1064-nm laser beam is expanded $\times$3.5 using a pair of plano-concave and plano-convex singlet lenses (L1 and L2) and the beam path is folded to form a more compact assembly for enclosure within a box, as seen in Figure 4.3.

4.4.3 Timing of Optical Gradient Force Triggering

In setting up for sorting, the trajectory over which the 1064-nm laser spot scans is adjusted downstream from the photobleaching beams, as shown in Figure 4.4. The orientation and voltage limits of the piezo-tilt mirror are set to make a triangular trajectory, 123, shown by the dashed red line in Figure 4.4, where the 1064-nm laser turns on over path 12 and turns off over path 31. When a cell passes through the photobleaching beams (green lines at left in Figure 4.4), the signals are analyzed and if the cell is selected, the 1064-nm spot must turn on with correct start time and scan with a speed matched to that of the cell so that it intercepts the cell.

To accomplish this, the camera image is used to measure the displacements shown in Figure 4.4: A, between the 1st and last green photobleaching beams; B, between the last photobleaching beam and point 2 of the 1064-nm spot trajectory; C, the down-channel component between points 1 and 2 of the trajectory; and D, between the last photobleaching beam and the monitor beam, which is positioned in the sort channel (channel E of Figure 4.2) as a means of counting cells that pass into that channel. The program on the Target PC measures T_A the time of passage of a cell between the 1st and last photobleaching beams, which

Figure 4.4: Camera image of microfluidic device with overlay of laser beam positions and trajectories. The 8 green lines at left represent line-focused 532-nm fluorescence excitation beams. The red dashed triangle is the trajectory of the 1064-nm optical deflection laser spot. The dashed yellow lines envelope the trajectories of cells as they pass into the exit channel at lower right. The image in this camera frame has captured a cell that was deflected along the light blue line to point 3, is now within the light blue circle, and will subsequently pass into the sort channel at upper right, to be counted as it passes through the 9th 532-nm laser line at far right.

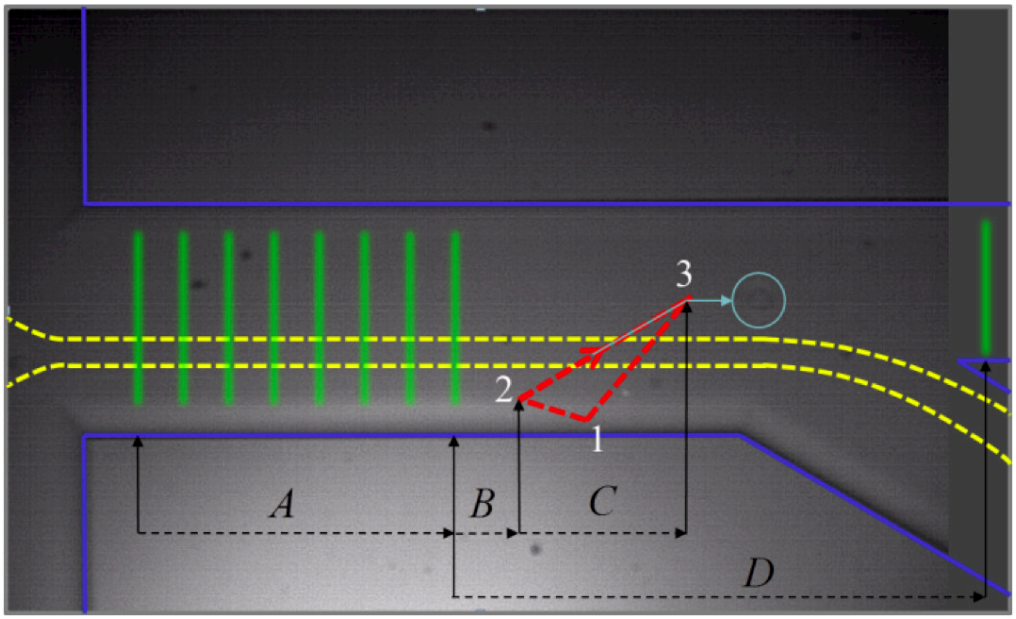

depends on the setting of the pressures that drive the flow. (Due to the pressure-driven parabolic flow profile, the passage time also depends on the exact depth of the cell within the channel, but all cells are carried close to the centre depth where the flow speed is greatest, so the variation is found to be only ± 9 % at most.) The start time of the trajectory of the 1064-nm spot is adjusted so that the time delay T_B from the moment that a cell passes the last photobleaching beam to the time when the 1064-nm spot passes point 2 in its trajectory is T_B = (B/A) T_A. The speed of the trajectory along path 23 is adjusted so that T_C = (C/A) T_A. Finally, the delay for recognition of a cell passing through the monitor beam is T_D = F (D/A) T_D, where a factor of F ≈ 1.67 is used to account for a slow-down in the flow speed beyond the channel junction, as the microfluidic device is designed with a main channel of width 150 μm and two exit channels each of width 125 μm, so that the net flow speed slows by a factor of 0.6 (=1/1.67). If the monitor beam is used, a peak that follows one from a cell passing the last photobleaching beam within a delay of (1±δ) T_D is categorized as due to that same cell passing through the monitor beam, where $\delta \approx 0.1$ is a tolerance parameter. However, such a peak could also be due to a new cell entering beam 1 with the required delay. Thus the monitor beam gives a useful indication of successful cell selection for optimizing efficiency, but the categorization of peaks on the basis of their timing leads to over-counting of sorted cells, particularly when the incoming rate of cells is high, and hence it provides only a low-limit estimate for the purity of the selected cells. As discussed below, the purity of the selected cells is better determined by subsequent spectroscopic analysis of the selected population of cells.

4.4.4 Real-Time Data Analysis for Cell Selection

A program operating on the Target PC is used to analyze the digitized data stream from the photomultiplier, recognize isolated bursts composed of sets of peaks due to the passage of cells through the of 532-nm photobleaching beams, make selection decisions based on photobleaching, program the DAQ card outputs using the calculated timing for cell selection, and count cells that pass through the monitor beam if this is used. With low priority, this program also transmits analysis results to the Host PC and adjusts its operating parameters upon command from the Host. The Host runs a separate interactive program that graphically presents analysis results received from the Target and allows parameters to be transmitted to

the Target for update.

Table 4.1 gives a flow diagram of the main parts of the algorithm of the Target PC program, which finds peaks, counts them into bursts, and categorizes and counts bursts of different types. In the main loop, at line 9 the program awaits a block of data (typically 625 points in 5 ms), then at line 10 it finds the locations and amplitudes of peaks in the data stream using the LabView library routine Peak Detector, which is a point-by-point routine that retains needed data from prior calls. This finds peaks above an adjustable level (set at the current average plus an adjustable threshold so as to recognize a wide dynamic range but yet distinguish partially overlapping peaks) by fitting a quadratic of given width to the data stream (so that peaks of small width due to noise are not found). In the for-loop of lines 11-37, the timings of peaks are used to count up peaks into bursts. The count, i, is reset to the beginning value (i = 0;) designating the first peak of a burst whenever the time since the last peak is not within the set limits (between Min and Max at lines 17 or 24, or for the monitor between (1-δ) T_D and (1+δ) T_D at line 33), or whenever the count equals the number of laser beams used (at lines 27 or 36). If this first peak follows the previous peak too closely, the burst that follows will be flagged as overlapping (line 40 or 41). An array (A[ ]) is used to store the amplitude of the first peak and the normalized amplitudes of subsequent peaks in a burst. After a cell has passed through all photobleaching laser beams, if all the amplitudes are between the lower limits and upper limits (which are defined in the arrays LL[ ] and UL[ ], i.e., LL[j]<A[j]<UL[j] for j=0,1, , N) and the burst is not overlapping with a prior one (O=false at line 21), the time and speed for the motion of the 1064-nm laser spot is calculated (line 22, Calculate timing) using the procedure discussed in the text in the section Timing set-up, taking into account the positions of the peaks in the data stream and the amount of time that has elapsed during the computation, as determined from readings of the Target PC clock. If the piezo-tilt mirror has completed its previous trajectory and if there is sufficient time to intercept the cell, a subprogram (line 22, Initiate selection), which will send the calculated voltages from the DAQ card with the calculated timing, is started; at this time the flag for Selected is set true.

After the peaks are counted for a cell passing through all photobleaching beams, the next peak will be reset to the beginning of a new burst if the monitor beam is not used (line 27) or will be tested to see if it corresponds to a monitor peak (line 30), in which case the next peak will be reset to the beginning of

a new burst (line 36). With completion of a burst in either of the two cases of these possible resets after all photobleaching beams are counted, the type of the burst is determined and a counter for the particular burst type is incremented. Note that (in line 21) a burst may be selected only if it does not overlap with the prior burst. However, whether selected or not, it will be designated as overlapping if it overlaps with either the prior or the following burst (lines 27, 28 or 33, 34, or 36, 37).

Figure 4.5 shows a screen shot of the Host PC program, captured during the execution of an experiment. The program, which runs on a PC that uses the Windows 7 operating system, receives the time and amplitude of each detected fluorescence peak over the network from the Target PC. It groups these peaks into bursts of peaks using the same algorithm that runs on the Target PC (as described above), but with its own (Host) values of adjustable parameters, to determine graphical representations of the passage of individual cells, and also the would-be sorting statistics displayed in the top right yellow box, i.e., those that would be obtained on the Target PC if that had used the same parameters. Thus at the start of an experiment, the parameters on the Host PC can be adjusted to optimize the grouping of peaks into bursts. These revised parameters can then be downloaded over the network to replace the parameters used by the Target PC, or otherwise discarded and replaced by values uploaded from the Target PC. The Target PC also collects its own (true) statistics, which are sent to the Host PC and displayed in the light blue region near top right. During this particular experiment, the 532-nm laser power was 0.98 W, with $\approx$ 0.1 W in each of the 9 beams, while the 1064-nm laser power was 14 W. The flow speed was 8 mm/s (240 μm/30 ms) and the time for the 1064-nm spot to move from 2 to 3 in Figure 4.4 was $\approx$15 ms.

The adjustable parameters (indicated by pink numbered arrows) are: (1) Threshold, (2) Width, which together are used by the LabView point-by-point library routine Peak Detector to find the locations and amplitudes of peaks in the data stream; (3) Minimum (time delay), and (4) Maximum (time delay), which are used together with counting of the peaks in a burst to piece together the peaks into bursts of up to 8 peaks and to determine whether a burst is overlapping with a previous burst (designated as Overlapping) or not overlapping (designated as Good); (5) a set of Switch Parameters, which define the voltages at the 3 vertices of the piezo-mirror triangular trajectory(A0, A1, B0, B1, C0, C1), the time for motion along the legs of the trajectory, 12 (designated as T-AB), 23 (designated as T-BC and readjusted to be T_C), and

Table 4.1: Flow diagram of target-PC algorithm.

```
1   N = 2, 3, 4, 5, 6, 7, or 8 = number of photobleaching beams used
2   M = 0, or 1 = if monitor beam is blocked, or used
3   i = N + M;  // initialize count of peaks in the present burst
4   S = false;    // initialize flag S to indicate if the burst is selected
5   O = false;   // initialize flag O to indicate if the burst overlaps with the prior one
6   sou = 0; nou = 0; som = 0; nom = 0; sgu = 0; ngu = 0; sgm = 0; ngm = 0;
7   // initialize counters of bursts, s/n = selected/not selected, o/g = overlapping/good, m/u =
    monitored/unmonitored
8
9   Read block of data points, find the Average
10  Call Peak Detector (Threshold + Average, Width )
11  For each peak found {
12      Find Δt = time since last peak, A = peak amplitude
13      if ( i = 0, 1, …, N−2 ) { // peak that precedes last photobleaching beam
14          if ( Min < Δt < Max ) {
15              i++; A[i] = A / A[0]; }
16          else {
17              Reset; } }
18      else if ( i = N−1 ) { // peak may be due to last photobleaching beam
19          if ( Min < Δt < Max ) {
20              i++; A[i] = A / A[0]; S = false;
21              if ( LL[ ] < A[ ] < UL[ ] and O = false ) {
22                  Calculate timing; Initiate selection; S = true; }}
23          else {
24              Reset; } }
25      else if ( i = N ) { // peak that follows that from last photobleaching beam
26          if ( M = 0 ) { // if no monitor beam is used
27              O2 = O; Reset;
28              if ( O or O2 ) { if ( S ) { sou++; } else {nou++; } } else { if ( S ) { sgu++; } else {ngu++; }
                } }
29          else {  // if a monitor beam is used, i.e., M = 1
30              if ((1−δ) T_D < Δt < (1+δ) T_D ) {
31                  i ++; }
32              else {
33                  O2 = O; Reset2;
34                  if ( O or O2 ) { if ( S ) { sou++; } else {nou++; } } else { if ( S ) { sgu++; } else
                    {ngu++; }  } } }
35      else if ( i = N+1 ) { // peak that follows that from monitor beam
36          O2 = O; Reset;
37          if ( O or O2 ) { if ( S ) { som++; } else {nom++; } } else { if ( S ) { sgm++; } else {ngm++; }  }
            } }
38  Go to line 9
39
40  Reset:   i = 0; A[0] = A; if (Δt < Max )        { O = true; } else {O = false; } Return;
41  Reset2: i = 0; A[0] = A; if (Δt < (1+δ) T_D ) { O = true; } else {O = false; } Return;
```

[a] Adjustable parameters are underlined; ++ means increment the counter by 1.

Figure 4.5: Screen shot of host-PC interface host program. During this particular experiment, the 532-nm laser power was 0.98 W, with ≈ 0.1 W in each of the 9 beams, while the 1064-nm laser power was 14 W. The flow speed was 8 mm/s (240 μm/30 ms) and the time for the 1064-nm spot to move from 2 to 3 in Figure 4.4 was ≈15 ms.

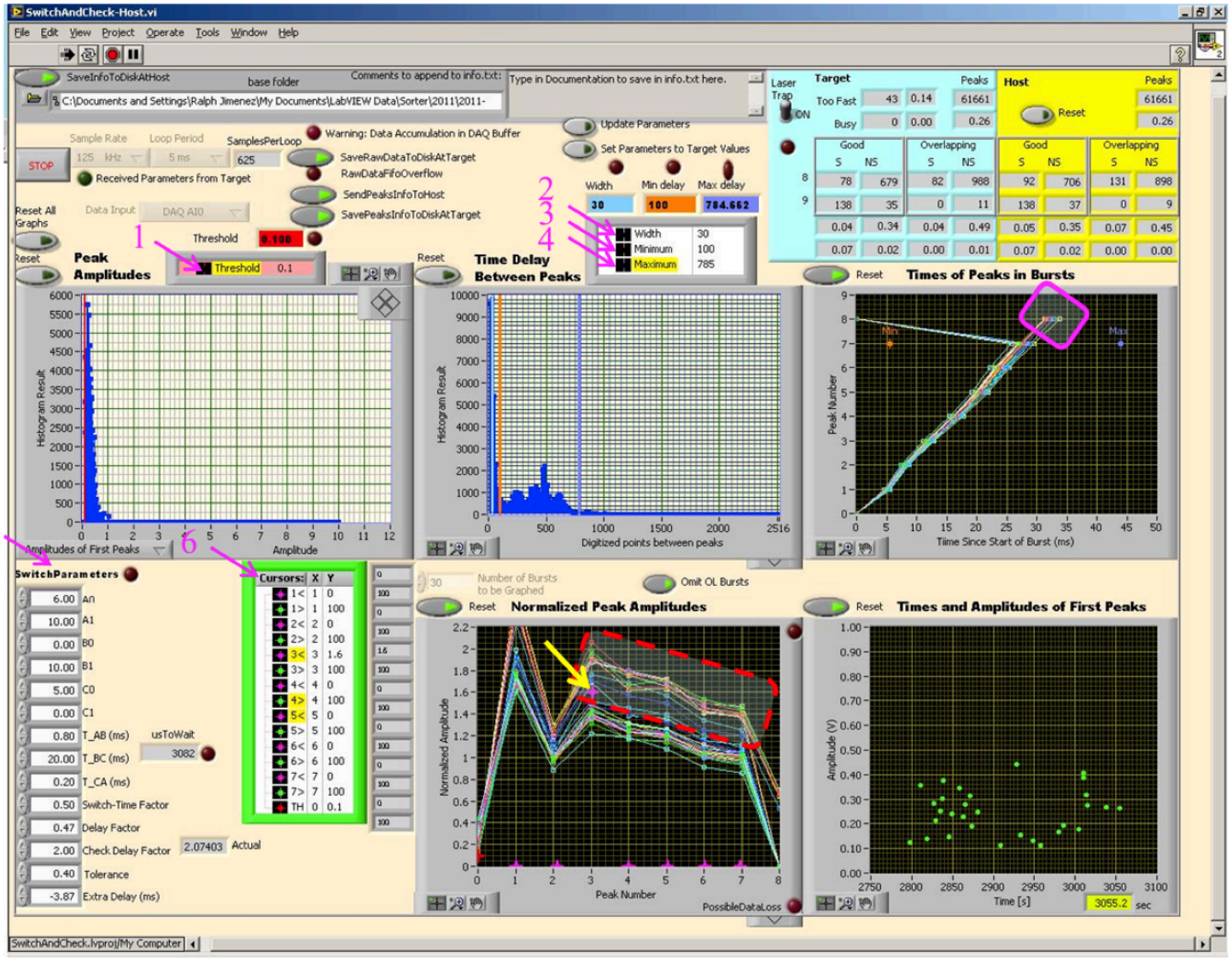

34 (designated as T-CA), the ratios B/A (Switch-Time Factor), C/A (Delay Factor), and F (D/A) (Check Delay Factor) needed to calculate the timings, the tolerance parameter δ (Tolerance) for designating a peak as due to a cell passing through the monitor beam, and an additional parameter (Extra Delay) to provide an empirically determined offset to T_B to account for slow-down of the flow near the junction and latency of the switch; (6) a set of values for peak amplitude ratios (listed within the green box), set by using the mouse to position cursors on the graph labelled Normalized Peak Amplitudes. These values select the photobleaching characteristics of cells that we wish to switch to the upper exit channel.

Note however, that the switch will only be attempted if the burst of fluorescence peaks from the cell is designated as Good (not Overlapping). The switch will also not be attempted if the calculated time to wait until the start of the switch cycle (shown as usToWait at lower left in Figure 4.5) is negative, in which case the cell is counted as Too Fast (in blue box at top right Figure 4.5)); or if the piezo-mirror trajectory from the previous selection will not be completed in time, which is counted as Busy (in blue box at top right Figure 4.5). After the peak of a burst as a cell passes the last photobleaching beam, whether the switch of the cell is selected (S) or not selected (NS), a peak that follows within a delay of $(1 \pm\delta)T_D$ is categorized as due to that same cell passing the monitor beam and the burst is designated as having 9 peaks, but this may also be due to a new cell passing into beam 1. Thus the monitor beam provides an indication of a successful cell selection useful for setting up the instrument (and is visually indicated by extending the line in the graph of Times of Peaks in Bursts, as highlighted within the pink diamond shape in Figure 4.5)), but as discussed in the main body of the paper, it over-counts the cells that pass into the sort channel (the bursts that have 9 peaks), particularly those cells that were not selected. While the success of a sort must ultimately be determined by further analysis of the sorted population of cells (as is reported in the section Cell selection based on irreversible photobleaching near the end of the body of the paper), the monitor beam provides data from which a lower limit of the purity of the sort can be determined. For the data displayed in Figure 4.5), this is: Relative purity >9GS/(9GS+9GNS) = 138/(138+35) = 0.8.

4.4.5 Solution and Flow Conditions

In typical operating conditions, the speed of HeLa cells through the 532-nm beams is ≈ 6-8 mm/s. It is possible to operate about 3 times faster, which still gives enough time for dark-state relaxation between beams, although the camera frame rate then becomes too slow to follow cell selection. A faster flow rate not only speeds sorting, but it helps prevent cells sticking to the walls of the microfluidic device, particularly at the apex of the junction.

To reduce the HeLa cells sticking or settling in the reservoirs, OptiPrep (60 % weight/volume iodixanol in water) is added to the buffer for the cells. The iodixanol increases the specific density to make the cells buoyant, but the refractive index of the solution also increases. Hence to maintain a difference between the refractive index of the medium and the cell, as needed to generate optical forces, the concentration of iodixanol is kept at ≈ 8 % weight/volume, similar to that used in earlier work [145], resulting in a refractive index of 1.3479[1] (≈ 1.36 for cells) and density of 1.049 g/ cm^3 (1.0357 g/cm^3 for HeLa cells [226]). The program only attempts to select cells that pass through the series of beams alone, without overlap between preceding or following cells. Although a greater number of 532-nm beams may provide better resolution of differences in irreversible photobleaching, there is an advantage to using fewer beams that

4.5 Instrument Operating Conditions

Figure 4.6 shows a series of images captured by the camera of a HeLa cell passing through the 8 photobleaching beams (1, 2), being selected by the 1064-nm beam (3, 4), and then passing towards the selection channel (5, 6) and through the monitor beam (7). The program only attempts to select cells that pass through the series of beams alone, without overlap between preceding or following cells. Although a greater number of 532-nm beams may provide better resolution of differences in irreversible photobleaching, there is an advantage to using fewer beams that span a smaller length of the microfluidic channel and to blocking the extra beam that is used to monitor cells passing into the sort channelnamely, the use of a smaller length of the flow channel reduces the overlapping of bursts from successive cells, which increases the effective rate at which cells may enter the sorter and be non-overlapping. In the approximation that

[1] http://www.freewebs.com/eldri123/Package%20insert/OptiPrep.pdf

cells enter at random times at a rate R, the time between cells is exponentially distributed with mean 1/R. Consequently, the probability that a cell does not overlap with the prior or following ones is e^{-2RT}, where T is the passage time from the first to the last beam. The maximum rate of non-overlapping cells (labeled Good in Figure 4.1 is then $R_G = 1/(2Te)$ when $R = 1/(2T)$. Both the rate of cells and their speed through the microfluidic device may be controlled by adjusting the pressures that drive the flow of the sample and the buffer streams. For the experiment of Figure 4.1, the time of passage from beam 1 to beam 8 (240 μm) is 30 ms, and from beam 1 to beam 9 (400 μm) is $\approx$ 113 ms, hence the maximum rate at which cells may be selected is $R_G \approx 1.6\ s^{-1}$, or if the monitor beam and the check for successful switching are turned off, $R_G \approx 6.1\ s^{-1}$. The actual selection rate will be $R_G \times$ the fraction of cells in the sample that have the desired photostability. As an indication of the fastest practical selection rate that can be expected, when the number of beams is reduced to 4 spread over $\approx$100 μm and the speed is increased by a factor of 3, so that T = 4 ms, the maximum rate of selectable cells is $R_G = 46\ s^{-1}$, which enables samples of $\approx 10^5$ cells with enhanced photostability to be obtained within a few hours.

4.6 Cell Selection Efficiency and Viability After Selection

To optimize operating conditions, experiments evaluating the selection efficiency and subsequent cell viability as a function of buffer conditions and 1064-nm laser power were undertaken using HeLa-S cells, which are suitable for use in experiments for developing new RFPs. To promote cell viability, especially during sorting experiments lasting longer than an hour, cells were suspended in a solution of phenol-red-free Minimum Essential Medium (Invitrogen, 41061-029), with 10 % Fetal Bovine Serum (Invitrogen), 14 % Optiprep (Sigma-Aldrich), and 1 % Penicillin Streptomycin (Invitrogen, Pen Strep). This medium was chosen instead of a low-nutrient buffer (e.g., Hepes-buffered Hanks Balanced Salt Solution), as it was found to give increased cell viability over time. Also, a medium free of phenol-red pH indicator was chosen to decrease background fluorescence. Selection experiments using 4 photobleaching beams and the monitor beam for assessing success were performed for various 1064-nm laser powers using either (i) the cell suspension medium described above, or (ii) a buffer solution composed of calcium-free, magnesium-free, phenol-red-free Hanks Balanced Salt Solution (Invitrogen, 14175) with 1 % Bovine Serum Albumin (Sigma-Aldrich, BSA) in the

Figure 4.6: Series of images from a movie demonstrating cell selection. Here, a cell traverses a series of photobleaching beams (images 1 and 2) before triggering of the optical trap (image 3), capturing the cell (image 4), and sweeping across the channel to be released into the selection channel (image 5 and 6). Success of sort is verified with monitor beam (image 7, middle).

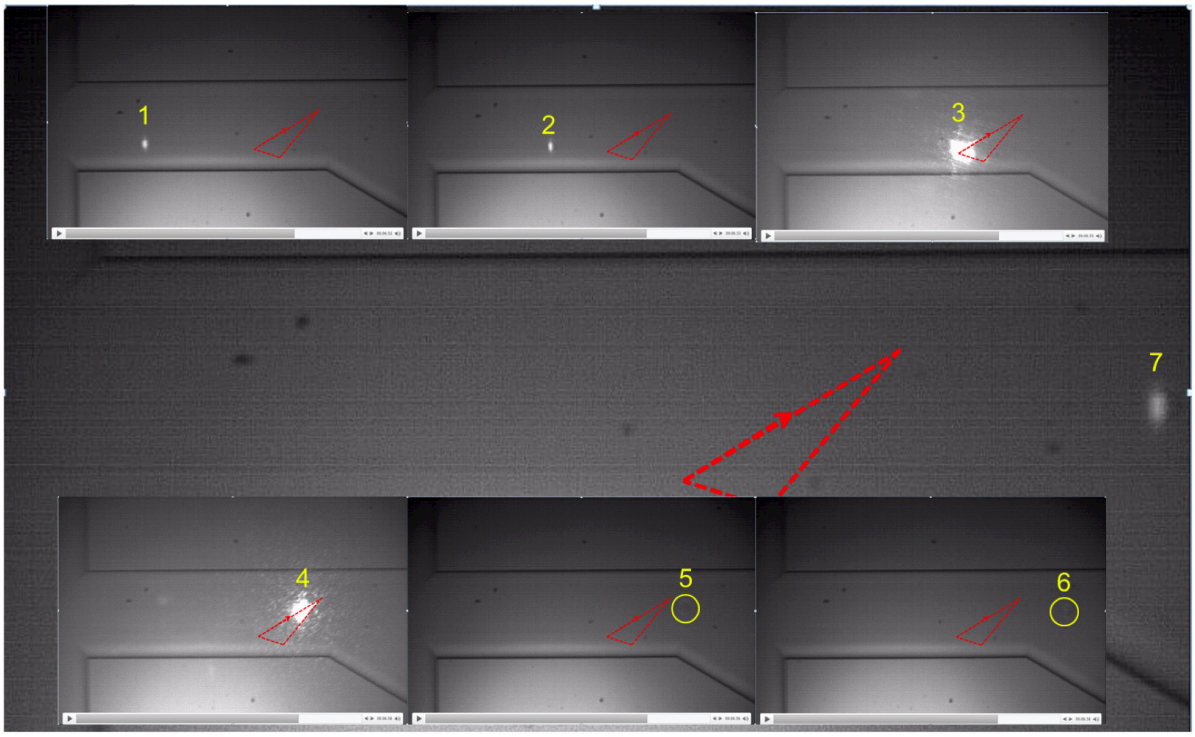

side channels (B of Figure 4.2) used for hydrodynamic focusing. In these experiments, the speed of cells through the photobleaching beams was kept constant at 6 mm/sec. The sample cell concentration was diluted to ≈250,000 cells/ml to decrease the rate R of cells entering the sorter and thereby decrease the probability of overlapping bursts and also increase the fidelity of the monitor beam for counting of successful selection events. For each power and fluid condition, 100 cells were assayed. As shown in Figure 4.7, the selection efficiency was found to be increased for the same 1064-nm laser power by using buffer in the side channels instead of media (possibly because the buffer contains no Optiprep and so leads to greater refractive index contrast and optical forces).

The viability for each 1064-nm laser power was then assessed for both solution conditions. In earlier work [145], mammalian cell viability was quantified by a trypan blue exclusion assay about 1 hour after exposure to the 1064-nm laser beam. However, this assay only accounts for immediate deterioration of the plasma membrane, and cannot identify cells in earlier stages of necrosis or apoptosis. To account for slower forms of cellular death, the cell viability was measured 24 hours after microfluidic analysis for both sorted and non-sorted cells using a Calcein-AM based assay. Calcein-AM (Invitrogen) was added directly to the cells (final concentration of 1 μM) within a 96-well plate and allowed to incubate at room temperature for 30 minutes. Calcein-AM becomes fluorescent upon hydrolysis of the acetoxymethyl moiety by intracellular esterases. In contrast, dead cells remain non-fluorescent, or very weakly fluorescent, and can be identified by comparison of fluorescence and differential interference contrast (DIC) images. Using this method, for higher laser exposure conditions, cell viability was found to be decreased after 24 hours relative to the same assay when performed immediately after microfluidic sorting (Table 4.2). Also, the viability was lowered when buffer was used in the side channels. However, the viability for each 1064-nm laser power was found to be identical ($\approx$ 80 %) when the selected cells were delivered into an on-chip reservoir pre-loaded with 750 μl of the running media to minimize the cells time spent in buffer to $\approx$ 0.5 sec (approximate transit time from interrogation region to outlet). Furthermore, cells were capable of continued replication over the course of several weeks.

Figure 4.7: Cell selection efficiency vs. 1064-nm laser power for: (i) cell suspension medium (lower curve, circle), or (ii) buffer without Optiprep (upper curve, diamond), in the side channels used for hydrodynamic focusing. Optiprep diminishes the refractive index difference between the cell its extracellular solution, thereby decreasing the optical force generated from the 1064-nm laser beam.

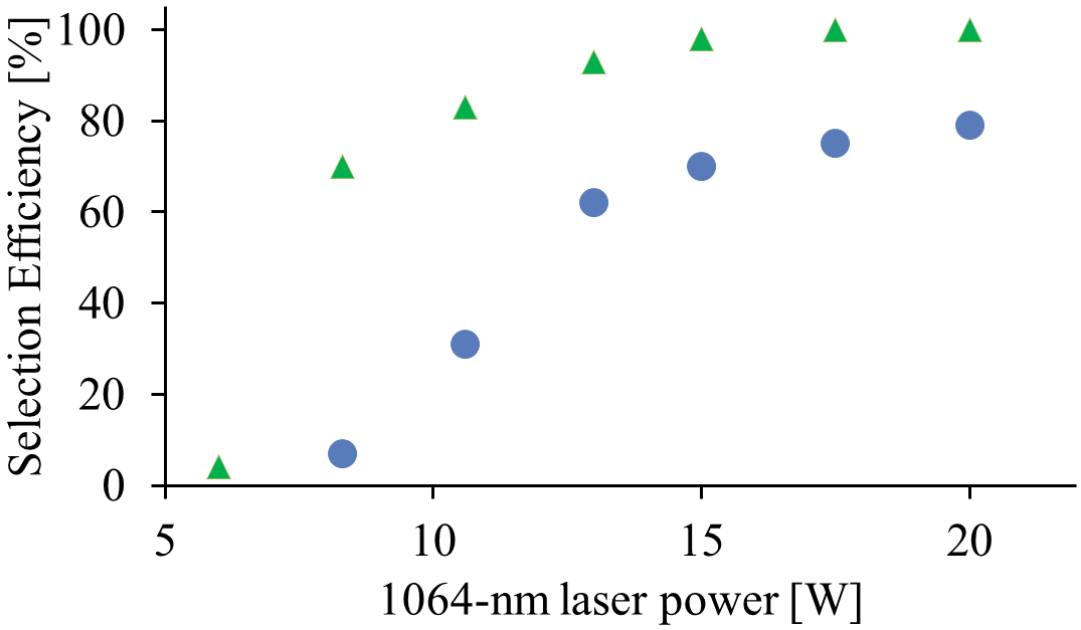

Table 4.2: Cell Viability Before and After 24 Hours of Recovery

Laser Power	Viability Post-Sort	Viability 24 Hours Post-Sort
50%	91% (N=85)	83% (N=120)
60%	39% (N=122)	20% (N=281)
70%	14% (N=121)	17% (N=129)

4.7 Cell Selection Based on Irreversible Photobleaching

To demonstrate the effectiveness of the instrument for selecting cells that have RFPs with lower irreversible photobleaching, experiments were performed using samples containing known mixtures of HeLa-S cells expressing either mCherry (25 % of cells) or mOrange2 (75 % of cells). Previously, we found that mCherry was $\approx$ 3.5$\times$ more photostable than mOrange2 under 532 nm pulsed illumination (See Chapter 2) [209]. In these tests, the instrument was configured to use 4 photobleaching beams and a monitor beam, with 0.09 W of power in each photobleaching beam (peak irradiance $\approx 2\times10^4$ W cm^{-2}). The flow speed of cells through the beams was 6.0 mm s^{-1}. As shown in Figure 4.5, the ratios of the peak amplitudes (beam 4/beam 1) are $\approx$0.63 for cells with mCherry, and $\approx$ 0.40 for cells with mOrange2, whereas in a separate experiment using fluorescently labelled beads (Invitrogen, F-8858 FluoSpheres, 4 μm, 580/605) the ratio is $\approx$ 0.98. The operating parameters were adjusted to select mCherry cells with lower irreversible photobleaching from the mixture using a 1064-nm laser power of $\approx$12 W. Over a duration of $\approx$ 2.5 hours, 4000-5000 cells were selected. The purity of the selected sample was then determined by imaging it using a wide-field fluorescence microscope in which mCherry and mOrange2 cells are spectrally distinguished by use of a set of appropriately chosen band-pass excitation filters (540/25 and 577/20). Figure 4.9 shows the spectra for these filters together with the excitation spectra of mCherry and mOrange2. As seen in Figure 4.10, the ratio of the fluorescence signals seen with each of these filters enables cells expressing mCherry or mOrange2 to be unequivocally distinguished. The purity of the selected sample was thus determined by counting the cells of either type in the image. As seen in Figure 4.8, cells expressing RFPs with lower irreversible photobleaching (mCherry) are selected from the mixture with greater than 99 % purity, which is considerably higher than that typically achieved in FACS and other prior reported microfluidic cell sorters [145].

Figure 4.8: Image of collected cells. Blue/pink pseudo color represents cells expressing mCherry; green pseudo color represents mOrange2. Only one cell expressing mOrange2 is visible. Larger diameter objects are clusters of cells in close enough proximity that their edges arent resolvable.

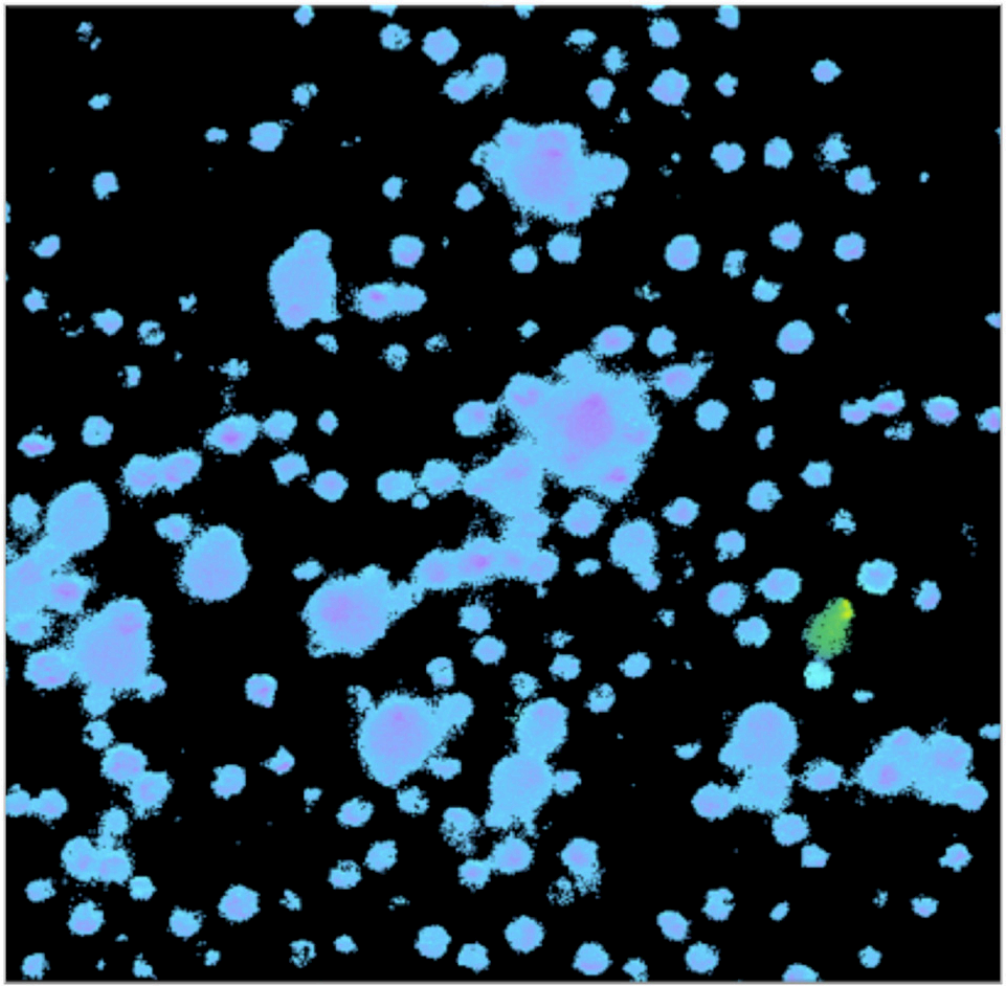

Figure 4.9: The normalized fluorescence excitation spectra for mOrange2 (blue) and mCherry (red) overlaid with the normalized filter transmittance for the two fluorescence excitation filters, 527-553 nm (dashed line, left) and 567-587 nm (solid line, right). The identity of imaged cells is determined from the ratio of the fluorescence signals obtained from each of the excitation bands.

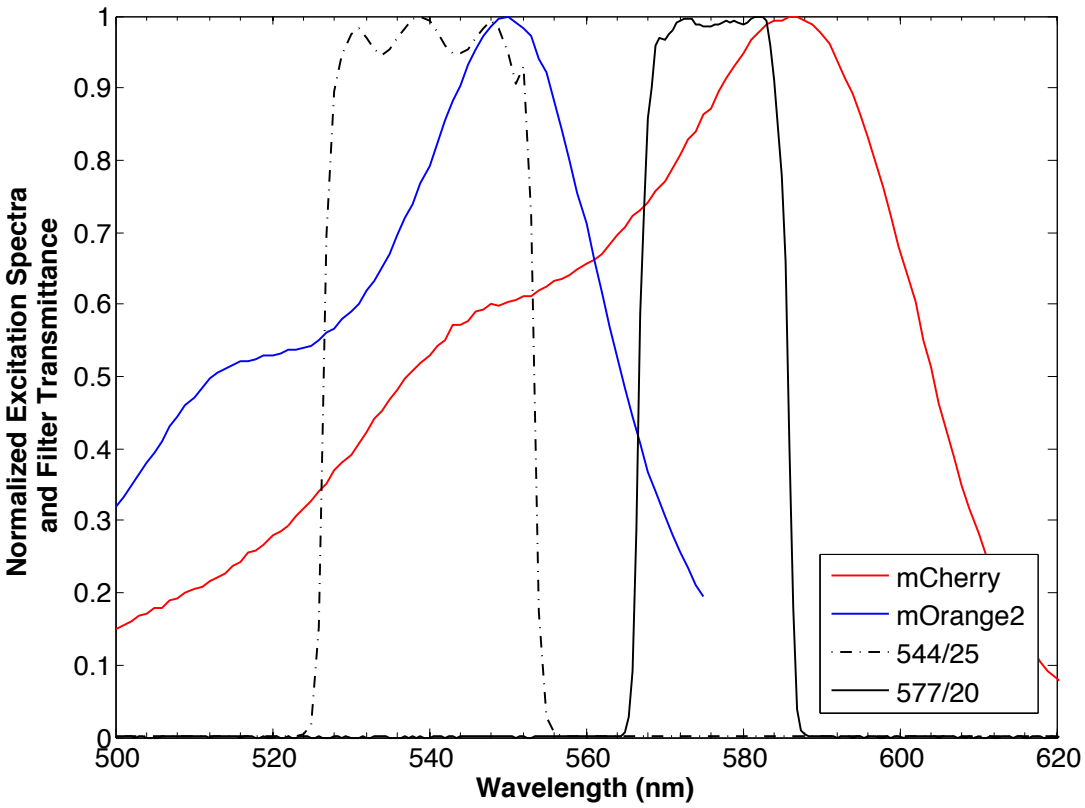

Figure 4.10: Histogram of the excitation ratiometric discrimination of mCherry and mOrange2. Excitation with 577/20 and 540/25 bandpass filters, and fluorescence was collected with a 630/60 emission filter. The ratio of $\frac{577/20}{540/25}$ provided a measure of the fluorescence red-shift, and provided clear resolution of mCherry cells (right peak) from mOrange2 cells (left peak). The two populations were fit to a sum of two gaussian distributions, and the resulting curve is provided in dashed-red. The mean and standard deviation for mOrange2 was 0.45 and 0.13, respectively. For mCherry, the mean and standard deviation was 1.1 and .073, respectively.

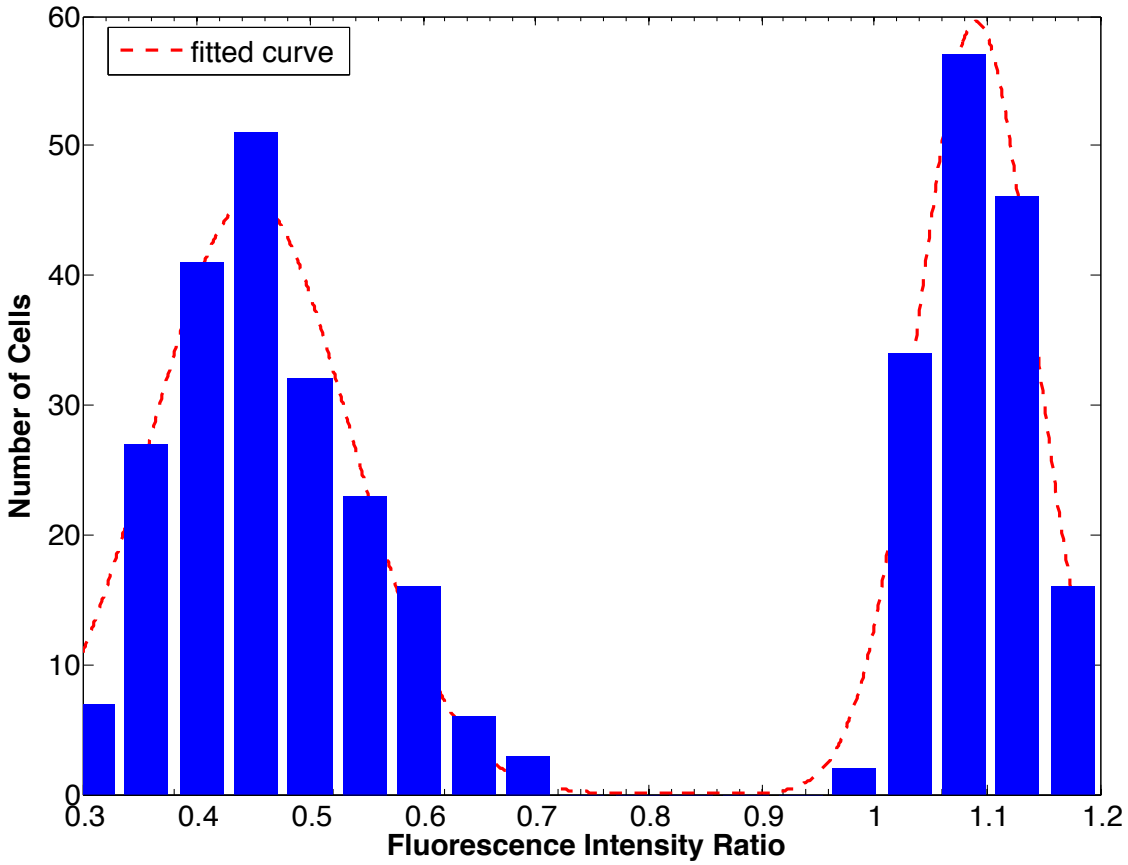

4.8 Discussion

This chapter reports a novel microfluidic cell sorter for live mammalian cells expressing red fluorescent proteins that enables selection of cells with proteins that have enhanced photostability. It uses the Real-Time module of LabView for analysis of multi-beam laser-induced fluorescence signals to determine irreversible photobleaching and to achieve sub-millisecond timing of the sweep of a 1064-nm laser spot to deflect individual selected cells by the optical gradient force to a separate collection channel. Suitable cell suspension media and laser operating conditions have been determined for efficiently selecting mammalian cells while maintaining their long-term viability and capability to proliferate. The effectiveness of the instrument has been demonstrated by selecting cells expressing a fluorescent protein with higher photostability (lesser irreversible photobleaching) at a rate exceeding 0.5 s^{-1} from a sample containing a known mixture of cells expressing either mCherry (25 %) or mOrange2 (75 %). Subsequent analysis of the collected cells on the basis of differences in the fluorescence excitation and emission spectra of mCherry and mOrange2 found that >99 % of the selected cells express mCherry, indicating a remarkably high purity in the selection. The sorter is being used in on-going research to develop new fluorescent proteins with improved photostability.

Chapter 5

Use of a Microfluidic Cell-Sorter to Generate Improved Fluorescent Protein Variants

5.1 Abstract

The chapter discusses the use of a microfluidic cell-sorter to isolate RFP mutants with improved photostabilities. Libraries are created from mCherry, mRuby2, tdTomato, and TagRFP, and are discussed in depth. One library involving saturated mutagenesis at positions Val16, Met66, Trp143, Ile161, and Gln163 in mCherry, is enriched for photostability, and new mutants identified. All RFP mutants found have improved photostabilities, but suffer from decreased fluorescence quantum yields. Oxygen-dependent photobleaching and time-correlated single photon counting methods suggest that improvements in photostability may result from diminished fluorescence lifetimes. Additional spectroscopic selection pressures are recommended, that when coupled with the proper mutagenesis strategies, should lead to improved RFP variants.

5.2 Publication Status and Author Contributions

The work presented here is unpublished.

K.M.D., J.L.L., A.E.P., and R.J. designed research. K.M.D. designed fluorescent protein libraries. K.M.D. and J.L.L. performed research. K.M.D. performed spectroscopic measurements and data analysis.

5.3 Introduction

Countless biological experimental systems would benefit from brighter and more photostable FPs. To date, most FP mutants have been generated using error-prone PCR, site-directed mutagenesis, and/or gene-shuffling followed by bacterial colony screening and/or fluorescence-activated cell sorting (FACS) [14, 18–20, 52, 66, 70, 123, 227]. These approaches, although responsible for the wealth of FPs we now have, primarily use brightness as the sole selection criterion. Unfortunately, the brightness of an FP-expressing cell is a complex parameter that depends upon a variety of criteria, including genome integration site (virally transduced mammalian cells), copy number (transfected mammalian cells), mRNA stability, the rate of protein-folding and degradation, chromophore maturation, extinction coefficient at the wavelength of excitation, the quantum yield of fluorescence, dark-state conversion, and the wavelength dependence of the optics used to measure the fluorescence (emission filters, lenses, photomultiplier tubes, etc.). As a result, selections based upon brightness are at best considered qualitative, and therefore likely suffer from an increased rate of false-positives and false-negatives. Consequently, biological screens for brightness often rely upon large library sizes and multiple rounds of selection to decrease round-to-round variability. To overcome these challenges, researchers are increasingly turning towards more complex, quantitative, and multiparametric screening strategies [120]. Improved quantification and isolation of specific photophysical parameters (e.g., quantum yield, photostability, dark state conversion, etc.) ultimately enables researchers greater liberty in spectroscopic tuning of FPs for modern applications.

Recently, a quantitative and photophysically specific metric, fluorescence lifetime, was used to screen FPs in a low-throughput colony based assay [40]. Given that the fluorescence lifetime is dependent upon the radiative and non-radiative rates out of the excited state, the fluorescence lifetime provides information on the fluorescence quantum yield. After screening a semi-saturated mutagenesis library at position T65 in SCFP3A (originally evolved from ECFP), a single mutation was discovered,T65S, that increased the quantum yield from 0.56 to 0.84. Incredibly, subsequent structure-guided mutagenesis coupled with excited-state calculations on this FP resulted in mTurquoise2, a cyan FP with a quantum yield of 0.93 [41].

In addition to brightness, irreversible photobleaching is particularly important. Photobleaching is

described as light-induced degradation of the fluorescent moiety, and in live-cell imaging, is commonly responsible for diminished fluorescence contrast and limited observation times. Unfortunately, RFPs emit 10-100x less photons than their small-molecule counterparts, and therefore remain poorly suited for next-generation experiments that focus on low-abundance or single-copy expression [94,228]. With the exception of Shaner et al. [23], most FP selections to date have not used photobleaching as a selection parameter. Shaner et al. screened bacteria colonies by eye and with the assistance of a macro-imaging system before and after photobleaching with a solar illuminator [23]. The work presented in this chapter, however, offers several improvements over Shaner et al [23]. By performing the selection on RFP-expressing mammalian cells, the RFPs must remain non-cytotoxic, and be compatible with the eukaryotic machinery. The use of microfluidic technology enables much greater throughput than bacterial colony screening. As opposed to a macro-imager, the microscopy format is more sensitive, more quantitative, and enables screens for RFP photostability over a much larger range of excitation intensities (0.1 to >1,000 kW cm^{-2}) [225]. To evaluate the effectiveness of this cytometer in directed evolution, several libraries were prepared using site-directed mutagenesis and error-prone PCR of different RFPs: mCherry, TagRFP-T, tdTomato, and mRuby2. Preliminary results towards RFPs with improved photostability are presented.

5.4 Experimental Methods

5.4.1 Library Construction

The original DNA templates for tdTomato [20], TagRFP-T [23] mCherry [20], and mRuby2 [129] were amplified with gene-specific primers (See Table 5.1), cloned into pDonr221 using the Gateway recombination system (Life Technologies), and sequenced prior to mutagenesis. The forward primer for each FP included a recombination recognition sequence (attB1), a Shine-Dalgarno sequence for prokaryotic expression, a BamHI restriction endonuclease site, a Kozak sequence for mammalian expression, and an $\approx$ 30 nucleotide sequence complementary to the FP. The reverse primer for each FP included $\approx$ 30 nucleotides complementary to the FP, a stop-codon, an EcoRI restriction endonuclease site, and an attB2 recombination recognition sequence (See Figure 5.1). The BamHI and EcoRI restriction sites facilitated in-frame sub-cloning into pBAD (Life

Figure 5.1: Library construction design. PCR-amplification of the fluorescent protein gene incorporated the attB1 and attB2 recombination sites, a Shine-Dalgarno sequence (SD) for prokaryotic expression, a Kozak sequence for mammalian expression, a stop codon, and BamHI and EcoRI sites for sub-cloning into alternative expression vectors.

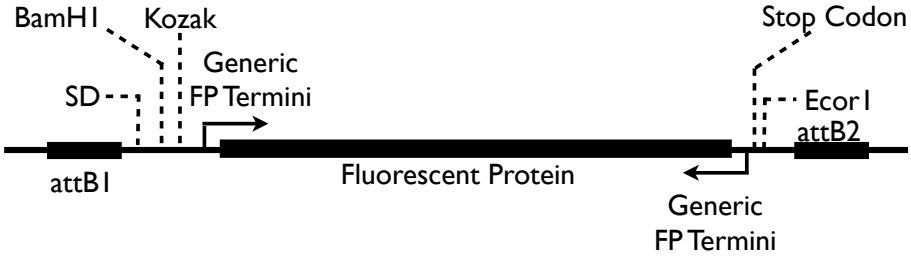

Technologies) and pcDNA3.1 (Life Technologies), for bacterial and mammalian expression, respectively.

The retroviral vector pCLNCX was converted into a Gateway-compatible destination vector according to the manufacturer's directions (Gateway Conversion Kit, Life Technologies). As a result of both positive selection (ampicillin resistance), and negative selection (ccdB toxin:antitoxin system), this system proved valuable in eliminating background clones while preserving high cloning efficiency ($\approx$ 0.5-4.0$\times 10^6$ colony forming units (CFU) per reaction).

To introduce mutations in a site-specific manner, primers were designed with codon wildcards at the appropriate positions (see Table 5.2). Using mutagenic primers, and primers specific to the pDonr221 vector backbone (M13Fwd and M13Rev), fragments of the gene were amplified, gel-purified, and subsequently reassembled using site-overlap extension [130,229]. For most reactions, amplification and reassembly was performed with homemade Pfu DNA polymerase. However, some challenging reassembly reactions necessitated the use of Taq DNA polymerase (NEB).

After reassembly of the gene, an "LR" reaction with the modified pCLNCX vector was carried out for $\approx$ 18 hours at 25 °C , followed by proteinase-K treatment at 37 °C for $\approx$ 15 minutes, and subsequent ethanol precipitation and electroporation into *E. coli* (ElectroMax DH10B, Life Technologies). After recovery of the E. coli in 2 mL of SOB for one hour at 37° with shaking, 200 μL of bacteria are serially diluted into 1.8 mL of SOB 3×, creating 10^{-1}, 10^{-2}, and 10^{-3} solutions. Prior to each dilution, the solutions are thoroughly vortexed, and a fresh pipette is used. Of these solutions, 200 μL is removed from the 10^{-2} solution, and plated on LB agar supplemented with 100 μg/mL ampicillin, providing a working dilution of 10^{-3}. Similarly, 200 μL is

Table 5.1: Primer names, sequences, and FP. Codon wildcards are shown in bold font.

Primer Name	FP	Sequence (5' → 3')
Lib3.0 Fwd	mCherry	GGGGACAAGTTTGTACAAAAAAGCAGGCTTCGAAGGAGGGGATCCCACCATGGTGAGCA AGGGCGAGGAGGATAACATG
Lib3.0 Rev	mCherry	GGGGACCACTTTGTACAAGAAAGCTGGGTCGAATTCTTACTTGTACAGCTCGTCCATGCC
Lib3.0 Fwd	tdTomato	GGGGACAAGTTTGTACAAAAAAGCAGGCTTCGAAGGAGGGGATCCCACCATGGTGAGCA AGGGCGAGG
Lib3.0 Rev	tdTomato	GGGGACCACTTTGTACAAGAAAGCTGGGTCGAATTCTTACAGGTGGTGGCCGCCCTCGGA
Lib3.0 Fwd	mRuby2	GGGGACAAGTTTGTACAAAAAAGCAGGCTTCGAAGGAGGGGATCCCACCATGGTGTCTAA GGGCGAAGAGCTG
S61NNK Fwd	mRuby2	GCCTTTGACATTCTTGCCACG**NNK**TTCATGTATGGCAGCCGTAC
S61NNK Rev	mRuby2	GTACGGCTGCCATACATGAA**MNN**CGTGGCAAGAATGTCAAAGGC
W90NNK Fwd	mRuby2	CCTTTCCTGAGGGTTTTACT**NNK**GAAAGAGTTACGAGATACG
W90NNK Rev	mRuby2	CGTATCTCGTAACTCTTTC**MNN**AGTAAAACCCTCAGGAAAGG
W140NNK Fwd	mRuby2	GATGCAGAAGAAGACCAAGGGT**NNK**GAGCCTAATACAGAGATG
W140NNK Rev	mRuby2	CATCTCTGTATTAGGCTC**MNN**ACCCTTGGTCTTCTTCTGCATC
M160NNK Fwd	mRuby2	GGTGGTCTGAGGGGATACACTCAT**NNK**GCACTGAAAGTTGATGGTGG
M160NNK Rev	mRuby2	CCACCATCAACTTTCAGTGC**MNN**ATGAGTGTATCCCCTCAGACCACC
W58NNKF Rev	tdTomato	GAAMNNGGGGGACAGGATGTC**MNN**GGCGAAGGGCAGGG
Q64NNK Fwd	tdTomato	NNKGACATCCTGTCCCCC**NNK**TTCATGTACGGCTCCAAGGCG
W93NNK Fwd	tdTomato	CCCCGAGGGCTTCAAG**NNK**GAGCGCGTGATGAACTTC
W93NNK Rev	tdTomato	GAAGTTCATCACGCGCTC**MNN**CTTGAAGCCCTCGGGG
W143NNK Fwd	tdTomato	GCAGAAGAAGACCATGGGC**NNK**GAGGCCTCCACCGAGCG
W143NNK Rev	tdTomato	CGCTCGGTGGAGGCCTC**MNN**GCCCATGGTCTTCTTCTGC
Q163MWS Fwd	tdTomato	GGCGAGATCCAC**MWS**GCCCTGAAGCTGAAGG
W153MWS Rev	tdTomato	GGCCGCCGTCCTTCAGCTTCAGGGC**SWK**GTGGATCTCGC
V16RMS Fwd	mCherry	GGAGTTCATGCGCTTCAAG**RMS**CGCATGGAGGGC
V16RMS Rev	mCherry	GCCCTCCATGCG**SKY**CTTGAAGCGCATGAACTCC
Q66NWS Fwd	mCherry	CCTGTCCCCTCAGTTC**NWS**TACGGCTCCAAGGCC
Q66NWS Rev	mCherry	GGCCTTGGAGCCGTA**SWN**GAACTGAGGGGACAGG
W143NNK Fwd	mCherry	CGTAATGCAGAAGAAGACCATGGGC**NNK**GAGGCCTCCACCGAGCGG
W143NNK Rev	mCherry	CCGCTCGGTGGAGGCCTC**MNN**GCCCATGGTCTTCTTCTGCATTAC
I161NTS K163NNK Fwd	mCherry	CTGAAGGGCGAG**NTS**AAG**NNK**AGGCTGAAGCTGAAGGACGGC
I161NTS K163NNK Rev	mCherry	GCCGTCCTTCAGCTTCAGCCT**MNN**CTT**SAN**CTCGCCCTTCAG
I197NWS Fwd	mCherry	CGGCGCCTACAAGACCGAC**NWS**AAGCTGGACATCACCTCCC
I197NWS Rev	mCherry	GGGAGGTGATGTCCAGCTT**SWN**GTCGGTCTTGTAGGCGCCG
T217RBC Fwd	mCherry	CAGTACGAGCGC**RB**CGAGGGCCGCCACTCCACCG
T217RBC Rev	mCherry	CGGTGGAGTGGCGGCCCTCG**VY**GCGCTCGTACTG
M13Fwd	pDonr221	TGTAAAACGACGGCCAGT
M13Rev	pDonr221	CAGGAAACAGCTATGAC

removed from the 10^{-3} solution, and plated, to provide a working dilution of 10^{-4}. The plates are allowed to grow at 37 °C for ≈ 18 hours. Counting the number of colonies present on each plate, and multiplication by the dilution factor for the plate (10^{-3} and 10^{-4}), provides an estimate for the number of colony-forming units present in the electroporation. The remainder of the library was allowed to grow overnight in 10 mL of LB broth supplemented with 100 μg/mL ampicillin (LB/Amp). After ≈ 15 hours of growth, 1 mL of the overnight culture was inoculated into 100 mL of LB/Amp for ≈ 18 hours of further growth and plasmid DNA isolation (Midi-Prep Kit, Qiagen), while the other 9 mL was used to create a 30 % glycerol stock. The binomial probability distribution was used to calculate the number of mutants necessary to sufficiently sample the entire library.

5.4.2 Library Construction, Cell Maintenance and Recovery of Sorted Cells

HeLa cells were cultured in Dulbecco's modified essential medium (DMEM) supplemented with 10 % Fetal Bovine Serum (FBS) and 1 % penicillin-streptomycin, as previously described [209]. HEK-293 FT cells were cultured similarly, using DMEM supplemented with 10 % FBS, 1 % penicillin-streptomycin, sodium pyruvate, and L-glutamate. For generation of virus, HEK-293 FT cells were allowed to grow to ≈ 60 % confluency within a 10 cm dish, and were cotransfected with pCL-Ampho, pVSV-G, and the pCLNCX-library using standard transfection reagents (Opti-MEM, Life Technologies, and TransIT-LT1, Mirus Bio LLC). After 24 hours, the media was gently replaced, and after 48 hours, the virus containing supernatant was carefully filtered through a 0.45 μm cellulose acetate syringe-filter, and then titrated onto HeLa cells in the presence of 12 μg/mL hexadimethrine bromide (Sigma-Aldrich). 24 hours later, the media was replaced, and 48 hours later, the cells were prepared for enrichment of the red-fluorescent clones using a Dako Cytomation Mo-Flo cytometer. In each case, the multiplicity of infection was kept low (ideally <10 %) to decrease the likelihood of multiple viral integrations per cell. For libraries with a small population of fluorescent clones, one week of 1 mg/mL G418 (Sigma-Aldrich) treatment preceded FACS to further eliminate non-virally transduced cells.

For microfluidics-based sorting, the library containing HeLa suspension cells were placed in a solution

Table 5.2: Codon wildcards and possible amino acid substitutions. Codon definitions: R = A/G, Y=C/T, M=A/C, K=G/T, S=C/G, W=A/T, H=A/C/T, B=C/G/T, V=A/C/G, D=A/G/T, N=A/C/G/T. Adapted from Campbell, et al. [19]

Codon	Possible Amino Acid Substitutions
VYC	T/I/A/V/P/L
MWS	Q/H/L/K/N/M/I
NCC	A/S/T/P
ARG	K/R
NNK	All 20 a.a.
DYC	A/T/S/V/I/F
RVS	T/K/S/N/R/A/E/G/D
NTS	L/M/V/I/F
VVS	G/R/A/P/T/E/Q/K/S/D/H/N
ASC	S/T
NHC	N/D/H/Y/T/A/P/S/I/L/V/F
NWS	K/E/Q/M/V/L/N/D/H/Y/I/F
YCC	S/P
GYC	V/A
WWK	N/K/I/M/Y/F/L
RMS	E/D/A/K/N/T
RYC	T/I/A/V
DCC	S/T/A
VVC	A/D/G/H/N/P/R/S/T
NYC	P/T/S/A/L/I/F/V
AYC	I/T
SCC	A/P
CRS	Q/H/R/R
NTS	L/M/V/I/F
VAS	E/Q/D/H/K/N
RBC	V/A/T/I/S/G

of phenol-free MEM-Alpha (Gibco) with the addition of 10 % FBS, 1 % penicillin-streptomycin, and 14 % Opti-Prep, filtered through a 40 μm nylon mesh cell-strainer (BD Biosciences), and deposited directly into a custom-built microfluidic manifold. The sheath channels were filled with Ca^{2+}-free, Mg^{2+}-free, $PO_4{}^{3-}$-free HHBSS with 1 % Bovine Serum Albumin (Sigma-Aldrich). Cells were sorted directly into DMEM supplemented with 30 % FBS and 1 % penicillin-streptomycin, and placed into a 96-well plate for maintenance at 37 °C and 5 % CO_2. After several weeks of expansion, a population of the cells were frozen in the presence of 10 % DMSO, and the remainder of the cells were subjected to additional rounds of selection.

After several rounds of sorting, mRNA was isolated from ≈ 300,000 HeLa S cells (RNeasy Micro Kit, Qiagen), cDNA was prepared using a random hexamer primer (SuperScript II, Life Technologies), and PCR amplification of the cDNA library was performed to clone the sorted RFP variants into a bacterial expression vector (pBad, Life Technologies). In each case, individual clones were isolated and submitted to commercial Sanger sequencing (Quintara Biosciences).

5.4.3 Photobleaching Measurements

Confocal photobleaching measurements were performed on a laser-scanning system (Nikon, A1R) with feedback for axial sample drift. A 561 nm laser was triggered with an acousto-optic tunable filter to excite the sample, the fluorescence was collected in the epi-direction, focused through a 1.2 Airy unit pinhole, filtered with a 600/50 bandpass filter, and detected with a photomultiplier tube. The image size was 512x512, and images were collected in a bidirectional scanning mode with the non-resonant galvometer-based scan-head. Accurate oxygen conditions were controlled with a stage-top environmental chamber (Pathology Devices). For widefield photobleaching measurements, illumination was provided with a metal halide lamp equipped with a shutter for rapid exposure and a liquid light guide for uniform illumination. Excitation was spectrally filtered through a 562/40 bandpass filter (Semrock) and reflected off of a 593 nm dichroic (Semrock) into the back-aperture of the objective; fluorescence was collected in the epi-direction, and emission filtered with a 624/40 bandpass filter (Semrock) prior to imaging with a EMCCD detector (iXon X3 DU897, Andor). In each case, the signal was corrected for background according to Equation 5.1. Dark-state conversion assays were performed as described previously [209].

$$Signal = 100 \times \frac{Data - Background}{Max(Data) - Max(Background)} \tag{5.1}$$

5.5 Library Design Hypotheses.

Proper library design is paramount to the success of a selection process. Under ideal circumstances, mutations are chosen that are known to influence the criteria that you are selecting for, and the size of the library is matched to the throughput of the selection method. However, given that the mechanism of photobleaching remains poorly understood, we decided to pursue a structure-guided library design. The crystal structure of mCherry reveals excellent interstrand hydrogen-bonding, with the exception of β-strands 7 and 10 (Figure 5.2). Molecular dynamics (MD) suggested that relative to Citrine, this region in mCherry is highly dynamic and subject to increased oxygen permeability [76]. We hypothesized that if we targeted this region in mCherry, that we could simultaneously decrease interstrand dynamics and permeability to molecular oxygen, thereby improving the fluorescence quantum yield and photostability of mCherry. In support of the photostability hypothesis, imaging under anaerobic conditions does appear to decrease the rate of photobleaching for mCherry (data not shown). Nevertheless, the incorporation of the three mutations recommended by the MD simulations, Trp143Lys, Gln163Arg, and Arg164Glu, resulted in a non-fluorescent mutant.

Despite this result, we decided to carry out a thorough literature search and evaluate other potential mutations that could act in a compensatory manner. Impressively, 1 in every 3 positions within the mFruit family had been mutated in the literature, demonstrating an impressive resilience to amino-acid changes. To distill this information into a more useful form, we created two pseudo-quantitative metrics to assess the likelihood of mutagenesis: "evolutionary readiness" and "evolutionary maximization." Here, evolutionary readiness is the product of the total number of mutations reported at a particular position in the literature, and the number of publications that report mutagenesis at this position. Hypothetically, evolutionary readiness identifies positions within mCherry that have high mutational potential. Evolutionary maximization, however, was the the number of citations squared, divided by the number of mutations identified. Unlike evolutionary readiness, the evolutionary maximization provided an estimate of consensus, a common amino-

Figure 5.2: Crystal structure (PDB 2H5Q) of mCherry, highlighting the decreased interstrand hydrogen-bonding between β-strands seven and ten (located near Trp143 and Gln163). Also included in the figure are the mutations identified from the literature search. The mutations identified are Val16, Met66, Trp143, Ile161, Gln163, Ile197 and Ala217. For the initial library, Val16, Met66, Trp143, Ile161, and Gln163 were subjected to semi-saturated and saturated mutagenesis.

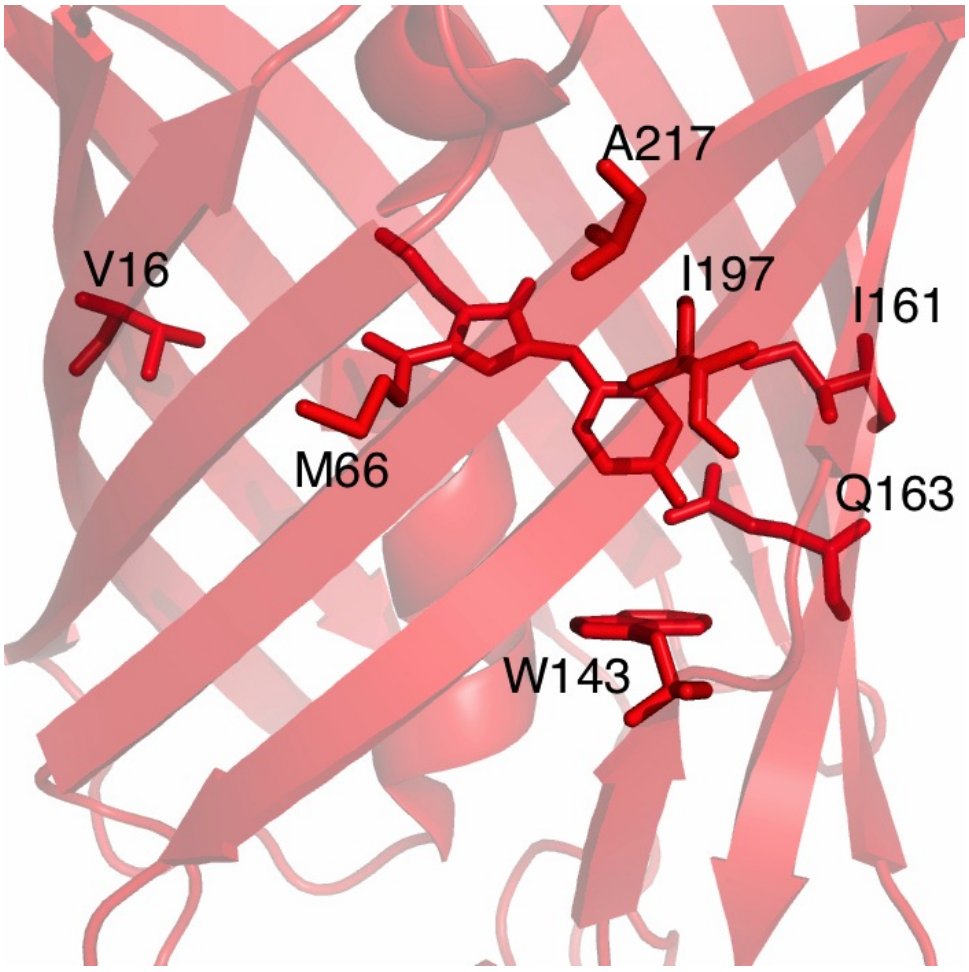

acid identified multiple times, in multiple publications. Mutations that were outward facing or located in the loops that connect the β-strands were excluded. It should be noted that these metrics are not based upon any legitimate statistical source, but were created to crudely assess the potential for mutagenesis at different positions. Additionally, these metrics are not ideal given that they rely upon published mutations, which are not representative of the true potential for mutagenesis at each position. Furthermore, many of the reported mutations may not be optimum, and although reported, are not incorporated in many RFP mutants.

Using these metrics, we identified mutations within the mFruit (e.g., monomeric descendants of DsRed) context that were high in evolutionary readiness, but low in evolutionary maximization. Interestingly, two of the positions recommended from the MD simulations, Trp143 and Gln163, were also identified in the literature analysis. However, the third mutation, Arg164, was reported to be critical for the disruption of the A/C dimerization interface [19]. The highest scoring positions, and their reported mutations, included: Val16E/T/I/S, Met66/C/S/Q/T/F, Trp143L/V/S/C/A/T/I/M/K, Ile161M/T/N/S, Gln163K/M/L, Ile197E/Y/T/A/S, and Ala217/S/C/N/T (See Figure 5.2). Given the agreement between the MD simulations and the literature analysis, we decided to pursue a library strategy that incorporated chemically similar mutations at these positions. Limitations of the genetic code and codon wildcards prohibited exact overlap between the library being constructed and the mutations identified in the literature (See Table 5.2). mCherry was selected as a template for mutagenesis given its superb photostability under laser excitation amongst the mFruits [209]. Table 5.3 lists the positions and the mutations incorporated into the library design. Positions Ile197 and Ala217 were omitted due to difficulties in the site-overlap extension reaction. The final library size was 144,000 mutants, and was named Kriek, after the Belgian beer that involves fermentation of cherries. Other libraries, including those prepared from TagRFP, mRuby2, and tdTomato, are presented in Appendix A.

HeLa S cells were virally transduced with the 144,000-member Kriek library at a low multiplicity of infection and $\approx$ 80,000 red-fluorescent clones were enriched using FACS. Given the large population of non-fluorescent mutants in the library (<10 % fluorescent), this provided $\approx$ 6-fold coverage of the functional fluorescent protein population. Following enrichment, the library was subjected to multiple rounds of selec-

Table 5.3: Mutations incorporated into the site-directed library for mCherry. The final library size was 144,000 mutants.

Position	Potential Mutations
Val16	E/D/A/K/N/T
Met66	K/E/Q/M/V/L/N/D/H/Y/I/F
Trp143	All 20 Amino Acids
Ile161	L/M/V/I/F
Gln163	All 20 Amino Acids

tion using the high-throughput cell-sorting microfluidic system. At each stage of the process (e.g., after the initial FACS enrichment, first microfluidic sort, etc.), cells were gradually frozen down at a concentration of $\approx 2\times10^6$ cells/mL in DMEM supplemented with 10 % FBS and 10 % DMSO, and then stored indefinitely at $\approx$ -180 °C for future analysis.

5.6 Microfluidics Based Selection for an Improved RFP

The microfluidic photobleaching cytometer presented in Chapters 3 and 4 enables quantitative and high-throughput screens for irreversible photobleaching on single mammalian cells, and can be configured in 3 beam, 4 beam, and 8 beam modes [225]. To assess the spectroscopic diversity present in the Kriek library, the higher-throughput 4-beam microfluidic assay was employed, and the ratio of fluorescence intensities resulting from the first and fourth excitation events was used to quantitate the extent of photobleaching. Under ideal 4-beam microfluidic conditions, a coefficient of variation (the standard deviation divided by the mean) of $\approx$ 18 % is common for a single-FP cell population, with greater uncertainty arising from low-expression cells. However, for the initial library, a coefficient of variation of 186 % was observed, and a significant fraction of cells exhibited an improved photostability ratio (Figure 5.3). In agreement with previous work, mutations in proximity to the chromophore drastically alter the observed photobleaching [209].

Given the promising diversity in photostability, the library was subjected to multiple rounds of selection and expansion. In each round, the top third most photostable population was gated for optical gradient based sorting. Estimating that the functional library size after FACS enrichment was $\approx$ 14,000, enough cells were screened in each round to provide 3-fold coverage. After two rounds (referred to as Kriek2, or K2), it

Figure 5.3: Histogram of observed photostabilities for mCherry library. Ratios at higher values represent cells expressing mutant FPs with improved photostability. The absolute ratio of beam 4 to beam 1 depends upon the optical alignment of the microfluidic cytometer, and varies from day to day.

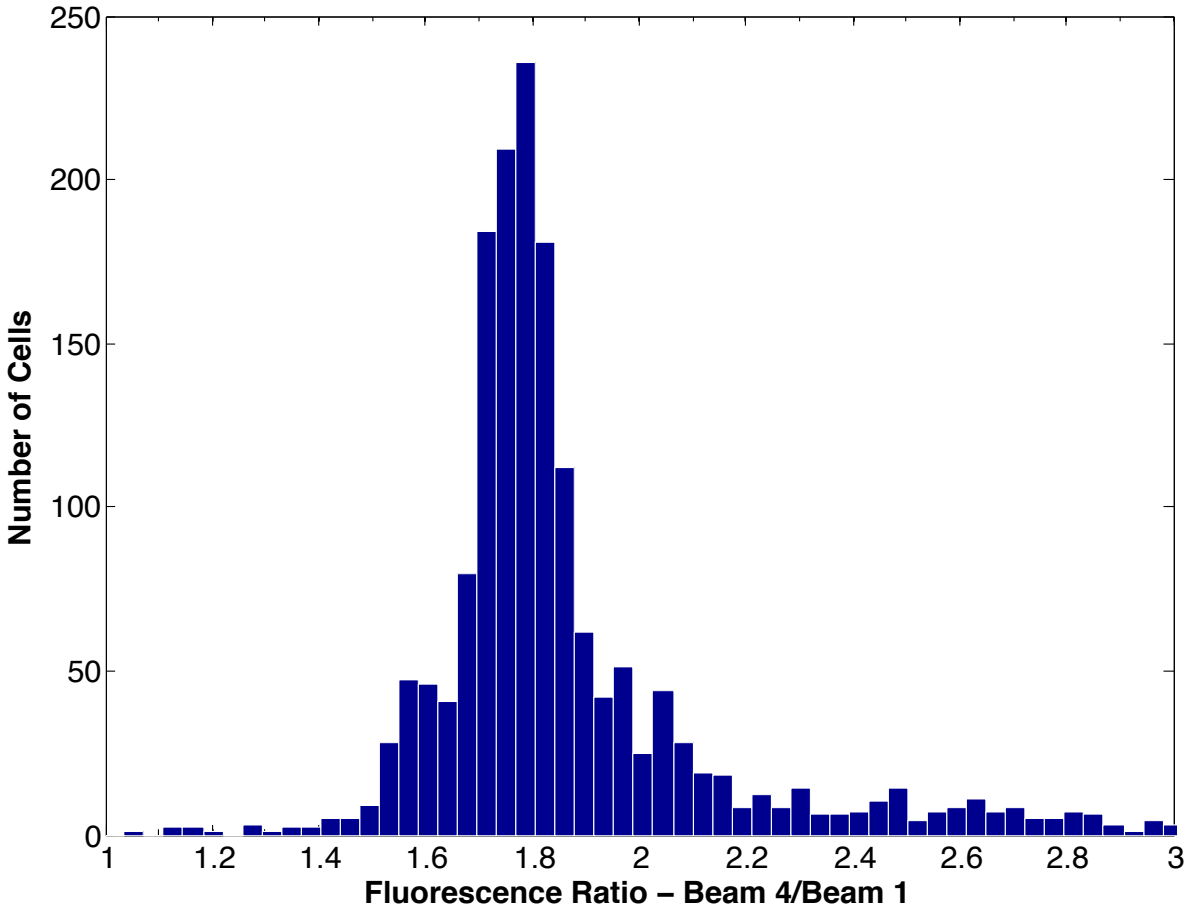

Figure 5.4: Summary of Kriek Library Sorting. Kriek1 and Kriek2 were sorted with photostability as the only selection parameter, whereas Kriek4 was generated by sorting Kriek1 with fluorescence intensity and photostability as the selection parameters.

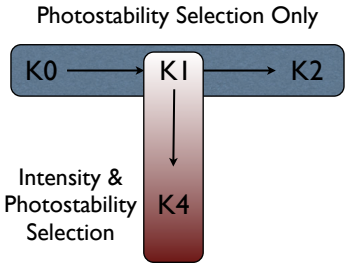

was immediately evident that a significant fraction of the library had shifted to a higher photostability (Figure 5.5). A third round of sorting (referred to as Kriek3, or K3) appears to have suffered from contamination with the parent library, and was subsequently discarded. In addition, after each library sort, the average fluorescence brightness of the population decreased. This could be result of diminished cellular health following multiple generations of optical sorting, or due to gradual enrichment of mutants with decreased fluorescence quantum yield and/or extinction coefficient. Given this observation, an alternative selection was performed on Kriek1 (K1), involving both photostability and fluorescence brightness, and is referred to as Kriek4 (K4, see Figure 5.4). Kriek2 and Kriek4 cells were harvested, the mRNA was purified, the cDNA was synthesized, PCR amplified, and cloned into pBAD. Fluorescence was confirmed in bacteria, and the DNA was submitted for commercial DNA sequencing. Interestingly, FACS-based sorts often require >7 rounds to converge on a population, likely resulting from cell-to-cell and round-to-round variability in fluorescence brightness. Our system, however, by looking at an intensive property (e.g., a ratio of fluorescence intensities) is less sensitive to cell-to-cell or round-to-round variability in fluorescence brightness.

5.7 Mutations Observed in the New RFPs

To identify the mutants arising from our microfluidic photobleaching cytometer selection method, sequencing was carried out on three separate occasions. K2A-F (Kriek-2, mutants A, B, C...F), K4A-F, and then an additional 12 mutants from both K2 and K4. In the third sequencing trial, but not the first and second, mCherry was found in 10 of the 24 mutants. These clones are likely the cause of the residual mCherry-

Figure 5.5: Shift in observed photostability before and after two-rounds of selection. The first round, designated as K0, is represented in light grey. The photostability distribution after the second round of selection, is designated as K2, and is represented in black. Measurements were collected on the same day. Given that the instrument was configured to provide a $\frac{Beam_4}{Beam_1}$ ratio of ≈ 1 for mCherry, the subsequent mutants with improved photostabilities show a >1 ratio.

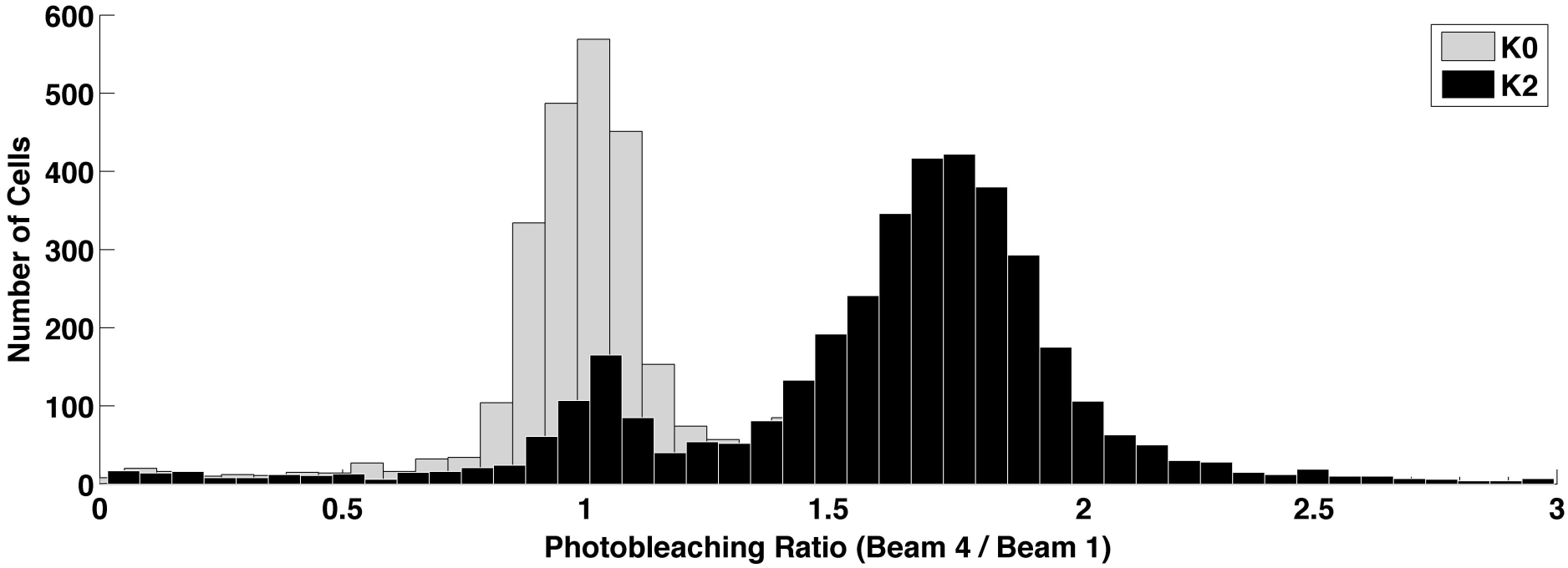

like population in Figure 5.5. Of the remaining mutants, several of the amino-acid changes shared similar chemical properties (Table 5.4). For example, out of 24 mutants sequenced, only 3 had mutated Val16, and of those, all were mutated to an alanine. His17Arg was always observed in mutants with Val16Ala, likely arising from improper synthesis of the DNA oligonucleotide. Met66, the first amino-acid within the chromophore forming tripeptide, was mutated to a glutamine in 4 out of the 24 mutants. A glutamine in this position is also found in DsRed [13, 14, 18], mRFP1 [19], mHoneydew [20], select green-fluorescent proteins and non-fluorescent chromoproteins [112,127,230], as well as the photosensitizing KillerRed [63,65]. The majority of mutations at Trp143 were hydrophobic in nature, and included alanine (10/24), tryptophan (5/24), methionine (2/24), isoleucine (1/24), although polar residues were also observed, including serine (5/24) and cysteine (1/24). At position Ile161, only non-polar residues were discovered, including leucine (9/24), valine (8/24), isoleucine (6/24), and methionine (1/24). Lastly, Gln163 was found to be mutated to isoleucine (9/24), leucine (6/24), glutamine (3/24), threonine (1/24), valine (1/24), tryptophan (1/24). Given these results, the overall consensus for mutations appeared to be mCherry Trp143Ala Ile161Leu and Gln163Ile, a series of mutations found in K2A.

5.8 Spectroscopic Features of New RFPs

The spectroscopic characteristics of RFPs, including the extinction coefficient (ϵ_{abs}), λ_{ex}, λ_{em}, and quantum yield (ϕ) remain important determinants in the overall functionality of RFP variants. To evaluate the spectroscopic characteristics, many of the K2 mutants, as well as mCherry, were grown under identical conditions and subsequently purified and dialyzed into 15 mM MOPS, 100 mM KCl, pH=7.5 for *in vitro* analysis of their spectral properties. To generate a useful concentration of protein, relative to K2A, K2B, and K2C, twice as much bacteria was harvested for the purification of K2D, K2E, and K2F. An absorption spectrum was collected, and normalized to the λ_{230nm} peak to qualitatively gauge protein expression and chromophore maturation (Figure 5.6). From this graph, mCherry showed the greatest $\frac{\lambda_{590nm}}{\lambda_{230nm}}$ ratio, indicative of the greatest extent of protein folding and/or chromophore maturation, followed by K2A, K2C, K2B, K2D, K2E, then K2F. Although λ_{230nm} measures all of the aromatic amino-acids (Trp/Tyr/Phe) present in the solution, and can be subject to impurities, this result is consistent with the decreased brightness of the

Table 5.4: Mutations observed in Kriek2 (K2) and Kriek4 (K4). K2A, K2B, K2C, etc., are mutants identified after the second round of sorting the Kriek2 library. In mutants with Val16Ala mutations, an unintended mutation, likely arising from primer synthesis, also incorporated His17Arg. Sequencing was carried out on three separate occasions, first for Kriek2, then Kriek4, and then a second round involving both Kriek2 and Kriek4. Only in the third sequencing event was mCherry observed.

RFP	16	66	143	161	163
mCherry	Val	Met	Trp	Ile	Gln
K2A			Ala	Leu	Ile
K2B			Cys	Val	Thr
K2C			Ile	Met	Val
K2D	Ala	Gln	Met	Val	Leu
K2E	Ala	Gln	Ser	Val	Leu
K2F	Ala	Gln	Met	Val	Trp
K4A			Ala	Leu	Ile
K4B			Ser	Val	Leu
K4C			Ser	Val	Leu
K4D			Ala	Leu	Ile
K4F		Gln	Ala	Leu	Ile
K4H			Ser	Val	Leu
K4I			Ala	Leu	Ile
K4J			Ser	Val	Leu
K4K					
K4L			Ala	Leu	Ile
K4M			Ala	Leu	Ile
K4P			Ala		
K4Q			Ala	Leu	Ile
K4S					
K4T			Ala	Leu	Ile

Table 5.5: Spectral properties of K2 mutants. In cases where mCherry was mutated, the specified mutation is listed. N.D. means that the property has not been determined.

RFP	λ_{abs} (nm)	λ_{ex} (nm)	λ_{em} (nm)	Q.Y.
K2A	588	510	610	0.12
K2B	585	586	607	0.12
K2C	592	593	613	0.08
K2D	588	588	607	N.D.
K2E	583	583	603	N.D.
K2F	587	588	606	N.D.
mCherry	587	591	608	0.23
mCherry W143I	583	583	611	N.D.
mCherry I161M	588	592	617	N.D.
mCherry Q163V	585	586	614	N.D.
mCherry W143I I161M	589	592	618	N.D.
mCherry W143I Q163V	587	588	618	N.D.
mCherry I161M Q163V	588	590	612	N.D.

bacterial colonies and pellets for mutants K2D, K2E, and K2F. Additionally, a population of the "GFP-like" chromophore, $\lambda_{Abs} \approx 510$ nm, was present in all three of these mutants (Figure 5.7). Photophysical properties are summarized in Table 5.5, including the measured quantum yield, absorption, excitation, and emission wavelengths. K2C is also red-shifted relative to mCherry, and individual analysis of mutants harboring permutations of mutations found in K2C (also reported in Table 5.5) suggests that Ile161Met is responsible for the red-shift in the absorption and emission spectra, while also potentially stabilizing the excited-state, resulting in an increased Stokes shift. Similar results for Ile161Met were found two screens where the principal selection pressure was a red-shift in the fluorescence wavelength [111, 129].

To evaluate the photostability of the mutants, fluorescent proteins were subjected to a variety of photobleaching conditions. As an initial test, octanol microdroplets containing purified protein were examined under λ=561 nm CW laser-scanning confocal conditions. K2A, K2B, K2C, K2D, K2E, and K2F showed improvement in photostability over mCherry, with K2C showing the greatest improvement by qualitative analysis. Given this result, as well as the decreased expression of K2D, K2E, and K2F, and only modest improvements in photostability for K2A, K2B, only K2C was pursued further. To assess the photostability under more biologically relevant conditions, additional studies were carried out on freely diffusing yet nuclear-localized RFPs within adherent HeLa cells. Measurements were performed with 100 % and 10 %

Figure 5.6: Absorption spectra of K2 mutants, normalized at λ_{abs}=230 nm. Most K2 mutants showed excellent maturation to a red-emitting state, with only a small population of "GFP-like" chromophores present in K2D, K2E, and K2F.

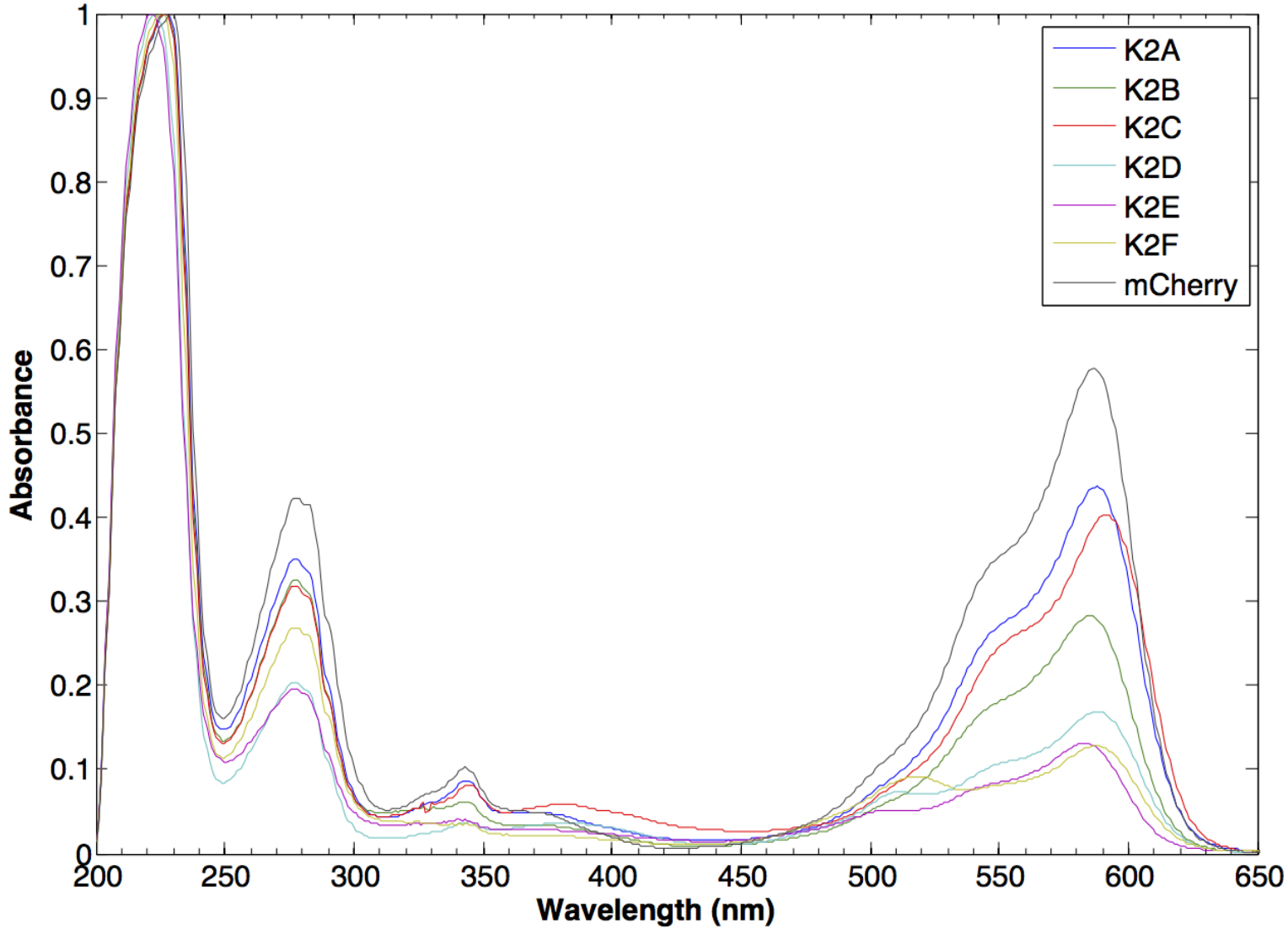

Figure 5.7: Absorption spectra of K2 mutants normalized at $\lambda_{abs} \approx 590$ nm. Red-shifts relative to mCherry are obvious, as well as the extent of incomplete chromophore maturation in K2D, K2E, and K2F.

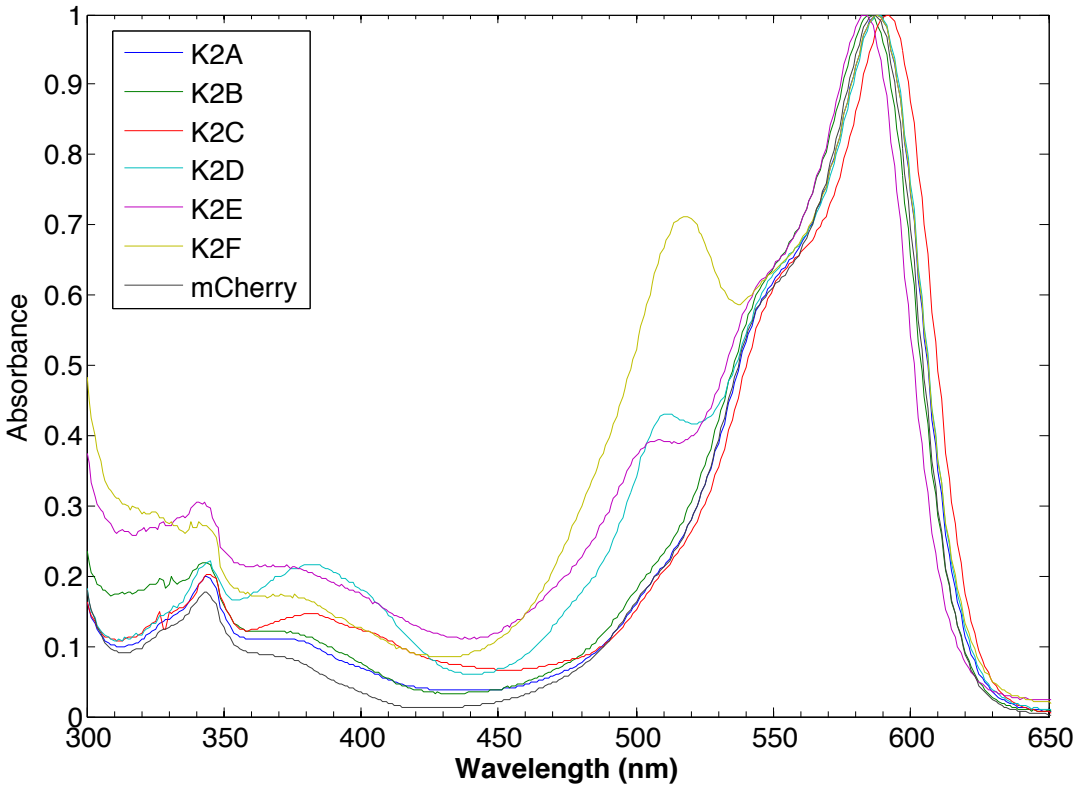

laser powers in a 561 nm CW laser-scanning confocal mode, as well as in a widefield epifluorescence mode (Figure 5.8). For laser illumination, K2C and mCherry had biexponential photobleaching decays, and the weighted lifetime was used to compare the photostability between the RFP variants (Figure 5.8). At 100 % laser power, K2C and mCherry had photostability time-constants of 58 and 37 seconds, respectively, providing a $\approx$ 50 %-fold improvement. At 10 % laser-power, K2C and mCherry had photostability time-constants of 1700 and 600 seconds, respectively, providing an $\approx$ 180 % improvement. Here, even after 10 minutes of continual confocal illumination, K2C only decreased $\approx$ 20 % in fluorescence intensity (Figure 5.8, middle panel). The non-linearity between the rate of photobleaching and laser-power is common in RFPs [209]. Under continuously exposed widefield illumination, mCherry and K2C had photostability time-constants of 111 and 284 seconds, respectively, again providing $\approx$ 150 % improvement in photostability.

Dark-state conversion is an important contributor to irreversible photobleaching, and dark-states in RFPs can be photolabile or photoprotective [209]. To preliminarily assess the percent dark-state conversion in K2C, purified protein in octanol microdroplets was subjected to rapid photobleaching with a 25 kW/cm^2 λ_{ex}=532 nm CW laser (See Chapter 2) [209]. In agreement with the results presented in Chapter 2, K2C had three distinct phases of fluorescence decay (Figure 5.9). An initial and reversible decay in fluorescence intensity (<500 μs), a steady-state phase (500 μs to 1 ms), and an irreversible (>1 ms) phase. As anticipated for FPs with smaller quantum yields, the initial phase occurs rapidly ($\approx$ 10 μs), and only $\approx$ 20 % of the protein is converted to a dark-state.

5.9 Potential Causes of the Improved Photostability

There are several potential causes that could account for the observed increase in photostability for K2C. In a classical photophysics sense, improvements in photostability can be attributed to decreased excited state lifetimes for the first excited singlet state and triplet state, reduced excited-state absorption to higher-order singlet and triplet states, and attenuated excited-state reaction pathways, including photoionization and oxidation by molecular oxygen [114, 115, 159, 231–234]. To evaluate the excited-state singlet lifetime, time-correlated single-photon counting measurements were performed. K2C has a fluorescence lifetime of $\approx$ 1.0 ns, as opposed to mCherry, which has a fluorescence lifetime of $\approx$ 1.9 ns (Figure 5.10). To evaluate if the

Figure 5.8: Photobleaching of K2C and mCherry. Under widefield photobleaching conditions, K2C was 250 % more photostable than mCherry (Top Panel). For low-power confocal photobleaching (10 % laser power), K2C was 150 % more photostable than mCherry (Middle Panel). For high-power confocal photobleaching (100 % laser power), K2C was 280 % more photostable than mCherry (Bottom Panel).

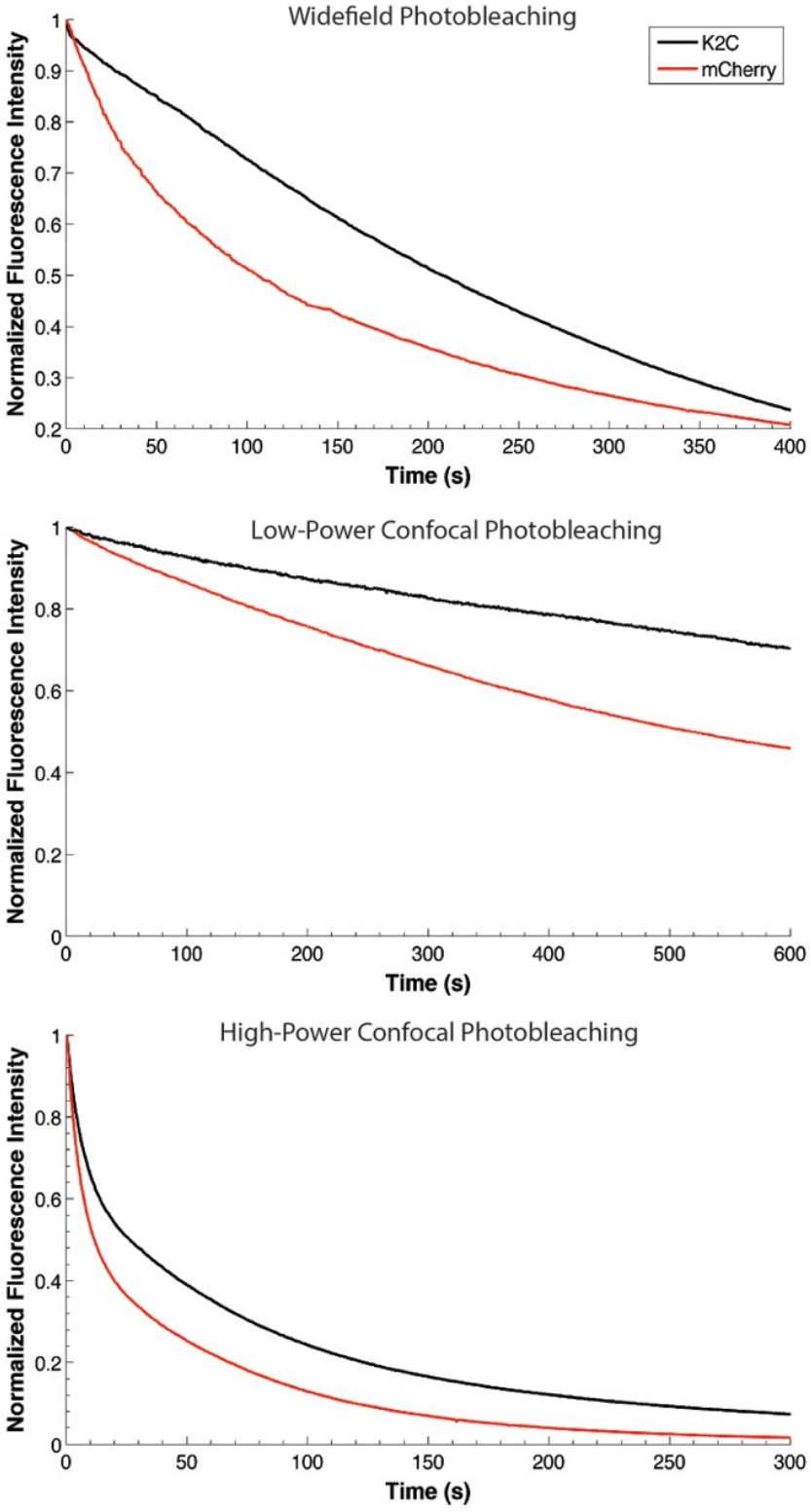

Figure 5.9: Dark-state conversion in K2C. Following sub-μs illumination of purified protein containing octanol microdroplets, three distinct phases are observed. The first phase, occurring $\approx$ 10 μs, is reversible, and is related to the rate of recovery from the dark-state to the ground-state. The second-phase, occurring between $\approx$ 500μs and 1 ms, is indicative of a steady-state population of fluorescent and dark-states. The final phase, >1 ms, is irreversible, and thus reflects photobleaching.

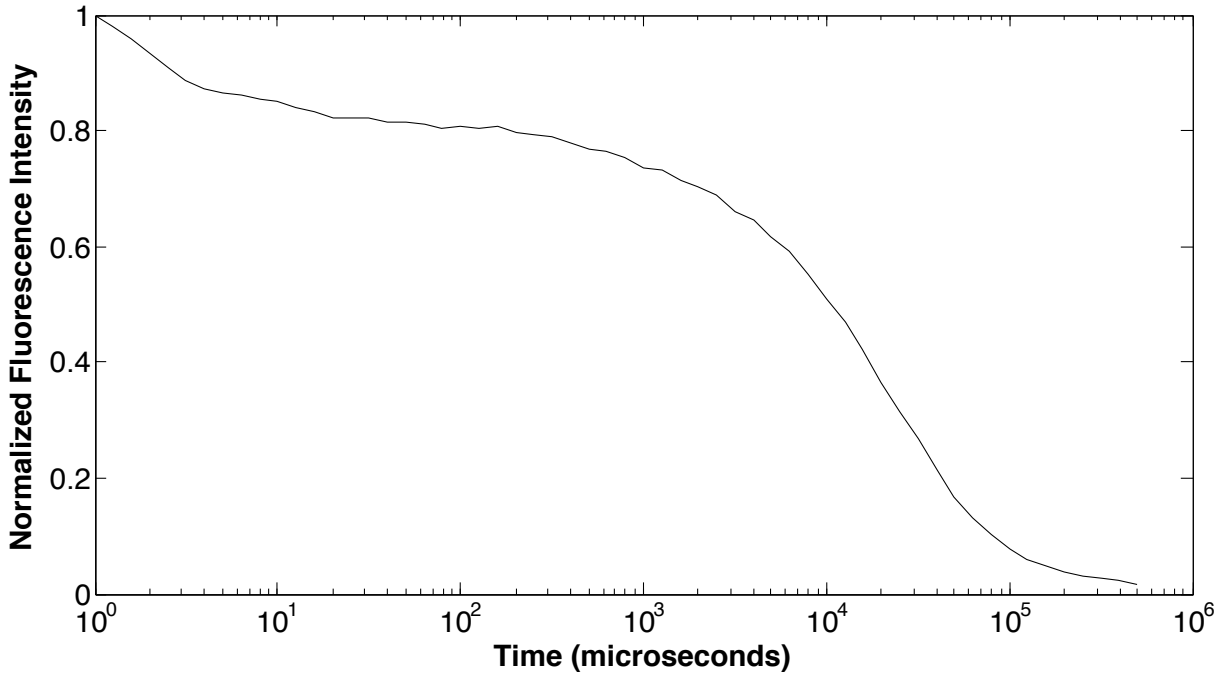

decreased fluorescence lifetime could account for improvements in photostability, a numerical simulation was performed for a simple two-state model, with ground and excited singlet-states, and a photodegradation path out of the first excited singlet-state. The rates of excitation and photodegradation were kept constant, and the amount of photodegradation was examined for different fluorescence lifetimes. Modeling suggests that in a simple 2-state system, photobleaching scales linearly with the excited-state fluorescence lifetime. All things being equal except fluorescence lifetime, we expect mCherry to photobleach $\approx 2\times$ faster than K2C. Therefore, the decreased fluorescence lifetime, in part, can explain the improved photostability of K2C.

Given that all three mutations in K2C were located in the 7/10 β-strand region, we were curious to see if decreased oxygen accessibility to the chromophore could account for the remainder of improvement. Preliminary results using molecular dynamics suggested that the mutations in K2C decreased β-strand 7 and 10 dynamics relative to mCherry (Data not shown). To evaluate this, E. coli were transformed and allowed to adhere to poly-l-lysine coated coverslips. Photobleaching was measured in a widefield illumination mode before and after continuous purging of the environment with 100 % nitrogen for anaerobic measurements, or 100 % oxygen for super-aerobic conditions. Under anaerobic conditions, both mCherry and K2C showed decreased rates of photobleaching; whereas photobleaching measurements taken in the presence of 100 % oxygen, showed photobleaching was accelerated. The results of the data remain qualitative due to a non-constant background contribution throughout the course of the measurements, and the inability to quantify aqueous oxygen concentrations. Nevertheless, the measurements highlight qualitatively the importance of molecular oxygen in photodegradation processes. Although further work is necessary to conclusively determine oxygen sensitivity, crude preliminary evidence does not suggest that oxygen access at the 7/10 β-strand can fully account for the differences in the photostability observed (Data not shown). Indeed, molecular dynamics did show alternative pathways for oxygen diffusion. Unfortunately, the oxygen sensitivity of photobleaching not only depends upon the rate of molecular collisions with oxygen, but also the excited-state lifetime of the oxygen-sensitive states (typically, the triplet state), the amount of population build-up in these states, and the rates of conversion into these states relative to the excited-state lifetime. Additionally, molecular oxygen can improve photostability in some cases, by quenching otherwise reactive triplet states [235]. Consequently, oxygen-dependent photobleaching measurements on K2C and mCherry remain inconclusive.

Figure 5.10: Fluorescence Lifetime of K2C ($\tau \approx 1.0$ ns) and mCherry ($\tau \approx 1.9$ ns). Both mCherry and K2C are predominantly described by a monoexponential decay. Fitting K2C to a biexponential decay may have revealed a longer-lived species ($\tau \approx 8$ ns), although the contribution of this spcies was negligable ($\approx 2\%$). Numerical modeling suggests that photobleaching scales linearly with the fluorescence lifetime.

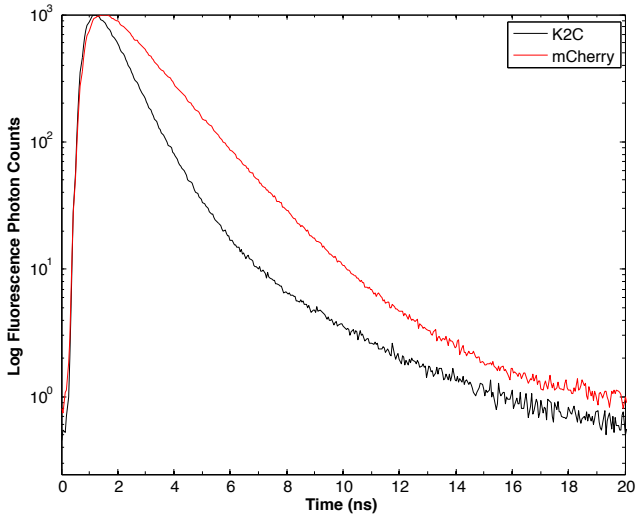

5.10 Discussion

Numerical modeling of the four-state system in Chapter 2 suggested two undesirable photophysical mechanisms that could result in a more photostable RFP. These mechanisms included rapid conversion to a photoprotective (e.g., non-absorbing) dark-state and/or rapid quenching of the first-excited singlet state [209]. Several pieces of evidence suggest that we selected for RFPs that achieve improved photostability through a photophysical mechanism that is more closely related to the latter. For example, all of the mutants identified from our first selection, despite having slower kinetics of photobleaching, have decreased fluorescence lifetimes ($\approx$ 1 ns) and quantum yields ($\approx$ 0.10). After each round of sorting, the library progressively decreased in fluorescence intensity, likely due to further enrichment of low quantum-yield mutants. When subjected to high-intensity CW photobleaching, K2C only underwent $\approx$ 20 % dark-state conversion. Although further studies would be needed to confirm if the dark-state in K2C is photoprotective or photoreactive, 20 % dark-state conversion is small in comparison to other mutants (>50 %, see Table 2.2) [209]. Lastly, further mutagenesis of the K2 and K4 mutants appeared to revert the photostability back to an mCherry-like population, while simultaneously improving the fluorescence intensity of the library (See Kriek2.1, Kriek2.2, Appendix A). If the mutations present in the K2 and K4 influenced a photodegradation pathway, presumably further mutagenesis would not entirely negate the former gains in photostability.

As mentioned previously, library design is critical to the success of a selection and/or directed-evolution process. The library discussed here, Kriek, was guided by MD simulations, mutations reported in the literature, and predominantly involved amino-acids proximal to β-strands 7 and 10 [76]. Nevertheless, the β-strand 7 and 10 interface may be the wrong region to target in RFPs, MD simulations may only approximate reality, and given that most publications attempt to improve brightness, using published mutations may have substantially biased our outcome. Indeed, the mutants discovered here all had decreased brightness, perhaps indicating that positions 143, 161, and 163 tune quantum yield of fluorescence, but remain uninvolved in photodegradation. Future libraries should seek to identify positions that alter the photostability in a manner that is independent of the fluorescence quantum yield, or synergistically improves photostability and fluorescence quantum yield. Identifying these positions is a challenging task. Selectively choosing positions

for site-directed mutagenesis requires accurate hypotheses, and accurate hypotheses necessitates an improved understanding of the mechanisms governing irreversible photobleaching. Alternatively, much of what the FP community has learned to date has arisen from random mutagenesis. However, given that a large proportion of the mutations in error-prone PCR arise in regions that do not affect the photophysics (e.g., outward facing on the β-barrel), random mutagenesis is an inefficient way to create spectroscopic diversity. Furthermore, our microfluidic cytometer has restricted throughput ($\approx$ 20,000 cells/day), thereby limiting the size of diversity that may be realistically screened. The rate of screening is dictated by the Poisson nature of cell arrival in the microfluidic laser analysis region, and is largely unavoidable. However, optical-trap induced catastrophic burning of the microfluidic device limits the duration of time that screening may be carried out. Decreases in the frequency and severity of the laser burning would enable screening for longer, and thus higher-throughput. Nevertheless, error-prone libraries, based off of a spectrum of RFPs from different backgrounds, may be the best way to proceed in the future.

The negative outcome of the Kriek selection could reflect poor library design, insufficient spectroscopic diversity, or mCherry being a poor candidate for mutagenesis. Alternatively, it could reflect insufficient selection criteria. The additional selection, K4, which included fluorescence intensity and irreversible photobleaching, did not provide any additional improvements to the outcome. Given the large distribution of fluorescence intensity for a single-FP population of cells (>200-fold), screening for fluorescence brightness in addition to irreversible photobleaching remains insufficient. A conceptual shift is necessary, with less emphasis on the rate of photobleaching, and more emphasis on the total number of photons emitted prior to photobleaching. Total photon output depends upon the extinction coefficient, quantum yield of fluorescence, and quantum yield of photobleaching. A threefold improvement in the rate of photobleaching, if accompanied by a threefold decrease in fluorescence quantum yield, results in an RFP with identical total photon output. Additionally, time spent in dark-states also contributes to a decreased fluorescence photon flux, and thus limits signal. Consequently, the quantum yield of fluorescence, the percent dark-state conversion, and the rate of irreversible photobleaching should all be actively selected for. Importantly, there are spectroscopic methods that enable this. For example, rapid dark-state conversion results in a highly asymmetric signal that can be measured in a high-throughput fashion. Fluorescence lifetime provides a proxy for fluorescence

quantum yield and can also be measured rapidly using frequency-domain fluorescence lifetime techniques. By incorporating these two additional selection mechanisms into our microfluidic cytometer, coupled with improved library design, synergistic advances in RFP photophysics should result.

5.11 Future Directions

Future work should seek to identify positions that influence the rate of photodegradation but not the fluorescence quantum yield. Several different methods should be executed in parallel. Mutating different RFP variants (e.g., mCherry vs TagRFP vs mRuby2 vs tdTomato) provides an excellent opportunity, and many of these libraries are ready for selection (See Appendix A). tdTomato is particularly promising given its large quantum yield, stabilizing dimer interface, and is less engineered relative to other RFPs (e.g., mCherry). Alternative methods for generating diversity should also be explored. Although error-prone PCR libraries remain too large given the throughput of our microfluidic device, multiple fluorescence intensity-based selections using FACS may decrease the diversity to a more realistically feasible library size (e.g., mRuby2 Error-Prone PCR library, Appendix A). Additionally, given the high likelihood of mutations being incorporated into non-photophysically relevant positions, the error-prone PCR library can be remutated following FACS-based fluorescence intensity-based enrichment. Sequential mutagenesis should increase the likelihood of functional mutations in the library prior to enrichment for photostability in our microfluidic photobleaching flow-cytometer. The photobleaching selection criteria should remain under constant analysis until it has been definitively shown to be sufficient for the generation of improved RFPs. If it is found to be insufficient, incorporation of fluorescence lifetime techniques will be necessary, which is discussed in depth in Chapter 6.

Chapter 6

Progress Towards Frequency Domain Lifetime Measurements

6.1 Abstract

Fluorescence lifetime reports on the radiative and non-radiative deactivation rates out of the excited-state, and thus provide information on the fluorescence quantum yield. This chapter discusses the development of a high-bandwidth I/Q demodulator that can rapidly measure the fluorescence lifetime in a high-throughput manner. The theory of I/Q demodulation is discussed in detail, and numerical simulations are carried out to identify the best operating conditions. By incorporating the fluorescence lifetime measurements into our microfluidic photobleaching cytometer, a multi-parametric screen for photostability and fluorescence lifetime on a known population of fluorescent proteins (TagRFP-T, mOrange2, and mCherry) identifies three distinct populations. Further work is necessary to improve the fluorescence lifetime technique, and suggestions are provided that should allow substantial progress with regard to this. Importantly, the work presented here reflects the first multi-parametric flow-cytometer in existence, and has widespread implications for other high-speed frequency-domain fluorescence lifetime measurements, including applications in imaging.

6.2 Publication Status and Author Contributions

The work presented here is unpublished.

K.M.D., J.L.L., A.E.P., and R.J. designed research. J.L.L. built intensity modulation setup. K.M.D. and J.L.L. performed research. K.M.D. performed numerical simulations and data analysis.

6.3 Introduction

Today, two methods are commonly used to measure the fluorescence lifetime, and each has their own advantages and disadvantages [109]. In the time-domain method, a laser pulse on the picosecond or faster timescale is used to synchronously excite a population of fluorophores, and the fluorescence photon arrival-time is "binned" into time-intervals relative to the excitation pulse. Over multiple laser pulse cycles, a histogram is populated that can be deconvoluted from the instrument response function, and fit to determine the fluorescence lifetime of the fluorochrome. The time-resolution for this method, referred to as time-correlated single-photon counting (TCSPC), is primarily limited by the detector photoelectron transit-time spread ($\approx$ 25 ps) [236]. However, TCSPC requires expensive instrumentation and must operate under Poisson photon counting conditions. The latter disadvantage requires that one detect less than one fluorescence photon per pulse, restricting sample, excitation, and detection conditions, and requiring longer dwell-times for accurate determination of the fluorescence lifetime.

In the frequency-domain method, a light source is modulated with a frequency of >10 MHz, and fluorescence emission, also modulating at the same frequency, is phase-shifted and the amplitude is demodulated relative to the excitation. For mono-exponential fluorescence decays, the measured phase-shift or amplitude demodulation at a single modulation frequency is sufficient to determine the fluorescence lifetime (Equation 6.5 and 6.2). Here, τ_{fl} is the fluorescence lifetime, ω is the modulation frequency in radians per second, m is the amplitude demodulation, and ϕ is the phase-shift between excitation and emission. For monoexponential decays, the lifetime from the phase-shift and the amplitude demodulation, should match. However, the primary disadvantage of frequency-domain fluorescence lifetime measurements is that for multi-exponential decays, the phase and modulation lifetimes disagree. Under these circumstances, the phase and modulation lifetimes need to be measured over a range of frequencies, and the "frequency response" of the system can then be used to determine the fluorescence lifetime. One major advantage to frequency-domain method is cost. In it's simplest implementation, it can be composed of a laser-diode or light-emitting diode, a frequency generator, a detector, a frequency mixer, and an electrical low-pass filter.

$$\tan(\phi) = \omega\tau_{fl} \tag{6.1}$$

$$m = \frac{1}{\sqrt{1+\omega^2\tau_m^2}} \tag{6.2}$$

Unlike steady-state fluorescence, the fluorescence lifetime provides unique insight into excited-state processes. For example, following absorption of a photon, a variety of non-radiative photophysical processes compete with radiative decay back to the ground state. These include internal conversion (IC), intersystem-crossing to the triplet state (ISC), resonance energy transfer (RET), photobleaching, and more. The average duration that a fluorophore spends in the excited state, also known as the fluorescence lifetime and defined as the inverse sum of all deactivation rates (Equation 6.3), is therefore a sensitive measure of the radiative and non-radiative processes. Importantly, the radiative rate for a particular fluorophore can be approximated by the Strickler-Berg equation (Equation 6.4). Here, the radiative rate is calculated by integrating over the transition from the ground singlet state to the first excited singlet state, and includes the refractive index of the solution (n^2), the extinction coefficient, absorption spectra $\epsilon(\bar{\nu})$ and emission spectra F($\bar{\nu}$), all in terms of cm^{-1}. Therefore, for chemically, and spectrally similar RFP chromophores, the radiative rate can be approximated as constant. Furthermore, given the relationship between fluorescence quantum yield (ϕ_{fl}) and fluorescence lifetime (τ_{fl}) (Equation 6.5), the fluorescence lifetime tends to increase proportionally with the quantum efficiency of fluorescence a particular RFP.

$$\tau_{fl} = (k_{rad} + k_{non-rad})^{-1} \tag{6.3}$$

$$\frac{1}{k_{rad}} = 2.88 \times 10^9 n^2 < \bar{\nu}^3 > \int \frac{\epsilon(\bar{\nu})\mathrm{d}\bar{\nu}}{\bar{\nu}} \approx 2.88 \times 10^9 n^2 \frac{\int F(\bar{\nu})\mathrm{d}\bar{\nu}}{\int F(\bar{\nu})\mathrm{d}\bar{\nu}/\bar{\nu}^3} \int \frac{\epsilon(\bar{\nu})}{\bar{\nu}}\mathrm{d}\bar{\nu} \tag{6.4}$$

$$\phi_{fl} = \frac{k_{rad}}{k_{rad} + k_{non-rad}} = k_{rad} \times \tau_{fl} \tag{6.5}$$

Both the time and frequency-domain methods have been widely used in imaging formats [237–239]. However, to date, only the frequency-domain method has been reported in flow-cytometry applications [201,

201,240]. This chapter aims to discuss progress towards the implementation of frequency-domain fluorescence lifetime methodology into our high-throughput microfluidic photobleaching cytometer. To our knowledge, by integrating fluorescence lifetime, fluorescence brightness, and irreversible photobleaching, this will be the first truly multi-parametric cell-sorter in existence. Furthermore, analogous to multidimensional NMR, additional spectroscopic dimensions will provide greater resolution, and should contribute to an improved molecular understanding of how different photophysical mechanisms act in concert. Consequently, our multi-parametric microfluidic cell-sorter should enable the generation of improved RFPs with vastly improved quantum yields and total photon outputs.

6.4 Experimental Methods

The TCSPC instrumentation used for preliminary studies has been described elsewhere [180]. All TCSPC traces were background corrected, the first nanosecond omitted to avoid complications arising from instrument response function deconvolution, and fit with a single or biexponential decay. In cases where a biexponential fit was necessary, the weighted fluorescence lifetime is reported. Proteins were purified essentially as previously described, except at pH=7.5 instead of 7.0 [209].

To measure the fluorescence lifetime of RFP expressing cells in a high-throughput fashion, we pursued a high-bandwidth frequency domain technique. A 532 nm CW laser was modulated by a resonant lithium niobate electro-optic modulator (EOM) with matched crystals to minimize thermal birefringence (ThorLabs). The EOM was driven by one output of an arbitrary waveform generator that supplied a 29.5 MHz sinusoidal waveform. The resulting frequency-modulated beam was directed through a cylindrical lens for beam-shaping and focused onto a microfluidic channel for cellular analysis using a 20x 0.45 NA microscope objective. The fluorescence was detected in the epi-direction, spectrally filtered, detected with a photomultiplier tube, and the photocurrent was immediately amplified using a custom RF-amplifier that separated the low-frequency (<1 MHz) and high-frequency (>1 MHz) frequency signals. The low-frequency component was passed to a second stage of amplification, AC-coupled, band-pass filtered, and provided a measure of the fluorescence intensity [225].

The high-frequency signal was subjected to an additional 20 dB stage of amplification and sent directly

into a custom high-bandwidth I/Q demodulator capable of operating at modulation frequencies from DC-200 MHz with dwell-times as short as 20 nanoseconds (AD8333, Analog Devices) [97]. The custom phase-detection circuitry included an optional low-phase dispersion variable-gain amplifier that was output matched to the optimal operating conditions of the I/Q demodulator. The local-oscillator of the I/Q demodulator was provided by the secondary output from the arbitrary waveform generator driving the EOM. A 16-position 22.5° toggle allows for user-specified phase-delays between the local-oscillator and the input fluorescence signal. After demodulation, the I and Q channels were low-pass filtered (user selectable cut-off frequency), digitized, and evaluated individually using custom software (LabView, National Instruments, or Matlab, Mathworks). It is worth noting that the I/Q demodulator can operate in an amplitude lock-in mode, as well as a double lock-in mode. In the double lock-in mode, the I/Q demodulator "locks-into" a high-frequency component, and a second frequency is provided to flip-flop the I and Q outputs, providing a secondary frequency component for standard lock-in amplifiers.

6.5 In Vitro Lifetime Measurements of RFPs

The Strickler-Berg equation suggests that for chemically and spectrally homologous chromophores, such as those in RFPs, the radiative rates should be similar. To evaluate this hypothesis, we measured the fluorescence lifetime using TCSPC for a spectrally diverse ensemble of RFPs, including mApple [23], mCherry [20], mKate [21], mKate2 [175], mOr1 [20], mOr2 [23], mPlum [111], mStrawberry [20], mRFP [19], TagRFP [22], and TagRFP-T [23]. A subset of the fluorescence lifetime traces is presented in Figure 6.1.

To avoid complications arising from improper deconvolution of the instrument response function and the ≈ 250 picosecond excitation pulse, the first nanosecond of the fluorescence decay was ignored. Quantum yields were obtained from reported literature values. Figure 6.2 shows the correlation between fluorescence quantum yield and fluorescence lifetime. Table 6.1 lists the RFP name, fluorescence lifetime, and quantum yield. Strong correlation between fluorescence lifetime and quantum yield was observed. According to Equation 6.5, we anticipate a linear correlation, with k_{rad} provided by the slope, and a y-intercept of zero. When fitting the correlation, we received a value of $k_{rad} = 0.17ns^{-1}$, and an $R^2 = 0.81$. If a y-offset is provided, a better fit results, with an $R^2 = 0.87$. The apparent discrepancy could be explained by the

Figure 6.1: Fluorescence lifetime decays for select mutant RFPs.

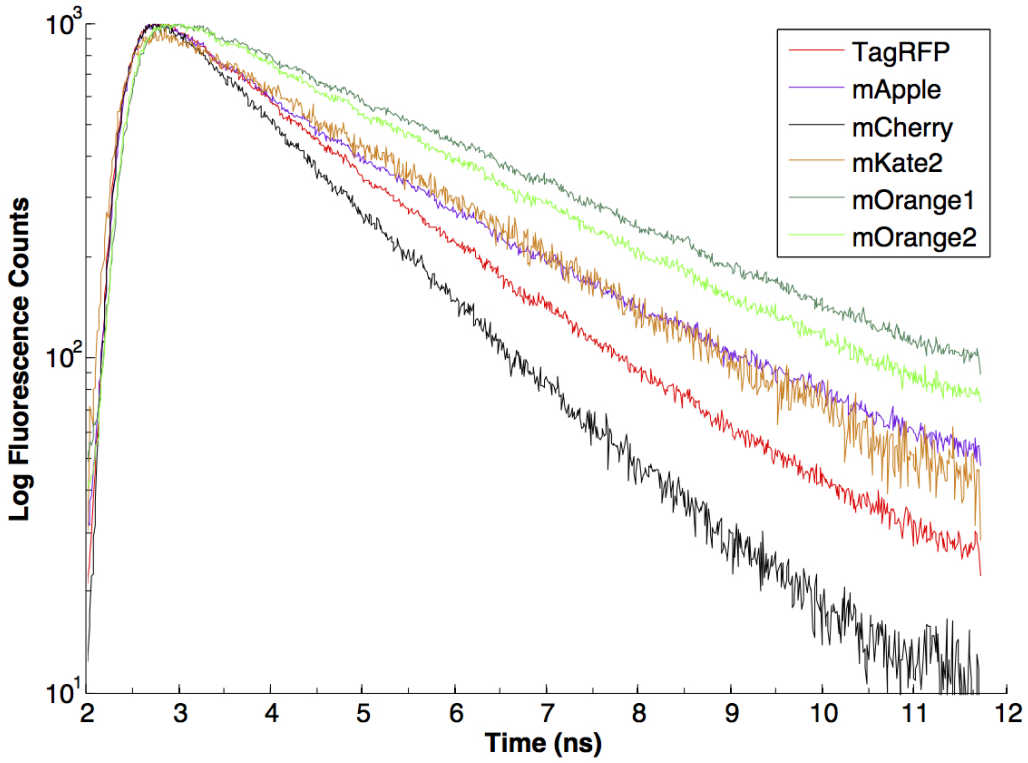

Figure 6.2: Correlation between fluorescence lifetime and quantum yield for a variety of RFP mutants.

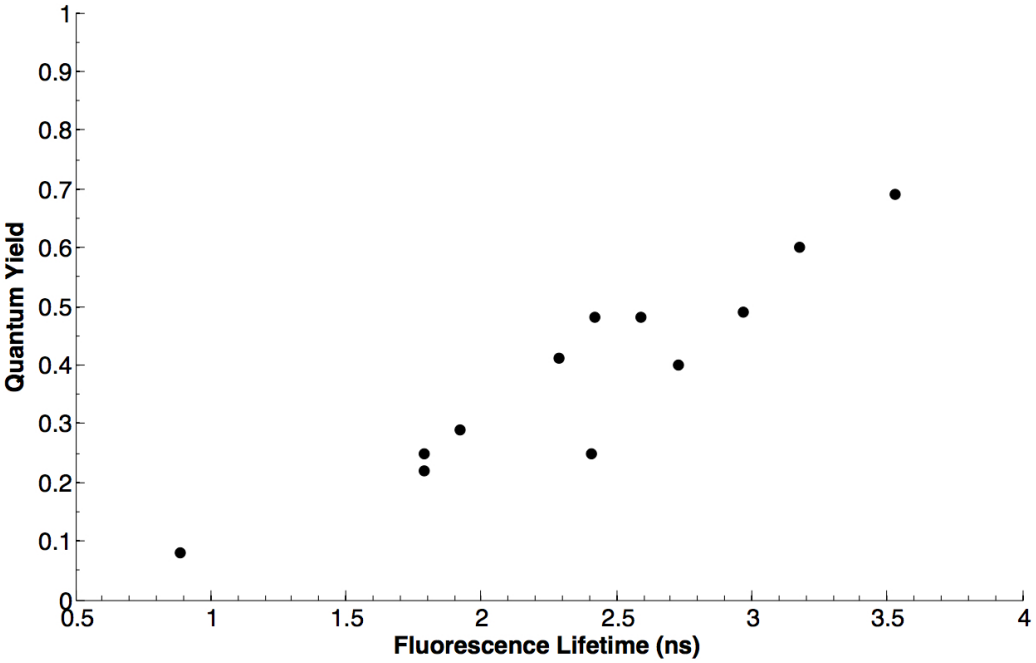

Table 6.1: Red-Fluorescent Proteins, Fluorescent Lifetimes, and Quantum Yields

RFP	Fluorescent Lifetime (ns)	Quantum Yield
mApple	2.97	0.49
mCherry	1.79	0.22
mKate2	2.73	0.40
mKate	2.41	0.25
mOrange1	3.53	0.69
mOrange2	3.18	0.60
mPlum	0.89	0.08
mStrawberry	1.92	0.29
mRFP	1.79	0.25
TagRFP-T	2.42	0.48
TagRFP	2.29	0.48

differences in the RFPs. For example, peak absorption and emission wavelengths for the RFPs studied here span a wavelength range of 547-589 nm and 562-633 nm, respectively. Furthermore a variety of chromophore states are present, including cis (e.g., mCherry, mKate), trans (e.g., TagRFP, TagRFP-T), and tricyclic (e.g., whereby the acylimine undergoes intramolecular nucleophilic attack, found in mOrange and mOrange2 [42]). Nevertheless, despite the chemical and spectral differences present in RFPs, a strong correlation exists. These results suggest that fluorescence lifetime can serve as a proxy for fluorescence quantum yield in RFPs, and that brighter RFPs could be identified through high-throughput fluorescence lifetime screens.

6.6 Simulations

A variety of simulations were carried out to better understand the frequency-domain methodology, how noise contributes to phase-detection, and to evaluate the anticipated signal waveform originating from our I/Q demodulator. The first simulation, based on a simplified two-state model consisting of the ground singlet state and first excited singlet state was evaluated essentially as described previously [209], except with sinusoidally modulated excitation. To decrease the computational demands of the simulation, the modulation frequency was decreased 10-fold, to 2 MHz, and the fluorescence lifetime was increased $\approx$ 10-fold, to 100 nanoseconds. As anticipated, a clear amplitude demodulation and phase-shift was observed (Figure 6.3). The excitation and emission waveforms were fitted with a sine wave and the phase-shift between the two waveforms permitted accurate retrieval of the 100 nanosecond fluorescence lifetime. The method proved

to be remarkably immune to noise degradation of the signal. Even at signal to noise ratios of 10 dB, the fluorescence lifetime determined by fitting of the waveform was within 2.5 % of the actual fluorescence lifetime (Figure 6.4). Furthermore, adjustment of the model to provide multi-exponential decay resulted in phase-shift that was equivalent to the weighted lifetime of each component (Figure 6.5).

Although these initial models were useful, the approach of fitting the waveform directly would require digital sampling of the signals at rates >50 MHz. Indeed, direct capture of the modulated signal has been used in flow-cytometry [201]. Alternatively, analog frequency mixing of the sample can be used to down-modulate the frequency into a more experimentally facile frequency range (heterodyne mixing), or into a DC signal (homodyne mixing). An I/Q demodulator operates on this principle, and will be explained quantitatively in the following analysis.

Accurate determination of the fluorescence lifetime necessitates a detailed understanding of the anticipated signal waveforms. Under microfluidic flow-conditions, the time-variant fluorescence signal, $I_{sig}(t)$, arising from a cell as it traverses the non-modulating excitation beam can be approximated as a Gaussian pulse, centered at time t_o, with a standard deviation σ, and a maximum fluorescence intensity of I_{max} (Equation 6.6). However, for frequency-domain lifetime measurements, the excitation beam is modulated at a high-frequency, ω, with ≈100 % depth of modulation, and a specific phase offset, ϕ_{lo} (Equation 6.7). Consequently, for a cell traversing a frequency-modulated beam, the resulting signal will be Equation 6.8, where m and ϕ_{fl} are the amplitude demodulation and fluorescence phase-shift, respectively.

$$I_{sig}(t) = I_{max} \times \exp \frac{(t - t_o)^2}{2\sigma^2} \tag{6.6}$$

$$I_{ex}(t) = 0.5 \times \Big[I_o \times \cos(\omega t - \phi_{lo}) + 1 \Big] \tag{6.7}$$

$$I_{sig}(t) = 0.5 \times \Big[I_{max} \times m \times \exp \frac{(t - t_o)^2}{2\sigma^2} \times \cos(\omega t - \phi_{lo} - \phi_{fl}) + 1 \Big] \tag{6.8}$$

An I/Q demodulator takes the complex waveform provided by Equation 6.8 and splits it into two channels. The first channel is an exact replicate of the original waveform, and is referred to as the "in-

Figure 6.3: Simulation of Frequency-Domain Lifetime Measurements. A simplified 2-state system consisting of the ground and excited singlet states was used. To decrease the computation time for the simulations, a modulation frequency of 2 MHz, and fluorescence lifetime of 100 nanoseconds were used. A phase-shift and amplitude demodulation is clearly observed. Fitting of the excitation and emission waveforms yields a phase-shift that is consistent with the simulated fluorescence lifetime.

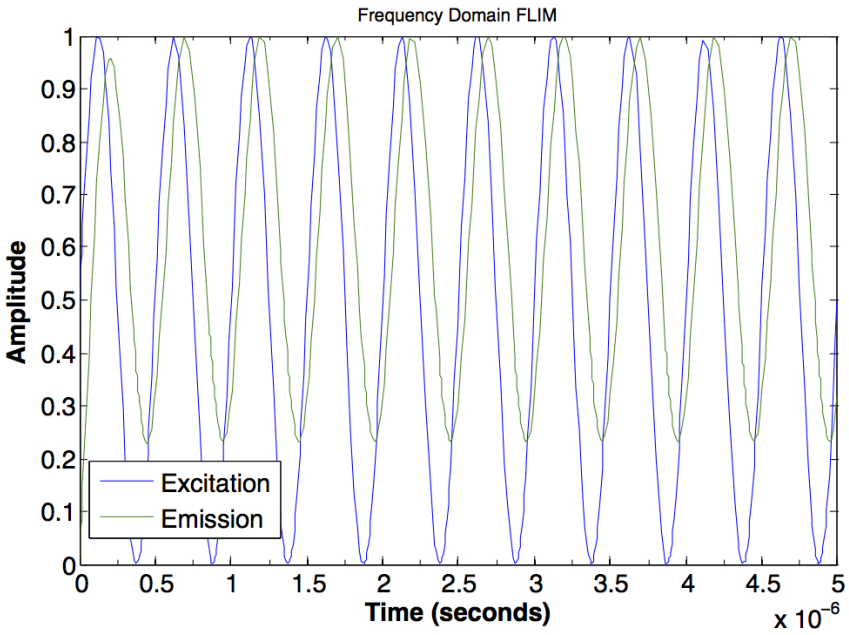

Figure 6.4: Simulation of frequency-domain lifetime measurements in the presence of noise. The reference signal, here shown as "Excitation" and the fluorescence signal were corrupted to a signal-to-noise ratio of 10 dB. Fitting of the observed waveforms and calculation of the fluorescence lifetime resulted in a lifetime within 2.5 % of the anticipated value.

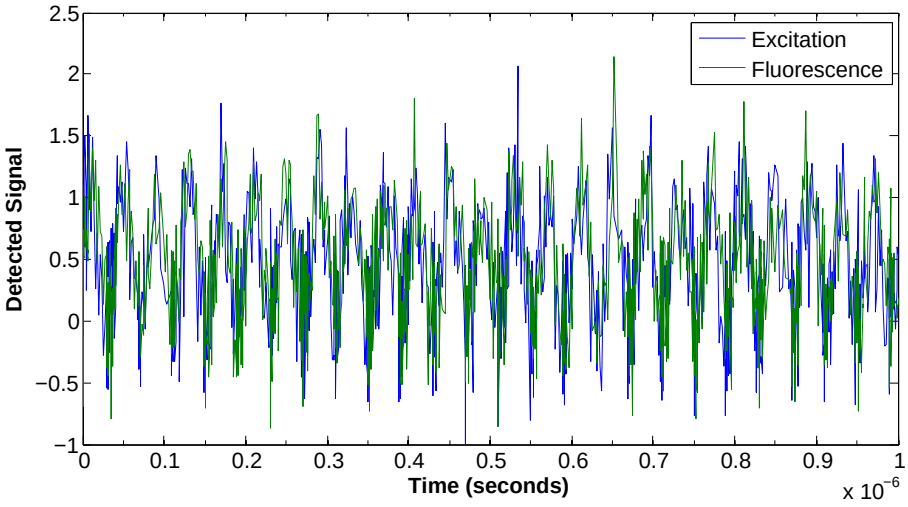

Figure 6.5: Simulation of frequency-response for biexponential fluorescence decay. The simulated decay was composed equally of 1 ns and 10 ns decays. Changing of the excitation modulation frequency resulted in the observed phase frequency-response. Calculation of the lifetime at any point along the frequency response provided the mean fluorescence lifetime of 5.5 nanoseconds.

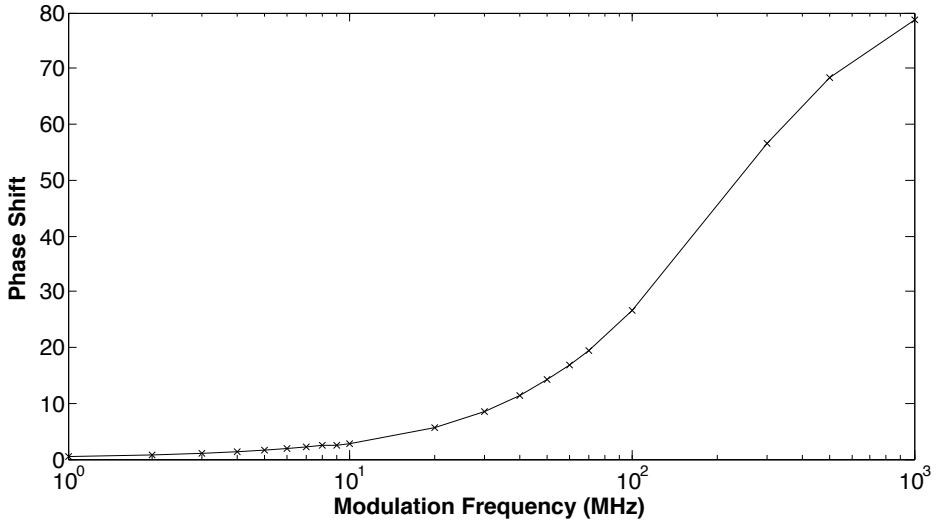

phase" or "I" channel ($I_I(t)$). The second channel is phase-shifted by $\pi/2$ relative to the original waveform, and is referred to as the "quadrature-phase" or "Q" channel ($I_Q(t)$). These signals can be visualized in "phase-space" where Q is on the ordinate, and I is on the abscissa (Figure 6.6). Homodyne frequency mixing of the in-phase and quadrature channels with the local-oscillator (Equation 6.7) creates two new waveforms, composed of the sum and difference frequency components, located at 2ω Hz. and 0 Hz., respectively. Low-pass filtering of the frequency-mixed signals eliminates the 2ω frequency component, providing in-phase and quadrature signals that depend upon the amplitude demodulation, m, the maximum intensity of the cell, I_{max}, the local-oscillator phase-shift arising from cables and electronic instrumentation, ϕ_{lo}, and the fluorescence phase-shift, ϕ_{fl} (Equations 6.9 and 6.10). The quotient of the quadrature channel and the in-phase channel eliminates the intensity and intensity demodulation contributions, providing a signal that is directly related to ϕ_{fl}, the fluorescence phase-shift (Equation 6.11).

$$\begin{aligned} I_Q(t) &= 0.5\Big[I_{max} \times m \times \exp\tfrac{(t-t_o)^2}{2\sigma^2} \times \cos(\phi_{lo} + \phi_{fl} - \tfrac{\pi}{2})\Big] \\ &= 0.5\Big[I_{max} \times m \times \exp\tfrac{(t-t_o)^2}{2\sigma^2} \times \sin(\phi_{lo} + \phi_{fl})\Big] \end{aligned} \tag{6.9}$$

$$I_I(t) = 0.5\Big[I_{max} \times m \times \exp\frac{(t-t_o)^2}{2\sigma^2} \times \sin(\phi_{lo} + \phi_{fl})\Big] \tag{6.10}$$

$$\frac{I_Q(t)}{I_I(t)} = \tan(\phi_{lo} + \phi_{fl}) \tag{6.11}$$

The in-phase and quadrature channels provide all of the necessary information to calculate the fluorescence lifetime. To better understand the anticipated output waveforms resulting from our I/Q demodulator, a numerical simulation was carried out on two non-overlapping Gaussian pulses, of different maximum amplitudes, but identical fluorescence lifetimes. The I and Q channels, given the cell intensity and frequency demodulation dependence, resembled a standard fluorescence time trace for a cell flowing through a non-modulating laser focus (Figure 6.7). The phase-signal (arctangent(Q/I)) produces a square-wave pulse with an amplitude that is independent of the cellular brightness. Importantly, this is the anticipated outcome, given that the fluorescence lifetime should remain constant, regardless of the position in the laser beam, or the relative brightness between cells. Nevertheless, taking the ratio of the Q and I channels does present

Figure 6.6: Phase-Space diagram of Q and I channels. The amplitude of the signal is represented by the vector originating form the origin, $\sqrt{I^2 + Q^2}$, and the phase is the angle between the vector and the x-axis $arctan(Q/I)$.

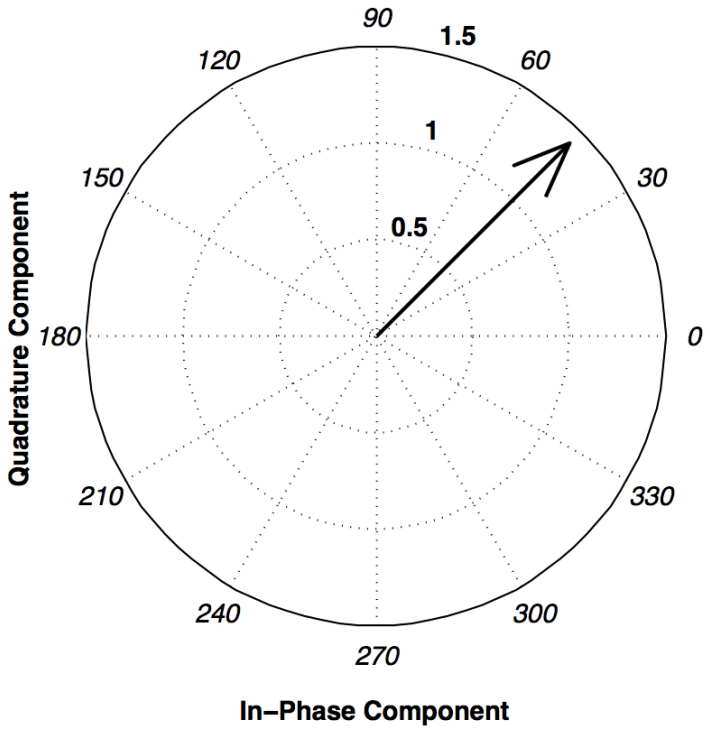

some challenges when the fluorescence signal is low, and noise contributions in each channel trigger large changes in the ratio of signals. However, integrating, or fitting the independent channels, and then taking the quotient of these measured values, decreases the noise contribution to the final outcome. Through careful analysis of the signal-processing involved in each step, and visualizing the anticipated input and output waveforms, numerical modeling permits a more rigorous and quantitative approach to experimental design.

6.7 Preliminary Results

To evaluate the performance of our I/Q demodulator, and our ability to measure fluorescence lifetime in a high-throughput fashion, initial studies were carried out on three RFP expressing cell-lines. These included TagRFP-T (ϕ_{fl}=0.48, τ_{fl}=2.42 ns), mCherry (ϕ_{fl}=0.22, τ_{fl}=1.79 ns), and mOrange2 (ϕ_{fl}=0.60, τ_{fl}=3.18 ns). Each cell-line was sequentially screened within the microfluidic under identical operating parameters on the same day. A schematic of the experimental setup is provided in Figure 6.8. Optimization of the signal in phase-space was accomplished by adjusting the user-controlled 4 bit phase-delay on the I/Q demodulator until both the I and Q channels had a maximum positive amplitude ($\approx 45^{\circ}$ in phase-space) for an RFP expressing cell-line. Following excitation with the frequency-modulated laser, the cells were also subjected to four photobleaching beams, providing multi-parametric screening of fluorescence lifetime and photobleaching. A time-trace for only the frequency-modulated detection (e.g., photobleaching beams blocked), is presented in Figure 6.9. As anticipated, the I and Q channels mirrored the fluorescence intensity channel, although with different amplitudes. Furthermore, the arctangent of the Q/I ratio provided a square-wave pulse, which is proportional to the sum of the fluorescence lifetime phase-shift and instrument arbitrary phase-shift. Importantly, no correlation was observed between the cell-intensity and the fluorescence phase-shift (TagRFP-T, R^2=0.01, n=168 cells). Each cell-line provided a unique fluorescence phase-shift and rate of irreversible photobleaching, facilitating clear differentiation of the populations. However, the rank-order of photostabilities for the RFPs, mOrange2 >mCherry >TagRFP-T, was incorrect (Figure 6.10). Under optimized photobleaching intensities, the rank-order should follow that mCherry >TagRFP-T >mOrange2. The observed phase-shifts were also reversed, with mCherry (ϕ=0.22, τ=1.79 ns) having the longest phase-shift, followed by TagRFP-T (ϕ=0.48, τ=2.42 ns), then mOrange2 (ϕ=0.60, τ=3.18 ns) (Figure 6.10). Table

Figure 6.7: Simulation of I/Q demodulation. The red-trace represents the low-frequency component obtained after low-pass filtering of the original signal. The blue and black traces are the Q and I channels, respectively. Depending upon the signals location in phase-space, these values can be either positive or negative. The phase signal, after thresholding by the original DC signal (.05 V). is shown in dashed black.

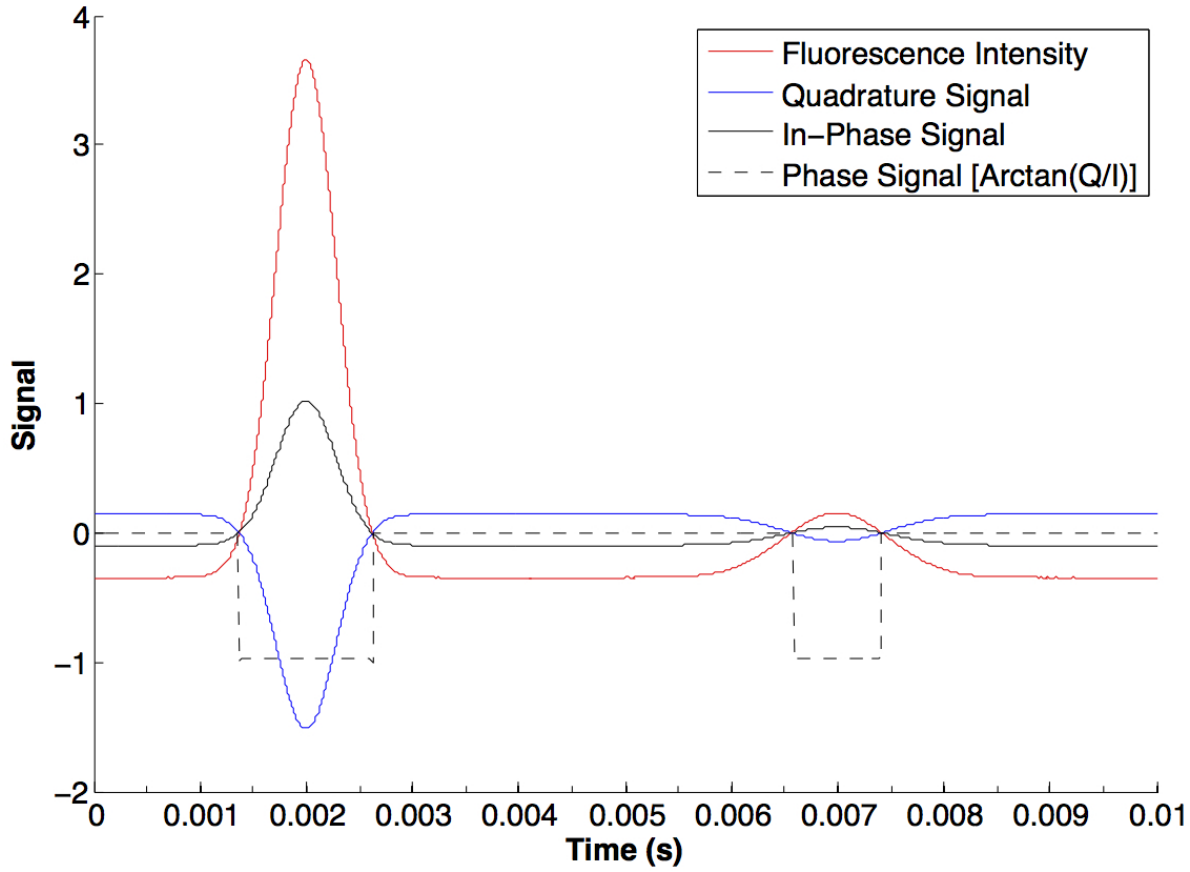

Figure 6.8: Schematic of the optical setup for the microfluidic cytometer. On the left, schematic shows cellular analysis region. Cells undergoing hydrodynamic focusing are subjected to high-frequency laser excitation ($\Delta\phi$) for the frequency-domain lifetime measurements, and subsequently a series of high-intensity photobleaching beams. Following interrogation, a high-power 1064 nm optical trap deflects the cells into the "keep" outlet or allows the cell to continue into the "discard" outlet. WLS=White light source for visualization. LPF2=Low-Pass Optical Filter. DM=Dichroic Mirror. 1064 nm laser is for optical sorting. LA=Lens Assembly. PM=Piezo-Mirror. 532 nm Lasers are for photobleaching and high-frequency modulation. L=Lens. EOM=Electro-optic modulator. SF=Spatial Filter. PD=Photodiode. BS=Beam splitter. CL=Cylindrical lens. CCD=CCD imaging detector. LPF=Long-pass optical filter. AL1=Aspheric lens.

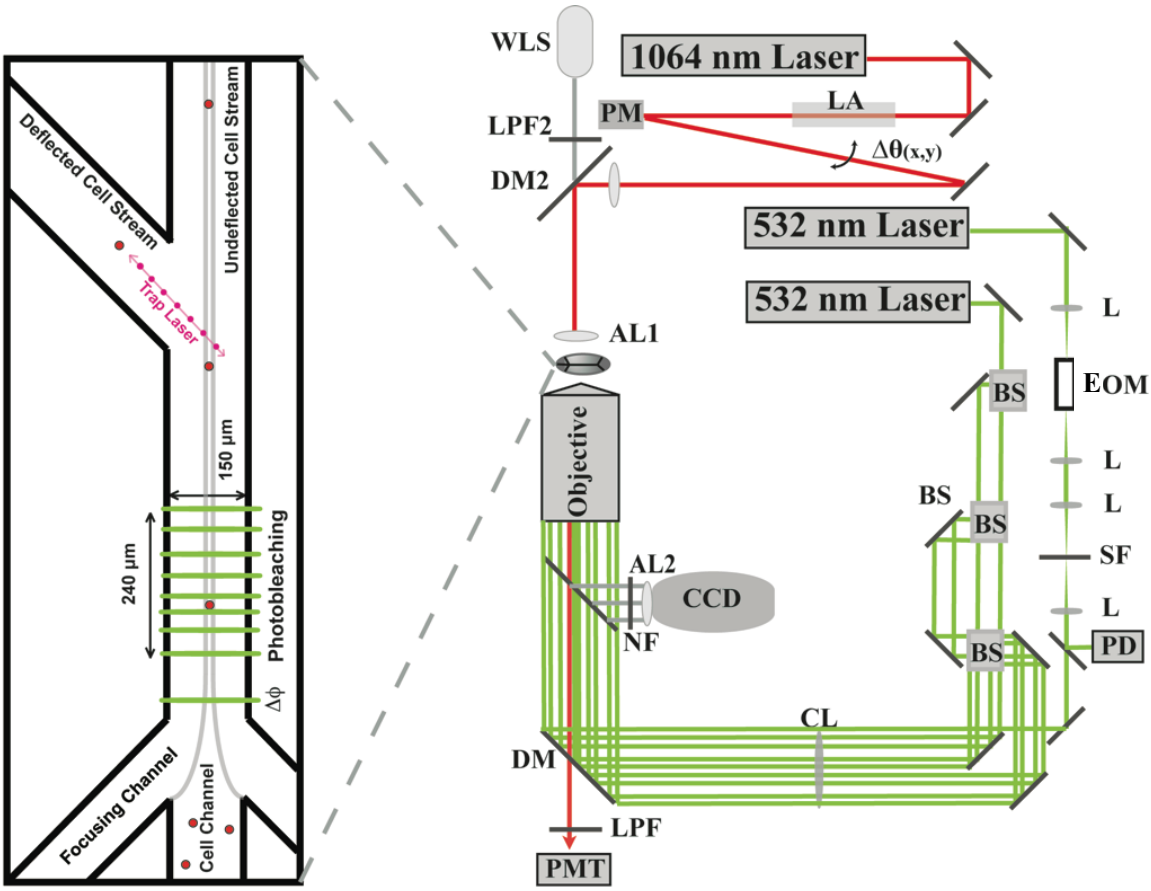

Table 6.2: Red-Fluorescent Proteins, Fluorescent Lifetimes, Quantum Yields, Mean Phase-Shift, and Coefficient of Variation (CV) of Phase Shift. The phase-shift should increase with fluorescence lifetime according to the relation $\tan(\Delta\phi_{phase}) = \omega \times \tau_{fl}$.

RFP	Fluorescent Lifetime (ns)	Quantum Yield	Mean Phase-Shift	Phase-Shift CV
mCherry	1.79	0.22	0.97	3.5 %
TagRFP-T	2.42	0.48	0.83	3.4 %
mOrange2	3.18	0.60	0.74	4.6 %

6.2 summarizes the observed phase-shifts. Potential causes for the observed phase-shifts is discussed in-depth in the discussion.

6.8 Discussion

Fluorescence-lifetime measurements provide unique insight into excited-state processes and has seen widespread adoption in spectroscopy, but remains underutilized in imaging and high-throughput formats. A major limitation of existing instrumentation, and the fundamental reason why it has not yet become more widely adopted in imaging and high-throughput applications, is the necessarily slow data-acquisition rate. For example, commercially available confocal microscopes can routinely capture multichannel images at 420 frames per second. In contrast, reported lifetime microscopes operate at 0.25 to 2 frames per second [237].[1] This chapter discusses the design and implementation of a high-speed frequency-domain fluorescence lifetime assay that could overcome many of the limitations facing fluorescence lifetime techniques. The fluorescence lifetime instrumentation developed here uses widely available radio-frequency I/Q demodulators that are found in medical imaging equipment (e.g., ultrasound), and enable high-bandwidth (50 MHz, 20 ns dwell-time) phase-detection. Consequently, in a 512×512 pixel confocal imaging format, this I/Q demodulator could improve the frame-rate 10 to 100-fold over commercially available lifetime instrumentation, so long as a sufficient signal to noise ratio is achieved.

A high-frequency intensity-modulated excitation beam was incorporated into our microfluidic photobleaching cytometer, and the fluorescence phase-shift and the rate of photobleaching was measured on mCherry, TagRFP-T, and mOrange2 expressing cell-lines (Figure 6.10). A unique phase-shift and photo-

[1] http://www.lambertinstruments.com

Figure 6.9: Time-Trace of an RFP Expressing Cell Following I/Q Demodulation. The black-curve represents the low-frequency fluorescence component as the cell traverses the frequency-modulated excitation beam. The blue and red curves are the Q and I channels, respectively. The phase-signal, shown in dashed-black, is obtained by taking the arctangent of the ratio of Q/I.

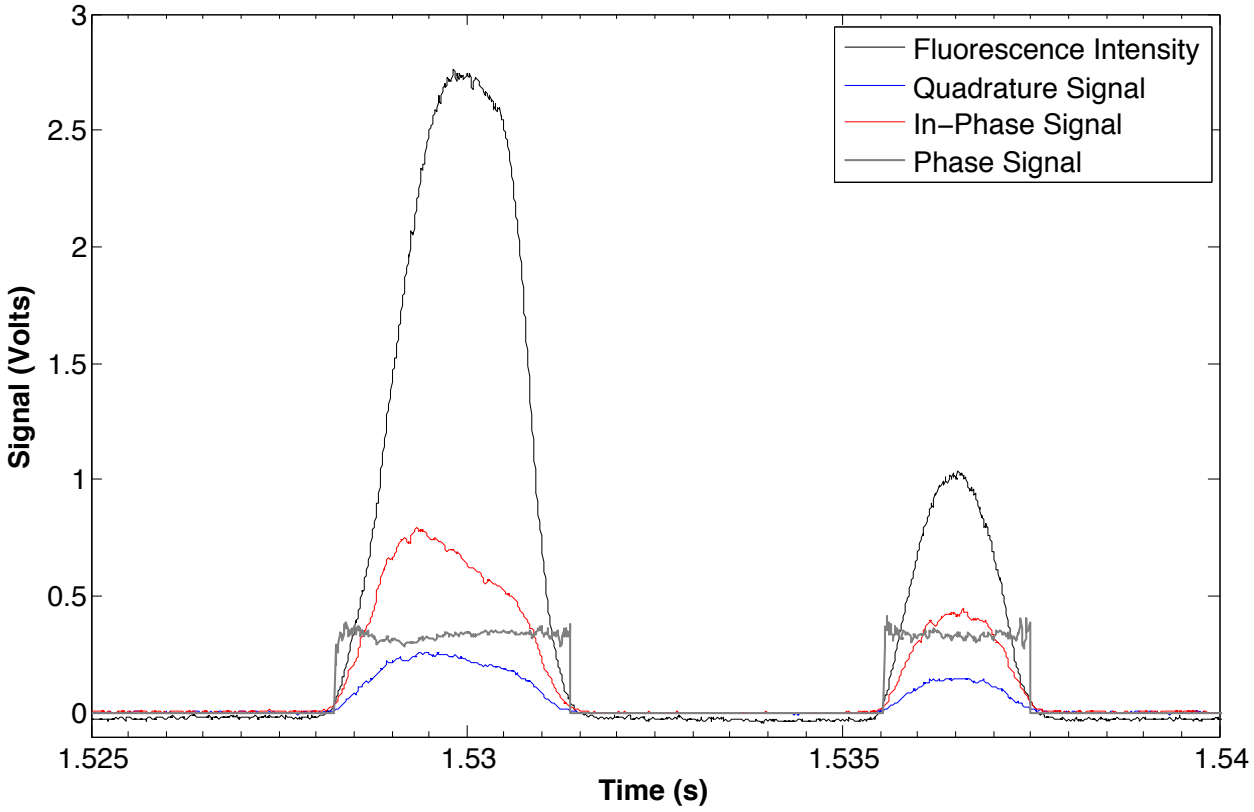

Figure 6.10: Multi-parametric photobleaching and fluorescence lifetime screen of RFP expressing cell-lines. mCherry is shown in blue, mOrange2 in red, and TagRFP-T in black. The phase-shift is uncorrected for instrument phase delays, and is therefore only relative. A much narrower distribution for each FP is observed on the photobleaching axis than the phase-axis, indicative that further work is necessary for accurate phase-shift determination.

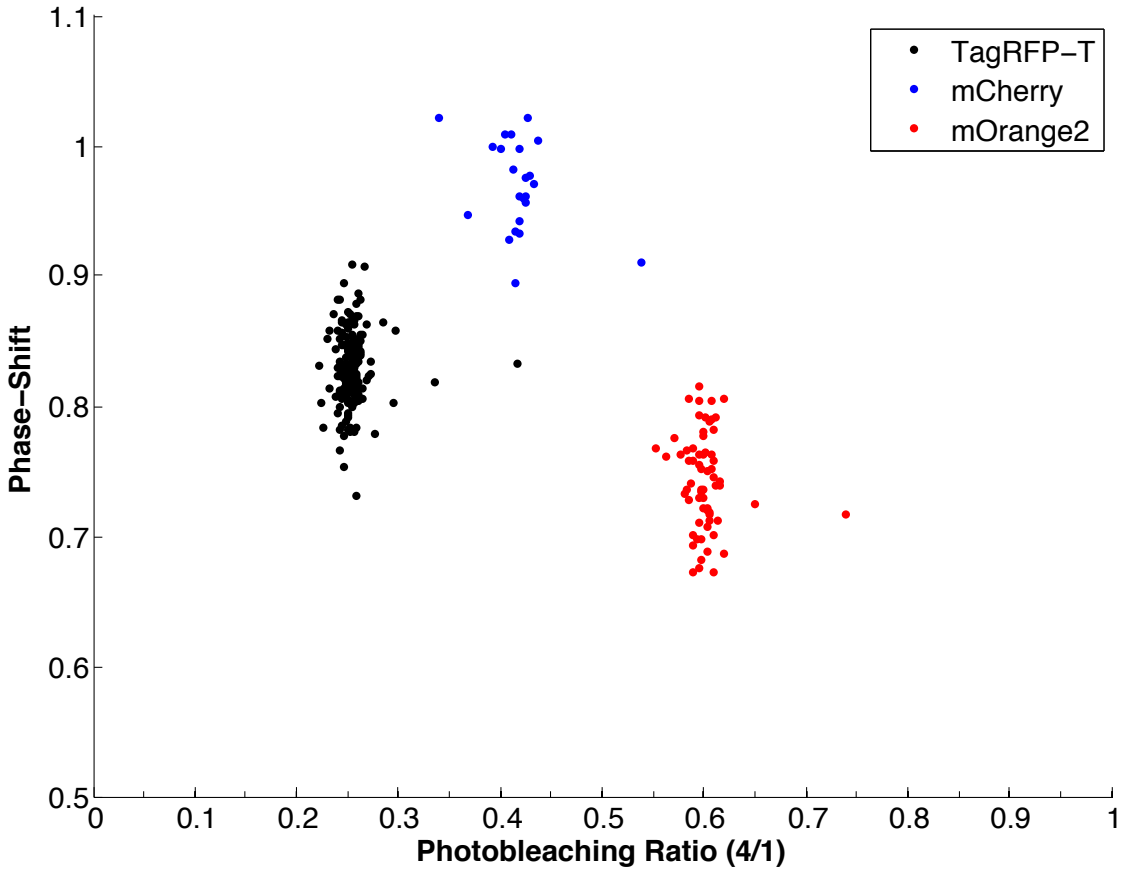

bleaching ratio was measured for the three RFP populations, and the anticipated waveform from numerical modeling agreed with the experimental waveform. Consequently, it appears that implementation of the frequency-domain fluorescence assay in the microfluidic photobleaching cytometer appears close to fruition. Unfortunately, the observed rank-order in photobleaching was incorrect, and the measured phase-shifts were reversed relative to the anticipated rank-order.

The rate of photobleaching and dark-state conversion in RFPs scales non-linearly with excitation intensity [209]. For example, and as discussed in depth in Chapter 2, mCherry was photostable at 2.5 kW/cm^2, but not 25 kW/cm^2. Furthermore, mOrange2, but not mCherry, undergoes rapid dark-state conversion. Consequently, adjustment of the laser into the correct intensity regime will likely correct the observed photostability order, as has been clearly demonstrated in Chapter 4.

The observed relative fluorescence phase-shift for the three populations, however, is incorrect. More specifically, that the rank-order of the three populations is reversed, with mCherry having the largest fluorescence phase-shift, followed by TagRFP-T, and then mOrange2 (Table 6.2). However, there are several interesting aspects to the data, that when put together, suggest a mechanism for this rank-order in fluorescence phase-shifts, and hence, fluorescence lifetimes. First, the appropriate correlations are present in the data. For example, the amplitude of the $I_I(t)$ and $I_Q(t)$ channels are directly correlated with the amplitude of the fluorescence intensity observed in the photobleaching beams. This is theoretically anticipated given the dependence of the $I_I(t)$ and $I_Q(t)$ channels on the peak fluorescence intensity, I_{max}, and the frequency-dependent amplitude demodulation term, m (Equations 6.9 and 6.10). Second, the fluorescence phase-shift for all 3 populations are uncorrelated with the peak fluorescence intensity of the cell, I_{max}, and all three populations have a unique phase-shift value. These first two points suggest that the I/Q demodulator is functioning, that it is identifying the appropriate signals, and that we are able to discriminate different RFPs based upon their fluorescence phase-shift.

However, I/Q demodulators are most sensitive when operating around 45° in phase-space, where small-changes in phase result in large changes in the amplitudes of $I_I(t)$ and $I_Q(t)$, and least sensitive when located near 0°, 90°, 180°, and 270°. Since the values for $I_I(t)$ and $I_Q(t)$ were both positive, it can be

assumed that the I/Q demodulator is operating in the upper-right quadrant of phase-space.[2] However, it is interesting to note that for mCherry, the I/Q demodulator could only measure $I_I(t)$ and $I_Q(t)$ signals for the brightest cells (average fluorescence intensity of 8.4 volts, as opposed to 6.5 volts for TagRFP-T, and 2.4 volts for mOrange2). Given that we anticipate a smaller phase-shift for mCherry relative to mOrange2, this is partially consistent with the amplitude of $I_Q(t)$ and $I_I(t)$ being linearly dependent upon on the fluorescence intensity and $\sin(\phi_{lo} + \phi_{fl})$ (Equation 6.9 and 6.10). However, we anticipate the $\sin(\phi_{lo} + \phi_{fl})$ to be a much smaller effect since mOrange2 and mCherry should only be separated by $\approx 20^\circ$ phase-shift. These observations, when placed together, suggests that mCherry was being detected in a less sensitive region of phase-space, likely closer to the abscissa, burying the signal in the output noise of the I/Q demodulator. Indeed, if the $I_I(t)$ and $I_Q(t)$ were reversed, either via hardware or software, mCherry does appear in a less-sensitive region of phase-space, and the rank-order of fluorescence phase-shift is consistent with the theoretically anticipated result. Further work is necessary to evaluate this possibility.

Several observations suggest potential mechanisms for improving the frequency-domain lifetime measurement presented here. For example, $\approx$ 85 % of the cells detected by the photobleaching beams went undetected by the I/Q demodulator. Yet, narrower distributions in the phase-shift were observed for lower excitation intensities.[3] This suggests that the amount of light exciting the sample was potentially sufficient to cause dark-state conversion, thereby changing the apparent fluorescence lifetime of the sample. Indeed, this would manifest itself as an imperfectly flat square-wave signal, or an asymmetric fluorescence signal, both of which are observable in Figure 6.9. Decreasing the excitation intensity, although appropriate for minimizing the contribution of dark-states to the measurement, is unfortunately accompanied by decreased signal amplitudes and diminished detection by the I/Q demodulator. To overcome this challenge, one or more additional stages of amplification should be provided prior to phase-detection by the I/Q demodulator. Additional amplification should not be problematic, since the I/Q demodulator only measures the signal located in the local-oscillator frequency-band, and it's double-balanced design minimizes noise contributions. Furthermore, as discussed previously, integration and division of the $I_I(t)$ and $I_Q(t)$ signals could further decrease the noise contribution to the final phase signal. Additionally, under ideal operating conditions, the

[2] One possible exception to this is if an inverting amplifier is present on the output of the I/Q demodulator.
[3] Personal communication, J.L. Lubbeck

I/Q demodulator will output an $\approx \Delta V_{Q-I} = 62$ mV signal for a 5° phase-shift. Therefore, adding an additional stage of amplification to the I/Q demodulator output, with user-adjustable DC-offsets, could provide for a greater amount of accuracy in the measured fluorescence phase-shift. Lastly, accurately correcting for the arbitrary, yet constant, phase-shift provided by the electronics will allow measurement of the fluorescence phase shift and calculation of the fluorescence lifetime for any RFP in a high-throughput manner [237].

In conclusion, we have developed a high-speed I/Q demodulator for rapid fluorescence lifetime measurements and integrated it into our microfluidic photobleaching flow cytometer. Further work is necessary to completely characterize the performance of the I/Q demodulator, but preliminary results appear promising. To our knowledge, this is the first fluorescence lifetime microfluidic cell-sorter, and the first multi-parametric cell-sorter of any kind (FACS, microfluidics, etc.). Further development of the I/Q demodulator for rapid fluorescence lifetime measurements could lead to improved imaging and high-throughput methodologies. Lastly, by selecting for RFP mutants with long fluorescence lifetimes and slow rates of photobleaching, we anticipate a deeper understanding of the molecular determinants dictating RFP photophysics, as well as the discovery of novel RFP variants with vastly improved photon outputs prior to photobleaching.

6.9 Future Directions

In the immediate future, evaluation of the whether the I and Q channels have been crossed via hardware or software, or subjected to inverting amplification, is critical. It is also necessary to decrease the observed distribution of fluorescence phase-shifts (Table 6.2, Figure 6.10). As previously discussed, slight modifications to the I/Q demodulator outputs, including further amplification, and DC-offsets, as well as integration of the I and Q channels, may decrease the distribution of fluorescence phase-shifts. Together, these suggestions stand as a good starting point for improving the fluorescence lifetime resolution of the instrumentation. Importantly, the electronic characteristics of the I/Q demodulator are known, as well as the noise contributions affiliated with our electronics (e.g., analog-to-digital converter, etc.), thereby allowing quantitative assessment of instrument performance.

Once the performance of the instrumentation has been optimized, a multi-parametric cell-sorting experiment on a mixed population of known RFPs should be executed, and the results submitted for publi-

cation. Subsequently, a multi-parametric screen, including selection criteria for fluorescence intensity, fluorescence lifetime, and rate of photobleaching, should be carried out on a RFP library. The identified mutants spectroscopic properties should then be measured, and a biological assay highlighting the improvement over existing RFPs performed. A potential assay includes high-speed volumetric mitochondrial fusion/fission imaging.

Bibliography

[1] O. Shimomura, F. H. Johnson, and Y. Saiga, "Extraction, purification and properties of aequorin, a bioluminescent protein from the luminous hydromedusan,aequorea," Journal of Cellular and Comparative Physiology, vol. 59, pp. 223–239, Jun 1962.

[2] O. Shimomura, "Structure of the chromophore of aequorea green fluorescent protein," FEBS Letters, vol. 104, pp. 220–222, Aug 1979.

[3] D. C. Prasher, V. K. Eckenrode, W. W. Ward, F. G. Prendergast, and M. J. Cormier, "Primary structure of the aequorea victoria green-fluorescent protein," Gene, vol. 111, pp. 229–233, 1992.

[4] M. Chalfie, Y. Tu, G. Euskirchen, W. Ward, and D. Prasher, "Green fluorescent protein as a marker for gene expression," Science, vol. 263, pp. 802–805, Feb 1994.

[5] R. Heim, D. C. Prasher, and R. Y. Tsien, "Wavelength mutations and posttranslational autoxidation of green fluorescent protein," Proceedings of the National Academy of Sciences, vol. 91, no. 26, pp. 12501–12504, 1994.

[6] R. Heim, A. B. Cubitt, and R. Y. Tsien, "Improved green fluorescence," Nature, vol. 373, pp. 663–664, Feb 1995.

[7] R. Heim and R. Y. Tsien, "Engineering green fluorescent protein for improved brightness, longer wavelengths and fluorescence resonance energy transfer," Current Biology, vol. 6, pp. 178–182, 1996.

[8] A. Miyawaki, J. Llopis, R. Heim, J. M. McCaffery, J. A. Adams, M. Ikura, and R. Y. Tsien, "Fluorescent indicators for ca^{2+} based on green fluorescent proteins and calmodulin," Nature, vol. 388, pp. 882–887, 1997.

[9] A. Miyawaki, O. Griesbeck, R. Heim, and R. Y. Tsien, "Dynamic and quantitative ca2+ measurements using improved cameleons," Proceedings of the National Academy of Sciences, vol. 96, pp. 2135–2140, Mar 1999.

[10] T. Pozzan, M. Zaccolo, F. De Giorgi, C. Y. Cho, L. Feng, T. Knapp, P. A. Negulescu, S. S. Taylor, and R. Y. Tsien, "A genetically encoded, fluorescent indicator for cyclic amp in living cells," Nature Cell Biology, vol. 2, pp. 25–29, Dec 1999.

[11] M. Orm, A. B. Cubitt, K. Kallio, L. A. Gross, R. Y. Tsien, and S. J. Remington, "Crystal structure of the aequorea victoria green fluorescent protein," Science, vol. 273, pp. 1392–1395, Sep 1996.

[12] F. Yang, L. G. Moss, and G. N. Phillips, "The molecular structure of green fluorescent protein," Nature Biotechnology, vol. 14, pp. 1246–1251, Oct 1996.

[13] M. V. Matz, A. F. Fradkov, Y. A. Labas, A. P. Savitsky, A. G. Zaraisky, M. L. Markelov, and S. A. Lukyanov, "Fluorescent proteins from nonbioluminescent anthozoa species.," Nature Biotechnology, vol. 17, pp. 969–973, Oct 1999.

[14] G. S. Baird, "Biochemistry, mutagenesis, and oligomerization of dsred, a red fluorescent protein from coral," Proceedings of the National Academy of Sciences, vol. 97, pp. 11984–11989, Oct 2000.

[15] L. A. Gross, "The structure of the chromophore within dsred, a red fluorescent protein from coral," Proceedings of the National Academy of Sciences, vol. 97, pp. 11990–11995, Oct 2000.

[16] D. Yarbrough, R. M. Wachter, K. Kallio, M. V. Matz, and S. J. Remington, "Refined crystal structure of dsred, a red fluorescent protein from coral, at 2.0-a resolution," Proceedings of the National Academy of Sciences, vol. 98, pp. 462–467, Jan 2001.

[17] R. Ranganathan, M. A. Wall, and M. Socolich, "The structural basis for red fluorescence in the tetrameric gfp homolog dsred," Nature Structural Biology, vol. 7, pp. 1133–1138, Dec 2000.

[18] B. J. Bevis and B. S. Glick, "Rapidly maturing variants of the discosoma red fluorescent protein (dsred)," Nature Biotechnology, vol. 20, pp. 83–87, Jan 2002.

[19] R. E. Campbell, "A monomeric red fluorescent protein," Proceedings of the National Academy of Sciences, vol. 99, pp. 7877–7882, Jun 2002.

[20] N. C. Shaner, R. E. Campbell, P. A. Steinbach, B. N. G. Giepmans, A. E. Palmer, and R. Y. Tsien, "Improved monomeric red, orange and yellow fluorescent proteins derived from discosoma sp. red fluorescent protein.," Nature Biotechnology, vol. 22, pp. 1567–1572, 2004.

[21] D. Shcherbo, E. M. Merzlyak, T. V. Chepurnykh, A. F. Fradkov, G. V. Ermakova, E. A. Solovieva, K. A. Lukyanov, E. A. Bogdanova, A. G. Zaraisky, S. Lukyanov, and et al., "Bright far-red fluorescent protein for whole-body imaging," Nature Methods, vol. 4, pp. 741–746, Aug 2007.

[22] E. M. Merzlyak, J. Goedhart, D. Shcherbo, M. E. Bulina, A. S. Shcheglov, A. F. Fradkov, A. Gaintzeva, K. A. Lukyanov, S. Lukyanov, T. W. J. Gadella, and D. M. Chudakov, "Bright monomeric red fluorescent protein with an extended fluorescence lifetime.," Nature Methods, vol. 4, pp. 555–557, 2007.

[23] N. C. Shaner, M. Z. Lin, M. R. McKeown, P. A. Steinbach, K. L. Hazelwood, M. W. Davidson, and R. Y. Tsien, "Improving the photostability of bright monomeric orange and red fluorescent proteins," Nature Methods, vol. 5, pp. 545–551, 2008.

[24] S. Kredel, K. Nienhaus, F. Oswald, M. Wolff, S. Ivanchenko, F. Cymer, A. Jeromin, F. J. Michel, K.-D. Spindler, R. Heilker, G. U. Nienhaus, and J. Wiedenmann, "Optimized and far-red-emitting variants of fluorescent protein eqfp611.," Chemistry & Biology, vol. 15, pp. 224–233, 2008.

[25] O. M. Subach, I. S. Gundorov, M. Yoshimura, F. V. Subach, J. Zhang, D. Grüenwald, E. A. Souslova, D. M. Chudakov, and V. V. Verkhusha, "Conversion of red fluorescent protein into a bright blue probe," Chemistry & Biology, vol. 15, pp. 1116–1124, Oct 2008.

[26] M. Z. Lin, M. R. McKeown, H.-L. Ng, T. A. Aguilera, N. C. Shaner, R. E. Campbell, S. R. Adams, L. A. Gross, W. Ma, T. Alber, and R. Y. Tsien, "Autofluorescent proteins with excitation in the optical window for intravital imaging in mammals," Chemistry & Biology, vol. 16, pp. 1169–1179, 2009.

[27] O. M. Subach, G. H. Patterson, L.-M. Ting, Y. Wang, J. S. Condeelis, and V. V. Verkhusha, "A photoswitchable orange-to-far-red fluorescent protein, psmorange," Nature Methods, vol. 8, pp. 771–777, Jul 2011.

[28] D. P. Barondeau, "Mechanism and energetics of green fluorescent protein chromophore synthesis revealed by trapped intermediate structures," Proceedings of the National Academy of Sciences, vol. 100, pp. 12111–12116, Oct 2003.

[29] L. J. Pouwels, L. Zhang, N. H. Chan, P. C. Dorrestein, and R. M. Wachter, "Kinetic isotope effect studies on the de novo rate of chromophore formation in fast- and slow-maturing gfp variants," Biochemistry, vol. 47, pp. 10111–10122, Sep 2008.

[30] V. V. Verkhusha, D. M. Chudakov, N. G. Gurskaya, S. Lukyanov, and K. A. Lukyanov, "Common pathway for the red chromophore formation in fluorescent proteins and chromoproteins," Chemistry & Biology, vol. 11, pp. 845–854, Jun 2004.

[31] O. M. Subach, V. N. Malashkevich, W. D. Zencheck, K. S. Morozova, K. D. Piatkevich, S. C. Almo, and V. V. Verkhusha, "Structural characterization of acylimine-containing blue and red chromophores in mtagbfp and tagrfp fluorescent proteins," Chemistry & Biology, vol. 17, pp. 333–341, Apr 2010.

[32] S. Pletnev, F. V. Subach, Z. Dauter, A. Wlodawer, and V. V. Verkhusha, "Understanding blue-to-red conversion in monomeric fluorescent timers and hydrolytic degradation of their chromophores," Journal of the American Chemical Society, vol. 132, pp. 2243–2253, Feb 2010.

[33] R. M. Wachter, J. L. Watkins, and H. Kim, "Mechanistic diversity of red fluorescence acquisition by gfp-like proteins," Biochemistry, vol. 49, pp. 7417–7427, Sep 2010.

[34] R. L. Strack, D. E. Strongin, L. Mets, B. S. Glick, and R. J. Keenan, "Chromophore formation in dsred occurs by a branched pathway," Journal of the American Chemical Society, vol. 132, pp. 8496–8505, Jun 2010.

[35] J. L. Tubbs, J. A. Tainer, and E. D. Getzoff, "Crystallographic structures of discosoma red fluorescent protein with immature and mature chromophores: Linking peptide bond trans?cis isomerization and acylimine formation in chromophore maturation," Biochemistry, vol. 44, pp. 9833–9840, Jul 2005.

[36] W. Tomosugi, T. Matsuda, T. Tani, T. Nemoto, I. Kotera, K. Saito, K. Horikawa, and T. Nagai, "An ultramarine fluorescent protein with increased photostability and ph insensitivity," Nature Methods, vol. 6, pp. 351–353, Apr 2009.

[37] M. A. Mena, T. P. Treynor, S. L. Mayo, and P. S. Daugherty, "Blue fluorescent proteins with enhanced brightness and photostability from a structurally targeted library," Nature Biotechnology, vol. 24, pp. 1569–1571, Nov 2006.

[38] G.-J. Kremers, J. Goedhart, D. J. van den Heuvel, H. C. Gerritsen, and T. W. J. Gadella, "Improved green and blue fluorescent proteins for expression in bacteria and mammalian cells," Biochemistry, vol. 46, pp. 3775–3783, Mar 2007.

[39] M. A. Rizzo, G. H. Springer, B. Granada, and D. W. Piston, "An improved cyan fluorescent protein variant useful for fret," Nature Biotechnology, vol. 22, pp. 445–449, Feb 2004.

[40] J. Goedhart, L. van Weeren, M. A. Hink, N. O. E. Vischer, K. Jalink, and T. W. J. Gadella, "Bright cyan fluorescent protein variants identified by fluorescence lifetime screening," Nature Methods, vol. 7, pp. 137–139, Jan 2010.

[41] J. Goedhart, D. von Stetten, M. Noirclerc-Savoye, M. Lelimousin, L. Joosen, M. A. Hink, L. van Weeren, T. W. Gadella, and A. Royant, "Structure-guided evolution of cyan fluorescent proteins towards a quantum yield of 93%," Nature Communications, vol. 3, p. 751, Mar 2012.

[42] X. Shu, N. C. Shaner, C. A. Yarbrough, R. Y. Tsien, and S. J. Remington, "Novel chromophores and buried charges control color in mfruits.," Biochemistry, vol. 45, no. 32, pp. 9639–9647, 2006.

[43] S. KARASAWA, T. ARAKI, T. NAGAI, H. MIZUNO, and A. MIYAWAKI, "Cyan-emitting and orange-emitting fluorescent proteins as a donor/acceptor pair for fluorescence resonance energy transfer," Biochemical Journal, vol. 381, pp. 307–312, 2004.

[44] A. Kikuchi, E. Fukumura, S. Karasawa, H. Mizuno, A. Miyawaki, and Y. Shiro, "Structural characterization of a thiazoline-containing chromophore in an orange fluorescent protein, monomeric kusabira orange," Biochemistry, vol. 47, pp. 11573–11580, Nov 2008.

[45] K. Nienhaus, "Structural basis for photo-induced protein cleavage and green-to-red conversion of fluorescent protein eosfp," Proceedings of the National Academy of Sciences, vol. 102, pp. 9156–9159, Jun 2005.

[46] J. Wiedenmann, S. Ivanchenko, F. Oswald, F. Schmitt, C. Röcker, A. Salih, K.-D. Spindler, , and G. U. Nienhaus, "Eosfp, a fluorescent marker protein with uv-inducible green-to-red fluorescence conversion," Proceedings of the National Academy of Sciences, vol. 101, pp. 15905–15910, Nov 2004.

[47] H. Mizuno, T. K. Mal, K. L. Tong, R. Ando, T. Furuta, M. Ikura, and A. Miyawaki, "Photo-induced peptide cleavage in the green-to-red conversion of a fluorescent protein," Molecular Cell, vol. 12, pp. 1051–1058, 2003.

[48] R. Ando, H. Hama, M. Yamamoto-Hino, H. Mizuno, and A. Miyawaki, "An optical marker based on the uv-induced green-to-red photoconversion of a fluorescent protein," Proceedings of the National Academy of Sciences, vol. 99, pp. 12651–12656, Sep 2002.

[49] H. Niwa, S. Inouye, T. Hirano, T. Matsuno, S. Kojima, M. Kubota, M. Ohashi, and F. Tsuji, "Chemical nature of the light emitter of the aequorea green?fluorescent?protein," Proceedings of the National Academy of Sciences, vol. 93, no. 24, pp. 13617–13622, 1996.

[50] P. Abbyad, W. Childs, X. Shi, and S. G. Boxer, "Dynamic stokes shift in green fluorescent protein variants.," Proceedings of the National Academy of Sciences, vol. 104, pp. 20189–20194, 2007.

[51] R. M. Wachter, M.-A. Elsliger, K. Kallio, G. T. Hanson, and S. J. Remington, "Structural basis of spectral shifts in the yellow-emission variants of green fluorescent protein," Structure, vol. 6, pp. 1267–1277, 1998.

[52] O. Griesbeck, G. S. Baird, R. E. Campbell, D. A. Zacharias, and R. Y. Tsien, "Reducing the environmental sensitivity of yellow fluorescent protein. mechanism and applications," Journal of Biological Chemistry, vol. 276, pp. 29188–29194, 2001.

[53] D. Shcherbo, I. I. Shemiakina, A. V. Ryabova, K. E. Luker, B. T. Schmidt, E. A. Souslova, T. V. Gorodnicheva, L. Strukova, K. M. Shidlovskiy, O. V. Britanova, and et al., "Near-infrared fluorescent proteins," Nature Methods, vol. 7, pp. 827–829, Sep 2010.

[54] M. Chattoraj, B. A. King, G. U. Bublitz, and S. G. Boxer., "Ultra-fast excited state dynamics in green fluorescent protein: multiple states and proton transfer.," Proceedings of the National Academy of Sciences, vol. 93, pp. 8362–8367, 1996.

[55] C. Fang, R. R. Frontiera, R. Tran, and R. A. Mathies, "Mapping gfp structure evolution during proton transfer with femtosecond raman spectroscopy," Nature, vol. 462, pp. 200–204, Nov 2009.

[56] O. Zapata-Hommer and O. Griesbeck, "Efficiently folding and circularly permuted variants of the sapphire mutant of gfp," BMC Biotechnology, vol. 3, no. 1, p. 5, 2003.

[57] K. D. Piatkevich, V. N. Malashkevich, S. C. Almo, and V. V. Verkhusha, "Engineering espt pathways based on structural analysis of lssmkate red fluorescent proteins with large stokes shift," Journal of the American Chemical Society, vol. 132, pp. 10762–10770, Aug 2010.

[58] K. D. Piatkevich, J. Hulit, O. M. Subach, B. Wu, A. Abdulla, J. E. Segall, and V. V. Verkhusha, "Monomeric red fluorescent proteins with a large stokes shift," Proceedings of the National Academy of Sciences, vol. 107, pp. 5369–5374, Mar 2010.

[59] M. Drobizhev, S. Tillo, N. S. Makarov, T. E. Hughes, and A. Rebane, "Color hues in red fluorescent proteins are due to internal quadratic stark effect.," The Journal of Physical Chemistry B, vol. 113, pp. 12860–12864, 2009.

[60] M. Drobizhev, T. E. Hughes, Y. Stepanenko, P. Wnuk, O. Kieran, J. N. Scott, P. R. Callis, A. Mikhaylov, L. Dokken, and A. Rebane, "Primary role of the chromophore bond length alternation in reversible photoconversion of red fluorescence proteins," Scientific Reports, vol. 2, Sep 2012.

[61] M. Andresen, M. C. Wahl, A. C. Stiel, F. Gr ater, L. V. Sch afer, S. Trowitzsch, G. Weber, C. Eggeling, H. Grubm uller, S. W. Hell, and S. Jakobs, "Structure and mechanism of the reversible photoswitch of a fluorescent protein," Proceedings of the National Academy of Sciences, vol. 102, pp. 13070–13074, Sep 2005.

[62] M. Andresen, A. C. Stiel, S. Trowitzsch, G. Weber, C. Eggeling, M. C. Wahl, S. W. Hell, and S. Jakobs, "Structural basis for reversible photoswitching in dronpa," Proceedings of the National Academy of Sciences, vol. 104, pp. 13005–13009, Aug 2007.

[63] P. Carpentier, S. Violot, L. Blanchoin, and D. Bourgeois, "Structural basis for the phototoxicity of the fluorescent protein killerred," FEBS Letters, vol. 583, pp. 2839–2842, Sep 2009.

[64] S. Pletnev, N. G. Gurskaya, N. V. Pletneva, K. A. Lukyanov, D. M. Chudakov, V. I. Martynov, V. O. Popov, M. V. Kovalchuk, A. Wlodawer, Z. Dauter, and V. Pletnev, "Structural basis for phototoxicity of the genetically encoded photosensitizer killerred," The Journal of Biological Chemistry, vol. 284, no. 46, pp. 32028–32039, 2009.

[65] M. E. Bulina, D. M. Chudakov, O. V. Britanova, Y. G. Yanushevich, D. B. Staroverov, T. V. Chepurnykh, E. M. Merzlyak, M. A. Shkrob, S. Lukyanov, and K. A. Lukyanov, "A genetically encoded photosensitizer," Nature Biotechnology, vol. 24, pp. 95–99, Dec 2005.

[66] G. H. Patterson and J. Lippincott-Schwartz., "A photoactivatable gfp for selective photolabeling of proteins and cells," Science, vol. 297, pp. 1873–1877, Sep 2002.

[67] J. J. van Thor, T. Gensch, K. J. Hellingwerf, and L. N. Johnson, "Phototransformation of green fluorescent protein with uv and visible light leads to decarboxylation of glutamate 222," Nature Structural Biology, vol. 9, pp. 37–41, Dec 2001.

[68] G.-J. Kremers, K. L. Hazelwood, C. S. Murphy, M. W. Davidson, and D. W. Piston, "Photoconversion in orange and red fluorescent proteins," Nature Methods, vol. 6, pp. 355–358, Apr 2009.

[69] F. V. Subach and V. V. Verkhusha, "Chromophore transformations in red fluorescent proteins," Chemical Reviews, vol. 112, pp. 4308–4327, Jul 2012.

[70] T. Nagai, K. Ibata, E. S. Park, M. Kubota, K. Mikoshiba, and A. Miyawaki, "A variant of yellow fluorescent protein with fast and efficient maturation for cell-biological applications," Nature Biotechnology, vol. 20, pp. 87–90, Jan 2002.

[71] A. Rekas, J.-R. Alattia, T. Nagai, A. Miyawaki, and M. Ikura, "Crystal structure of venus, a yellow fluorescent protein with improved maturation and reduced environmental sensitivity," The Journal of Biological Chemistry, vol. 277, no. 52, pp. 50573–50578, 2002.

[72] J.-D. Pédelacq, S. Cabantous, T. Tran, T. C. Terwilliger, and G. S. Waldo, "Engineering and characterization of a superfolder green fluorescent protein," Nature Biotechnology, vol. 24, pp. 79–88, Dec 2005.

[73] S. Cabantous, T. C. Terwilliger, and G. S. Waldo, "Protein tagging and detection with engineered self-assembling fragments of green fluorescent protein," Nature Biotechnology, vol. 23, pp. 102–107, Dec 2004.

[74] M. S. Lawrence, K. J. Phillips, and D. R. Liu, "Supercharging proteins can impart unusual resilience," Journal of the American Chemical Society, vol. 129, pp. 10110–10112, Aug 2007.

[75] A. G. Evdokimov, M. E. Pokross, N. S. Egorov, A. G. Zaraisky, I. V. Yampolsky, E. M. Merzlyak, A. N. Shkoporov, I. Sander, K. A. Lukyanov, and D. M. Chudakov, "Structural basis for the fast maturation of arthropoda green fluorescent protein," EMBO reports, vol. 7, pp. 1006–1012, Aug 2006.

[76] P. P. Chapagain, C. K. Regmi, and W. Castillo, "Fluorescent protein barrel fluctuations and oxygen diffusion pathways in mcherry," The Journal of Chemical Physics, vol. 135, no. 23, p. 235101, 2011.

[77] K. Mauring, J. Deich, F. I. Rosell, T. B. McAnaney, W. E. Moerner, and S. G. Boxer, "Enhancement of the fluorescence of the blue fluorescent proteins by high pressure or low temperature," The Journal of Physical Chemistry B, vol. 109, pp. 12976–12981, Jul 2005.

[78] A. Keppler, S. Gendreizig, T. Gronemeyer, H. Pick, H. Vogel, and K. Johnsson, "A general method for the covalent labeling of fusion proteins with small molecules in vivo," Nature Biotechnology, vol. 21, pp. 86–89, Dec 2002.

[79] S.-H. Shim, C. Xia, G. Zhong, H. P. Babcock, J. C. Vaughan, B. Huang, X. Wang, C. Xu, G.-Q. Bi, and X. Zhuang, "Super-resolution fluorescence imaging of organelles in live cells with photoswitchable membrane probes," Proceedings of the National Academy of Sciences, vol. 109, pp. 13978–13983, Aug 2012.

[80] J. C. Vaughan, S. Jia, and X. Zhuang, "Ultrabright photoactivatable fluorophores created by reductive caging," Nature Methods, vol. 9, pp. 1181–1184, Oct 2012.

[81] L. M. Wysocki, J. B. Grimm, A. N. Tkachuk, T. A. Brown, E. Betzig, and L. D. Lavis, "Facile and general synthesis of photoactivatable xanthene dyes," Angewandte Chemie International Edition, vol. 50, pp. 11206–11209, Nov 2011.

[82] R. Y. Tsien, "A non-disruptive technique for loading calcium buffers and indicators into cells," Nature, vol. 290, pp. 527–528, Apr 1981.

[83] E. Tomat, E. M. Nolan, J. Jaworski, and S. J. Lippard, "Organelle-specific zinc detection using zinpyr-labeled fusion proteins in live cells," Journal of the American Chemical Society, vol. 130, pp. 15776–15777, Nov 2008.

[84] R. Civitelli, B. J. Bacskai, M. P. Mahaut-Smith, S. R. Adams, L. V. Avioli, and R. Y. Tsien, "Single-cell analysis of cyclic amp response to parathyroid hormone in osteoblastic cells," Journal of Bone and Mineral Research, vol. 9, pp. 1407–1417, Sep 1994.

[85] Q. T. Nguyen, E. S. Olson, T. A. Aguilera, T. Jiang, M. Scadeng, L. G. Ellies, and R. Y. Tsien, "Surgery with molecular fluorescence imaging using activatable cell-penetrating peptides decreases residual cancer and improves survival," Proceedings of the National Academy of Sciences, vol. 107, pp. 4317–4322, Mar 2010.

[86] J. F. Buckman, H. Hernandez, G. J. Kress, T. V. Votyakova, S. Pal, and I. J. Reynolds, "Mitotracker labeling in primary neuronal and astrocytic cultures: influence of mitochondrial membrane potential and oxidants," Journal of Neuroscience Methods, vol. 104, pp. 165–176, 2001.

[87] S. L. Sensi, D. Ton-That, J. H. Weiss, A. Rothe, and K. R. Gee, "A new mitochondrial fluorescent zinc sensor," Cell Calcium, vol. 34, pp. 281–284, 2003.

[88] M. Howarth, "Targeting quantum dots to surface proteins in living cells with biotin ligase," Proceedings of the National Academy of Sciences, vol. 102, pp. 7583–7588, May 2005.

[89] I. Chen, M. Howarth, W. Lin, and A. Y. Ting, "Site-specific labeling of cell surface proteins with biophysical probes using biotin ligase," Nature Methods, vol. 2, pp. 99–104, Jan 2005.

[90] R. H. Newman, M. D. Fosbrink, and J. Zhang, "Genetically encodable fluorescent biosensors for tracking signaling dynamics in living cells," Chemical Reviews, vol. 111, pp. 3614–3666, May 2011.

[91] J. Livet, T. A. Weissman, H. Kang, R. W. Draft, J. Lu, R. A. Bennis, J. R. Sanes, and J. W. Lichtman, "Transgenic strategies for combinatorial expression of fluorescent proteins in the nervous system," Nature, vol. 450, pp. 56–62, Nov 2007.

[92] L. Tian, S. A. Hires, T. Mao, D. Huber, M. E. Chiappe, S. H. Chalasani, L. Petreanu, J. Akerboom, S. A. McKinney, E. R. Schreiter, and et al., "Imaging neural activity in worms, flies and mice with improved gcamp calcium indicators," Nature Methods, vol. 6, pp. 875–881, Nov 2009.

[93] D. J. Wallace, S. M. zum Alten Borgloh, S. Astori, Y. Yang, M. Bausen, S. Kgler, A. E. Palmer, R. Y. Tsien, R. Sprengel, J. N. D. Kerr, and et al., "Single-spike detection in vitro and in vivo with a genetic ca2+ sensor," Nature Methods, vol. 5, pp. 797–804, Aug 2008.

[94] G. S. Harms, L. Cognet, P. H. M. Lommerse, G. A. Blab, and T. Schmidt, "Autofluorescent proteins in single-molecule research: applications to live cell imaging microscopy.," Biophysical Journal, vol. 80, pp. 2396–2408, 2001.

[95] L. Zhang, H. N. Patel, J. W. Lappe, and R. M. Wachter, "Reaction progress of chromophore biogenesis in green fluorescent protein," Journal of the American Chemical Society, vol. 128, pp. 4766–4772, Apr 2006.

[96] C. W. Freudiger, W. Min, B. G. Saar, S. Lu, G. R. Holtom, C. He, J. C. Tsai, J. X. Kang, and X. S. Xie, "Label-free biomedical imaging with high sensitivity by stimulated raman scattering microscopy," Science, vol. 322, pp. 1857–1861, Dec 2008.

[97] B. G. Saar, C. W. Freudiger, J. Reichman, C. M. Stanley, G. R. Holtom, and X. S. Xie, "Video-rate molecular imaging in vivo with stimulated raman scattering," Science, vol. 330, pp. 1368–1370, Dec 2010.

[98] M. Bannwarth, I. R. Corra, M. Sztretye, S. Pouvreau, C. Fellay, A. Aebischer, L. Royer, E. Ros, and K. Johnsson, "Indo-1 derivatives for local calcium sensing," ACS Chemical Biology, vol. 4, pp. 179–190, Mar 2009.

[99] M. Kamiya and K. Johnsson, "Localizable and highly sensitive calcium indicator based on a bodipy fluorophore," Analytical Chemistry, vol. 82, pp. 6472–6479, Aug 2010.

[100] T. Klein, A. Lschberger, S. Proppert, S. Wolter, S. van de Linde, and M. Sauer, "Live-cell dstorm with snap-tag fusion proteins," Nature Methods, vol. 8, pp. 7–9, Jan 2011.

[101] B. Hein, K. I. Willig, C. A. Wurm, V. Westphal, S. Jakobs, and S. W. Hell, "Stimulated emission depletion nanoscopy of living cells using snap-tag fusion proteins," Biophysical Journal, vol. 98, pp. 158–163, Jan 2010.

[102] C. Uttamapinant, K. A. White, H. Baruah, S. Thompson, M. Fernández-Suárez, S. Puthenveetil, and A. Y. Ting, "A fluorophore ligase for site-specific protein labeling inside living cells," Proceedings of the National Academy of Sciences, vol. 107, no. 24, pp. 10914–10919, 2010.

[103] C. Uttamapinant, A. Tangpeerachaikul, S. Grecian, S. Clarke, U. Singh, P. Slade, K. R. Gee, and A. Y. Ting, "Fast, cell-compatible click chemistry with copper-chelating azides for biomolecular labeling," Angewandte Chemie, pp. n/a–n/a, May 2012.

[104] B. A. Griffin, "Specific covalent labeling of recombinant protein molecules inside live cells," Science, vol. 281, pp. 269–272, Jul 1998.

[105] S. R. Adams, R. E. Campbell, L. A. Gross, B. R. Martin, G. K. Walkup, Y. Yao, J. Llopis, and R. Y. Tsien, "New biarsenical ligands and tetracysteine motifs for protein labeling in vitro and in vivo: Synthesis and biological applications," Journal of the American Chemical Society, vol. 124, pp. 6063–6076, May 2002.

[106] O. Tour, S. R. Adams, R. A. Kerr, R. M. Meijer, T. J. Sejnowski, R. W. Tsien, and R. Y. Tsien, "Calcium green flash as a genetically targeted small-molecule calcium indicator," Nature Chemical Biology, vol. 3, pp. 423–431, Jun 2007.

[107] K. M. Marks, M. Rosinov, and G. P. Nolan, "In vivo targeting of organic calcium sensors via genetically selected peptides," Chemistry & Biology, vol. 11, pp. 347–356, Mar 2004.

[108] S. Habuchi, M. Cotlet, T. Gensch, T. Bednarz, S. Haber-Pohlmeier, J. Rozenski, G. Dirix, J. Michiels, J. Vanderleyden, J. Heberle, and et al., "Evidence for the isomerization and decarboxylation in the photoconversion of the red fluorescent protein dsred," Journal of the American Chemical Society, vol. 127, pp. 8977–8984, Jun 2005.

[109] J. R. Lakowicz, Principles of fluorescence spectroscopy. Springer, 2006.

[110] J. J. van Thor and J. T. Sage, "Charge transfer in green fluorescent protein," Photochemical & Photobiological Sciences, vol. 5, no. 6, p. 597, 2006.

[111] L. Wang, "Evolution of new nonantibody proteins via iterative somatic hypermutation," Proceedings of the National Academy of Sciences, vol. 101, pp. 16745–16749, Nov 2004.

[112] N. O. Alieva, K. A. Konzen, S. F. Field, E. A. Meleshkevitch, M. E. Hunt, V. Beltran-Ramirez, D. J. Miller, J. Wiedenmann, A. Salih, M. V. Matz, and H. A. El-Shemy, "Diversity and evolution of coral fluorescent proteins," PLoS ONE, vol. 3, 2008.

[113] A. M. Bogdanov, E. A. Bogdanova, D. M. Chudakov, T. V. Gorodnicheva, S. Lukyanov, and K. A. Lukyanov, "Cell culture medium affects gfp photostability: a solution," Nature Methods, vol. 6, pp. 859–860, Dec 2009.

[114] J. Vogelsang, R. Kasper, C. Steinhauer, B. Person, M. Heilemann, M. Sauer, and P. Tinnefeld, "A reducing and oxidizing system minimizes photobleaching and blinking of fluorescent dyes," Angewandte Chemie International Edition, vol. 47, pp. 5465–5469, Jul 2008.

[115] G. Donnert, C. Eggeling, and S. W. Hell, "Major signal increase in fluorescence microscopy through dark-state relaxation," Nature Methods, vol. 4, pp. 81–86, 2007.

[116] J. N. Henderson, H.-w. Ai, R. E. Campbell, and S. J. Remington, "Structural basis for reversible photobleaching of a green fluorescent protein homologue," Proceedings of the National Academy of Sciences, vol. 104, pp. 6672–6677, Apr 2007.

[117] R. M. Dickson, A. B. Cubitt, R. Y. Tsien, and W. E. Moerner, "On/off blinking and switching behaviour of single molecules of green fluorescent protein.," Nature, vol. 388, pp. 355–358, 1997.

[118] Y.-T. Kao, X. Zhu, and W. Min, "Protein-flexibility mediated coupling between photoswitching kinetics and surrounding viscosity of a photochromic fluorescent protein," Proceedings of the National Academy of Sciences, vol. 109, pp. 3220–3225, Feb 2012.

[119] X. X. Zhou, H. K. Chung, A. J. Lam, and M. Z. Lin, "Optical control of protein activity by fluorescent protein domains," Science, vol. 338, pp. 810–814, Nov 2012.

[120] F. V. Subach, K. D. Piatkevich, and V. V. Verkhusha, "Directed molecular evolution to design advanced red fluorescent proteins," Nature Methods, vol. 8, pp. 1019–1026, Nov 2011.

[121] W. P. C. Stemmer, "Rapid evolution of a protein in vitro by dna shuffling," Nature, vol. 370, pp. 389–391, Aug 1994.

[122] H. Zhao, L. Giver, Z. Shao, J. A. Affholter, and F. H. Arnold, "Molecular evolution by staggered extension process (step) in vitro recombination," Nature Biotechnology, vol. 16, pp. 258–261, Mar 1998.

[123] A. Crameri, E. A. Whitehorn, E. Tate, and W. P. Stemmer, "Improved green fluorescent protein by molecular evolution using dna shuffling," Nature Biotechnology, vol. 14, pp. 315–319, Mar 1996.

[124] A. W. Nguyen and P. S. Daugherty, "Evolutionary optimization of fluorescent proteins for intracellular fret," Nature Biotechnology, vol. 23, pp. 355–360, Feb 2005.

[125] H. Hoi, N. C. Shaner, M. W. Davidson, C. W. Cairo, J. Wang, and R. E. Campbell, "A monomeric photoconvertible fluorescent protein for imaging of dynamic protein localization," Journal of Molecular Biology, vol. 401, pp. 776–791, Sep 2010.

[126] C. Kiss, J. Temirov, L. Chasteen, G. S. Waldo, and A. R. Bradbury, "Directed evolution of an extremely stable fluorescent protein," Protein Engineering Design and Selection, vol. 22, pp. 313–323, Feb 2009.

[127] M. Dai, H. E. Fisher, J. Temirov, C. Kiss, M. E. Phipps, P. Pavlik, J. H. Werner, and A. R. Bradbury, "The creation of a novel fluorescent protein by guided consensus engineering," Protein Engineering Design and Selection, vol. 20, pp. 69–79, Feb 2007.

[128] T. P. Treynor, C. L. Vizcarra, D. Nedelcu, and S. L. Mayo, "Computationally designed libraries of fluorescent proteins evaluated by preservation and diversity of function," Proceedings of the National Academy of Sciences, vol. 104, pp. 48–53, Jan 2007.

[129] R. A. Chica, M. M. Moore, B. D. Allen, and S. L. Mayo, "Generation of longer emission wavelength red fluorescent proteins using computationally designed libraries," Proceedings of the National Academy of Sciences, vol. 107, pp. 20257–20262, Nov 2010.

[130] F. H. Arnold and G. Georgiou, eds., Directed Evolution Library Creation: Methods and Protocols, vol. 231 of Methods in Molecular Biology. Humana Press, 2003.

[131] H. wang Ai, J. N. Henderson, S. J. Remington, and R. E. Campbell, "Directed evolution of a monomeric, bright and photostable version of clavularia cyan fluorescent protein: structural characterization and applications in fluorescence imaging," Biochemical Journal, vol. 400, pp. 531–540, 2006.

[132] F. V. Subach, G. H. Patterson, S. Manley, J. M. Gillette, J. Lippincott-Schwartz, and V. V. Verkhusha, "Photoactivatable mcherry for high-resolution two-color fluorescence microscopy," Nature Methods, vol. 6, pp. 153–159, Jan 2009.

[133] F. V. Subach, G. H. Patterson, M. Renz, J. Lippincott-Schwartz, and V. V. Verkhusha, "Bright monomeric photoactivatable red fluorescent protein for two-color super-resolution sptpalm of live cells," Journal of the American Chemical Society, vol. 132, pp. 6481–6491, May 2010.

[134] F. V. Subach, L. Zhang, T. W. Gadella, N. G. Gurskaya, K. A. Lukyanov, and V. V. Verkhusha, "Red fluorescent protein with reversibly photoswitchable absorbance for photochromic fret," Chemistry & Biology, vol. 17, pp. 745–755, Jul 2010.

[135] R. L. Strack, D. E. Strongin, D. Bhattacharyya, W. Tao, A. Berman, H. E. Broxmeyer, R. J. Keenan, and B. S. Glick, "A noncytotoxic dsred variant for whole-cell labeling," Nature Methods, vol. 5, pp. 955–957, Oct 2008.

[136] G. S. Waldo, B. M. Standish, J. Berendzen, and T. C. Terwilliger, "Rapid protein-folding assay using green fluorescent protein," Nature Biotechnology, vol. 17, pp. 691–695, Jul 1999.

[137] J. U. Peled, F. L. Kuang, M. D. Iglesias-Ussel, S. Roa, S. L. Kalis, M. F. Goodman, and M. D. Scharff, "The biochemistry of somatic hypermutation," Annual Review of Immunology, vol. 26, pp. 481–511, Apr 2008.

[138] K. M. Esvelt, J. C. Carlson, and D. R. Liu, "A system for the continuous directed evolution of biomolecules," Nature, vol. 472, pp. 499–503, Apr 2011.

[139] H. Y. Park, X. Qiu, E. Rhoades, J. Korlach, L. W. Kwok, W. R. Zipfel, W. W. Webb, and L. Pollack, "Achieving uniform mixing in a microfluidic device: Hydrodynamic focusing prior to mixing," Analytical Chemistry, vol. 78, pp. 4465–4473, Jul 2006.

[140] P. A. Sims, W. J. Greenleaf, H. Duan, and X. S. Xie, "Fluorogenic dna sequencing in pdms microreactors," Nature Methods, vol. 8, pp. 575–580, Jun 2011.

[141] Y. Rondelez, G. Tresset, K. V. Tabata, H. Arata, H. Fujita, S. Takeuchi, and H. Noji, "Microfabricated arrays of femtoliter chambers allow single molecule enzymology," Nature Biotechnology, vol. 23, pp. 361–365, Feb 2005.

[142] D. Huh, B. D. Matthews, A. Mammoto, M. Montoya-Zavala, H. Y. Hsin, and D. E. Ingber, "Reconstituting organ-level lung functions on a chip," Science, vol. 328, pp. 1662–1668, Jun 2010.

[143] S. Nagrath, L. V. Sequist, S. Maheswaran, D. W. Bell, D. Irimia, L. Ulkus, M. R. Smith, E. L. Kwak, S. Digumarthy, A. Muzikansky, and et al., "Isolation of rare circulating tumour cells in cancer patients by microchip technology," Nature, vol. 450, pp. 1235–1239, Dec 2007.

[144] H. C. Fan, J. Wang, A. Potanina, and S. R. Quake, "Whole-genome molecular haplotyping of single cells," Nature Biotechnology, vol. 29, pp. 51–57, Dec 2010.

[145] M. M. Wang, E. Tu, D. E. Raymond, J. M. Yang, H. Zhang, N. Hagen, B. Dees, E. M. Mercer, A. H. Forster, I. Kariv, and et al., "Microfluidic sorting of mammalian cells by optical force switching," Nature Biotechnology, vol. 23, pp. 83–87, Dec 2004.

[146] K. Ahn, C. Kerbage, T. P. Hunt, R. M. Westervelt, D. R. Link, and D. A. Weitz, "Dielectrophoretic manipulation of drops for high-speed microfluidic sorting devices," Applied Physics Letters, vol. 88, no. 2, p. 024104, 2006.

[147] T. Franke, S. Braunmller, L. Schmid, A. Wixforth, and D. A. Weitz, "Surface acoustic wave actuated cell sorting (sawacs)," Lab on a Chip, vol. 10, no. 6, p. 789, 2010.

[148] M. V. Patel, A. R. Tovar, and A. P. Lee, "Lateral cavity acoustic transducer as an on-chip cell/particle microfluidic switch," Lab on a Chip, vol. 12, no. 1, p. 139, 2011.

[149] H. Sugino, K. Ozaki, Y. Shirasaki, T. Arakawa, S. Shoji, and T. Funatsu, "On-chip microfluidic sorting with fluorescence spectrum detection and multiway separation," Lab on a Chip, vol. 9, no. 9, p. 1254, 2009.

[150] C. F. Zhong, E. R. Tkaczyk, T. Thomas, J. Y. Ye, A. Myc, A. U. Bielinska, Z. Cao, I. Majoros, B. Keszler, J. R. Baker, and et al., "Quantitative two-photon flow cytometryin vitro and in vivo," Journal of Biomedical Optics, vol. 13, no. 3, p. 034008, 2008.

[151] H. Ma, E. A. Gibson, P. J. Dittmer, R. Jimenez, and A. E. Palmer, "High-throughput examination of fluorescence resonance energy transfer-detected metal-ion response in mammalian cells," Journal of the American Chemical Society, vol. 134, pp. 2488–2491, Feb 2012.

[152] H.-W. Wang, N. Bao, T. L. Le, C. Lu, and J.-X. Cheng, "Microfluidic cars cytometry," Opt. Express, vol. 16, pp. 5782–5789, Apr 2008.

[153] S. L. Anna, N. Bontoux, and H. A. Stone, "Formation of dispersions using flow focusing in microchannels," Applied Physics Letters, vol. 82, no. 3, p. 364, 2003.

[154] E. Brouzes, M. Medkova, N. Savenelli, D. Marran, M. Twardowski, J. B. Hutchison, J. M. Rothberg, D. R. Link, N. Perrimon, and M. L. Samuels, "Droplet microfluidic technology for single-cell high-throughput screening," Proceedings of the National Academy of Sciences, vol. 106, pp. 14195–14200, Aug 2009.

[155] J.-C. Baret, O. J. Miller, V. Taly, M. Ryckelynck, A. El-Harrak, L. Frenz, C. Rick, M. L. Samuels, J. B. Hutchison, J. J. Agresti, and et al., "Fluorescence-activated droplet sorting (fads): efficient microfluidic cell sorting based on enzymatic activity," Lab on a Chip, vol. 9, no. 13, p. 1850, 2009.

[156] J. J. Agresti, E. Antipov, A. R. Abate, K. Ahn, A. C. Rowat, J.-C. Baret, M. Marquez, A. M. Klibanov, A. D. Griffiths, and D. A. Weitz, "Ultrahigh-throughput screening in drop-based microfluidics for directed evolution," Proceedings of the National Academy of Sciences, vol. 107, pp. 4004–4009, Mar 2010.

[157] L. Granieri, J.-C. Baret, A. D. Griffiths, and C. A. Merten, "High-throughput screening of enzymes by retroviral display using droplet-based microfluidics," Chemistry & Biology, vol. 17, pp. 229–235, Mar 2010.

[158] B. K. McKenna, J. G. Evans, M. C. Cheung, and D. J. Ehrlich, "A parallel microfluidic flow cytometer for high-content screening," Nature Methods, vol. 8, pp. 401–403, Apr 2011.

[159] J. Widengren, A. Chmyrov, C. Eggeling, P.-. L ofdahl, and C. A. M. Seidel, "Strategies to improve photostabilities in ultrasensitive fluorescence spectroscopy," The Journal of Physical Chemistry A, vol. 111, pp. 429–440, Jan 2007.

[160] Y. Chen, J. D. Mu uller, P. T. C. So, , and E. Gratton, "The photon counting histogram in fluorescence fluctuation spectroscopy," Biophysical Journal, vol. 77, pp. 553–567, 1999.

[161] M. Drobizhev, N. S. Makarov, T. Hughes, and A. Rebane, "Resonance enhancement of two-photon absorption in fluorescent proteins," The Journal of Physical Chemistry B, vol. 111, pp. 14051–14054, Dec 2007.

[162] M. Drobizhev, S. Tillo, N. S. Makarov, T. E. Hughes, and A. Rebane, "Absolute two-photon absorption spectra and two-photon brightness of orange and red fluorescent proteins," The Journal of Physical Chemistry B, vol. 113, pp. 855–859, Jan 2009.

[163] E. Gatzogiannis, X. Zhu, Y.-T. Kao, and W. Min, "Observation of frequency-domain fluorescence anomalous phase advance due to dark-state hysteresis," The Journal of Physical Chemistry Letters, vol. 2, pp. 461–466, Mar 2011.

[164] Y. Fu, J. Zhang, and J. R. Lakowicz, "Metal-enhanced fluorescence of single green fluorescent protein (gfp)," Biochemical and Biophysical Research Communications, vol. 376, pp. 712–717, Nov 2008.

[165] J. W. Taraska, M. C. Puljung, and W. N. Zagotta, "Short-distance probes for protein backbone structure based on energy transfer between bimane and transition metal ions," Proceedings of the National Academy of Sciences, vol. 106, pp. 16227–16232, Sep 2009.

[166] W. Min, S. Lu, S. Chong, R. Roy, G. R. Holtom, and X. S. Xie, "Imaging chromophores with undetectable fluorescence by stimulated emission microscopy," Nature, vol. 461, pp. 1105–1109, Oct 2009.

[167] V. Ntziachristos, "Going deeper than microscopy: the optical imaging frontier in biology," Nature Methods, vol. 7, pp. 603–614, Jul 2010.

[168] A. A. Heikal, S. T. Hess, G. S. Baird, R. Y. Tsien, and W. W. Webb, "Molecular spectroscopy and dynamics of intrinsically fluorescent proteins: coral red (dsred) and yellow (citrine).," Proceedings of the National Academy of Sciences, vol. 97, pp. 11996–12001, 2000.

[169] P. Schwille, S. Kummer, A. A. Heikal, W. E. Moerner, and W. W. Webb, "Fluorescence correlation spectroscopy reveals fast optical excitation-driven intramolecular dynamics of yellow fluorescent proteins.," Proceedings of the National Academy of Sciences, vol. 97, pp. 151–156, 2000.

[170] U. Haupts, S. Maiti, P. Schwille, and W. W. Webb, "Dynamics of fluorescence fluctuations in green fluorescent protein observed by fluorescence correlation spectroscopy," Proceedings of the National Academy of Sciences, vol. 95, pp. 13573–13578, 1998.

[171] K. Mudalige, S. Habuchi, P. M. Goodwin, R. K. Pai, F. D. Schryver, and M. Cotlet, "Photophysics of the red chromophore of hcred: Evidence for cis-trans isomerization and protonation-state changes.," The Journal of Physical Chemistry B, vol. 114, pp. 4678–4685, 2010.

[172] J. Hendrix, C. Flors, P. Dedecker, J. Hofkens, and Y. Engelborghs, "Dark states in monomeric red fluorescent proteins studied by fluorescence correlation and single molecule spectroscopy.," Biophysical Journal, vol. 94, pp. 4103–4113, 2008.

[173] F. Malvezzi-Campeggi, M. Jahnz, K. G. Heinze, P. Dittrich, and P. Schwille, "Light-induced flickering of dsred provides evidence for distinct and interconvertible fluorescent states.," Biophysical Journal, vol. 81, pp. 1776–1785, 2001.

[174] A. Schenk, S. Ivanchenko, C. Rocker, J. Wiedenmann, and G. U. Nienhaus, "Photodynamics of red fluorescent proteins studied by fluorescence correlation spectroscopy.," Biophysical Journal, vol. 86, pp. 384–394, 2004.

[175] S. Pletnev, D. Shcherbo, D. M. Chudakov, N. Pletneva, E. M. Merzlyak, A. Wlodawer, Z. Dauter, and V. Pletnev, "A crystallographic study of bright far-red fluorescent protein mkate reveals ph-induced cis-trans isomerization of the chromophore.," Journal of Biological Chemistry, vol. 283, pp. 28980–28987, 2008.

[176] M. Chalfie and S. R. Kain, Green Fluorescent Protein: Properties, Applications, and Protocols, vol. 47. Wiley-Interscience, second ed., 2005.

[177] T. Karstens and K. Kobs, "Rhodamine-b and rhodamine-101 as reference substances for fluorescence quantum yield measurements.," The Journal of Physical Chemistry, vol. 84, pp. 1871–1872, 1980.

[178] D. Magde, J. H. Brannon, T. L. Cremers, and J. Olmsted, "Absolute luminescence yield of cresyl violet - standard for the red.," The Journal of Physical Chemistry, vol. 83, pp. 696–699, 1979.

[179] F. Mueller, P. Wach, and J. G. McNally, "Evidence for a common mode of transcription factor interaction with chromatin as revealed by improved quantitative fluorescence recovery after photobleaching.," Biophysical Journal, vol. 94, pp. 3323–3339, 2008.

[180] J. L. Fiore, J. H. Hodak, O. Piestert, C. D. Downey, and D. J. Nesbitt, "Monovalent and divalent promoted gaaa tetraloop-receptor tertiary interactions from freely diffusing single-molecule studies.," Biophysical Journal, vol. 95, pp. 3892–3905, 2008.

[181] J. C. Butcher, Numerical methods for ordinary differential equations. Wiley, 2008.

[182] A. C. Hindmarsh, P. N. Brown, K. E. Grant, S. L. Lee, R. Serban, D. E. Shumaker, and C. S. Woodward, "Sundials: Suite of nonlinear and differential/algebraic equation solvers.," ACM Transactions on Mathematical Software, vol. 31, pp. 363–396, 2005.

[183] K. Nienhaus, H. Nar, R. Heilker, J. Wiedenmann, and G. U. Nienhaus, "Trans-cis isomerization is responsible for the red-shifted fluorescence in variants of the red fluorescent protein eqfp611.," Journal of the American Chemical Society, vol. 130, pp. 12578–12579, 2008.

[184] W. Yan, D. Xie, and J. Zeng, "The 559-to-600 nm shift observed in red fluorescent protein eqfp611 is attributed to cis-trans isomerization of the chromophore in an anionic protein pocket.," PhysChemChemPhys, vol. 11, pp. 6042–6050, 2009.

[185] G. H. Patterson, S. M. Knobel, W. D. Sharif, S. R. Kain, and D. W. Piston, "Use of the green fluorescent protein and its mutants in quantitative fluorescence microscopy.," Biophysical Journal, vol. 73, pp. 2782–2790, 1997.

[186] Z. Petrášek and P. Schwille, "Photobleaching in two-photon scanning fluorescence correlation spectroscopy.," Chemphyschem, vol. 9, pp. 147–158, 2008.

[187] G. Nishimura and M. Kinjo, "Systematic error in fluorescence correlation measurements identified by a simple saturation model of fluorescence.," Analytical Chemistry, vol. 76, pp. 1963–1970, 2004.

[188] I. Gregor, D. Patra, and J. Enderlein, "Optical saturation in fluorescence correlation spectroscopy under continuous-wave and pulsed excitation.," ChemPhysChem, vol. 6, pp. 164–170, 2005.

[189] S. W. Hell, "Far-field optical nanoscopy.," Science, vol. 316, pp. 1153–1158, 2007.

[190] S. Veettil, N. Budisa, and G. Jung, "Photostability of green and yellow fluorescent proteins with fluorinated chromophores, investigated by fluorescence correlation spectroscopy.," Biophysical Chemistry, vol. 136, pp. 38–43, 2008.

[191] B. Hinkeldey, A. Schmitt, and G. Jung, "Comparative photostability studies of bodipy and fluorescein dyes by using fluorescence correlation spectroscopy.," ChemPhysChem, vol. 9, pp. 2019–2027, 2008.

[192] C. Eggeling, J. Widengren, L. Brand, J. Schaffer, S. Felekyan, , and C. A. M. Seidel, "Analysis of photobleaching in single-molecule multicolor excitation and forster resonance energy transfer measurement.," The Journal of Physical Chemistry A, vol. 110, pp. 2979–2995, 2006.

[193] H. M. Shapiro, "Multistation multiparameter flow cytometry: A critical review and rationale," Cytometry, vol. 3, pp. 227–243, Jan 1983.

[194] C. G. Wade, J. Richard H. Rhyne, W. H. Woodruff, D. P. Bloch, and J. C. Bartholomew, "Spectra of cells in flow cytometry using a vidicon detector.," Journal of Histochemistry and Cytochemistry., vol. 27, 1979.

[195] G. Goddard, J. C. Martin, M. Naivar, P. M. Goodwin, S. W. Graves, R. Habbersett, J. P. Nolan, and J. H. Jett, "Single particle high resolution spectral analysis flow cytometry," Cytometry Part A, vol. 69A, pp. 842–851, Aug 2006.

[196] P. F. Mullaney, "Cell sizing: A light scattering photometer for rapid volume determination," Review of Scientific Instruments, vol. 40, no. 8, p. 1029, 1969.

[197] H. R. Hulett, W. A. Bonner, J. Barrett, and L. A. Herzenberg, "Cell sorting: automated separation of mammalian cells as a function of intracellular fluorescence," Science, vol. 166, no. 3906, pp. 747–749, 1969.

[198] W. A. Bonner, "Fluorescence activated cell sorting," Review of Scientific Instruments, vol. 43, no. 3, p. 404, 1972.

[199] H. Hulett, W. Bonner, R. Sweet, and L. Herzenberg, "Development and application of a rapid cell sorter," Clinical Chemistry, vol. 19, pp. 813–816, 1973.

[200] J. A. Steinkamp, T. M. Yoshida, and J. C. Martin, "Flow cytometer for resolving signals from heterogeneous fluorescence emissions and quantifying lifetime in fluorochrome-labeled cells/particles by phase-sensitive detection," Review of Scientific Instruments, vol. 64, no. 12, p. 3440, 1993.

[201] J. P. Houston, M. A. Naivar, and J. P. Freyer, "Digital analysis and sorting of fluorescence lifetime by flow cytometry," Cytometry Part A, vol. 77A, pp. 861–872, Sep 2010.

[202] H. H. Engelhard, J. L. Krupka, and K. D. Bauer, "Simultaneous quantification of c-myc oncoprotein, total cellular protein, and dna content using multiparameter flow cytometry," Cytometry, vol. 12, no. 1, pp. 68–76, 1991.

[203] G. van den Engh and C. Farmer, "Photo-bleaching and photon saturation in flow cytometry," Cytometry, vol. 13, no. 7, pp. 669–677, 1992.

[204] R. M. P. Doornbos, B. G. de Grooth, and J. Greve, "Experimental and model investigations of bleaching and saturation of fluorescence in flow cytometry," Cytometry Part A, vol. 29, no. 3, pp. 204–214, 1998.

[205] R. Y. Tsien, "The green fluorescent protein," Annual Review of Biochemistry, vol. 67, pp. 509–544, 1998.

[206] N. C. Shaner, G. H. Patterson, and M. W. Davidson, "Advances in fluorescent protein technology," Journal of Cell Science, vol. 120, pp. 4247–4260, Dec 2007.

[207] H. Mizuno, T. K. Mal, M. Walchli, A. Kikuchi, T. Fukano, R. Ando, J. Jeyakanthan, J. Taka, Y. Shiro, M. Ikura, and et al., "Light-dependent regulation of structural flexibility in a photochromic fluorescent protein," Proceedings of the National Academy of Sciences, vol. 105, pp. 9227–9232, Jun 2008.

[208] D. Sinnecker, P. Voigt, N. Hellwig, and M. Schaefer, "Reversible photobleaching of enhanced green fluorescent proteins," Biochemistry, vol. 44, pp. 7085–7094, May 2005.

[209] K. M. Dean, J. L. Lubbeck, J. K. Binder, L. R. Schwall, R. Jimenez, and A. E. Palmer, "Analysis of red-fluorescent proteins provides insight into dark-state conversion and photodegradation," Biophysical Journal, vol. 101, pp. 961–969, Aug 2011.

[210] D. Li, ed., Encyclopedia of microfluidics and nanofluidics. Springer-Verlag, 2008.

[211] J. B. Knight, A. Vishwanath, J. P. Brody, and R. H. Austin, "Hydrodynamic focusing on a silicon chip: mixing nanoliters in microseconds," Physical Review Letters, vol. 80, pp. 3863–3866, 1998.

[212] J. T. Verdeyen, Laser electronics. Prentice Hall, 3rd ed., 1995.

[213] D. P. Schrum, C. T. Culbertson, S. C. Jacobson, and J. M. Ramsey, "Microchip flow cytometry using electrokinetic focusing," Analytical Chemistry, vol. 71, pp. 4173–4177, Oct 1999.

[214] Y. Morimoto, W.-H. Tan, and S. Takeuchi, "Three-dimensional axisymmetric flow-focusing device using stereolithography," Biomedical Microdevices, vol. 11, pp. 369–377, Apr 2009.

[215] X. Mao, S.-C. S. Lin, C. Dong, and T. J. Huang, "Single-layer planar on-chip flow cytometer using microfluidic drifting based three-dimensional (3d) hydrodynamic focusing," Lab on a Chip, vol. 9, no. 11, p. 1583, 2009.

[216] C. H. Chen, S. H. Cho, F. Tsai, A. Erten, and Y.-H. Lo, "Microfluidic cell sorter with integrated piezoelectric actuator," Biomedical Microdevices, vol. 11, pp. 1223–1231, Dec 2009.

[217] P. C. H. Li and D. J. Harrison, "Transport, manipulation, and reaction of biological cells on-chip using electrokinetic effects," Analytical Chemistry, vol. 69, pp. 1564–1568, Apr 1997.

[218] S. R. Quake, A. Y. Fu, C. Spence, A. Scherer, and F. H. Arnold, "A micro fabricated fluorescence-activated cell sorter," Nature Biotechnology, vol. 17, pp. 1109–1111, Nov 1999.

[219] T.-H. Wu, Y. Chen, S.-Y. Park, J. Hong, T. Teslaa, J. F. Zhong, D. Di Carlo, M. A. Teitell, and P.-Y. Chiou, "Pulsed laser triggered high speed microfluidic fluorescence activated cell sorter," Lab on a Chip, vol. 12, no. 7, p. 1378, 2012.

[220] A. Ashkin, J. M. Dziedzic, and T. Yamane, "Optical trapping and manipulation of single cells using infrared laser beams," Nature, vol. 330, pp. 769–771, Dec 1987.

[221] J. Robert Applegate, J. Squier, T. Vestad, J. Oakey, and D. Marr, "Optical trapping, manipulation, and sorting of cells and colloids in microfluidic systems with diode laser bars," Optics Express, vol. 12, pp. 4390–4398, Sep 2004.

[222] S.-K. Hoi, C. Udalagama, C.-H. Sow, F. Watt, and A. A. Bettiol, "Microfluidic sorting system based on optical force switching," Applied Physics B, vol. 97, pp. 859–865, Dec 2009.

[223] X. Wang, S. Chen, M. Kong, Z. Wang, K. D. Costa, R. A. Li, and D. Sun, "Enhanced cell sorting and manipulation with combined optical tweezer and microfluidic chip technologies," Lab on a Chip, vol. 11, no. 21, p. 3656, 2011.

[224] T. D. Perroud, J. N. Kaiser, J. C. Sy, T. W. Lane, C. S. Branda, A. K. Singh, and K. D. Patel, "Microfluidic-based cell sorting of francisella tularensis infected macrophages using optical forces," Analytical Chemistry, vol. 80, pp. 6365–6372, Aug 2008.

[225] J. L. Lubbeck, K. M. Dean, H. Ma, A. E. Palmer, and R. Jimenez, "Microfluidic flow cytometer for quantifying photobleaching of fluorescent proteins in cells," Analytical Chemistry, vol. 84, pp. 3929–3937, May 2012.

[226] G. Czerlinski, D. Reid, A. Apostol, K. Bauer, and D. Scarpelli, "Determination of the density of cells from sedimentation studies at 1g," Journal of Biological Physics, vol. 15, pp. 29–32, 1987.

[227] B. P. Cormack, R. H. Valdivia, and S. Falkow, "Facs-optimized mutants of the green fluorescent protein (gfp)," Gene, vol. 173, pp. 33–38, Jan 1996.

[228] C. Eggeling, J. Widengren, R. Rigler, and C. A. M. Seidel, "Photobleaching of fluorescent dyes under conditions used for single-molecule detection: Evidence of two-step photolysis," Analytical Chemistry, vol. 70, pp. 2651–2659, Jul 1998.

[229] S. N. Ho, H. D. Hunt, R. M. Horton, J. K. Pullen, and L. R. Pease, "Site-directed mutagenesis by overlap extension using the polymerase chain reaction," Gene, vol. 77, pp. 51–59, Apr 1989.

[230] W. W. Ward and M. J. Cormier, "An energy transfer protein in coelenterate bioluminescence. characterization of the renilla green-fluorescent protein," Journal of Biological Chemistry, vol. 254, pp. 781–788, 1979.

[231] J. Schuster, F. Cichos, and C. von Borczyskowski, "Influence of self-trapped states on the fluorescence intermittency of single molecules," Applied Physics Letters, vol. 87, no. 5, p. 051915, 2005.

[232] L. Greenbaum, C. Rothmann, R. Lavie, and Z. Malik, "Green fluorescent protein photobleaching: a model for protein damage by endogenous and exogenous singlet oxygen," Biological Chemistry, vol. 381, Jan 2000.

[233] A. Jimnez-Banzo, S. Nonell, J. Hofkens, and C. Flors, "Singlet oxygen photosensitization by egfp and its chromophore hbdi," Biophysical Journal, vol. 94, pp. 168–172, Jan 2008.

[234] R. Zondervan, F. Kulzer, S. B. Orlinskii, and M. Orrit, "Photoblinking of rhodamine 6g in poly(vinyl alcohol): Radical dark state formed through the triplet," The Journal of Physical Chemistry A, vol. 107, pp. 6770–6776, Sep 2003.

[235] C. Eggeling, A. Volkmer, and C. A. M. Seidel, "Molecular photobleaching kinetics of rhodamine 6g by one- and two-photon induced confocal fluorescence microscopy.," ChemPhysChem, vol. 6, pp. 791–804, 2005.

[236] W. Becker, Advanced Time-Correlated Single Photon Counting Techniques. Springer, first ed., 2005.

[237] M. J. Booth and T. Wilson, "Low-cost, frequency-domain, fluorescence lifetime confocal microscopy," Journal of Microscopy, vol. 214, pp. 36–42, Apr 2004.

[238] H. Murakoshi, H. Wang, and R. Yasuda, "Local, persistent activation of rho gtpases during plasticity of single dendritic spines," Nature, vol. 472, pp. 100–104, Mar 2011.

[239] S.-J. R. Lee, Y. Escobedo-Lozoya, E. M. Szatmari, and R. Yasuda, "Activation of camkii in single dendritic spines during long-term potentiation," Nature, vol. 458, pp. 299–304, Mar 2009.

[240] B. G. Pinsky, J. J. Ladasky, J. R. Lakowicz, K. Berndt, and R. A. Hoffman, "Phase-resolved fluorescence lifetime measurements for flow cytometry," Cytometry, vol. 14, no. 2, pp. 123–135, 1993.

[241] R. C. Cadwell and G. F. Joyce, "Randomization of genes by pcr mutagenesis.," Genome Research, vol. 2, pp. 28–33, Aug 1992.

[242] J. N. Henderson, R. Gepshtein, J. R. Heenan, K. Kallio, D. Huppert, and S. J. Remington, "Structure and mechanism of the photoactivatable green fluorescent protein," Journal of the American Chemical Society, vol. 131, pp. 4176–4177, Apr 2009.

[243] V. Adam, P. Carpentier, S. Violot, M. Lelimousin, C. Darnault, G. U. Nienhaus, and D. Bourgeois, "Structural basis of x-ray-induced transient photobleaching in a photoactivatable green fluorescent protein," Journal of the American Chemical Society, vol. 131, pp. 18063–18065, Dec 2009.

[244] A. F. Bell, D. Stoner-Ma, R. M. Wachter, and P. J. Tonge, "Light-driven decarboxylation of wild-type green fluorescent protein," Journal of the American Chemical Society, vol. 125, pp. 6919–6926, Jun 2003.

[245] G. S. Filonov, K. D. Piatkevich, L.-M. Ting, J. Zhang, K. Kim, and V. V. Verkhusha, "Bright and stable near-infrared fluorescent protein for in vivo imaging," Nature Biotechnology, vol. 29, pp. 757–761, Jul 2011.

[246] J. Fuchs, S. Böhme, F. Oswald, P. N. Hedde, M. Krause, J. Wiedenmann, and G. U. Nienhaus, "A photoactivatable marker protein for pulse-chase imaging with superresolution," Nature Methods, vol. 7, pp. 627–630, 2010.

[247] F. V. Subach, O. M. Subach, I. S. Gundorov, K. S. Morozova, K. D. Piatkevich, A. M. Cuervo, and V. V. Verkhusha, "Monomeric fluorescent timers that change color from blue to red report on cellular trafficking," Nature Chemical Biology, vol. 5, pp. 118–126, Jan 2009.

[248] A. M. Bogdanov, A. S. Mishin, I. V. Yampolsky, V. V. Belousov, D. M. Chudakov, F. V. Subach, V. V. Verkhusha, S. Lukyanov, and K. A. Lukyanov, "Green fluorescent proteins are light-induced electron donors," Nature Chemical Biology, vol. 5, pp. 459–461, Apr 2009.

[249] J.-W. Choi, Y.-S. Nam, W.-H. Lee, D. Kim, and M. Fujihira, "Rectified photocurrent of the protein-based bio-photodiode," Applied Physics Letters, vol. 79, no. 10, p. 1570, 2001.

[250] H. Hoi, N. C. Shaner, M. W. Davidson, C. W. Cairo, J. Wang, and R. E. Campbell, "A monomeric photoconvertible fluorescent protein for imaging of dynamic protein localization," Journal of Molecular Biology, vol. 401, pp. 776–791, Sep 2010.

[251] M. E. Martin, F. Negri, and M. Olivucci, "Origin, nature, and fate of the fluorescent state of the green fluorescent protein chromophore at the caspt2//casscf resolution," Journal of the American Chemical Society, vol. 126, pp. 5452–5464, May 2004.

Appendix A

Other Libraries

A.1 Other Libraries

A wide-variety of libraries have been pursued to varying extents. Each stage of mutagenesis and selection was accompanied by a significant learning curve. This appendix aims to summarize the construction and status of each of the other libraries.

A.1.1 Error-Prone PCR for TagRFP Arg67K Asn143Ser Ser158Thr

TagRFP Arg67Lys Asn143Ser Ser158Thr is spectrally similar to mCherry, but >2-fold brighter due to it's large extinction coefficient, decent maturation to a red-fluorescent chromophore, and moderate quantum yield (0.41). As a result of it's excellent photophysical properties, we hypothesized that it would be a good candidate for early library attempts. This library was prepared using an error-prone PCR protocol that called for biased dNTP concentrations (0.2 mM dGTP and DATP, 1 mM dCTP and DTTP), an elevated pH of 8.3, the addition of Mn^{2+} (7 mM $MgCl_2$ and 0.5 mM $MnCl_2$), and Taq-polymerase [241]. Approximately 1.4×10^6 clones were in the prepared in pDonr221, and sequentially transferred to the custom destination vector, pCLNCX-Dest. Given the sequential transfer between vectors, it is unlikely that the genetic diversity was preserved in the process. Future libraries circumvented this by directly constructing the library with PCR from a pDonr221-FP template. Here, primers specific to pDonr221 (M13Fwd and M13Rev) were used as the outermost primers, which amplify the appropriate gateway recombination sites, as well as the gene, and can be directly recombined into a destination vector.

Following viral infection of the HeLa S cells, it was found that 0.96 % of the cells were fluorescent.

FACS was used to sort ≈ 250,000 clones, and the cells were subsequently expanded, and enriched three additional times to remove non-fluorescent clones. The cells were harvested, the mRNA was isolated, the cDNA was constructed, and 20 genes were identified by commercial sequencing. Despite the high error-prone mutagenesis rate of >8 mutations per 1000 basepairs, 11 of the 20 mutants sequenced were the parent template. Of the remaining 9 clones sequenced, 17 mutations were observed, with an average of 1.88 amino-acid changes per RFP. Seven of these mutations had already been observed in the TagRFP to mKate evolutionary trajectory (positions 67, 158, 174, 197). Of the remaining 10 mutations, 8 were outward facing on the barrel, or located in one of the interstrand loops. The library was screened, and no further work was carried out due to the perceived low probability of success after sequencing of the 20 clones. Given that the library was screened without a separate single-FP calibration, it is difficult to assess the accuracy of the spectroscopic diversity observed in Figure A.2.

A.1.2 TagRFP Arg67Lys Ser158Thr Saturated Mutagenesis

From our rapid photobleaching and dark-state conversion measurements, TagRFP R67K S158T was identified to be the most photostable of the RFPs measured at high laser intensity (25 kW/cm^2) [209]. As a result, we pursued a library strategy that identified positions that could further optimize the steric packing surrounding the chromophore, thereby minimizing cis/trans isomerization. Positions Thr60, Met160, His197, and Leu199 were chosen since they formed Van der Waals contacts with the chromophore. Thr60, Met160, and Leu199 were mutated to all 20 amino acids, and I197 was mutated to a subset of amino acids, including K/E/Q/M/V/L/N/D/H/Y/I/F. The final library size was 96,000 unique proteins, and is shown in Figure A.2.

The individual fragments incorporating the appropriate codon wildcards were amplified and reassembled using site-overlap extension. Sequencing confirmed the incorporation of mutations at the appropriate locations. Similar to the TagRFP Arg67Lys Ser158Thr Ser158Thr Error-Prone PCR library, this library was shuttled through pDonr221 to pCLNCX-Dest for viral expression, and likely suffered a decrease in genetic diversity. To approximate the percentage of mutants that were fluorescent, as well as the multiplicity of infection, pCLNCX-DsRed virus and cell-lines were created alongside the saturated mutagenesis library under

Figure A.1: Photostability distribution observed for TagRFP Arg67Lys Asn143Ser Ser158Thr error-prone PCR. Given that a single-FP population was also not screened on the same day, it is difficult to assess the reliability of the spectroscopic diversity observed.

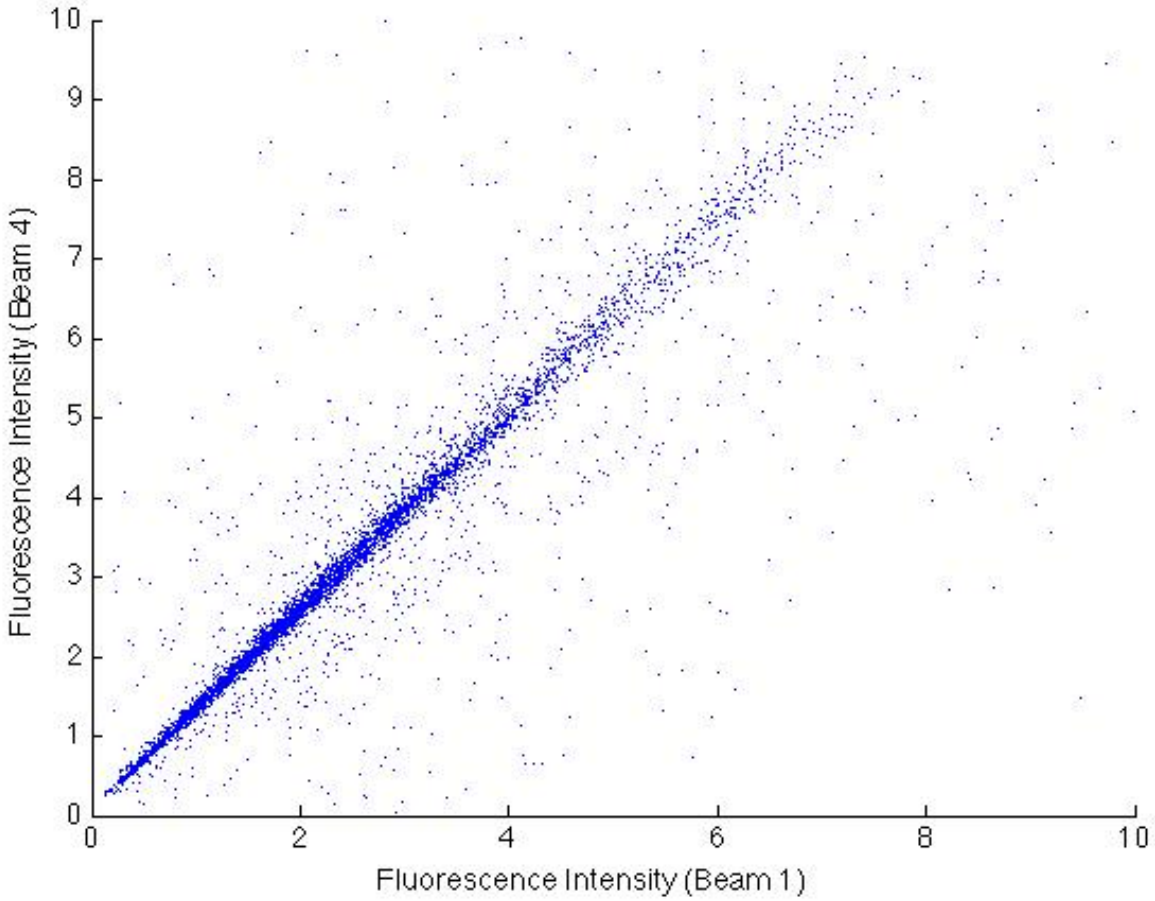

Figure A.2: Positions mutated in the TagRFP Arg67Lys Ser158Thr library. Positions included Thr60, Met160, His197, and Leu199.

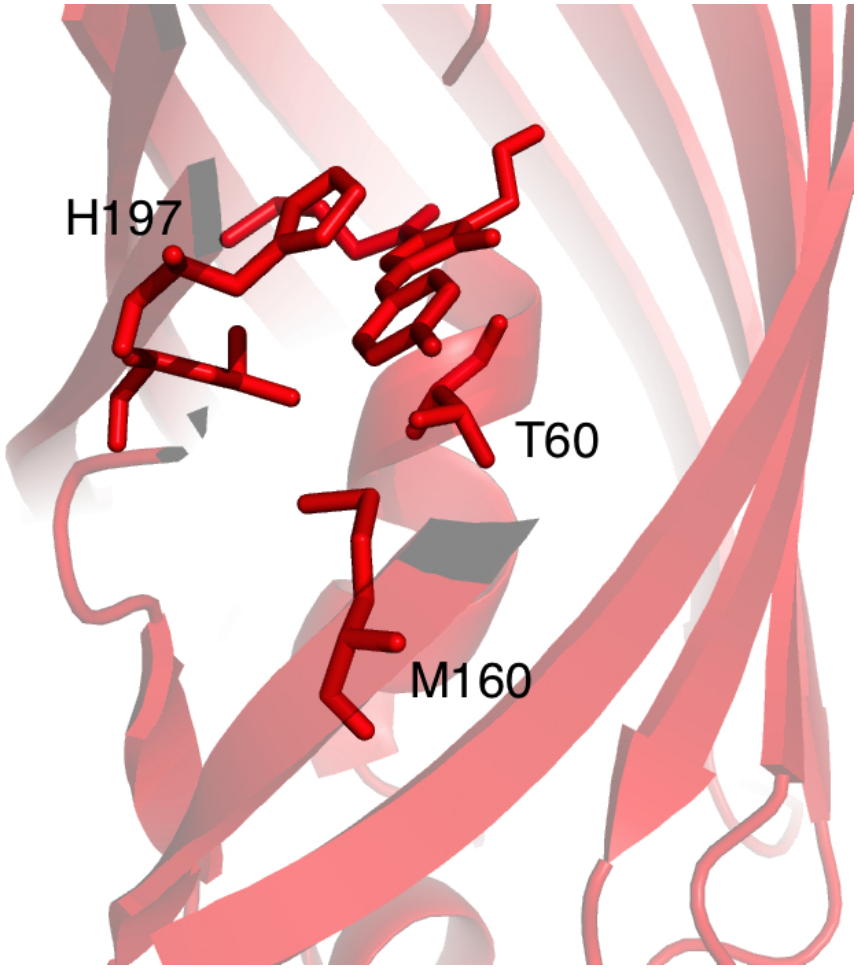

identical conditions. Via FACS analysis, the DsRed infection was found to occur in 16.5 % of cells (10,521 total cells screened), as opposed to 0 % of the saturated mutagenesis library. Even after 2 weeks of G418 selection, only .03 % of the cells were found to be positive for red-fluorescence, or roughly 29 mutants out of 96,000. Given these results, the library was deemed non-functional and it was abandoned.

A.1.3 Kriek2.0 Directed Evolution

As discussed earlier in this chapter, the "Kriek" library (mCherry mutated at Val16, Met66, Trp143, Ile161, and Gln163) was subjected to multiple rounds of selection using the microfluidic photobleaching cytometer. After the initial round of sorting, the population, referred to as the Kriek1 mutants, were subjected to two separate selection criteria. Kriek2 was selected from Kriek1 using only photobleaching as the selection criteria. Kriek4, however, was selected from Kriek1 using both fluorescence intensity and photobleaching as the selection criteria. In an effort to "rescue" the poor fluorescence quantum yield of these resulting library members, while maintaining or improving the photostability, the DNA for the Kriek2 and Kriek4 mutants were combined in an equimolar fashion, and subjected to further mutagenesis. Below are the results from these attempts at directed evolution of the Kriek2 and Kriek4 mutants.

Kriek2.1 Saturated Mutagenesis Kriek2.1 is a saturated mutagenesis library that targets potential compensatory amino-acids located near the mutations present in Kriek2 and Kriek4. Positions targeted include Asp59, Ser62, and Leu199 (Figure A.3). Interestingly, Leu199, in the mCherry crystal structure exhibits multiple rotamer conformations. Since multiple templates were used (Kriek2 and Kriek4), the total library size was $\approx$ 80,000 mutants. Pfu was used to amplify the individual fragments, as well as to carry out the site-overlap extension reaction. Given that the RFP templates were in pDonr221, M13Fwd and M13Rev were used as the outermost primers, and the full-length amplicon was immediately recombined into pCLNCX-Dest, resulting in 900,000 CFU after electroporation (>10x coverage). Sequencing of ten of these mutants revealed efficient mutagenesis at the targeted positions, with two spontaneous mutations located outside of these regions. After viral transduction and G418 treatment of HeLa S cells, approximately 12 % of the library was found to be fluorescent, and $\approx 2\times10^6$ cells were enriched for red-fluorescence. Cells were then

screened in the microfluidic photobleaching cytometer, and found to have decreased photostability relative to Kriek2 (Figure A.4). Despite this result, this library was combined with Kriek2.2 (see below) in a manner proportional to the approximate library size of each, and sorted once in the microfluidic photobleaching cytometer. As a result of an optical-trap induced burn during the sort, the libraries were under-sampled. Regardless, the sorted cells were expanded, the mRNA was isolated, the cDNA was constructed, the RFPs were PCR amplified, and the library is awaiting cloning and sequencing.

Kriek2.2 Saturated Mutagenesis Kriek2.2 is a saturated mutagenesis library that aimed to identify compensatory mutations for Kriek2 and Kriek4, while further improving the photostability. These mutations, located away from the β-bulge, were targeted due to their proximity to Glu215, an amino-acid known to undergo decarboxylation and thought to be involved in irreversible photobleaching and photoconversion [67, 68, 108, 132, 242–244]. Three positions were mutated to all 20 amino acids. These positions included Lys70, an amino-acid originating from the central α-helix and located directly above the chromophore, that was shown to be important for the photostability of TagRFP variants [209]. The second position was Ile197, a position analogous to the Π-stacking Thr203Tyr mutation in yellow-fluorescing GFP mutants (e.g., Citrine and Venus) [51, 52], and also immediately adjacent to the chromophore. And lastly, Glu215 was also mutated, which is equivalent to Glu222 in GFP (See Figure A.5).

Given the close proximity of positions 197 and 215, the library was constructed in two consecutive steps. First, Pfu was used to amplify 3 fragments that included mutations at K70 and I197. These fragments were subsequently combined in a site-overlap extension reaction and recombined into pDonr221, and the resulting >2,000 colonies were combined and their DNA was isolated. Since there were $\approx$ 8 templates involved in the original PCR amplification, this library was under-sampled. The resulting DNA was then further mutated at position 215 via site-overlap extension with Pfu, recombined into pCLNCX-Dest, and electroporated to create $\approx 1.5\times10^6$ colonies. Sequencing of 10 of the colonies revealed mutations located in the appropriate locations, with one spontaneous mutation outside of the targeted positions. Virus was prepared and HeLa S cells were infected, placed under G418 selection, and the fluorescent population ($\approx$ 6.5 %) was enriched using FACS. Subsequent screening of Kriek2.2 in the microfluidic photobleaching cytometer

Figure A.3: Positions mutated in the Kriek2.1 saturated mutagenesis library. The positions included Asp59, Ser62, and Leu199.

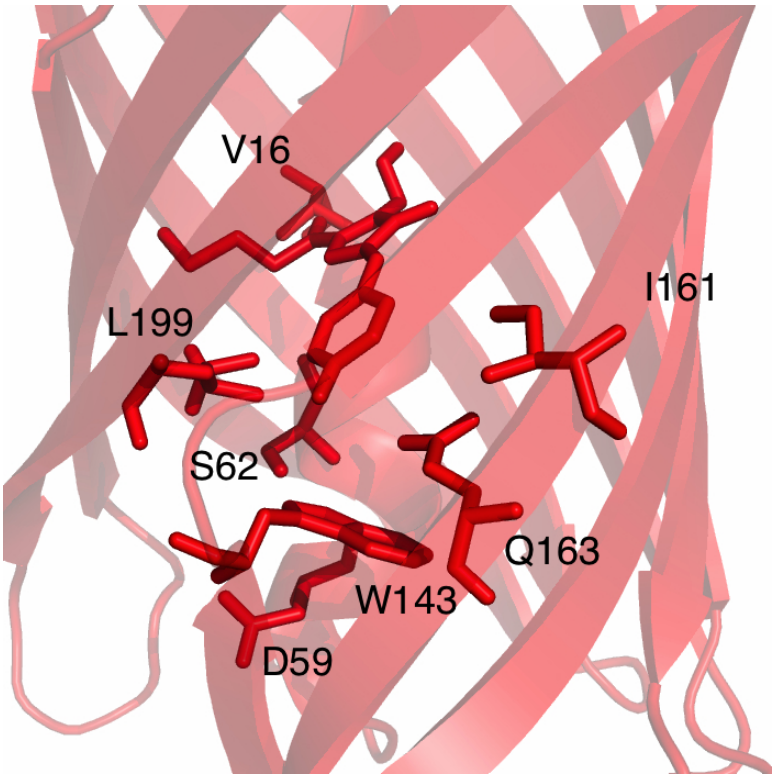

Figure A.4: Photostability distribution observed for Kriek2 and Kriek2.1.

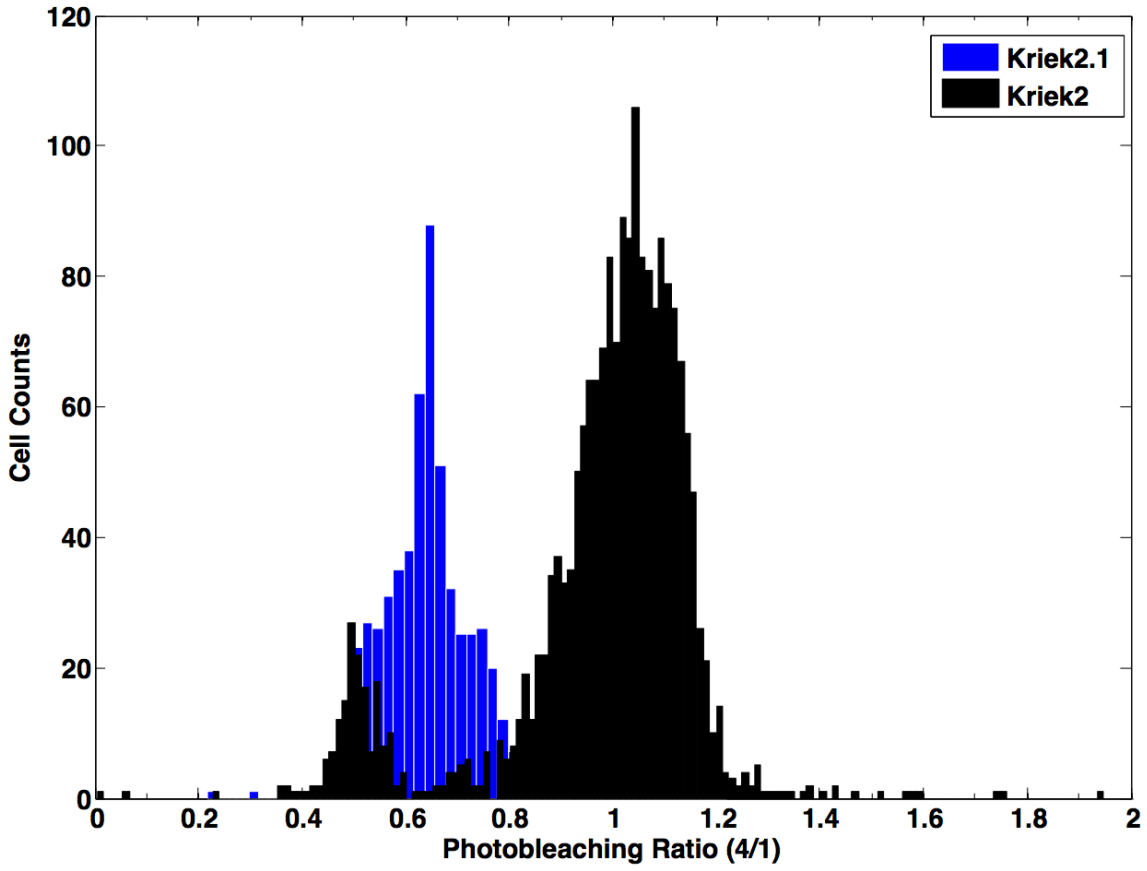

showed that the majority of the fluorescent population reverted back to mCherry-like photostability (Figure A.6). As mentioned above, this library was combined with Kriek2.1 in a weighted-manner with respect to their anticipated diversity and sorted in the microfluidic flow cytometer (although without enough coverage), the cells were expanded, the mRNA was isolated, the cDNA was constructed and PCR amplified, and the library is awaiting cloning and sequencing.

Kriek2.3 Kriek2.3 is an error-prone PCR library of the Kriek2 and Kriek4 mutants. The library was amplified according to manufacturer's recommendations (GeneMorph II Random Mutagenesis Kit, Agilent), with a low error-rate of 0-4.5 mutations/kilobase. The low-error rate was selected to increase the likelihood of functional mutants (e.g., fluorescent) within the library, and we hypothesized that only a small number of amino-acid changes could improve the quantum yield of fluorescence. Modest error-rates of 2-4 mutations per kb (1,000 base pairs) have been reported for the fine-tuning of FPs [19, 124], although upwards of 16 mutations per kb is also common [23, 25, 27, 57, 132, 133, 245–247]. After error-prone PCR, the library was recombined into pDonr221 and electroplated into *E. coli* cells. A subset of the electroporation was removed and diluted to determine the library size ($\approx 3.2\times10^6$), and the remainder was allowed to grow overnight in 10 mL of LB/Kan. The next day, DNA was purified from the overnight culture and double-digested with BamHI and EcoRI, and the resulting error-prone PCR fragment was gel-purified and ligated into a pBad.

The resulting clones were plated onto LB/Amp with L-arabinose (final concentration .02 % mass fraction), and subjected to a trial round of colony screening. To minimize artifacts, the colony screener was realigned to provide uniform illumination and detection. As a result of the low-error rate, the vast majority of bacterial colonies were fluorescent, and the fluorescence intensity appeared to be approximately equal amongst all of the colonies screened (>20,000) using standard camera thresholding techniques. Given that we were interested in even modest improvements, a more rigorous approach was necessary. Consequently, a Matlab image acquisition and analysis program was developed to further correct for non-uniform illumination, identify fluorescent colonies, and measure their properties (maximum intensity, mean intensity, and colony size), to provide guidance for selection. Nevertheless, given the low-throughput nature of the method, it was

Figure A.5: Positions mutated in the Kriek2.2 saturated mutagenesis library. Positions included Lys70, Ile197, and Glu215.

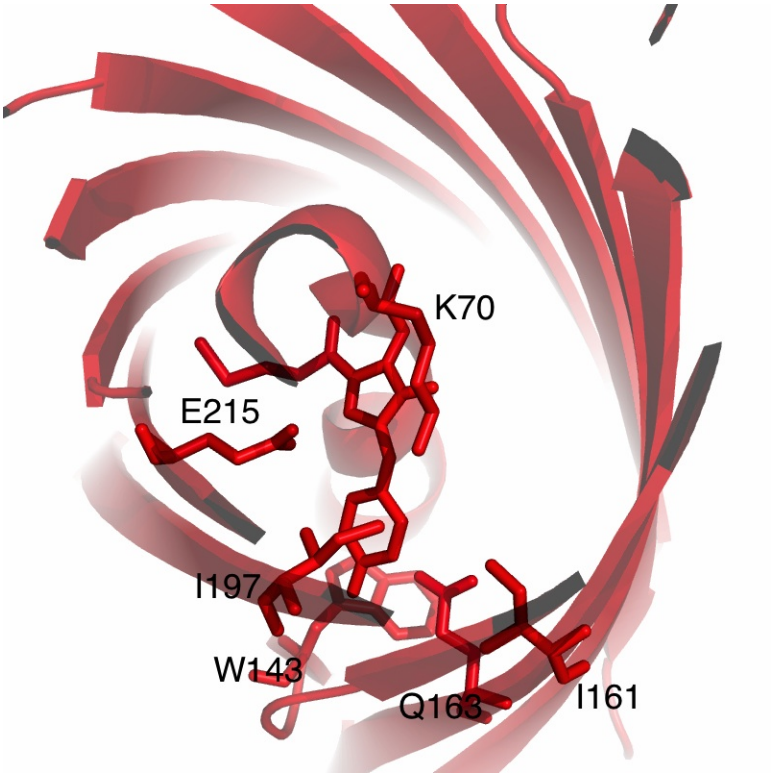

Figure A.6: Photostability distribution observed for Kriek2 and Kriek2.2.

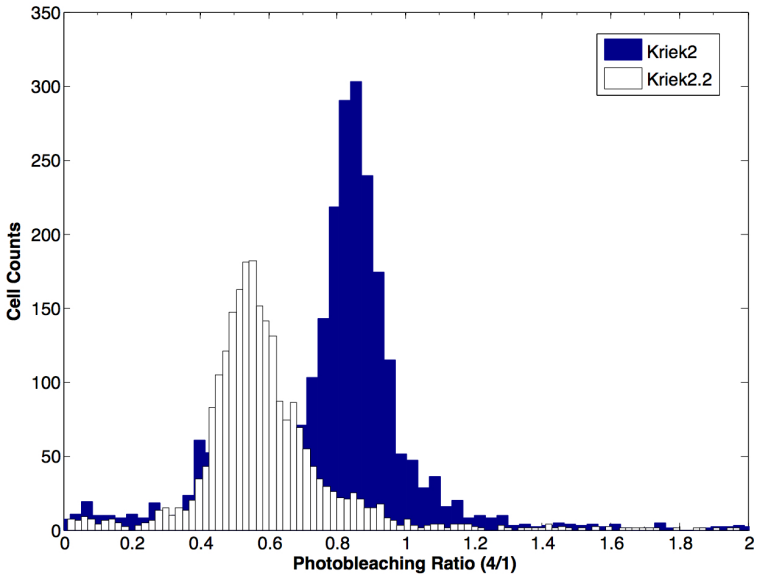

Figure A.7: Overlay of crystal-structures for mCherry (PDB 2H5Q) and mTurquoise2 (PDB 4AR7). mCherry and mTurquoise2 are red and teal, respectively.

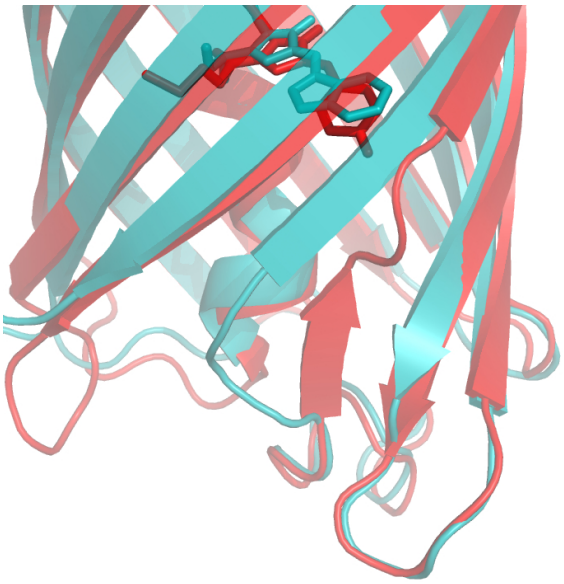

postponed due to prioritization of other library. The pBad-Kriek2.3 library currently exists as both purified DNA and as a frozen glycerol stock of bacteria.

Kriek2.4 With the exception of mTurquoise2 [41], all FPs, to varying extents, suffer from decreased hydrogen-bonding between β-strand 7 and 10. This interstrand distance is more pronounced in RFPs. Nevertheless, Goedhart et al. managed to trigger a reorganization in this region that eliminated the β-bulge, concomitantly increasing the quantum yield and photostability [41]. In an effort to recapitulate this in mCherry, as well as the Kriek2 and Kriek4 mutants, the two crystal structures were overlaid and differences in the FPs were evaluated (Figure A.7). Interestingly, all of the β-strands except 7 and 10, as wells as the interstrand loops, shared a high degree of similarity. For the β-strands in the 7 and 10 region, clear differences in the crystal structures, as well as the properties of the amino-acids at particular positions, were observed. In an effort to eliminate these differences, a sequence of 8 amino-acids in mCherry (TMGWEASS) was converted to the analogous 9 amino-acid region in mTurquoise2 (LEYNYISDN). As anticipated, the resulting clones (mCherry mutants, Kriek2 and Kriek4 mutants) were non-fluorescent.

In an attempt to rescue fluorescence, all of the variants, including the modified mCherry, were used as

templates for error-prone PCR under highly mutagenic conditions (up to 16 mutations/kb). The error-prone PCR fragment was recombined with pDonr221, resulting in $\approx 6\times10^6$ mutants. The DNA for this library was double-digested with BamHI and EcoRI and ligated into pBad, resulting in $\approx 1.3\times10^6$ CFU. After overnight growth, several glycerol stocks of the library were prepared. As a preliminary screen, *E. coli* was transformed and induced with L-arabinose, and $\approx$ 1200 colonies were analyzed. After 24 hours of growth at 37° C and a week of induction at 4° C, no fluorescent clones were observed. To increase the throughput, and identify even weakly fluorescent clones, the library was screened with FACS. To prepare the library, a glycerol stock was thawed, and allowed to grow overnight at 25° C in the presence of L-arabinose. The following morning, bacteria were centrifuged, subjected to two consecutive 100-fold dilutions with HHBSS, and screened with the cytometer. Given the high-throughput nature of FACS, $\approx 50\times10^6$ bacteria were screened, and what appeared to be genuinely fluorescent clones ($\approx$ 6300), were sorted were sorted into SOB and plated on agar plates supplemented with ampicillin and L-arabinose. Nevertheless, the resulting clones did not become fluorescent even after multiple days of induction at 4° C.

A.1.4 Morello

A large amount of spectroscopic diversity was observed in the transition of TagRFP to mKate [209]. Consequently, we hypothesized that the same positions, if mutated within the mCherry context, may also provide improvements to the photophysical properties of mCherry (Figure A.9). Consequently, the analogous positions, Lys70, Ser146, Val177, and Ile197, were submitted to saturated mutagenesis using site-overlap extension coupled with error-prone PCR.

2.73×10^6 mutants were prepared. Sequencing of 10 mutants provided an estimation of the error-rate (6.25 mutation/kb) and the fraction of the library suffering from insertions/deletions ($\approx$ 50 %). After viral transduction and G418 treatment of HeLa S cells, 330,000 clones were sorted (4.3 % fluorescent). Screening in the microfluidic photobleaching cytometer revealed a broadened distribution in photostability relative to mCherry (Figure A.9). No further work has been carried out on this library.

Figure A.8: Positions mutated in the "Morello" library. Positions included K70, S146, V177, and I197. These four positions caused drastic changes to the photostability background, so their influence was also checked within the mCherry context.

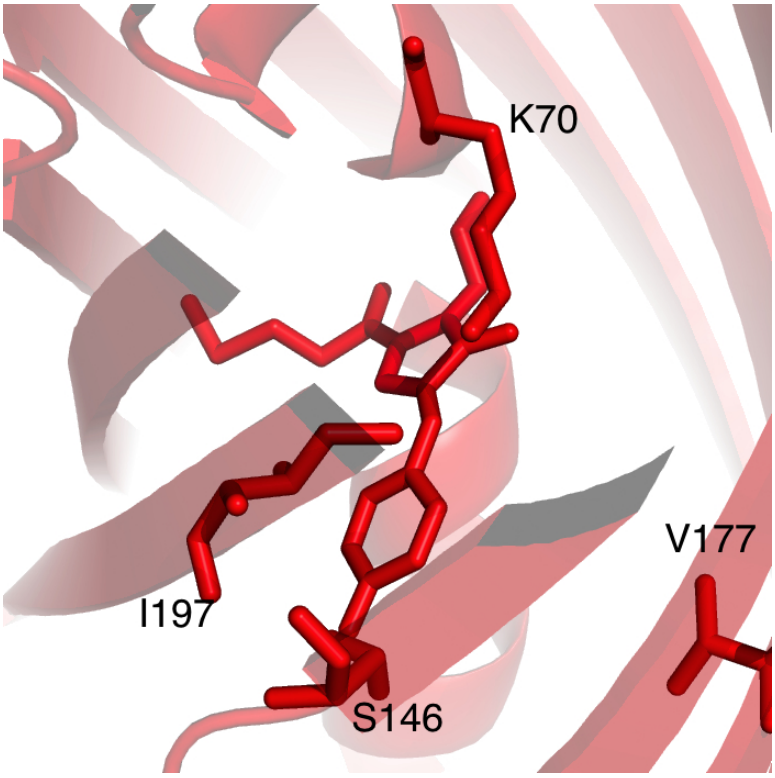

Figure A.9: Photostability distribution observed for "Morello" library relative to mCherry.

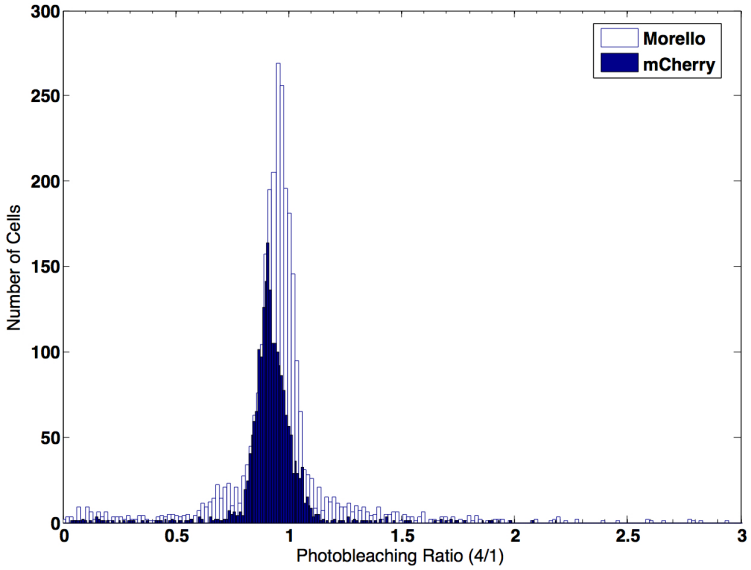

A.1.5 Targeted Tryptophan Mutagenesis of mRuby2 and dTomato

In small-molecule fluorophores, it has become evident that radical states exist as a primary cause of photodegradation [114]. Consequently, we hypothesized that electron-transfer, and subsequent oxidation of the chromophore, could be a mechanism for irreversible photobleaching [248]. Residues capable of participating in electron-transfer include tryptophan, tyrosine, phenylalanine, histidine, methionine, and cysteine. In fluorescent proteins, there is precedence for electron-transfer reactions. For example, GFP has been used to create a bio-photodiode [249], and light-induced oxidation is common in both photoactivatable and photoconvertible fluorescent proteins [45, 47, 244, 250]. The rate of electron-transfer, in proteins is governed by Marcus Theory, and depends upon the distance of transfer, packing density within the protein, free energy of transfer, and the energy necessary for reorganization of the residues following electron transfer. Impressively, it can occur at tremendous rates ($\approx 10^5$-10^{13} s^{-1}), easily competing with excited-state processes ($\approx 10^6$ for triplet states, and 10^9 for singlet states). *Ab initio* studies have also found that the formation of a biradical species is favorable along the reaction coordinate for cis-trans isomerization in FP chromophores [251]. Interestingly, two of the mutations found in K2C (Trp143Ile and Ile161Met), the best mutants from the Kriek library, could potentially be involved in electron-transfer.

Given this hypothesis, we decided to pursue a library strategy that targeted all tryptophans within mRuby2 and tdTomato. mRuby2 was chosen because it was derived from eqFP611, an RFP that has undergone substantially less mutagenesis than DsRed and the mFruits. Furthermore, mRuby2 has been shown to be excellent for fusion-proteins as well as green-red fluorescence resonance energy transfer (FRET) sensors. tdTomato was chosen given its excellent quantum yield, and because of the potentially stabilizing affect of the native A/C interface. Furthermore, it is quite popular amongst neuroscientists for *in vivo* 2-photon imaging, despite its poor photostability.

For mRuby2, a library of 160,000 members was created by mutating positions Ser61, Trp90, Trp140, and M160 to all 20 amino-acids. The library was created using site-overlap extension, and was subsequently recombination into pCLNCX-Dest, $\approx 2.3 \times 10^6$ CFU were generated, providing >14-fold coverage. Following viral transduction of the HeLa S cells, G418 selection was applied, and FACS was used to enrich library.

Expectedly, given the importance of tryptophan residues in stabilizing the core of proteins, less than 1 % of the library was fluorescent. Cells were expanded, the mRNA was isolated, the cDNA was prepared, and the FPs were PCR amplified. This library is awaiting commercial sequencing and will likely be subjected to error-prone PCR following characterization.

For tdTomato, which consists of two identical FP subunits tethered with a flexible peptide linker, saturated mutagenesis posed a technical challenge. Two domains doubles the number of positions targeted, creating an impossibly large amount of diversity. For example, targeting four positions simultaneously generates 20^4, or 160,000 mutants. Targeting eight positions, however, would result in 25.6×10^9 mutants. Furthermore, different permutations of the mutations would likely be present in each subunit, and the spectral phenotype would be a weighted average of the two individual subunits. Targeting one subunit would also suffer from a weighted spectral phenotype. To circumvent this challenge, the peptide linker was removed, and the N and C-termini were modified so that dimerization could occur spontaneously *in vivo*. Using this strategy, a single protein domain could be mutated. Accordingly, dTomato (as opposed to tdTomato), was found to be fluorescent in HeLa cells.

To model dTomato, two of the subunits were removed from the crystal structure of DsRed (see Figure A.10). dTomato contains three tryptophans, two located near the opening in β-strand 7 and 10, and the third is in the immediate vicinity of the chromophore. Trp58, Gln64, Trp93, and Trp143 were mutated to all twenty amino acids, and Gln163 was mutated to a subset of amino-acids (Gln/His/Leu/Lys/Met/Ile/Asp). Gln64 was selected for it's hypothesized role as a "gateway" residue for molecular oxygen diffusion [76]. Gln163 was mutated as a result of its close proximity to Trp143. The total library size was 1.12×10^6 mutants. A total of 1.7×10^6 CFU have been prepared to date.

A.1.6 Error-Pronce PCR of mRuby2 and dTomato

The majority of libraries presented here have relied upon saturated mutagenesis. However, error-prone PCR can be used to identify positions that alter a specific photophysical property, particularly when the mechanism governing that property is unknown. Once the positions have been identified, they can then be submitted to saturated mutagenesis at these positions to identify the best amino-acid substitution. In an

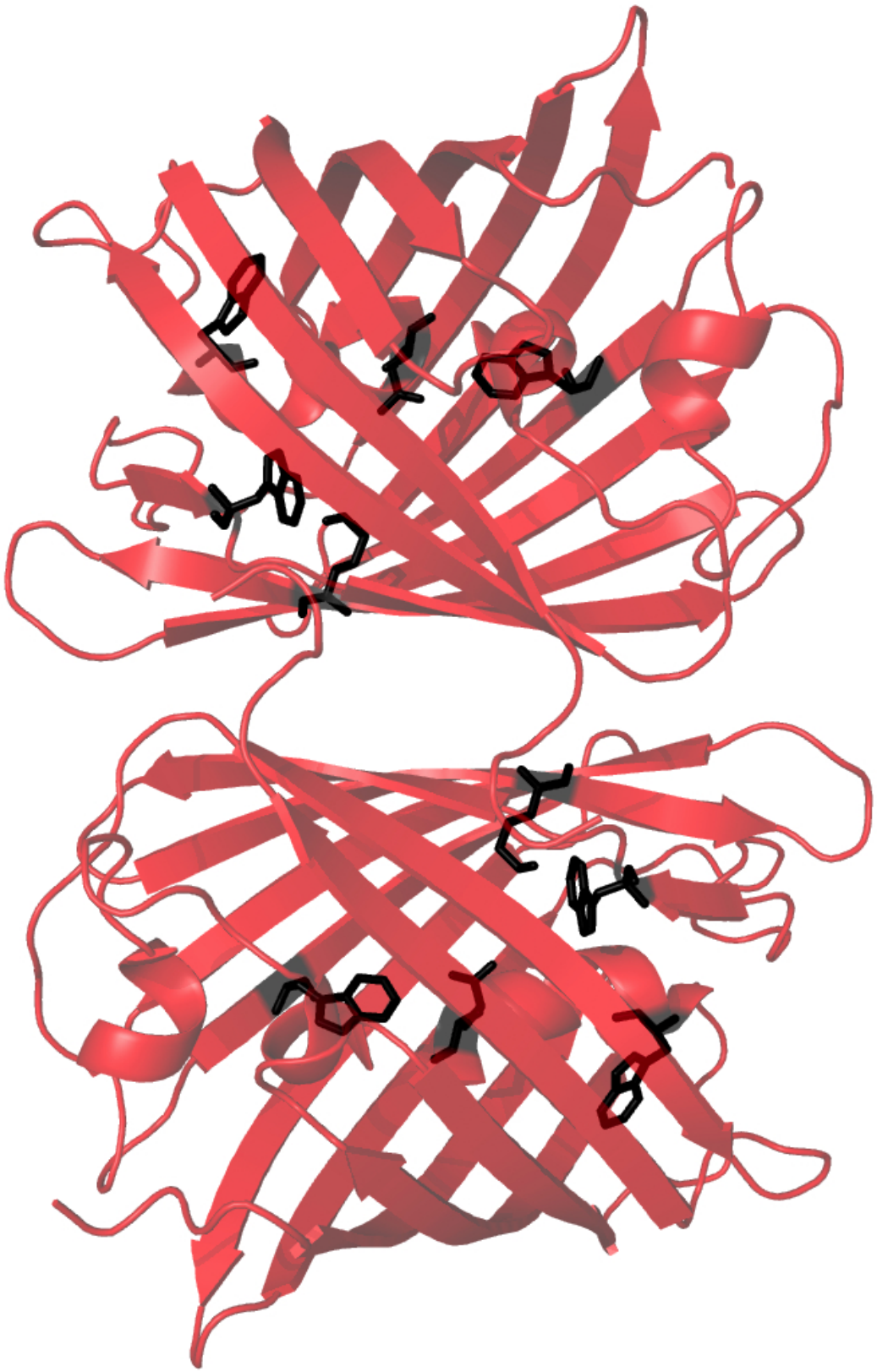

Figure A.10: Positions mutated in the dTomato library.

attempt to identify positions that could influence the photostability of mRuby2 and dTomato, error-prone PCR was carried out under conditions that cause 9-16 mutations per kb. Libraries of 1.7×10^6 and 1.5×10^6 mutants were prepared for dTomato and mRuby2, respectively.

HeLa S cells were transduced with virus containing the mRuby2 library. Given the size of the library and constraints on throughput for the microfluidic photobleaching cytometer, it was subjected to multiple rounds of selection to diminish the size of the diversity present. In the first round of selection, $\approx$ 600,000 of the top-third brightest cells were collected. For the second round, $\approx$ 100,000 of the brightest 3 % cells were collected. Cells are ready for analysis in the microfluidic photobleaching cytometer. The DNA for the dTomato library has been purified and is ready to generate virus for transduction of HeLa S cells.

A.1.7 K2C Oxygen Gateway Mutations

Molecular dynamics carried out on K2C suggested that the dynamics between β-strand 7 and 10 were diminished relative to mCherry (data not shown). However, preliminary data suggested that photobleaching of K2C remained sensitive to oxygen. Two other positions, Gln64 and Phe99, however, were thought to possibly be a secondary route for oxygen diffusion [76]. Consequently, K2C was submitted to saturated mutagenesis at these positions, and cloned into pBad. The library has been prepared, fluorescent clones have been confirmed, and it is awaiting screening and testing for sensitivity to oxygen.

Appendix B

Detailed Protocols

B.1 Saturated Mutagenesis

Design primers to introduce mutations at the specified position within the gene. The nucleotide wildcards should be approximately located within the center of the primers, secondary structure should be minimized, and the annealing temperature should be kept high (>65°). In general, the fragments of the gene that you amplify should be greater than ≈ 70 base pairs because of difficulties in PCR amplification and purification of smaller DNA fragments. Pfu is always used for amplification of the fragments. For site-overlap extension, Pfu is preferred over Taq given that it will introduce less errors outside of the regions of interest. However, for some challenging site-overlap extension reactions where Pfu fails, Taq has been used.

- In separate PCR reactions, amplify fragments using Pfu. Standard PCR conditions apply:

  40 μL deionized H_2O

  5 μL 10x Pfu Buffer

  1 μL 10 mM dNTP

  1 μL 1DNA template (≈ 100 ng/1 μL)

  1 μL 25 μM Primer 1

  1 μL 25 μM Primer 2

  1 μL 25 of Pfu Polymerase

1x 95 degrees - 2 minutes

3x 95 degrees - 2 minutes, 56 degrees - 30 seconds, 72 degrees - (1 min/kb)

3x 95 degrees - 2 minutes, 54 degrees - 30 seconds, 72 degrees - (1 min/kb)

20x 95 degrees - 2 minutes, 52 degrees - 30 seconds, 72 degrees - (1 min/kb)

1x 72 degrees - 10 minutes

- Purify DNA fragments with 2% agarose gel, and determine the reaction yield for each individual fragment with a NanoDrop UV-Vis spectrophotometer.

- Take 5 μL of each fragment ($\approx$ 100 ng each fragment) and combine in a single PCR tube using Pfu reaction components (buffer, etc.). Repeat with PCR reaction, as above, except with 60 seconds of annealing time instead of 30 seconds, and with the elongation time adjusted to provide amplification of the entire gene.

- Gel purify resulting DNA fragment with 1% ultra-pure agarose with ethidium bromide. If fragment size is as expected, continue to ligation, gateway recombination, etc. It is very common to see partially amplified fragments in this reaction.

B.2 DNA Shuffling

- PCR Amplify the genes of interest, and gel-purify to remove template and primers.

- In 100 μL, combine 3 μg of the DNA substrate(s), 0.3 units of DNase I (Promega), 10x RQ1 DNaseI and incubate for 15-20 minutes at 20° Celsius. Add to the reaction with RQ1 Stop Buffer, and incubate at 65° Celsius for 10 minutes.

- Purify 50-200 basepair fragments by electrophoresis onto a DE81 paper, elute with 1 M NaCl, and purify DNA by ethanol precipitation. Alternatively, for larger fragments (e.g., >80 basepair), the appropriate sized bands can be excised from the 2% gel and gel-purified using a commercial kit.

- Prepare “primer less” PCR mix:

10-30 ng/μL DNA

2 μL 10 mM dNTPs

10x Taq Buffer (2.2 mM MgCl2, 50 mM KCl, 10 mM Tris-HCl, pH 9.0, 0.1% Triton X-100)

2.5 U Taq Polymerase

100 μL total reaction volume

- Setup PCR Thermocycler:

  45x:

  95° Celsius for 30s

  50° Celsius for 30s

  72° Celsius for 30s

  1x:

  72° Celsius for 10 min

- Dilute primerless PCR reaction 1:40 into typical PCR mixture, with store-bought Taq Polymerase Buffer and Taq Polymerase. Use of Pfu, or homemade Taq buffer (as above in step 3) appears to give an unnecessarily large amount of frame-shifts.

- The paper, Optimization of DNA shuffling for high-fidelity recombination provides useful tips for how to control the error-rate. For example, using Mn(II) instead of Mg(II) during the DNase I fragmentation step improves fidelity 3-fold (10x reaction buffer: 500 mM Tris-HCl pH 7.4, 100 mM MnCl2). Also, use of higher fidelity polymerases (they use Pfu) for both the original PCR amplification, primerless amplification, and standard primer amplification, can improve fidelity. Additionally, obtaining the fragments to be DNaseI treated from restriction digest of a plasmid can decrease the errors. Protocol adopted from Stemmer, PNAS, 1994.

B.3 Error-Prone PCR

- 1 μL of dilute DNA to be mutated (10's of fmol) - Concentration important for final error rate. 1 μL of 25 μM forward primer 1 μL of 25 μM reverse primer 4 μL of 5 mM dGTP 4 μL of 5 mM dATP 20 μL of 5 mM dCTP 20 μL of 5 mM dTTP 1 μL of Taq Polymerase (5 units) 5 μL of 10 mM MnCl2 3 μL of H2O 40 μL of 2.5x buffer

- Add MnCl2 after all the other PCR components except for Taq to prevent precipitation. Total reaction buffer should be 100 μL, with 30 cycles of denaturing, annealing, and elongating. Finish with a 10 minute elongation period at 72 degrees Celsius.

- 2.5x Buffer: 125 mM KCl, 25 mM Tris-HCl pH-8.3, .03% by mass BSA, 17.5 mM MgCl2

B.4 Gateway Cloning

- BP and LR clonases have different optimal conditions. For optimal efficiency, absolutely necessary to perform Proteinase k digestion (>4x improvement).

- If the initial library is made by recombining into pDonr221 and then maxi-prepping the library, one should perform EcorV digestion of the pDonr221-library prior to the LR reaction.

- For electroporation of library, combine two 10 μL LR reactions, remove salts through ethanol precipitation, and resuspend into 2.5 μL of T.E. Combining two reactions for every 50 μL of electrocompetent cells appears to work well. No additional gain observed when combining four reactions.

- BP Reactions - 2 μL of pDonr221 (150 ng/μL) in T.E. 60 ng of attB PCR product. 2 μL of BP clonase, 5 uL of T.E. 18 hours at 25 degrees Celsius. Gives around 600,000 clones.

- LR - 2 μL of Destination Vector (150 ng/μL), 200 ng/μL of pDonr221 library. The LR reaction works best if the donor fragment has been relaxed. So long as your gene does not contain EcorV, this restriction endonuclease works well at site-specifically cleaving the vector backbone of

pDonr221. Alternatively, the gene to be cloned into your destination vector with LR Clonase II can be amplified from a pDonr221 parent with M13Forward and M13Reverse. The latter is ideal for generating libraries since this decreases cost, preserves diversity of the library, and saves time.

B.5 Ethanol Precipitation of DNA

- For 20 μL reaction (ligation, recombination, etc.), add 1 μL of 20 μg/μL glycogen, 2 μl of 3 M Sodium acetate (pH=8.5), and 50 μl of 100% Ethanol. I find that the round-bottomed Eppendorf tubes are the easiest to work with, since they enable facile visualization and air-drying of the DNA precipitate.
- Precool chiller to 4° Celsius.
- Put reaction in -80° Celsius freezer for 15 minutes. Longer durations appear to increase yield.
- Spin at 14,000 RPM for 30 min
- Wash with 200 μL of 75% Ethanol, spin for 15 minutes at 14,000 G.
- Repeat 200 μL 75% Ethanol rinse, spin again for 15 minutes at 14,000 G.
- Very gently remove the ethanol, careful not to distrub the pellet.
- Resuspend in desired volume (usually 2.5 μL) of TE (Tris-EDTA)

B.6 Electroporation of E. coli

- Allow the electrodes to warm up for at least a half hour, settings are 2 kV, 200 Ω, and 25 μF.
- Keep everything very cold throughout the process. Only use prechilled electrode cuvettes, tips, solutions, etc.
- Very gently add 50 μL of the electrocompetent cells into the tube with the resuspended DNA from the ethanol precipitation. Allow to sit $\approx$ 30 seconds, and then very gently transfer the

electrocompetent cells and DNA into the prechilled electrode cuvette. Gently tap the cuvette on a benchtop to get the cells the bottom and eliminate bubles.

- Allow to cells to incubate with DNA for 5 minutes on ice within electrode cuvette. The smaller the volume of DNA added to the cells, the higher the competency.
- Insert electrode cuvette into the electroporation equipment, and press the "pulse" buttons simultaneously. It will flash, and then beep. Immediately after electroporating the cells, add prewarmed 450 μL of prewarmed SOC to the cuvette.
- Gently transfer the 500 μL of SOC/cell mixture to a sterile culture tube, and rinse the electrode cuvette 3x with 500 μL of SOC, bringing the total volume up to 2 mL. Place in shaker for 1 hour at 37° Celsius
- Plate a dilution of the transformation (10^{-3}, 10^{-4}), and back-calculate the total number of colonies. Dilute remainder of culture to 10 mL, add appropriate antibiotic, and place in shaker overnight.
- The following day, proceed to purify DNA with a mini-prep, inoculate a larger culture for a midi-prep, or create glycerol stock of bacteria.

B.7 Screening Bacteria by Colony Fluorescence

- Transform or electroporate library into an appropriate cell line. For pBAD, Omnimax, Electromax, and Top10 cells work best. For pET vectors, Bl21 (DE3) pLysS is most appropriate.
- Perform dilution after transformation or electroporation to estimate total number of colony forming units (CFU), and dilute remainder of library to a final concentration of 20% glycerol for storage at -80° Celsius.
- Plate the remainder of the library, aiming for around 2000-3000 colonies per plate, with arabinose present in the plate at a concentration of .02% mass fraction or an IPTG concentration of 1 mM (can be toxic at too high of concentrations). If control of the induction time is necessary, plate the

library on a nitrocellulose membrane, grow overnight, and transfer to arabinose or IPTG containing agar for the desired amount of time (e.g., $\approx$ 3 hours at 37° Celsius).

- Pick clones for growth in 96-well Deep-Well plates. After sufficient time for growth, make 20% glycerol stocks, pool different clones, and subject to additional rounds of mutagenesis and selection.

B.8 Sorting of Bacteria by Fluorescence Activated Cell Sorting

- Grow 3 mL of LB cultures of library (or positive control).
- Dilute overnight cultures 100-fold in fresh 3-mL LB culture.
- Grow for 2 hours at 37° degrees or until it reaches an optical density of 0.6 and then induce for 3 hours. Induction can be carried out at 25° or 37° Celsius. Inducing for 3 hours is advantageous because it also selects for quickly maturing fluorescent proteins, but can be carried out overnight as well.
- Perform two successive 400x dilutions into HHBSS and screen by FACS. Flow-cytometer should be configured to trigger off of side-scatter with 488-excitation, and the threshold of triggering should be decreased to just above the scatter generated by an empty droplet. Forward scatter, side-scatter, and fluorescence channels should all be in 'log' mode. It is often nice to set the sort-logic to include a side-scatter/forward-scatter gate and a red-fluorescence gate, while excluding cells that appear in the autofluorescence and green-fluorescence region. Typical PMT voltages including 400 and 520 volts, for GFP and RFP, respectively. A "sort single" mode is most typical, but an "enrich" mode can also be used. In the literature, it has been reported that fluorescence intensity can be scaled by the scattering amplitude to account for cell size and morphology.
- Sort cells into 500 μL of LB or SOB without antibiotic, and allow cells to recover at 37° Celsius with shaking for $\approx$ 30 minutes. Plate on LB/Agar with the appropriate antibiotic. It is pretty common to only have $\approx$ 30-50% efficiency for sorting for bacteria on a FACS.

B.9 Screening Solubility of Protein

- Pellet 3 mL of culture in a 1.5 mL eppendorf tube.
- Rinse pellet twice with 1 mL of 10 mM Tris, pH 7.5, 0.15 M NaCl.
- Resuspend in 150 uL of 10 mM Tris, pH 7.5, 0.15 M NaCl.
- Subject to 10 pulses of sonication, with a minimum power setting and 80% duty cycle.
- Centrifuge sonicant at 14,000 g for 15 minutes, remove supernatant.
- Wash pellet twice with 1 mL of 10 mM Tris, pH 7.5, 0.15 M NaCl. Finally resuspend in final volume of 150 μL.
- Remove a 5 uL aliquot of the pellet and supernatant, mix with 5 μL of SDS buffer containing DTT, heat for 15 minutes at 100 degrees in a thermocycler.
- Resolve protein using a 12.5% acrylamide gel, stain with Coomassie, fix. Image gel using densiometry, allowing analysis of soluble and insoluble fraction. Can use internal standard of BSA at 2 mg/mL.

B.10 Colony PCR

- Mix 35 μL of distilled water, 5 μL of Taq 5x buffer, 5 μL of Taq Mg Stock, 1 μL of 10 mM dNTPs, 1 μL of 25 μM forward primer, 1 μL of 25 μM reverse primer.
- Dip pipette tip onto the top of the colony, and then pipette vigorously (>20×) into the mixture above.
- Boil at 95 degrees Celsius for 20 minutes
- Spike in .5-1.0 μL of Taq Polymerase, and carry out normal PCR conditions thereafter. Cheap polymerases are preferred, particularly homemade polymerases, to decrease the cost of the screening.

B.11 DNA Purification of Fragments >300 Basepair in Size

- Add 150 μL of TE, pH 8.0 to a 50 μL amplification reaction containing your PCR product.
- Add 100 μL of 30% PEG 8000/ 30 mM MgCl2. Vortex to mix thoroughly and centrifuge immediately at 10,000 G for 15 minutes at room temperature. Increasing the centrifugation time and/or speed will increase the yield.
- Carefully remove the supernatant. The pellet will be clear and nearly invisible.
- Dissolve the pellet in 50 μL of TE, pH 8.0. (If this is for attB recombination, the concentration should remain greater than 10 ng/μL.)
- Check the quality and quantity of the recovered PCR product on an agarose gel.

B.12 Generation of Retrovirus - pCLNCX, pCL-TetON, pCL-Ampho

- Day 1: Plate 293 cells in 10 cm dishes. Cell density should be such that cells are $\approx$ 70% confluent tomorrow.
- Day 2: Transfect virus into 293 cells using Trans-IT.

  1 μg pVSV-G.

  8 μg desired DNA in viral vector (usually pCLNCX, or pCL-TetOn).

  8 μg packaging vector (usually pCL-Ampho)

  700 μL OptiMem

  20 μL Trans-IT

  Let mixture sit at room temperature at least 15 min, then add to cells.
- Day 3: Change medium of transfected HEK293 cells. You need to do this very carefully since HEK293 cells do not adhere to the plate strongly.

- Day 4: Look at cells to see if transfection worked. If you are using a fluorescent protein, pCLNCX transfected cells should be brightly fluorescent. If you are using pCL-TetOn, addition of doxycycline (final concentration $<1\mu$g/mL) can trigger gene expression.

- Remove media and gently filter through a cellulose acetate or polysulfonic 0.45 micron filter (dont use nitrocellulose) to remove any unwanted cell debris. At this point virus can be used to infect cells or can be frozen for future use. In general, after 48 hours, virus production is at its maximum rate. However, additional virus can be obtained at 72 hours if the HEK293 cells are still adhering to the plate. If you would like to freeze the virus, flash freezing in liquid nitrogen and storage at -80 ° Celsius is recommended. Note that the titer (infectability) of the virus will decrease after being frozen.

- To carry out infection, the cells should be exponentially growing, and have not been trypsinized for $\approx$ 24 hours. Retrovirus can only infect dividing cells, and relies upon receptors for internalization. Change the media, keeping in mind that you will also be adding virus containing supernatant. Add polybrene to fresh media and cells, and swirl in dish to distribute. The final concentration of polybrene should be $\approx$ 12 μg/mL (although polybrene can be titrated from 2 - 12 μg/mL if 12 μg/mL is found to be toxic). Add viral supernatant ($\approx$ 100 μL to 3 mL, depending upon how optimized the transfection was). Virus integration follows a Poisson distribution, and high enough concentrations of virus supernatant can inhibit infection. For libraries, a multiplicity of infection of $\approx$ 10% is desired, and titrating the virus can help achieve this. For Tet-inducible virus (pCL-TetOn), you will need to also infect the cells with pCL-TRE (Tet-Resonsive Element)

- Day 5: Change the media on the cells that were infected, since polybrene can alter cell growth.

- Day 6-7: Select for positive cells. If fluorescent, this can be FACS. If you infected cells with a library that has variable fluorescence, e.g., a mutated FP library, you can treat the cells for 1 week at 1 mg/mL G418 to eliminate non-infected cells.

B.13 Recovery of Small HeLa Cell Populations

In conditions where a low-number of cells are being sorted (down to 1 cell), altering the media conditions can help recovery. I have typically used 30% FBS DMEM. However, I have also heard of people supplementing their media with 10% preconditioned and sterile filtered DMEM. Alternatively, I have also heard about DMEM with 50% FBS.

B.14 Quantum Yield Protocol

- Measuring the fluorescence quantum yield is relatively easy, but time-consuming, and often somewhat inaccurate. The inaccuracies of the method can be overcome by minimizing the number of transfers, i.e., between the spectrophotometer and the fluorimeter, performing the appropriate zero/baseline, cleaning vigorously between measurements, and minimizing the time between the measurements. All of these things decrease the amount of protein/dye that can absorb onto the cuvette, or evaporation that can decrease the sample volume. Overall error within 10% of established values is deemed a success. The first step is to decide which wavelength region that you are particularly interested in. Below is a list of established quantum yield references. For citations regarding these references, refer to Lakowicz - Principles of Fluorescence Spectroscopy. Be cautious however, many of these dyes show a rather large concentration, pH, and temperature dependence with regard to their quantum yield. The dye should be selected such that your sample, and the dye can both be excited at the same wavelength, and the entire emission can be observed. The excitations listed below are not absolute, and I recommend measuring the excitation/emission spectra of your sample and the reference dye, and picking a wavelength that works best for you. Furthermore, the use of two reference dyes is far better than one, preferably one with a quantum yield greater than your sample, and one with a quantum yield less than your sample. This not only gives you two measures of quantum yield, thus providing a measure of error, but allows you to cross-calibrate each reference dye with the other and estimate the amount of error in the measurement

- Cuvette Choice - All measurements must take place on a dilute sample whereby the maximum absorbance red-shifted of where you measuring the absorbance is 0.1 for a 1 cm cuvette, or 0.4 for a 4 cm cuvette. For example, if you are measuring the absorbance at 530, but the dye has an absorbance maximum at 560, then the peak at 560 should never be greater than the aforementioned ODs. In JILA, I have machined a cuvette holder for the 4 cm cuvette and highly recommend its use given that the error decreases substantially with the longer path-length.

- Spectrophotometer Choice - I prefer to use the Cary spectrophotometer in JILA given that this instrument is extremely sensitive and reproducible. One needs to make sure that the instrument is in dual-beam mode such that intensity changes are corrected for. Also, prior to reading your sample, one should place the cuvette into the spectrophotometer with your buffer solution, zero, then baseline this solution, and then without moving the cuvette, add your protein and measure the absorbance. It is at this stage that I write down the absorbance at the exact wavelength that I will excite at in the fluorimeter, transfer about a mL (4 cm cuvette) into an eppendorf tube, dilute the original sample without introducing bubbles, and measure again. I repeat this process until I have 4-5 samples of appropriate intensity (OD= .4, .3, .2, .1, .05). Under ideal conditions, one would be able to take the cuvette directly from the spectrophotometer and place it into the fluorimeter, thereby measuring the exact same solution. This will no doubt decrease your error, but in cases with multiple samples, the duration of time to do this would be too onerous.

- Fluorimeter Choice - The Perkins lab fluorimeter is nice because it offers temperature controll, and is also much faster and appears to be more sensitive than the PTI fluorimeter in BioFrontiers. Furthermore, it is in the same building as the spectrophotometer, an obvious advantage. However, I have measured the exact same solutions on both fluorimeters, and both fluorimeters have given me the exact same quantum yield.

- Once you have repeated this for all of your solutions, you can plot a graph of the integrated fluorescence versus absorbance. Make sure that you measure the fluorescence on a blank sample for each different solvent that you use, and subtract this value from your integrated fluorescence

values. This graph, if everything is done properly, should be linear and have a y-intercept of 0 (0 absorbance should mean 0 fluorescence).

- Fit the integrated fluorescence intensity versus absorbance plot to a linear equation, and force the y-axis through 0. Take the slopes from the fit, and insert the values into the following equation:

$$phi_x = phi_{ref} \times \frac{Slope_x}{Slope_{ref}} \times \frac{\eta_x^2}{\eta_{ref}^2} \tag{B.1}$$

Here, ϕ is the quantum yield of your unknown (subscript x) and your reference standard (subscript ref). The slopes are determined from the aforementioned linear-fit. η is the refractive indices for the solutions used, and NIST reported refractive indices are the following: water (1.3336), Methanol (1.3290), Ethanol (1.3614). One can also measure the refractive index yourself with the refractometer that is available in Dr. Robert Kutchta's lab. It is likely that the refractive index between buffered solutions and deionized water will be different.

- Signs of Success:

  Linear relationship between absorbance and fluorescence

  Graph naturally goes through zero.

  Cross-calibration of each reference dye gives the reported value within 10% error

B.15 Preparation, Use, and Cleaning of Microfluidic Devices.

- In general, no microfluidics or any part of the device holder can leave the optics table tent without being sealed in a jar. They can never be exposed to ambient air. Exposure to particulates will increase the rate of clogging of the microfluidic channels, and laser-induced burning with the 1064 nm trap laser.

- Never touch any microfluidics or any parts of the device manifold (white manifold, "o" rings, and orange rubber stoppers) with anything other than tweezers.

- Make sure that the water level of the sonicator is never higher than the lids of the containers since they are obviously not water proof jars. However, keep the water level at minimum level indicated on sonicator tank.
- If you need to change the liquids in the reservoirs, use tweezers and put the orange stoppers into their water jar. The metal lid and screws do not go into the water jar.
- Try to never use high pressure (>20 psi), as this will likely cause more junk to appear, and will increase the likelihood of 'lodging' the junk into an immobile position within the microfluidic.
- Every liquid (except cells) goes through 0.2 μm filter
- Ultrapure water out of jug does not need to be filtered for cleaning purposes but does need to be filtered if being pumped through microfluidic
- Refrigerate any solutions other than bleach and water
- Use a new syringe and filter each day (0.2 μm filters are in the wet lab, be on-top of ordering more filters/syringes when you are running low...they do not magically appear)
- Never store anything (e.g., O-rings, screws, etc.) other than glass chips in bleach solutions
- If liquid backs up into pressure-supply tubes, disconnect them from the device manifold but leave them connected to the pressure controllers and run air through them at high pressure until dry
- If you need to use new tubes or want to clean the tubes, cut them to the required length (located in JILA stock room) and sonicate them in ultrapure water for >40 minutes in a sealed jug. Then, attach them to the 20 PSI air (on microscope) and run air through them to dry them out for >20 min.
- PRE-RUN (will take ≈1.5-2 hrs):
    * Sonicate the device in the same ≈10% bleach solution that it was stored in overnight for 40 minutes

* Simultaneously sonicate jar of "o" rings and orange rubber stoppers (could add small amount of alconox before)
* Hold jar with manifold and ultra pure water (could add small amount of alconox before) in sonicator for a few minutes (do not want it to change temperature though..temperature swings will distort the plastic (Kel-F) manifold)
* Rinse white manifold three times with ultrapure water (leave third rinse water in container to store manifold in when experiments are over)
* Rinse "o" rings and stoppers three times with ultrapure water and then leave in third aliquot of water
* Remove microfluidic from the jar with tweezers and hold it over the waste bucket to rinse off with the ultrapure water from jug
* Put microfluidic into bottom of metal device holder
* Place "o" rings on manifold with tweezers
* Place manifold on top of microfluidic
* Screw manifold retaining ring on (not too tight!)
* Fill reservoirs with 0.2 μm filtered ultrapure water
* Place stoppers into holes with tweezers
* Attach metal lid with two screws (can be done without tweezers) C
* lean outsides of device interrogation region (top and bottom) with pink objective cleaner and/or MeOH with lens tissue (after it is mounted so that ports are covered!) so that lasers to not scatter from possible dirt
* Pump water through device at 10-20 PSI for 5-10 minutes
* Replace water with BSA solution (at this point, bubbles should not have appeared and so the device is primed and you should not use or need to use >2 psi for BSA solution or any

solutions with proteins/cells in them) and pump BSA solution at 2 psi for ≈>30 min (could prep cells during this time...)

  * Empty outlets
  * Ready to run! (remember to filter cells with 40 μm filter and buffers with 0.2 μm filter) If you want to recover the cells after the experiment, load the outlet reservoir ("keep" reservoir) with 75 μL pink cell media

- POST-RUN (will take ≈40 minutes unless you wait for sonication to end):
  * Remove cells
  * Run buffer through device for 5-10 minutes to try and get rid of as many cells as possible at 2 psi
  * Empty outlets
  * Replace buffer with water and run for ≈10 min at 10-20 psi
  * Empty outlets
  * Replace water with 100% filtered bleach from bottle (use a different pipette tip each time you dip into bleach bottle) and run ≈10 minutes at 10-20 psi
  * Empty inlets and outlets
  * Disassemble device holder and all parts of manifold except stainless steel quick connects.
  * Put microfluidic into its conical tube with new ≈10-20% bleach solution (filtered bleach and ultrapure water...neither need to be re-filtered at this point)
  * Sonicate for 40 minutes (can put on timer and leave overnight in sonication bath)
  * Everything else is just stored in water overnight with possible addition of alconox...bleach will cause rust to metal and degrade rubber so never leave these parts in bleach for any length of time longer than ≈10 min.

Appendix C

Electrical Diagrams

This appendix provides electrical diagrams for several instruments designed by the Electronics Shop at JILA, and will provide short descriptions of their purpose, and how one can use them.

C.1 PMT Transimpedance Amplifier

The PMT transimpedance amplifier is a fundamental component in our microfluidic flow-cytomer, and it's electronic layout is provided in Figure C.1 It has one input, and directly accepts the PMT photocurrent, and two outputs. The DC output provides a 1 volt signal for a 100 μA input, which if sustained, is capable of damaging the PMT. The AC output provides 10 volts of signal for a 100 μA input, but is AC-coupled with a bandpass of 0.16-10.6 kHz. The high pass time constant is determined by R3, R4, and C5. The low pass time constant is determined by R3, R4, and C6. The output signal is accordingly conditioned, and has decreased noise relative to the DC output. In general, AC-coupling is always trying to average the signal to 0. Therefore, following a bright pulse of light, you will see the output voltage go negative temporarily.

Figure C.1: PMT Transimpedance Amplifier

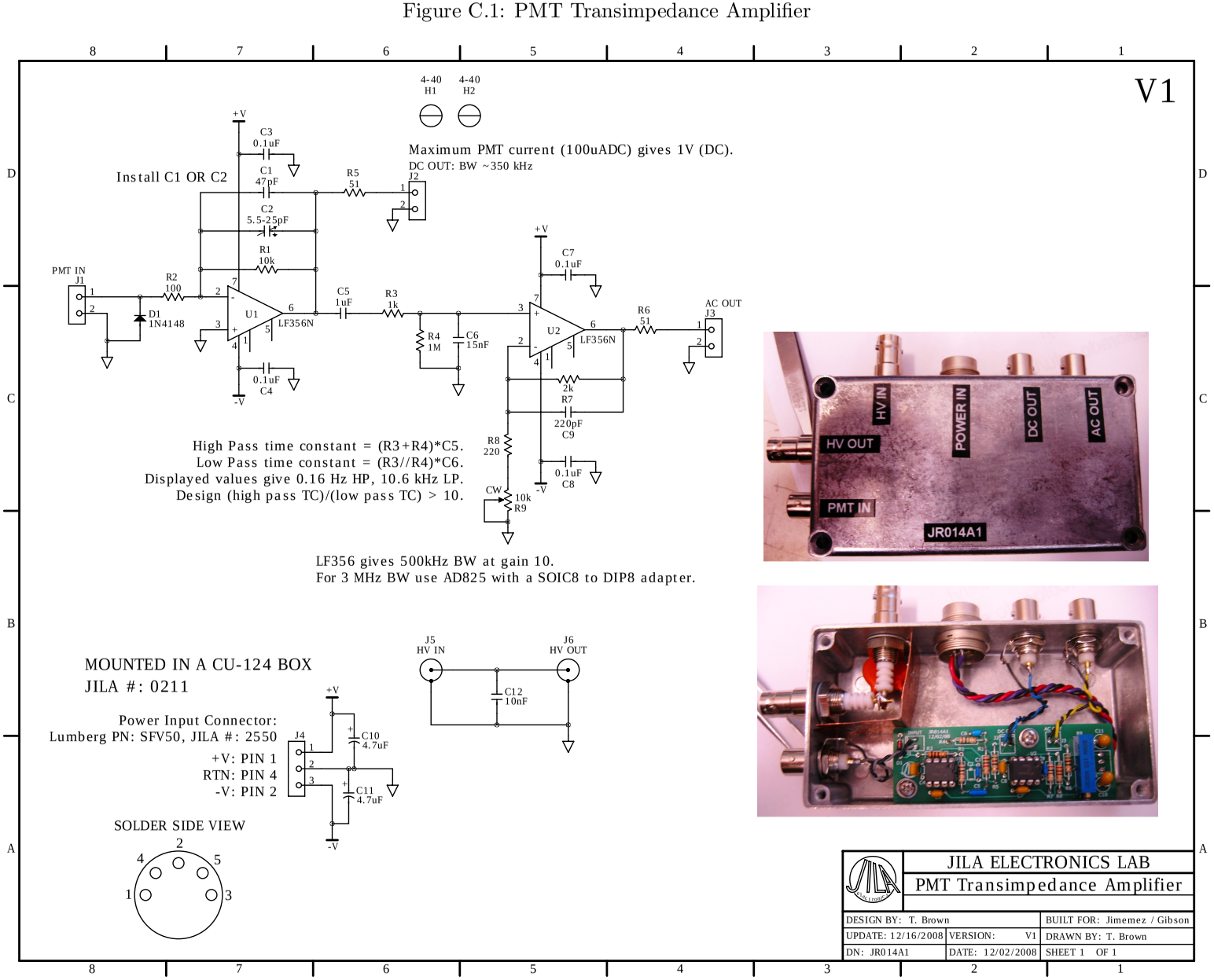

C.2 Phase Detector Auxiliary Board

The high-bandwidth phase-detection electronics described here is composed of an Analog Devices AD8333 Dual I/Q demodulator evaluation board. There are several inputs to the I/Q demodulator. The first input is a 20 dB pre-amplifier that shows high amplitude-dependent phase shifts, and should be avoided. The second input is an AGC amplifier that provides up to 40 dB gain so that the output voltage is matched to the ideal input for the I/Q demodulator, which is 63 mV_{RMS} (I/Q demodulator input impedance is 200 Ω). The AGC also has a power monitor that is proportional to the gain added to the signal, and may be used to back-calculate the signal amplitude. Furthermore, the AGC should have >7 mV_{RMS} AC signal to properly amplify the signal for subsequent phase-detection. The third input goes directly into the I/Q demodulator for phase-detection. Arbitrary phase-delays between the signal and the local-oscillator can be provided in 22.5° increments through adjustment of the thumbwheel on the front of electronics box. Given that the I/Q demodulator is built in dual-channel configuration, I and Q outputs can be individually measured, or the same signal can be delivered to two channels, and subsequently the I and Q outputs from the two channels can be summed for improved noise-immunity. A 180° toggle on the front of the electronics can also be used to lock-into the I/Q signals accurately. The I/Q outputs can also be low-passed filter with user-specified cut-off frequencies, as determined by the electronics front-panel. Currently, the I/Q demodulator is designed to only provide a 62 mV difference in signal between the I and Q channels for a 5° phase-shift, when operating at 45° in phase-space. Increased resolution may be provided with additional amplifications and user-specified DC-offsets.

Appendix D

Matlab Code

D.1 Introduction

Several pieces of code are provided in this section, and provided with a concise comment on what each command is performing. If executing this code, it is necessary to only use the commands.

D.2 Four-Beam Microfluidic Raw File Analysis

Command	Comment
clc;	Clears command window
clear;	Clears Workspace variables
LowerLimit14 = 22;	Specifies low limit for transit from beam 1 to beam 4.
UpperLimit14 = 27;	Specifies upper limit for transit from beam 1 to beam 4
fid1 = fopen('peaklocationsk2-2a.bin','r','b');	Open binary file of Peak Locations
fid2 = fopen('peakamplitudesk2-2a.bin','r','b');	Open binary file of Peak Amplitudes
time = fread(fid1,[1,inf],'float64');	Reads raw data file under 64 bit unsigned integer
time = time';	Reorients time data into a single column
time = time/125;	Converts from data points to milliseconds, assumes 125 kHz Sampling Rate
PeakAmp = fread(fid2,[1,inf],'float64');	Reads raw data file under 64 bit unsigned interger
PeakAmp = PeakAmp';	Reorients amplitude data into a single column

DataSize = size(time);	Determines size of data
dT14 = [ ];	Creates empty vector for transit-time from beam 1 to 4
for m = 4:(DataSize(:,1));	Specifies number of for loops
dT14 = [dT14 time(m)-time(m-3)];	Calculates time between pulses apart by 4 in time
end	Finishes for loop
dT13 = [ ];	Creates empty vector for transit-time from beam 1 to 3.
for m = 3:(DataSize(:,1));	Specifies number of for loops
dT13 = [dT13 time(m)-time(m-2)];	Calculates time between pulses apart by 3 in time
end	Finishes for loop
dT12 = [ ];	Creates empty vector for transit-time from beam 1 to 2.
for m = 2:(DataSize(:,1));	Specifies number of for loops
dT12 = [dT12 time(m)-time(m-1)];	Calculates time between pulses apart by 2 in time
end	Finishes for loop
dT12 = dT12'; dT13 = dT13'; dT14 = dT14';	Reorients transit-time vectors into columns
dT12(max(size(dT14)):end-1,:) = [ ];	Deletes last value in vector
dT13(max(size(dT14)):end-1,:) = [ ];	Deletes last value in vector
dT = [dT12 dT13 dT14];	Assembles transit-times into a single matrix
clear dT12 dT13 dT14 fid1 fid2 m DataSize	Clear specific workspace variables
A(:,3) = (dT(:,3) <UpperLimit14);	Identify peaks (4 and 1) with transit-time smaller than maximum allowed
B(:,3) = (dT(:,3) >LowerLimit14);	Identify peaks (4 and 1) with transit-time larger than minimum allowed

C(:,3) = A(:,3)&B(:,3);	Create logic vector for peaks that satisfy both minimum and maximum transit-times.
A(:,2) = (dT(:,2) <UpperLimit14.*(2/3));	Identify peaks (3 and 1) with transit-time smaller than maximum allowed
B(:,2) = (dT(:,2) >LowerLimit14.*(2/3));	Identify peaks (3 and 1) with transit-time larger than minimum allowed
C(:,2) = A(:,2)&B(:,2);	Create logic vector for peaks that satisfy both minimum and maximum transit-times.
A(:,1) = (dT(:,1) <UpperLimit14.*(1/3));	Identify peaks (2 and 1) with transit-time smaller than maximum allowed
B(:,1) = (dT(:,1) >LowerLimit14.*(1/3));	Identify peaks (3 and 1) with transit-time larger than minimum allowed
C(:,1) = A(:,1)&B(:,2);	Create logic vector for peaks that satisfy both minimum and maximum transit-times.
clear A B LowerLimit14 UpperLimit14	Clear specific workspace variables
data = zeros((max(size(C))),5);	Preallocate matrix for data
for n = 4:1:(max(size(C)));	Specify number of for loops
if C(n-3,3) = = 1;	If transit-time for 4 to 1 is good...
if C(n-3,2) = = 1;	If transit-time for 3 to 1 is good...
if C(n-3,1) = = 1;	if transit-time for 2 to 1 is good...
data(n-3,1) = PeakAmp(n-3,1);	Take peak 1
data(n-3,2) = PeakAmp(n-2,1);	Take peak 2
data(n-3,3) = PeakAmp(n-1,1);	Take peak 3
data(n-3,4) = PeakAmp(n,1);	Take peak 4

```
data(n-3,5) = dT(n-3,3);                    Specify total transit-time
end                                         End loop
end                                         End loop
end                                         End loop
end                                         End loop
clear n time                                Clear specific workspace variables

data2 = zeros(size(data));                  Preallocate matrix for data
C = ((data(:,1:4))) <10;                    Create binary vector for data less than 10 Volts
GOOD = [1 1 1 1];                           Data is good if all four columns is less than 10 Volts
for o = 1:1:length(C);                      Specify number of for loops
if all(C(o,1:4) = = GOOD);                  If data is "good"...
data2(o,:) = data(o,:);                     Transfer data to new matrix
end                                         End loop
end                                         End loop
clear C GOOD o                              Clear specific workspace variables

NumberRows = max(data2);                    Determine size of data
C = data2>0;                                Create logic array for positive values in data2
GOOD = [0;1;0;0;0];                         Makes sure bursts of cells don't overlap in time
data3 = nan(size(data));                    Pre-allocate memory for data2 by creating a column vector
                                            of NaNs.
for o = 5:1:length(data2);                  Specify number of for loops
if all(C ( (o-4) : (o) ,3) = = GOOD);       If bursts that don't overlap in time...
data3(o-3,:) = data2(o-3,:);                Transfer data to new vector
end                                         End loop
end                                         End loop
```

clear o	Clear specific workspace variables
data3 = data3(isfinite(data3(:,1)),:);	Remove NaNs from DATA3.
FinalData = sortrows(data3,5);	Sort data based upon transit time.
clear o GOOD DataSize C data2 data PeakAmp NumberRows data3	Clear specific workspace variables

FinalData is a 5-column matrix that is organized with as Beam 1, Beam 2, Beam 3, Beam 4, and Transit-Time from Beam 1 to Beam 4. It can be immediately used for histograms, statistical analysis, scatter plots, etc...

D.3 Frequency-Domain FLIM Numerical Simulations

Command	Comment
clc;	Clears command window
clear;	Clears Workspace variables
m1 = sbiomodel('untitled');	Create SimBiology Model
c1 = addcompartment(m1, 'unnamed');	Add compartment to model
cs1 = getconfigset(m1, 'default');	Assign variable name to object
set(cs1, 'StopTime', 0.0001);	Assign duration of time for simulation
set(cs1, 'SolverType', 'sundials');	Assign simulation solver type
set(cs1.CompileOptions, 'DimensionalAnalysis', false);	Turn off dimensional analysis
p1 = addparameter(m1, 'k1', 1.0);	Add rates to model
p2 = addparameter(m1, 'k2', 1.0);	Add rates to model
set(p1, 'ConstantValue', false);	Turn off constant value for parameter 1

rule1 = addrule(m1, '(1.25E6+2.5E6*sin(25E6*time))-k1');	Add Rule for Time-Dependent Excitation
s1 = addspecies(c1, 'S0');	Add Ground-State as a Species
s2 = addspecies(c1, 'S1');	Add Excited-State as a Species
r1 = addreaction(m1, 'S0 -¿ S1');	Add excitation reaction to model
k1 = addkineticlaw(r1, 'Unknown');	Set rate of excitation to 'Unknown' reaction type
set(r1, 'ReactionRate', 'k1*S0');	Configure excitation rate equations
set(p1, 'ValueUnits', '1/second');	Configure excitation rate units
set(s1, 'InitialAmount', 10000.0);	Configure initial number of ground-state molecules
set(s1, 'InitialAmountUnits', 'molecule');	Configure ground-state units
r2 = addreaction(m1, 'S1 -¿ S0');	Add emission reaction to model
k2 = addkineticlaw(r2, 'MassAction');	Add kinetic law to emission
set(k2, 'ParameterVariableNames', 'k2');	Add emission rate-constant to model
set(p2, 'Value', 2500000.0);	Set rate of emission
set(p2, 'ValueUnits', '1/second');	Set units for rate of emission
set(s2, 'InitialAmountUnits', 'molecule');	Configure excited-state units
s4 = addspecies(c1, 'F');	Add species to model as proxy for fluorescence
rule3 = addrule(m1, 'F = S1*k2*.1');	Add rule to calculate species F
set(rule3, 'Rule', 'F = S1*k2*.1');	Redefine rule for species F
set(rule3, 'RuleType', 'repeatedAssignment')	Set assignment to repeated for F
cs = getconfigset(m1, 'default');	Retrieve configuration settings
(t-ode, x-ode, names) = sbiosimulate(m1);	Run Simulation
y=[x-ode(:,1)];	Retrieve signal from column 1 of x-ode
x=[t-ode];	Retrieve time axis from t-ode
hold on;	Prepare to graph data
plot(x,y,'–');	Plot data

title('Photokinetics');	Add title
xlabel('Time (s)')	Add x-axis
ylabel('FLIM');	Add y-axis
hold off	Finish modifying plot

Additional data is available in the variable x-ode, including the populations of the ground-state (S0), excited state (S1), the proxy for fluorescence (F), and the rate of excitation (k_1). The variable 'names' provides the order at which these variables are stored within x-ode. Numerical simulations are easier to set up in the "SimBiology" workspace provided by Matlab. However, generating a script for the simulations allows you to place the entire simulation within a loop, greatly facilitating simulations where one parameter needs to be iteratively adjusted.

D.4 I/Q Demodulation Simulation

Command	Comment
clc;	Clears command window
clear;	Clears Workspace variables
t=1E-9:1E-9:1E-2;	Create time vector in 1 ns steps to 10 ms
LOphaseDelay=5;	Local-Oscillator Arbitrary Phase Delay in Degrees.
RFphaseDelay=0;	Fluorescence Phase Delay in Degrees
NoiseAmplitude=0.01;	Amplitude of Additive Noise in Volts
threshold=0.05;	Threshold for peak detection.
sig1=8*exp(-(((t-2E-3)$\hat{}$2))/(4E-4)$\hat{}$2);	First signal, 400 μs standard deviation, centered at 2 ms
sig2=1*exp(-(((t-7E-3)$\hat{}$2))/(7E-4)$\hat{}$2);	Second signal, 700 μs standard deviation, centered at 7 ms
freqModSig=0.5*sin((2*pi*29.5E6)*t+ ((RF-phaseDelay*pi)/180))+0.5;	Local Oscillator Signal

freqModQ=sin(2*pi*29.5E6*t+ (LOphaseDelay*180/pi));	Local Oscillator for Q
freqModI=cos(2*pi*29.5E6*t+ (LOphaseDelay*180/pi));	Local Oscillator for I
noise=NoiseAmplitude.*randn(1,1E7);	Generate randomly distributed noise
sig=((sig1+sig2).*freqModSig)+noise;	Combine Oscillator, Gaussian Pulses, and noise
sigThresh=sig¡threshold;	Find values in signal that are below threshold
mixQ=timeseries(freqModQ,t);	Generate Local Oscillator timeseries for Q
mixI=timeseries(freqModI,t);	Generate Local Oscillator timeseries for I
signal=timeseries(sig,t);	
clear sig1 sig2 freqModI freqModQ sig freqModSig noise	Delete specific workspace variables
ACsig=idealfilter(signal,[0 5E4],'notch');	Create low-pass filter between 0 and 50k Hz.
DCsig=idealfilter(signal,[5E4 1E9],'notch');	Create high-pass filter between 50k and 1E9 Hz.
ACsigQ=ACsig.*mixQ;	Frequency Homodyne in Q Channel
ACsigI=ACsig.*mixI;	Frequency Homodyne in I Chanel
ACsigQMix=idealfilter(ACsigQ,[5E4 1E9],'notch');	Apply low-pass filter to signal
ACsigIMix=idealfilter(ACsigI,[5E4 1E9],'notch');	Apply low-pass filter to signal
clear mixQ mixI ACsigI ACsigQ	Delete specific workspace variables
ACsigQMixData = getdatasamples(ACsigQMix, [1:1E7]);	Retrieve Q data
ACsigIMixData = getdatasamples(ACsigIMix, [1:1E7]);	Retrieve I data

Q=[];	Assemble Q vector from data structure.
I=[];	Assemble Q vector from data structure.
for i=1:1:1E7	Specify limits of for loop
Q(i,1)=ACsigQMixData(1,1,i);	Retrieve Q data
I(i,1)=ACsigIMixData(1,1,i);	Retrieve I data
end	End loop
ACsigQMixData(sigThresh)=[];	Apply threshold
clear ACsigQMixData ACsigIMixData	Clear specific workspace variables
ratio=timeseries(atan(Q./I),t);	Takes ratio, and arctangent to retrieve phase
plot(ratio);	Plots phase as a function of time
hold on;	Holds plot for adding additional variables
plot(DCsig);	Adds original low-frequency component to the plot
hold off;	Ends hold on plot

This script closely mimics the electronics that we have built for phase-detection. The DCsig vector resembles the standard fluorescence intensity signal that we use for photobleaching detection. The high-frequency component is AC-coupled, and I/Q demodulated, and the resulting waveform of I and Q resembles the DCsig vector. The arctangent of the ratio of Q/I however, provides a square-wave, and the amplitude of this waveform is directly proportional to the fluorescence phase-shift due to high-frequency excitation.

D.5 Photobleaching Spline-Fit and Curve-Fitting

Command	Comment
clc;	Clears command window
clear;	Clears Workspace variables

data = importdata('file-name.csv');	Import data file to be analyzed.
[signalMax , timeMax] = max(data);	Determine maximum value of signal, and time at which it happens.
data2 = data;	Reorient data into a column
data2(1:timeMax-1) = [ ];	Eliminates duration of time prior to laser trigger.
linearX = 1:1:numel(data2);	Create linear time array same size as data.
splineFit = csaps(linearX, data2, .5);	Perform spline fit.
splineY = [ ];	Create empty vector for spline fit values.
splineX = $10.^{(0:0.1:5.7)}$;	Create vector of equally-spaced in log-time time-points
for i = $10.^{(0:0.1:5.7)}$	Specify number of for loops
splineY = [splineY, fnval(splineFit, i)];	Retrieve data values from spline-fit at each time-point
end	End loop
splineY = splineY./max(splineY);	Normalize spline-fit.
(xData,yData)=prepareCurveData(splineX(1:27),splineY(1:27));	Fit Dark-State Conversion decay (First 1/2 millisecond).
ft1 = fittype('a*exp(-x/b) + c', 'independent', 'x', 'dependent', 'y');	Specify fit options
opts = fitoptions(ft1);	Set fit options
opts.Display = 'Off';	
opts.Lower = [0 1 0];	Specify lower bounds
opts.StartPoint = [max(splineY) 50 0.7];	Specify starting values
opts.Upper = [1 2000 1];	Specify upper bounds
(fitResultDSC, gofResultDSC) = fit(xData, yData, ft1, opts);	Fit model to data.

(xData, yData) = prepareCurve-	Fit photobleaching decay (time beyond 1/2 millisecond).
Data(splineX(30:end),splineY(30:end));	
ft2 = fittype('a*exp(-x/b) +c*exp(-x/d) + e', 'in-	Specify fit options
dependent', 'x', 'dependent', 'y');	
opts = fitoptions(ft2);	Set fit options
opts.Display = 'Off';	
opts.Lower = [0 100 0 100 0];	Specify lower bounds
opts.StartPoint = [max(splineY) 2000	specify starting points
max(splineY) 4000 0];	
opts.Upper = [inf inf inf inf 1];	Specify upper bounds
(fitResultPB, gofResultPB) = fit(xData, yData,	Fit model to data.
ft2, opts);	
(xData, yData) = prepareCurve-	Fit entire decay to triexponential decay.
Data(splineX,splineY);	
ft3 = fittype('a*exp(-x/b) +c*exp(-x/d) +	Set up fittype and options.
e*exp(-x/f)+g', 'independent', 'x', 'dependent',	
'y');	
opts = fitoptions(ft3);	Set fit options
opts.Display = 'Off';	
opts.Lower = [0 0 0 0 0 0 0];	Specify lower bounds
opts.StartPoint = [(fitResultDSC.a + fitRe-	Specify start points from previous fits
sultDSC.c) fitResultDSC.b fitResultPB.a	
fitResultPB.b fitResultPB.c fitResultPB.d	
fitResultPB.e];	
opts.Upper = [inf inf inf inf inf inf inf];	Specify upper bounds

(fitResultFinal, gofResultFinal) = fit(xData, yData, ft3, opts);	Perform final triexponential fit
figure;	Create a new figure
hold on;	Have all changes made to existing figure
plot-name = input('Save plot as: ', 's');	Prompt to save plot and data
data-plot = subplot(2,1,1);	Create subplot
h = plot(fitResultFinal, splineX, splineY);	Plot final fit over spline-fit
set(gca,'XScale','log');	Set x-axis to log in time
xlim([min(xData), max(xData)]);	Constrain axis limits to the minimum and maximum values
legend(h, 'Photobleaching Decay', 'Tri-Exponential Fit', 'Location', 'NorthEast');	Provide a legend
xlabel('Time (microseconds)');	Label x-axis
ylabel('Normalized Photobleaching Decay');	Label y-axis
grid on	Turn grid on
title(plot-name,'fontsize',12);	Add plot name as title
data-plot = subplot(2, 1, 2);	Create subplot
h = plot(fitResultFinal,xData, yData, 'Residuals');	Plot residuals
set(gca,'XScale','log');	Set x-axis to log in time
legend('Residuals', 'Zero Line', 'Location', 'North-East');	Provide a legend
xlabel('Time (microseconds)');	Label x-axis
ylabel('Residuals');	Label y-axis
grid on	Turn grid on
xlim([min(xData), max(xData)]);	Constrain axis limits to the minimum and maximum values

hold off;	Turn hold off
saveas(data-plot, plot-name, 'fig');	Specifies figure name
save(plot-name);	Saves figure

The code here executes an iterative fitting procedure, was designed for photobleaching decays that involve a substantial mount of dark-state conversion, and therefore anticipates a prominent dark-state conversion decay followed by a more gradual irreversible decay. The code first fits the dark-state conversion decay, then the irreversible decay, and then combines the results from these fits into a starting point of the final triexponential fit.